Spray and Combustion for Aerospace Propulsion Applications

Lead Guest Editor: Qiaofeng Xie
Guest Editors: Wei Lin and Zhaoxin Ren,

Spray and Combustion for Aerospace Propulsion Applications

Spray and Combustion for Aerospace Propulsion Applications

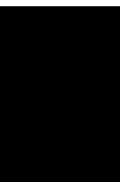Lead Guest Editor: Qiaofeng Xie
Guest Editors: Wei Lin and Zhaoxin Ren,

Contents

Research Article

Effects of Flow Compressibility on Two-Phase Mixing in Supersonic Droplet-Laden Flows

Zhaoxin Ren [1], **Bing Wang** [2], **and Fan Zhang** [3]

[1]*School of Power and Energy, Northwestern Polytechnical University, Xi'an 710072, China*
[2]*School of Aerospace Engineering, Tsinghua University, Beijing 100084, China*
[3]*China Academy of Launch Vehicle Technology, Beijing 100076, China*

Correspondence should be addressed to Zhaoxin Ren; renzhaoxin@nwpu.edu.cn

This research addresses a numerical analysis on the effects of flow compressibility on the characteristics of droplet dispersion, evaporation, and mixing of fuel and air according to the simulation of the spatially developing supersonic shear flows laden with evaporating *n*-decane droplets. A sixth-order hybrid WENO numerical scheme is employed for capturing the unsteady wave structures. The influence of inflow convective Mach number (M_c), representing the high-speed flow compressibility, on the two-phase mixing is analyzed, in which M_c is specified from 0.4 to 1.0. It is found that the shearing vortex is compressed spatially as M_c increases, associated with the alternate distributions of compression and expansion regimes in the flow field. The flow compressibility changes not only the vortex structures but also the aerothermal parameters of the shear flows, and further influences the dispersion and evaporation of droplets. The two-phase mixing efficiency is observed to decrease as M_c increases.

1. Introduction

Supersonic shear layer laden with dispersed fuel droplets is considered as the physical model for the supersonic c-based engine [1–4]. The research on supersonic two-phase flow includes the dispersion of sprayed droplet, the droplet evaporation, and the mixing between fuel vapors and air in the carrier phase, which are very important and complicated scientific issues for supersonic multiphase flow and combustion.

The unsteady entrainment due to the vortex dynamics promotes the fuel-oxidant mixing in supersonic shear flows. The velocity difference between the two parallel shearing flows results in the momentum transfer from the high-speed flow to the low-speed side, associated with the mass and heat transfer. The motion of vortices control the mixing process, and chemical reaction will not begin until the mixing reaches the molecular level. Therefore, the studies on the features of vortices with multiscales and their influence on combustion are of importance for engineering applications. Brown and Roshko [5] first found that the unsteady vortices

have coherent structures when they experimentally studied the incompressible shear layers. The large-scale vortices formed in the shearing have a significant on the energy transport and mixing of species [6]. There are various sizes of flow structures in the shear layer. The Reynolds number, Re, dominates the scale of the eddy structure. As Re increases, the small-scale vortex structures are found to be more and more abundant. For the compressible shear layers, the flow compressibility is of importance for the flow dynamics, and the convective Mach number, $M_c = \Delta U/(a_1 + a_2)$, characterizes the flow compressibility (where a_1 and a_2 are the sound velocity of two streams). In addition, there are parameters, such as density ratio of two shear flows, gradient of velocity and pressure, and heat release, which are found to have an effect on the dynamics of the shear layer.

For the compressible shear layer, the variation of convective Mach number influences the development of the shear layer [7]. Clemens and Mungal [8] experimentally studied the compressible flow. They found that the shear flow develops more slowly with the increase of M_c, and the flow

with higher speed has a more significant suppression. Kourta and Sauvage [9] and Vreman et al. [10] applied numerical simulations and indicated that the initiation of vortex shedding is depressed as the flow compressibility is intensified. In particular, as the M_c rise above 1.2, the pairing process of vortices cannot be formed. Wang et al. [11] investigated the mixing process of supersonic shear layers by numerical simulations and focused on the influence of flow compressibility and gradients of velocity and density on the mixing efficiency. The results showed that the growth rates of shear layer and mixing efficiency are reduced with the increase of M_c. The increasing density ratio enlarges the shear layer thickness but has a negative effect on the mixing efficiency. The mixing efficiency is promoted but the shear layer thickness decreases with the increase of velocity ratio. In addition, the level of turbulence fluctuations represents the strength of turbulent eddies, and the previous researchers investigated the influence of flow compressibility on the turbulence fluctuations. Elliott and Samimy [12] applied the experimental studies on the compressible shear layer with High Re and showed that the fluctuating velocities and Reynolds stresses are reduced with the increase of M_c. Olsen and Dutton [13] used particle image velocimetry (PIV) for obtaining the velocity fields of the shear layer with weak compressibility. They found that the fluctuation of transverse velocity and Reynolds shear stress is reduced but the fluctuation of streamwise velocity remains constant, as compared with the incompressible flow. Pantano and Sarkar [14] numerically analyzed the turbulent shear layer with subsonic and supersonic speeds and found that the decrease of pressure-strain term contributes to the reduction of the turbulent fluctuation and the decreasing growth rate of the shear layer. Atoufi et al. [15] measured the compressible shear flow by large eddy simulations and studied the kinetic energy exchange. Their results showed that the production term is suppressed with the enhancement of flow compressibility, which results in the deceleration of the shear layer growth rate. The turbulent viscous dissipation term is also suppressed due to the increase of the flow compressibility.

The previous research provides a wealth of information on the characteristics of the shear layer thickness and the fluctuations of turbulence in the compressible shear layer flow. In general, the growth rate of the supersonic shear layer thickness is suppressed with the enhancement of the flow compressibility. The increase of M_c leads to the suppression of pressure fluctuations, which prohibits the momentum transfer between the vortices, associated with the decrease of entrainment rates. In addition, the reduction of the production terms from the turbulent kinetic energy correlates with the suppression of the turbulent diffusion. However, it is noteworthy that the studies are absent for the influence of the flow compressibility on the droplet evaporation and two-phase mixing in supersonic shear flows despite its importance for understating the physics of the spray combustion in the supersonic flow. The previous research has shown that the high-speed flow compressibility affects the flow dynamics, which can expect to influence the dispersion and evaporation of droplets and fuel-air mixing. Furthermore, the ignition and flame will be altered in the supersonic combustor of the scramjet. The related physics should be revealed.

The present study is aimed at evaluating the impact of flow compressibility on the two-phase mixing in a supersonic shear layer laden with fuel (n-decane, $C_{10}H_{22}$) droplets. The numerical simulations with high order schemes are applied to mimic the unsteady two-phase flow. The convective Mach number (M_c) increases from 0.4 to 1.0. The remainder of this paper is organized as follows. The governing equations, numerical methods, and validations are introduced in Section 2. The results are presented in Section 3, including the effects of flow compressibility on the carrier flow, and the features of droplet dispersion, evaporation, and fuel-air mixing. Finally, the concluding remark and discussion are drawn in Section 4.

2. Governing Equations and Numerical Methods

2.1. Governing Equations for Fluid Phase. In this paper, the motion of inertial evaporating fuel droplets is considered in the compressible shear layer. The governing equations, comprising the equations of mass, momentum, and energy and transport equations of three chemical species ($C_{10}H_{22}$, O_2, N_2), supplemented by the equation of state for the ideal multispecies gas, are solved in the following form:

$$\frac{\partial \rho}{\partial t} + \frac{\partial}{\partial x_j}\left(\rho u_j\right) = S_m, \tag{1}$$

$$\frac{\partial}{\partial t}\left(\rho u_i\right) + \frac{\partial}{\partial x_j}\left(\rho u_i u_j + P\delta_{ij} - \tau_{ij}\right) = S_{F,i}, \tag{2}$$

$$\frac{\partial}{\partial t}\left(\rho e_t\right) + \frac{\partial}{\partial x_j}\left(\left(\rho e_t + P\right)u_j - u_i \tau_{ij} - q_j\right) = S_Q, \tag{3}$$

$$\frac{\partial}{\partial t}\left(\rho Y_k\right) + \frac{\partial}{\partial x_j}\left(\rho Y_k u_j\right) + \frac{\partial}{\partial x_j}\left(\rho Y_k\left(V_{k,j} + V_j^c\right)\right) = S_{Y_k}, \tag{4}$$

$$P = \rho R T \sum_{k=1}^{N_S} \frac{Y_k}{W_k}, \tag{5}$$

where ρ is the density, u_i is the velocity in the ith direction, P is the static pressure, and T is the temperature. R is the universal gas constant. e_t is the total energy (kinetic energy plus internal energy) and is defined as

$$e_t = \sum_{k=1}^{N_S} Y_k\left(\int_{T_{ref}}^{T} c_{p,k}\,dT + h_{f,k}^0\right) - \frac{P}{\rho} + \frac{u_i u_i}{2}. \tag{6}$$

$c_{p,k}$ is the specific heat capacity at constant pressure, and $h_{f,k}^0$ is the specific chemical formation enthalpy at the reference temperature, T_{ref}. The values of $c_{p,k}$ are calculated by a fifth-order polynomial [16]. τ_{ij} is the Newtonian viscous stress tensor, and μ is the viscosity. Y_k is the mass fraction of the kth species. $Vc\,j$ is the correction velocity. N_S is the total number of the chemical species, and W_k is the molecule weight of the kth species. For the transport properties, the

kinetic theory [17] for a gaseous mixture is utilized. In particular, the Lennard-Jones potentials are used to obtain the intermolecular forces. The heat conductivity of each species is calculated by using the modified Eucken model. The dynamic viscosity and the binary diffusion coefficient are from the Chapman-Enskog theory.

$$\mu_k = \frac{26.69\sqrt{W_k T}}{\sigma_k^2 \Omega_{v,k}}, \tag{7}$$

$$\frac{\lambda_k W_k}{\mu_k C_{v,k}} = 1.32 + \frac{1.77}{(C_{p,k}/R) - 1}, \tag{8}$$

$$D_{AB} = \frac{0.00266 T^{3/2}}{P W_{AB}^{1/2} \sigma_{AB}^2 \Omega_D}. \tag{9}$$

Here, σ_k is the hard-sphere diameter of the kth species. D_{AB} is the diffusion coefficients for the binary gas A and B, W_{AB} is the combined molecular weights of A and B. σ_{AB} is the characteristic length of the intermolecular force law, and Ω_D is the collision integral for diffusion. The semiempirical expressions proposed by Wake and Wassiljewa are used to calculate the dynamic viscosity, μ, and heat conductivity, λ, of the gaseous mixture. The right-hand side terms S_m, $S_{F,i}$, and S_Q describing the interphase couplings of mass, momentum, and energy, respectively, and they are calculated via summing the total number of droplets N, existing in the grid, ΔV, of the gas phase calculation,

$$S_m = -\frac{1}{\Delta V} \sum_N (\dot{m}_d), \tag{10}$$

$$S_{F,i} = -\frac{1}{\Delta V} \sum_N (F_{d,i} + \dot{m}_d u_{d,i}), \tag{11}$$

$$S_Q = -\frac{1}{\Delta V} \sum_N \left(Q_d + \dot{m}_d \left(\frac{u_{d,i} u_{d,i}}{2} + h_{V,sf} \right) \right), \tag{12}$$

$$S_{Y_k} = \begin{cases} -\frac{1}{\Delta V} \sum_N (\dot{m}_d) & \text{for fuel,} \\ 0 & \text{for other species.} \end{cases} \tag{13}$$

Here, m_d and $\dot{m}_d$ are the droplet mass and the mass change rate, respectively. $u_{d,i}$ is the droplet velocity. $h_{V,sf}$ is the evaporated vapor enthalpy at the droplet surface.

2.2. Governing Equations for Droplet Phase. The dispersion of individual droplet in the supersonic flow is tracked by using the Lagrangian trajectory model. The droplets are considered as sparsely dispersion, and the droplets do not influence each other. The drag force due to the interphase slip velocity acting on the droplet is modeled, and the heat convection is calculated. Under the assumption made as such, the position ($x_{d,i}$), velocity ($u_{d,i}$), temperature (T_d), and mass (m_d) of a single droplet are controlled by the following equations [18]:

$$\frac{dx_{d,i}}{dt} = u_{d,i}, \tag{14}$$

$$\frac{du_{d,i}}{dt} = \frac{F_d}{m_d} = \left(\frac{f_F(Re_d)}{\tau_d} \right) (u_{i@d} - u_{d,i}), \tag{15}$$

$$\frac{dT_d}{dt} = \frac{Q_d + \dot{m}_d L_V}{m_d c_L} = \left(\frac{f_Q}{\tau_d} \right) \left(\frac{Nu}{3 Pr} \right) \left(\frac{c_p}{c_L} \right) (T_{@d} - T_d) + \left(\frac{\dot{m}_d}{m_d} \right) \frac{L_V}{c_L}, \tag{16}$$

$$\frac{dm_d}{dt} = \dot{m}_d = -m_d \left(\frac{1}{\tau_d} \right) \left(\frac{Sh}{3Sc} \right) \ln(1 + B_M), \tag{17}$$

where $u_{i@d}$ and $T_{@d}$ are the velocity and temperature of carrier flow at the droplet position. c_p is the specific heat of gas surrounding the droplet, c_L is the specific heat of the droplet, and L_V is the latent heat from evaporation. The momentum response time, τ_d, is as follows,

$$\tau_d = \frac{\rho_d d_d^2}{18\mu}, \tag{18}$$

where d_d is the droplet diameter. For the drag force, the correction function, $f_F(Re_d)$, for the influence of droplet Reynolds number, Re_d, is

$$f_F(Re_d) = \frac{Re_d}{24} \left(\frac{24}{Re_d} \left(1 + 0.15 Re_d^{0.687} \right) + \frac{0.42}{1 + 42500 Re_d^{-1.16}} \right) \text{ for } Re_d < 2 \times 10^5. \tag{19}$$

$Re_d = |u_i - u_{d,i}| d_d / \nu$ is based on the slip velocity between the droplet and the local gas. $Pr = \mu c_p / \lambda$ and $Sc = \mu / \rho D$ are Prandtl and Schmidt numbers, respectively. The Nusselt and Sherwood numbers are $Nu = 2 + 0.552 Re_d^{1/2} Pr^{1/3}$ and $Sh = 2 + 0.552 Re_d^{1/2} Sc^{1/3}$, respectively. The evaporation rate of droplets is calculated according to the mass transfer number, $B_M = (Y_{sf} - Y_V)/(1 - Y_{sf})$. Y_V is the fuel mass fraction on the far-field, and Y_{sf} is the fuel mass fraction at the droplet interface, which is obtained directly from the surface molar fraction (χ_{sf}) based on a nonequilibrium evaporation model [19],

$$Y_{sf} = \frac{\chi_{sf}}{\chi_{sf} + (1 - \chi_{sf}) W/W_V}, \tag{20}$$

$$\chi_{sf} = \frac{P_{atm}}{P} \exp \left(\frac{L_V}{R/W_V} \left(\frac{1}{T_{B,L}} - \frac{1}{T_d} \right) \right) - \frac{2L_k}{d_d} \beta, \tag{21}$$

$$L_k = \frac{\mu(2\pi T_d(R/W_V))^{1/2}}{ScP}. \tag{22}$$

W is the molecular weight of the carrier gas, W_V is the molecular weight of the fuel vapor, P_{atm} is the atmospheric pressure, and $T_{B,L}$ is the liquid boiling temperature at P_{atm}. L_k is the Knudsen layer thickness.

2.3. Numerical Methods. The supersonic shear flow laden with droplets is simulated by our in-house code, which has been utilized for the studies of supersonic flow and two-phase reacting flow [18, 20]. The numerical methods are summarized below. A finite difference methodology is performed. The convection fluxes are calculated by an
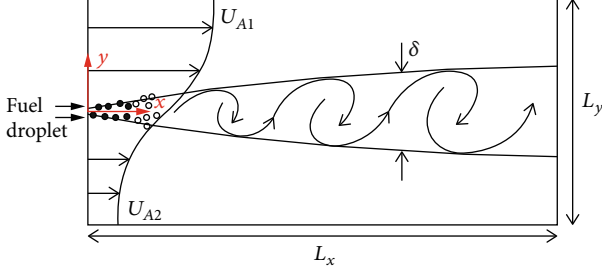
FIGURE 1: Schematic of the supersonic shear layer laden with droplets released from the inlet center.

adaptive central-upwind sixth-order WENO (WENO-CU6) scheme [21] for obtaining the smooth turbulent fields and for capturing the eddy shocklets and complex waves in the supersonic flow with strong compressibility. The viscous terms are discretized according to a sixth-order symmetrical compact difference scheme. For the time advancement of the governing equations for the gas phase, a third-order explicit Runge-Kutta method is applied. A third-order Adams approach is used for the time advancement for the droplet equations. In order to obtain the velocity, temperature, and other properties of the flow around the droplet, a fourth-order Lagrangian interpolation method is utilized. The dispersed droplets are treated as point sources, and the influence of the droplets on the carrier flow is modeled by adding the source terms, S, to the grids around the droplets, namely, the particle-source-in cell (PSI-CELL) model.

2.4. Numerical Setup and Simulation Parameters. The schematic diagram of the present computational configuration is depicted in Figure 1. As shown, the shear layer is formed by the upper and lower streams moving in a same direction with different speeds U_{A1} and U_{A2}. The letters x and y refer to the streamwise and transverse directions, respectively. The streamwise and transverse domain lengths are L_x and L_y, respectively. L_x is set to $3000\delta_0$ and L_y is set to $750\delta_0$. The initial mixing layer thickness is δ_0. By setting $L_x = 4L_y$, the transverse domain size is large enough to have minimal influence on the main interaction region of the droplet-laden shear layer. Stream 1 and 2 are both air ($T = 700$ K, $P = 0.1$ MPa) as a mixture of nitrogen (N_2) and oxygen (O_2) with (in terms of mass fraction) $Y_{N_2} = 0.77$ and $Y_{O_2} = 0.23$. The velocity ratio of two flows, U_{A2}/U_{A1}, equals to 0.6. At the inflow boundary, the streamwise velocity distribution is specified as a hyperbolic tangent profile by using a supersonic inlet boundary condition as follows,

$$u(x = 0, y) = \frac{U_1 + U_2}{2} + \frac{U_1 - U_2}{2} \tanh\left(\frac{y}{2\delta_0}\right),$$

$$v(x = 0, y) = 0. \tag{23}$$

The transverse perturbations are added to the inlet velocity in order to excite the growth of spanwise disturbances, and the random perturbations are added to the transverse component of the inflow velocity based on the most-unstable frequency in the flow field [22],

TABLE 1: Simulation cases.

Case	Mach number, M_{A1}, M_{A2}	Convective Mach number, M_c
0.4 M_c	2.0, 1.2	0.4
0.6 M_c	3.0, 1.8	0.6
0.8 M_c	4.0, 2.4	0.8
1.0 M_c	5.0, 3.0	1.0

- □ - Experiment
—— Simulation
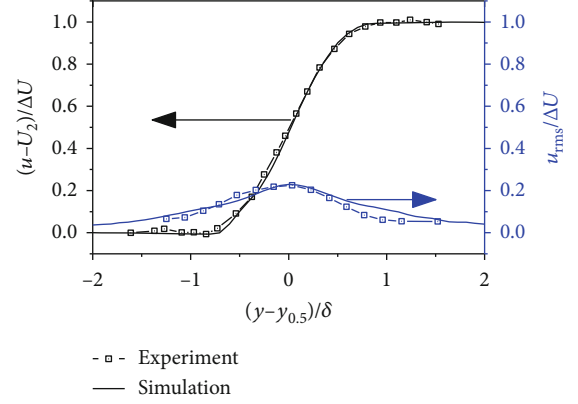
FIGURE 2: Comparison of the simulation results with experiment data for a supersonic shear layer.

$$v'(x = 0, y) = (U_1 - U_2)G(y)A \sin(2\pi f t + \xi),$$

$$u'(x = 0, y) = 0, \tag{24}$$

where $G(y)$ is the Gaussian function, A is the amplitude, and f is the most unstable frequency. The random phase is ξ. The most unstable frequency is usually obtained by means of the flow stability analysis based on the base flow profile given by Eq. [15]. The nonreflecting boundary conditions are set in the transverse directions [23]. At the outlet, the boundary conditions are zero-gradients that are interpolated by assuming first-order derivatives of all flow parameters.

Pure n-decane spray is injected at the centerline with a width of $5\delta_0$. The droplets are initially randomly seeded, with the same size. The initial droplet velocity is identical to the local gas velocity, and the initial droplet temperature is $T_d = 298.15$ K. The liquid fuel is preatomized, and the droplets are considered without further breakup process, since the Weber number based on the slip velocity (the initial velocity between the two phases is zero) is quite small for the concerned droplets in this study.

Table 1 provides the inlet parameters for the present simulation cases. Since the velocity ratio, U_{A2}/U_{A1}, has an important effect on the development of the shear layer flow, the velocity ratio is the same for all the simulation cases and the inflow Mach numbers of two streams; M_{A1} and M_{A2} are changed to study the influence of the flow compressibility and to exclude the interference of other factors. The convection Mach number, M_c, increases from 0.4 to 1.0 in the four simulation cases, associated with the strength of flow
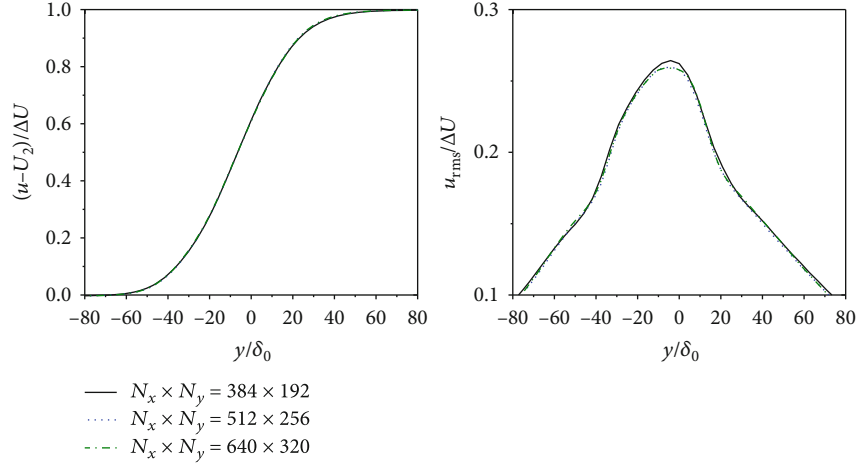
FIGURE 3: Comparison of numerical results at different grid sets: (left) mean streamwise velocity and (right) r.m.s streamwise velocity.
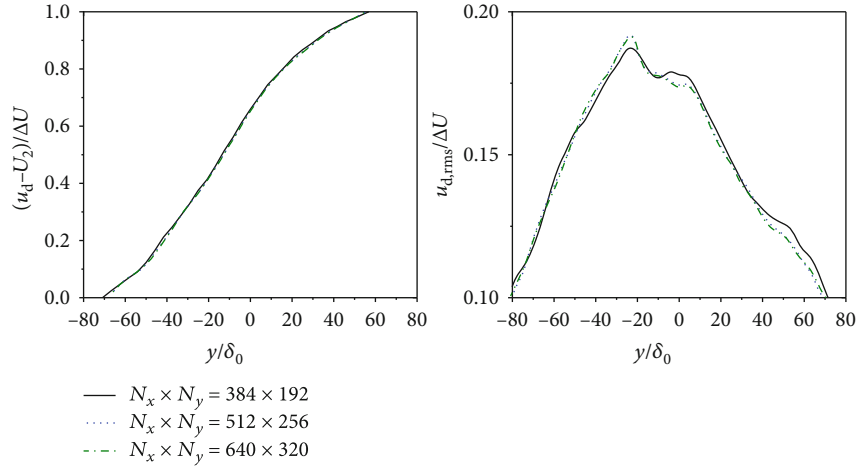
FIGURE 4: Comparison of numerical results at different grid sets: (left) mean streamwise velocity and (right) r.m.s streamwise velocity of droplets.

compressibility. Generally, the shear flow is considered to have strong compressibility with compression waves or shocklets, and the corresponding convection Mach number is $M_c > 0.8$. The present flows in this study consider both weak and strong flow compressibility. The cold droplet is injected into the hot stream to evaporate. The spray equivalence ratio, Φ_0, is defined as $\Phi_0 \cdot (\text{F/O})_{\text{st}} = \dot{m}_{\text{spray}}/(\dot{m}_{\text{air}} Y_{O_2})$. Here, $(\text{F/O})_{\text{st}}$ is the stoichiometric fuel-to-oxidizer ratio. $\dot{m}_{\text{spray}}$ and $\dot{m}_{\text{air}}$ are the mass flow rates of fuel and air, respectively. The high Φ_0 means that more fuel enters the flow field, which causes the influence of the dispersed phase on the local carrier flow (turbulence modulation). In the present study, the effects of flow compressibility are considered, and a low Φ_0 ($\Phi_0 = 0.1$) is selected for all simulation cases. The inflow velocities in these cases are different, and if the initial diameter of the droplets in each case is the same, the residence time of the droplets in the flow is expected to be different. In order to ensure the same residence time of the droplets in different cases, the Vaporization Damköhler number [24], Da_{vapor}, in the four cases keeps the same, and the expression of Da_{vapor} is as follows,

$$\text{Da}_{\text{vapor}} = \frac{t_r}{t_v} = \frac{L_P/\bar{U}_A}{(\rho_d d_d^2 c_p)/12\lambda} \propto \frac{1}{\bar{U}_A d_{d,0}^2}. \tag{25}$$

Here t_r is the residence time of the droplets in the supersonic flow, which is estimated as the ratio of the living distance L_P of the droplets to the averaged inflow velocity, and t_v is the evaporation time of the droplets [25]. Although the residence time and the evaporation time of the droplets are different in each case, the Da_{vapor} is the same and hence the simulation cases become comparable. Therefore, the influence of flow compressibility on the droplet phase can be studied.

2.5. Model Validation. Here, the computation of a supersonic shear layer without droplets is performed for the validation of the ability to simulate the gaseous flow. The experiment data for the supersonic shear layer conducted by Goebel et al. [26] is used for the comparison. The self-similarity profiles of the mean streamwise velocity and the standard deviation of the streamwise velocity are found to be same with the experimental measurements, as shown in Figure 2.

(a)

(b)

(c)

(d)
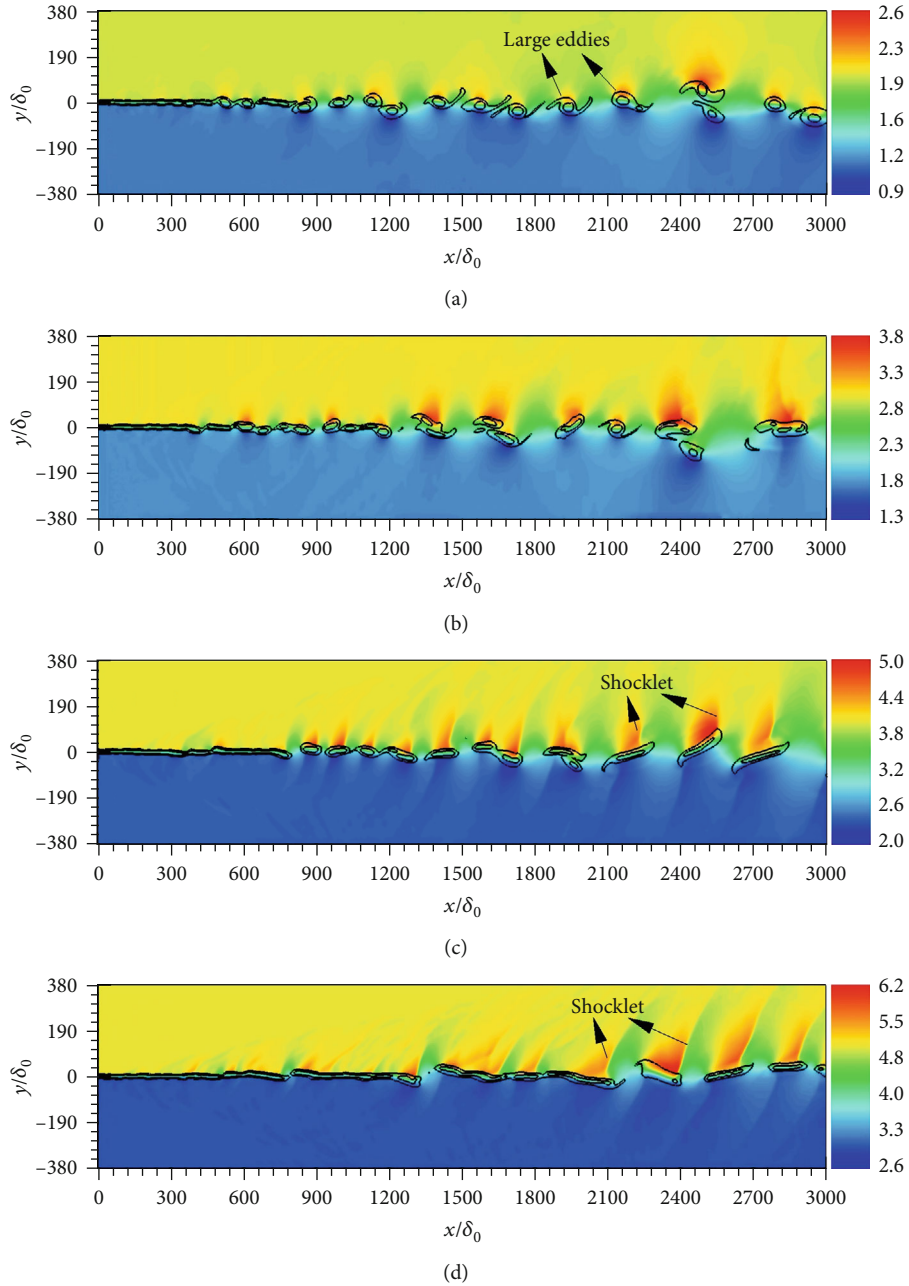
FIGURE 5: Instantaneous distributions of Mach numbers: (a) 0.4 M_c, (b) 0.6 M_c, (c) 0.8 M_c, and (d) 1.0 M_c. Here, the black lines refer to dimensionless spanwise vorticity $(\Omega_z/(\Delta U_A/\delta_0) = [-0.02, -0.005]$.

This validation verifies that the present code has the ability to mimic the supersonic shear flow.

For the droplet evaporation in the sparse spray, the evaporation of single droplet is slightly affected by the surrounding droplets. The numerical simulation is applied for the experiments of a single droplet evaporation [27]. The comparisons between the numerical simulations and experiments show that the nonequilibrium evaporation model used in the present study can reproduce the temporal evolution of the squared droplet diameter [18].

The grid scale should be carefully designed, and the study of grid independence is applied. Three sizes of grids are utilized,
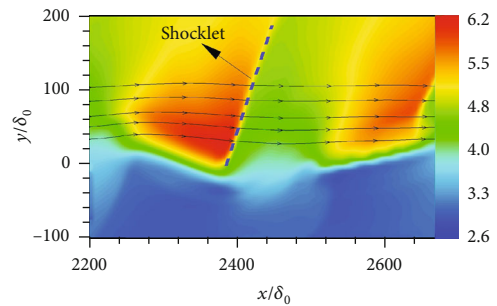
FIGURE 6: Local enlargement of the shocklet in Figure 2(d) with $M_c = 1.0$.
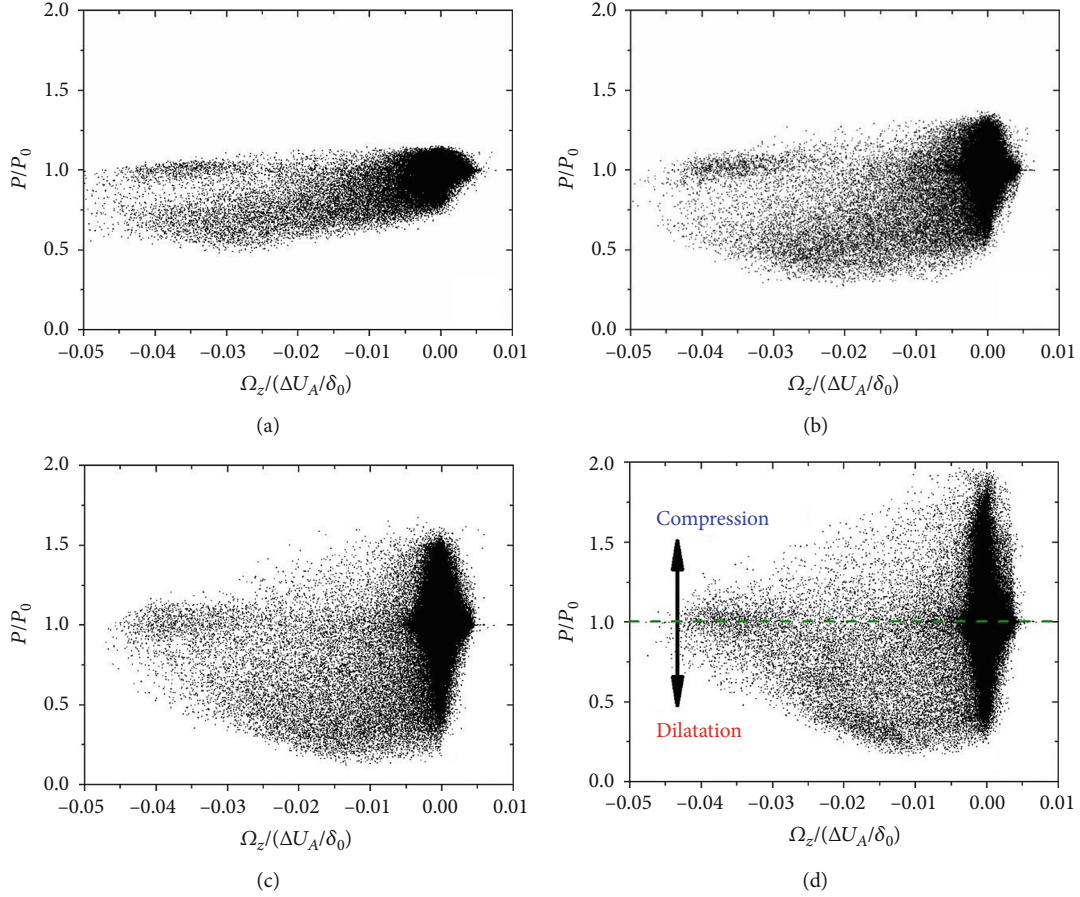
FIGURE 7: Scatter distributions of dimensionless pressure, P/P_0, in the coordinates of dimensionless spanwise vorticity, $\Omega_z/(\Delta U_A/\delta_0)$: (a) 0.4 M_c, (b) 0.6 M_c, (c) 0.8 M_c, and (d) 1.0 M_c.

and the grid numbers in the x and y directions are $N_x \times N_y = 384 \times 192$, 512×256 and 640×320, respectively. Figure 3 shows the statistical results of the mean and r.m.s streamwise velocities from the simulation using different grids, which achieve the self-similarity. It is observed that the independence results are achieved in different grid resolutions. The results from 512×256 and 640×320 are found to agree well.

The study of the grid independence on the statistics of the droplet-phase, including the mean streamwise velocity and r.m.s streamwise velocity of the droplets, is applied, and the results are illustrated in Figure 4. The profiles in different grid resolutions are found to achieve independence as the grid sets increase from 512×256 to 640×320. Based on the grid independence study for both gas-phase and droplet-phase, the computation grids are finally chose as 512×256 for the next-step investigation, considering the calculation costs.

3. Results and Discussion

3.1. Effects of Flow Compressibility on the Flow Features. Figure 5 shows the instantaneous distributions of Mach numbers, M_A, for the cases with M_c increasing from 0.4 to 1.0 without droplet laden. The black lines refer to the dimensionless spanwise vorticity $(\Omega_z/(\Delta U_A/\delta_0)) = [-0.02, -0.005]$ and indicate the shape of large-scale vortices in the shear

layer. For the case with $M_c = 0.4$, it is found that the supersonic flow loses the stability due to the shearing of the two streams, and the Kelvin-Helmholtz (K-H) instability. The flow processes of vortex rolling, shedding, pairing, merging, etc. in the shear layer occur, and the vortex structure is similar to that in the incompressible flow. With the increase of the flow compressibility, the streamwise location where the large-scale vortex begins to shed becomes far, and the shear layer flow is found to become difficult to lose its stability. From the results of the instantaneous flow fields, it is found that the vortex starts to shed at around the dimensionless streamwise distance $x/\delta_0 = 900$ for case 0.4 M_c, while for case 1.0 M_c, the obvious shedding occurs until $x/\delta_0 = 1300$. At the same time, the increasing flow compressibility results in the obvious change of vortex shape from the regular near-circular structure ($M_c = 0.4$) to the strip-shaped flat structure stretched along the streamwise direction ($M_c = 0.8$ and 1.0) with a thinner shear layer thickness. From the spatial distributions of M_A, it is observed that the compression and expansion wave structures appear in the flow field with the increase of M_c, as shown in Figure 5(c) with $M_c = 0.8$, and the shocklets around vortices occur. When M_c increases to 1.0, although the vortex shape becomes flatter, the structure of shocklets becomes more conspicuous, and their intensity is also found to be enhanced. In particular, Figure 6 shows
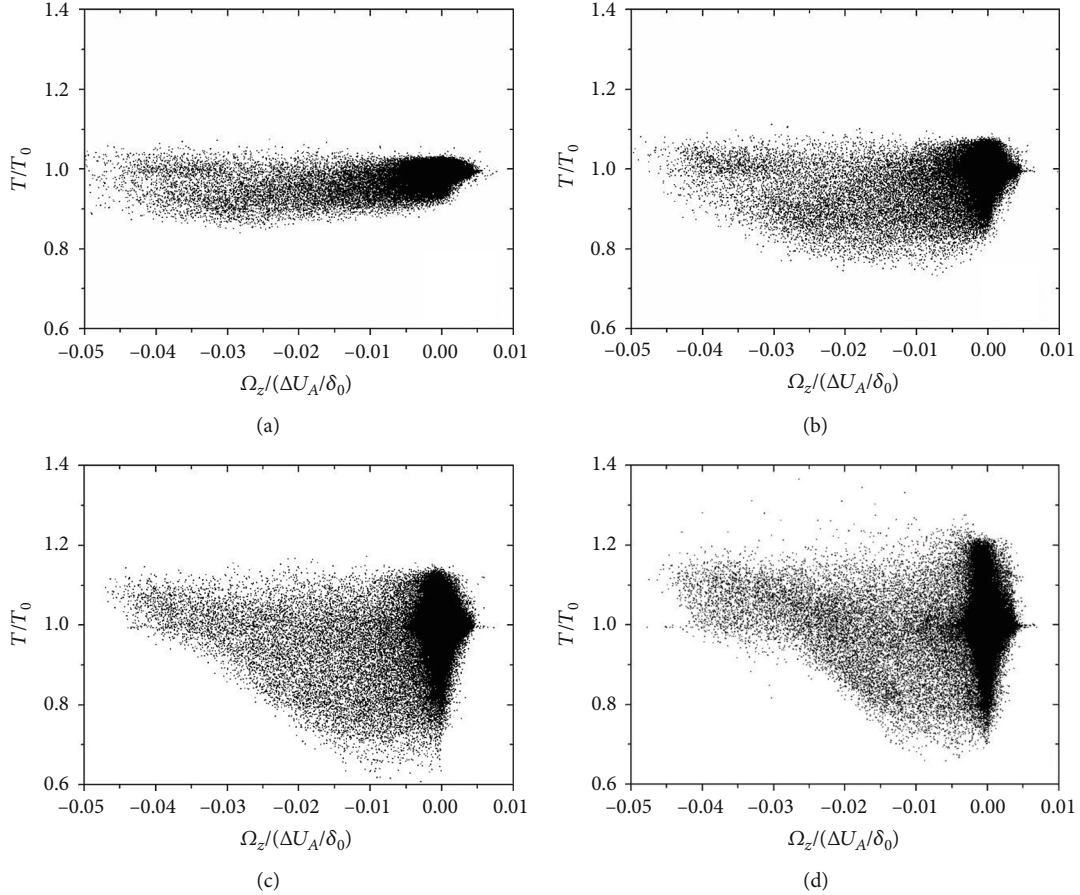
FIGURE 8: Scatter distributions of dimensionless temperature, T/T_0, in the coordinates of dimensionless spanwise vorticity, $\Omega_z/(\Delta U_A/\delta_0)$: (a) 0.4 M_c, (b) 0.6 M_c, (c) 0.8 M_c, and (d) 1.0 M_c.

a shocklet for case 1.0 M_c, and the dashed line characterizes the shocklet with the solid lines indicating the streamlines. It can be found that the Mach number decreases as the airflow passes through the shocklet. The shocklet can be considered as a weak oblique shock wave. If the preshock Mach number is M_1, the flow direction is deflected after the oblique shock wave and the postshock Mach number is M_2. After the measurement of the shock wave angle of the shocklet in Figure 6, the angle is 71.9° and the pressure increase ratio P_2/P_1 equals 3.5. For an oblique shock wave with angle 71.9°, the pressure increase ratio $Posw_2/Posw_1$ is 40.3. Therefore, the intensity of the shocklet is much smaller than the intensity of the oblique shock wave with the same wave angle.

For the supersonic flows with high flow compressibility, the compression waves (shocklets) and expansion waves in the shear flow can lead to the obvious change of local pressure and temperature, which affects the evaporation of fuel droplets in the carrier flow. The distribution of temperature and pressure in the shear layers under the influence of flow compressibility will be analyzed below.

Figure 7 gives the instantaneous distributions of the dimensionless gas pressure, P/P_0, in the coordinates of dimensionless spanwise vorticity for the whole flow field. For case 0.4 M_c, it is found that the maximum value of P/P_0 is around 1.0 and the minimum value is about 0.5. These

indicate that the compression waves are quite weak in the supersonic flow with low compressibility, and the pressure rise resulted from the compression process is unobvious. On the other hand, the expansion effect is relatively obvious. As the flow compressibility increases, such as cases 0.6 M_c and 0.8 M_c, the maximum pressure in the flow field increases significantly, and the values are found to be mainly located in the regions with low vorticity, namely, the high-strain vortex-braids between the vortices, which has relatively strong compression waves and even shocklets. It is also observed that the minimum pressure decreases as M_c increases, indicating that the strength of the expansion waves also increases as the flow compressibility increases. For $M_c = 1.0$, the compression and expansion in the supersonic shear layer flow are further intensified, and the pressure peaks in the high-strain, low-vorticity areas between the vortices is approximately doubled, compared with P_0, while the minimum value is found to have no significant change with that of case 0.8 M_c. A high M_c means that the acoustic time scale, δ/a, is of the same order as the characteristic vortex stretching time scale $\delta/\Delta U$. This leads to the gas pressure to experience strong fluctuations during the turnover of the large-scale vortex, which is of the same order as the dynamic pressure and can also cause strong density fluctuations in the shear layer flow. When the free supersonic stream is entrained
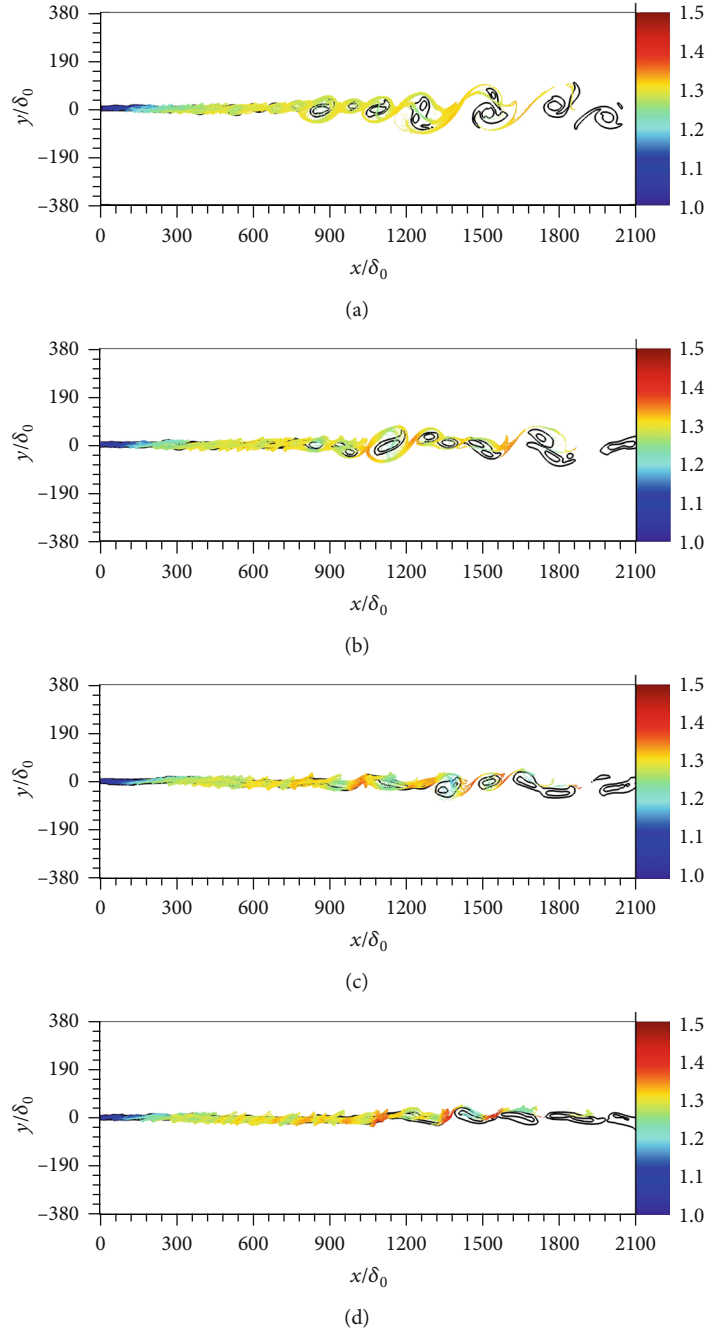
FIGURE 9: Instantaneous distributions of fuel droplets (color corresponding for the dimensionless droplet temperature $T_d/T_{d,0}$): (a) 0.4 M_c, (b) 0.6 M_c, (c) 0.8 M_c, and (d) 1.0 M_c. Here, the black lines refer to dimensionless spanwise vorticity $(\Omega_z/(\Delta U_A/\delta_0) = [-0.02, -0.005]$.

into the shear layer, it can encounter the areas with the decrease of velocity, even subsonic areas. Sometimes, these conditions occur abruptly between vortices carrying supersonic and subsonic flows. These flow regions with strong Mach number fluctuations were called as eddy shocklet [28] or shocklet in the previous research, and the shocklets mainly appear in the flows with higher Mach numbers, as shown by the shocklets in the upper high-speed airflow of Figure 5.

Figure 8 shows the instantaneous distributions of the dimensionless gas temperature, T/T_0, in the coordinates of dimensionless spanwise vorticity for the whole flow field.

For the shear flow with low M_c ($M_c = 0.4$), it is found that the temperature decrease caused by the flow expansion effect is more pronounced than the temperature increase from the compression effect. As the flow compressibility increases, the temperature rise caused by the compression effect becomes obvious. In particular, for cases 0.8 M_c and 1.0 M_c, it is clearly observed that the scatters with the temperature higher than T_0 are mainly concentrated in the regions with low-vorticity. When the free supersonic stream enters the shear layer, the high-speed compressibility causes the kinetic energy of the free stream to be converted into internal energy. Hence, the

(a)

(b)

(c)

(d)
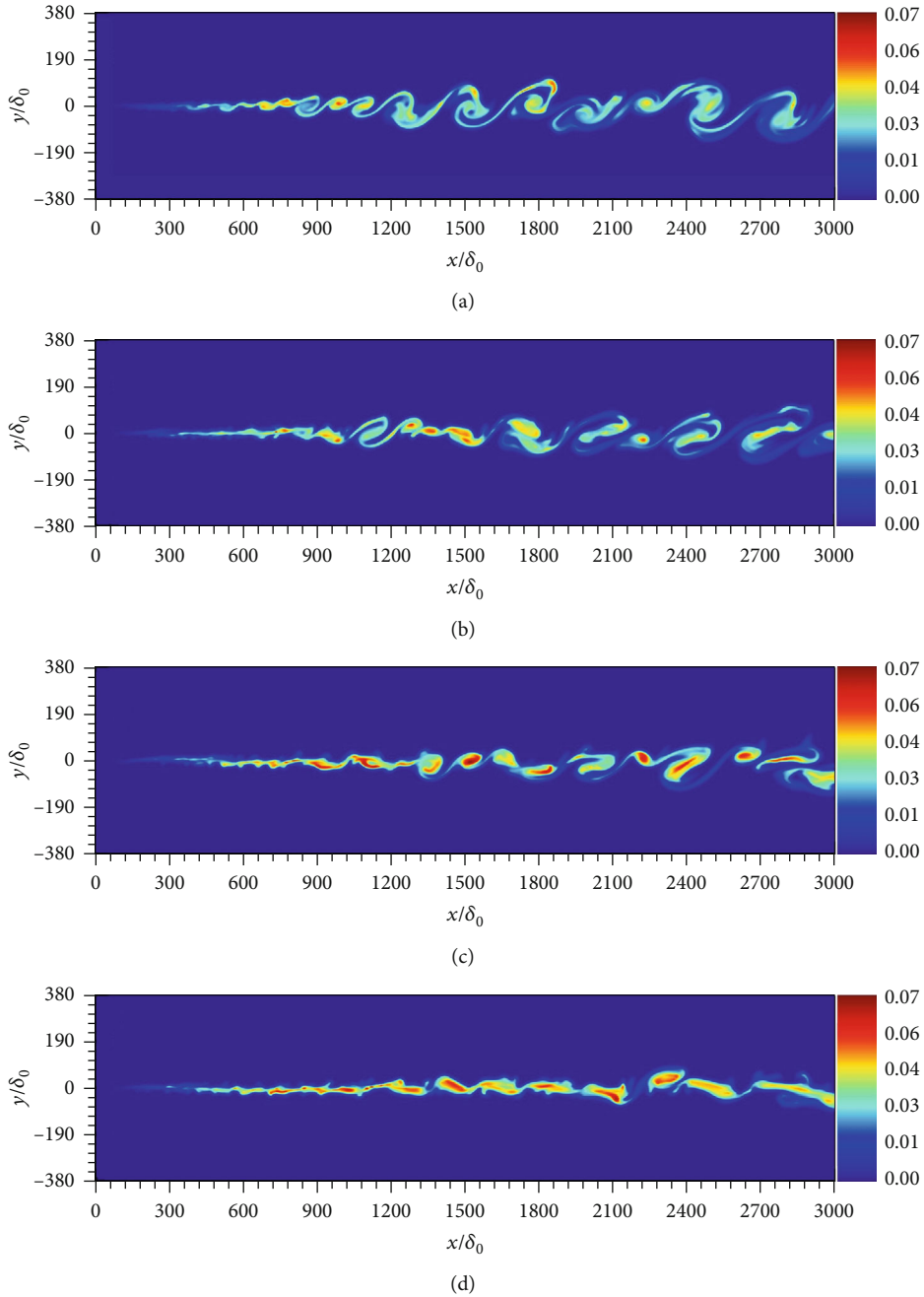
FIGURE 10: Instantaneous distributions of fuel vapor mass fraction Y_F: (a) 0.4 M_c, (b) 0.6 M_c, (c) 0.8 M_c, and (d) 1.0 M_c.

local gas temperature is increased by about 1.2 times than the temperature of the free stream, T_0, even if there is no chemical reaction. In addition, for the reactive flows with high compressibility, it is clear that a large part of the temperature rise in the flow field is due to the compressibility. The local high-temperature or low-temperature zone due to the flow compression or expansion effects will heat or cool the local fuel droplets, further affecting the evaporation, and these effects will be detailed in the following part.

3.2. Effects of Flow Compressibility on the Droplet Dispersion, Evaporation, and Fuel-Air Mixing. From the above analysis,

the flow compressibility affects the structures and dynamics of vortices in the supersonic shear layer, and the expansion and compression waves in the flow field are found to influence the spatial distributions of the aerothermal parameters, such as pressure and temperature, of the carrier flow, which affects the dispersion and evaporation of the laden droplets.

Figure 9 gives the spatial distributions of fuel droplets in the supersonic shear flow. The selected vorticity indicates the vortex, and the dots represent the evaporating droplets with colors for the dimensionless droplet temperature $T_d/T_{d,0}$. After the cold droplets disperse in the hot air stream, the heat

is transferred from the surrounding gas to the droplets, associated with the increase of droplet temperature. For the shear flow with low compressibility ($M_c = 0.4$), the vortex structure is relatively regular, and the evaporating droplets tend to accumulate in the periphery of the vortices as well as the vortex-braids after the vortices are rolled up and shed. After the droplet temperature increases gradually from $T_{d,\ 0}$ to the saturation temperature, it remains almost unchanged in the downstream region. With the increase of flow compressibility, the temperature of the carrier flow in the vortex-braids is found to be increased, and it is observed that the temperature of droplets in the vortex-braids is much higher than that around the vortices. The increase in droplet temperature promotes evaporation. However, the flow expansion in the vortex cores causes the local gas temperature to decrease, associated with the decrease of the droplet temperature, which inhibits the evaporation. The increase of flow compressibility results in the compression of the vortex structure along the transverse direction, and hence the distribution of droplets entrained by the vortex is found to be narrow.

Figure 10 shows the instantaneous distribution of the fuel vapor mass fraction Y_F in the supersonic shear layer. The spatial distribution of the fuel vapors depends on the injection position of the droplets as well as the dispersion characteristics of the evaporative droplets. The droplets are initially injected in the central region of the shear layer inlet before the vortex starts to shed, and the fuel vapors are enriched in the central region. For case $0.4\ M_c$, the droplets segregate in the central region of the shear layer before the vortex shedding, and the fuel vapors are enriched locally. After the vortex is shed, the vortex entrains vapors in the vortex cores. The turbulent motion of the vortex entrains the droplets, resulting in the preferential accumulation of droplets in the periphery of the vortex as well as the vortex-braid, and it is found that a large number of fuel vapors exists around the vortex. With the increase of flow compressibility, the vortex is compressed along the transverse direction and the structure becomes narrow, and the dispersion region of droplets is also narrowed, resulting in the concentrated distribution of fuel vapors. For case $1.0\ M_c$, it is observed that the fuel vapors are mainly concentrated inside the vortices. There are two main reasons attributed to this phenomenon. On one hand, the flow becomes difficult to lose the stability with the increase of flow compressibility, and the location for the rolling-up and shedding of vortices is found to move downstream. The droplets have evaporated to form many fuel vapors before the vortex shedding. Since the droplets segregate in the central region of the shear layer, the fuel vapors are concentrated in the shear layer center. As the vortex is shed, most of the fuel vapors accumulate inside the vortices. On the other hand, the flow compressibility affects the dynamics of vortices, the droplets entrained by the vortices distribute in the central region of the shear layer, and hence the fuel vapors are concentrated in the shear layer center.

In order to analyze the mixing degree of fuel vapors with air, the spatial mixing deficiency (SMD) [29] is used, which
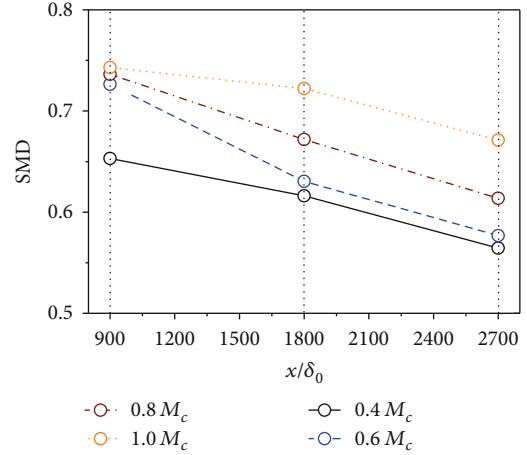
FIGURE 11: The distribution of SMD along the streamwise direction.

measures the ununiform distribution of chemical components. The expression is as follows,

$$\mathrm{SMD} = \frac{\mathrm{RMS}_{\mathrm{plane}}\left(\bar{Y}_i\right)}{\mathrm{Avg}_{\mathrm{plane}}\left(\bar{Y}_i\right)}, \qquad (26)$$

where RMS is the root mean square of the time-averaged species at a certain plane, $\bar{Y}_i$,

$$\mathrm{RMS}_{\mathrm{plane}}\left(\bar{Y}_i\right) = \sqrt{\frac{1}{m_{\mathrm{plane}} - 1} \sum_{i=1}^{m_{\mathrm{plane}}} \left(\bar{Y}_i - \mathrm{Avg}_{\mathrm{plane}}\left(\bar{Y}_i\right)\right)^2}, \qquad (27)$$

and Avg is the mean value of $\bar{Y}_i$,

$$\mathrm{Avg}_{\mathrm{plane}}\left(\bar{Y}_i\right) = \frac{1}{m_{\mathrm{plane}}} \sum_{i=1}^{m_{\mathrm{plane}}} \left(\bar{Y}_i\right). \qquad (28)$$

m_{plane} is the number of grids on this plane. As SMD equals to 0, it represents a complete mixing at this plane. For the mixing process in the supersonic shear layer, three transverse planes along the streamwise direction are selected, and x/δ_0 is taken as 900, 1800, and 2700 for the evaporating, the completion of evaporation, and the downstream regions, respectively. Figure 11 shows the distributions of SMD at different streamwise locations. It is found that the mixing is gradually completed with the development of the shear layer, and the SMD decreases. For the same streamwise location, the SMD increases with the increasing M_c, which indicates that the mixing is insufficient and demonstrates that the increase of flow compressibility inhibits the mixing of the chemical components.

4. Conclusions

In the present study, we present a systematic investigation for the influence of high-speed flow compressibility on the dispersion and evaporation of droplets, and two-phase mixing

in supersonic shear layers. The fuel droplets interact with the turbulent shear flows through the two-way coupling model, and the Eulerian-Lagrangian point source approach is adopted. The convective Mach numbers of the carrier flows increase from 0.4 to 1.0.

The overall features of the aerothermal field of the supersonics shear layer are first analyzed, and the effects of the flow compressibility are discussed. The compression and the dilatation in the compressible flow are found to be spatially intermittent, which is attributed to the high-speed flow compressibility, and they result in the switching between thermal and kinetic energies during the turnover of the large-scale vortices. The flow compressibility influences the carrier flow, which affects the dispersion, evaporation, and mixing of droplets. On one hand, the shear vortices are compressed along the transverse direction, and their sizes reduce as the flow compressibility increases. Therefore, the dispersion range of the fuel droplets transported by the local vortices becomes narrow, associated with the reduced distribution of fuel vapors from evaporation. On the other hand, it is found that the intermittent spatial distributions of the expansion zone with low temperature and the compression zone with high temperature occur due to the high flow compressibility and affect the heat and mass transfers from the carrier gas to the droplets. The strengthen of the flow compressibility reduces the mixing degree of fuel droplets. Generally, the increasing convective Mach number is found to suppress the dispersion, evaporation, and mixing. However, the increasing temperature of the carrier gas due to the flow compressibility is expected to contribute to the ignition and combustion, and the effects on combustion are worth further investigation.

Data Availability

Data available on request.

Conflicts of Interest

The authors declare that they have no conflicts of interest.

Acknowledgments

References

[1] W. Ao, Z. Chen, P. Liu, S. Shang, K. Ma, and B. Fu, "Mixing enhancement in a subsonic-supersonic shear layer with a cavity splitter plate," *Aerospace Science and Technology*, vol. 102, article 105847, 2020.

[2] K. Ma, J. Li, Q. Li, and Y. Liu, "Experimental study on evolution characteristics of plane subsonic-supersonic shear layer," *Aerospace Science and Technology*, vol. 100, p. 105791, 2020.

[3] G. Xiang, Z. Ren, S. Kim, and B. Wang, "Numerical analysis on the disintegration of gas-liquid interface in two-phase shear-layer flows," *Aerospace Science and Technology*, vol. 98, p. 105710, 2020.

[4] P. Guo, Z. Gao, Z. Wu, H. Liu, C. Jiang, and C. Lee, "Investigations on the accurate prediction of supersonic shear layers for detached eddy simulation," *Aerospace Science and Technology*, vol. 89, pp. 46–57, 2019.

[5] G. L. Brown and A. Roshko, "On density effects and large structure in turbulent mixing layers," *Journal of Fluid Mechanics*, vol. 64, no. 4, pp. 775–816, 1974.

[6] D. Papamoschou and A. Roshko, "The compressible turbulent shear layer: an experimental study," *Journal of Fluid Mechanics*, vol. 197, pp. 453–477, 1988.

[7] N. Chinzei, G. Masuya, T. Komuro, A. Murakami, and K. Kudou, "Spreading of two-stream supersonic turbulent mixing layers," *The Physics of Fluids*, vol. 29, no. 5, pp. 1345–1347, 1986.

[8] N. T. Clemens and M. G. Mungal, "Large-scale structure and entrainment in the supersonic mixing layer," *Journal of Fluid Mechanics*, vol. 284, pp. 171–216, 1995.

[9] A. Kourta and R. Sauvage, "Computation of supersonic mixing layers," *Physics of Fluids*, vol. 14, no. 11, pp. 3790–3797, 2002.

[10] A. W. Vreman, N. D. Sandham, and K. H. Luo, "Compressible mixing layer growth rate and turbulence characteristics," *Journal of Fluid Mechanics*, vol. 320, pp. 235–258, 1996.

[11] B. Wang, W. Wei, Y. Zhang, H. Zhang, and S. Xue, "Passive scalar mixing in Mc<1 planar shear layer flows," *Computers & Fluids*, vol. 123, pp. 32–43, 2015.

[12] G. S. Elliott and M. Samimy, "Compressibility effects in free shear layers," *Physics of Fluids A: Fluid Dynamics*, vol. 2, no. 7, pp. 1231–1240, 1990.

[13] M. G. Olsen and J. C. Dutton, "Planar velocity measurements in a weakly compressible mixing layer," *Journal of Fluid Mechanics*, vol. 486, pp. 51–77, 2003.

[14] C. Pantano and S. Sarkar, "A study of compressibility effects in the high-speed turbulent shear layer using direct simulation," *Journal of Fluid Mechanics*, vol. 451, pp. 329–371, 2002.

[15] A. Atoufi, M. Fathali, and B. Lessani, "Compressibility effects and turbulent kinetic energy exchange in temporal mixing layers," *Journal of Turbulence*, vol. 16, no. 7, pp. 676–703, 2015.

[16] A. Burcat and B. Ruscic, "Third millenium ideal gas and condensed phase thermochemical database for combustion (with update from active thermochemical tables)," in *Argonne National Lab*, (ANL), Argonne, IL (USA), 2005.

[17] B. E. Poling, J. M. Prausniz, and J. P. O'Connell, *The Properties of Gases and Liquids*, McGraw-Hill, New York, 2001, Chaps.

[18] Z. Ren, B. Wang, Q. Xie, and D. Wang, "Thermal auto-ignition in high-speed droplet-laden mixing layers," *Fuel*, vol. 191, pp. 176–189, 2017.

[19] R. S. Miller, K. Harstad, and J. Bellan, "Evaluation of equilibrium and non-equilibrium evaporation models for many-droplet gas-liquid flow simulations," *International Journal of Multiphase Flow*, vol. 24, no. 6, pp. 1025–1055, 1998.

[20] Z. Ren, B. Wang, and L. Zheng, "Numerical analysis on interactions of vortex, shock wave, and exothermal reaction in a supersonic planar shear layer laden with droplets," *Physics of Fluids*, vol. 30, no. 3, article 036101, 2018.

[21] X. Y. Hu, Q. Wang, and N. A. Adams, "An adaptive central-upwind weighted essentially non-oscillatory scheme," *Journal of Computational Physics*, vol. 229, no. 23, pp. 8952–8965, 2010.

[22] Y. Zhang, B. Wang, H. Zhang, and S. Xue, "Mixing enhancement of compressible planar mixing layer impinged by oblique shock waves," *Journal of Propulsion and Power*, vol. 31, no. 1, pp. 156–169, 2014.

[23] T. J. Poinsot and S. K. Lelef, "Boundary conditions for direct simulations of compressible viscous flows," *Journal of Computational Physics*, vol. 101, no. 1, pp. 104–129, 1992.

[24] M. Mikami, Y. Mizuta, Y. Tsuchida, and N. Kojima, "Flame structure and stabilization of lean-premixed sprays in a counterflow with low-volatility fuel," *Proceedings of the Combustion Institute*, vol. 32, no. 2, pp. 2223–2230, 2009.

[25] A. L. Sánchez, J. Urzay, and A. Liñán, "The role of separation of scales in the description of spray combustion," *Proceedings of the Combustion Institute*, vol. 35, no. 2, pp. 1549–1577, 2015.

[26] S. G. Goebel, J. C. Dutton, H. Krier, and J. P. Renie, "Mean and turbulent velocity measurements of supersonic mixing layers," *Mineralium Deposita*, vol. 29, no. 1, pp. 263–272, 1990.

[27] G. Xu, M. Ikegami, S. Honma et al., "Inverse influence of initial diameter on droplet burning rate in cold and hot ambiences: a thermal action of flame in balance with heat loss," *International Journal of Heat and Mass Transfer*, vol. 46, no. 7, pp. 1155–1169, 2003.

[28] S. Lee, S. K. Lele, and P. Moin, "Eddy shocklets in decaying compressible turbulence," *Physics of Fluids A: Fluid Dynamics*, vol. 3, no. 4, pp. 657–664, 1991.

[29] C. Priere, L. Y. M. Gicquel, P. Kaufmann, W. Krebs, and T. Poinsot, "Large eddy simulation predictions of mixing enhancement for jets in cross-flows," *Journal of Turbulence*, vol. 5, no. 5, pp. 1–24, 2004.

Research Article

Numerical Study of Disturbance Resistance of Oblique Detonation Waves

Yu Liu [iD], Baoguo Xiao [iD], Lan Wang, and Chao Wang

Science and Technology on Scramjet Laboratory, China Aerodynamics Research and Development Center (CARDC), Sichuan Mianyang 621000, China

Correspondence should be addressed to Baoguo Xiao; xiaobaoguo@cardc.cn

The stability of oblique detonation waves (ODWs) is a fundamental problem, and resistance of ODWs against disturbances is crucial for oblique detonation engines in high-speed propulsion. In this work, numerical studies on ODW stability in disturbed flows are conducted using the two-dimensional reactive Euler equations with a two-step induction-reaction kinetic model. Two kinds of flow disturbances are, respectively, introduced into the steady flow field to assess ODW stability, including upstream transient high-pressure disturbance (UTHD) and downstream jet flow disturbance (DJFD) with different durations. Generally, an ODW is susceptible to disturbances at larger wedge angles and stable at smaller wedge angles. In the unstable wedge angle range, different ODW structures and transition patterns are obtained after disturbances, including different locations of the primary triple points, different numbers of the steady triple points on the wave surface, and different transition patterns from the leading oblique shock wave to the ODW. It is found that the primary triple point tends to move upstream for the disturbances that can form a local strong detached bow shock wave near the wedge tip. In contrast, the wave surface and the transition pattern are susceptible to all of the disturbances introduced in this study. Despite the unstable responses of the ODWs to the disturbances, the ODWs can keep standing stability after disturbances, which is beneficial to the propulsion application of ODWs.

1. Introduction

Standing stability of ODWs is important for oblique detonation engines because it involves the realization of its advantages in hypersonic propulsion, including fast heat release and high thermodynamic cycle efficiency. A standing ODW should first satisfy the requirement of the wedge angle according to Pratt et al. [1]; that is, the wedge angle should lie between the minimum value called the Chapman-Jouguet (CJ) wedge angle and the maximum value called the detachment wedge angle. However, according to Ghorbanian and Sterling [2], the maximum allowable wedge angle should be less than the detachment wedge angle if a secondary CJ ODW forms following the leading shock. If the ODW initiation condition is not considered, the minimum wedge angle is not actually limited by the CJ wedge angle, according to Ashford and Emanuel [3]. In this situation, the ODW angle will remain constant at the CJ wave angle as the wedge angle decreases below the CJ wedge angle, with the Taylor rarefaction waves following the ODW itself. A series of studies on ODW structures [4–16] demonstrate ODW characteristics.

The aforementioned studies are based on two-dimensional flow fields. If a conical shock wave is considered, the flow field will differ from the wedge flow to some extent due to the curvature effect and the presence of the Taylor-Maccoll flow [9, 17, 18]. In addition to the wedge flow and conical flow, the spherical flow is another major concern for ODW initiation and standing stability. For the spherical flow, experiments on hypervelocity projectiles were comprehensively conducted by some researchers [19–23]. They conducted a series of parameter studies and investigated the criticality of stabilized ODWs around a spherical projectile. All of these results provide important benefits for ODW applications in propulsion.

TABLE 1: Numerical parameter setup.

Inflow Mach number, M_∞	Inflow static temperature, T_∞ (K)	Inflow static pressure, P_∞ (pa)	Specific heat ratio, γ	Dimensionless heat release, $\tilde{Q}$
4.0	650	20000	1.2	8
Dimensionless activation energy of the induction step, E_I/RT_S	Dimensionless activation energy of the heat release step, E_R/RT_S	Induction length corresponding to a CJ detonation, ΔI (mm)	Thermal pulse width corresponding to a CJ detonation, ΔR (mm)	Gas constant, R (J/kg·K)
4.8	1.0	2.12	0.95	377.9

One feature of a stabilized ODW is its stability or resistance to disturbances. If an ODW cannot maintain standing stabilization when experiencing additional disturbances, propulsion using ODW will be meaningless because, during a flight process, changes in the inflow conditions and flow disturbances are usually inevitable. The previous studies on the ODW disturbance resistance examined responses of ODWs to transient disturbances inside the flow field (see Li et al. [4], Fusina et al. [24], Teng et al. [25], Liu et al. [12], and Miao et al. [26]) or to nonuniform or nonconstant boundary conditions (see Fang et al. [27] and Yang et al. [28]). Recently, the influence of geometric disturbances on ODWs has also been investigated [29, 30]. For the transient disturbances, all of the papers indicated that an ODW is resilient to disturbances and can recover to its original state. However, Liu et al. [31] demonstrated the hysteresis phenomenon of the ODW recently. That means an ODW structure is not totally independent of the initial condition. ODW stability to inflow disturbances obtained by earlier studies [4, 12, 24–26] was probably due to the selected small wedge angles for which the ODWs are inherently stable or because of the transient feature of the disturbances giving insufficient time to trigger instability. Therefore, this study will introduce different kinds of flow disturbances at different wedge angles to investigate when and how an ODW becomes unstable to disturbances.

2. Numerical Treatment

The governing equations to be numerically solved are the two-dimensional unsteady reactive Euler equations given as follows.

The continuity equation is

$$\frac{\partial \rho}{\partial t} + \frac{\partial(\rho u)}{\partial x} + \frac{\partial(\rho v)}{\partial y} = 0, \tag{1}$$

where ρ, u, v, t, x, and y are the density, the x-direction velocity, the y-direction velocity, the time, the x coordinate, and the y coordinate, respectively.

The conservation equation of x-direction momentum is

$$\frac{\partial(\rho u)}{\partial t} + \frac{\partial(\rho u^2 + p)}{\partial x} + \frac{\partial(\rho uv)}{\partial y} = 0, \tag{2}$$

where p is the static pressure.
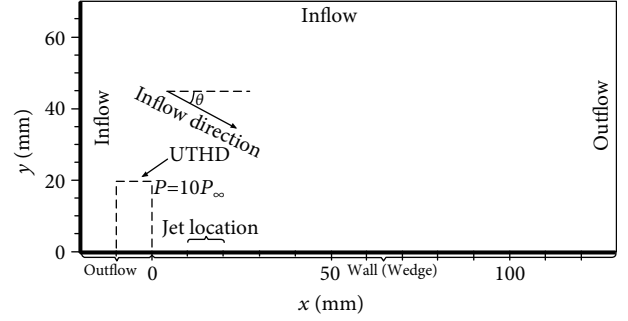
FIGURE 1: The computational domain.

The conservation equation of y-direction momentum is

$$\frac{\partial(\rho v)}{\partial t} + \frac{\partial(\rho uv)}{\partial x} + \frac{\partial(\rho v^2 + p)}{\partial y} = 0. \tag{3}$$

The conservation equation of energy is

$$\frac{\partial(\rho e)}{\partial t} + \frac{\partial[u(\rho e + p)]}{\partial x} + \frac{\partial[v(\rho e + p)]}{\partial y} = 0, \tag{4}$$

where e is the specific total energy and is described in Equation (6).

The equation of state for perfect gas is

$$p = \rho RT, \tag{5}$$

where R and T are the gas constant and the static temperature, respectively. Thus, the specific total energy can be written as

$$e = \frac{p}{\rho(\gamma - 1)} + \frac{(u^2 + v^2)}{2} - RT_0 \tilde{q}, \tag{6}$$

where γ, T_0, and $\tilde{q}$ are the specific heat ratio, the static temperature of the oncoming flow, and the dimensionless local heat release (using RT_0 for normalization, i.e., $\tilde{q} = q/RT_0$, where q is the dimensional local heat release), respectively.

A two-step induction-reaction kinetic model proposed by Ng et al. [32] and widely used in oblique detonation simulation [14, 33] consisting of a thermally neutral induction step and a heat release step is employed which allows us to easily change the induction length simply by modifying the
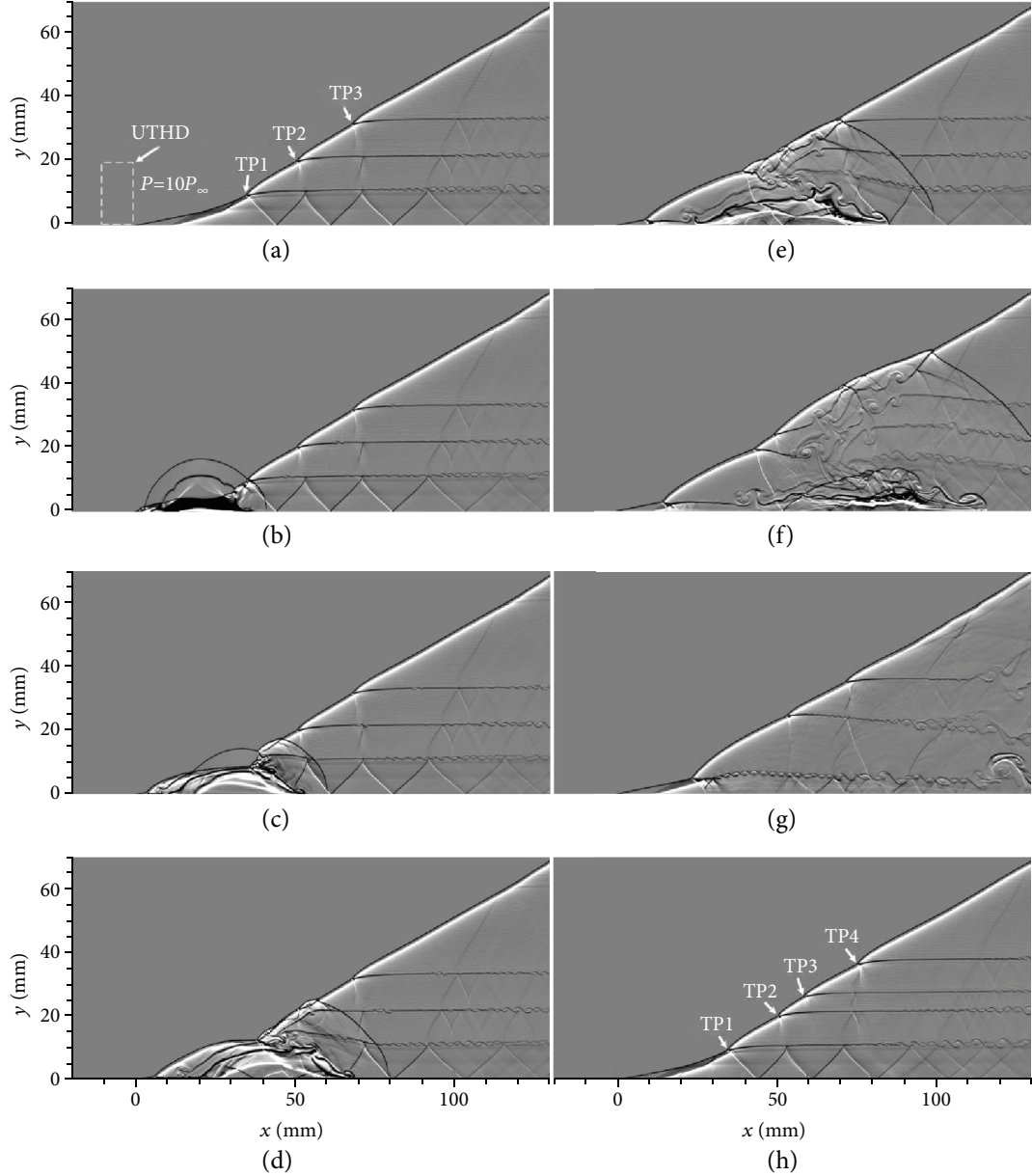
FIGURE 2: Evolution of the flow field after UTHD at $\theta = 32°$. (a) $t = 0$ (the disturbance has just been introduced into the flow field), (b) $t = 200\Delta t$, (c) $t = 300\Delta t$, (d) $t = 400\Delta t$, (e) $t = 500\Delta t$, (f) $t = 700\Delta t$, (g) $t = 1500\Delta t$, and (h) steady state after the disturbance.

reaction rate constant of the induction step. The reaction rate equations for both steps are given as

$$\frac{\partial(\rho\xi)}{\partial t} + \frac{\partial(\rho u\xi)}{\partial x} + \frac{\partial(\rho v\xi)}{\partial y} = H(1-\xi)\rho k_I \exp\left[E_I\left(\frac{1}{RT_S} - \frac{1}{RT}\right)\right],$$

$$\frac{\partial(\rho\lambda)}{\partial t} + \frac{\partial(\rho u\lambda)}{\partial x} + \frac{\partial(\rho v\lambda)}{\partial y} = [1 - H(1-\xi)]\rho k_R(1-\lambda) \exp\left(\frac{-E_R}{RT}\right),$$

$$\tag{7}$$

where ξ, k_I, and E_I are the reaction progress variable (indicating the finishing degree of the current step), the reaction rate constant, and the activation energy of the induction step, respectively, and λ, k_R, and E_R are that of the heat release

step, respectively. Note that the reaction rate constants k_I and k_R control the induction length and the thermal pulse width, respectively. Usually, the induction length corresponding to a CJ detonation, ΔI, and the thermal pulse width corresponding to a CJ detonation, ΔR, are used to reflect the values of k_I and k_R, respectively. In this study, the grid resolution satisfies that there are 32 grid points in ΔI (with the grid convergence test given in Section 3). T_S is the temperature inside the induction region. $H(1-\xi)$ is a step function written as

$$H(1-\xi) = \begin{cases} 1 & \text{if } \xi < 1, \\ 0 & \text{if } \xi < 1. \end{cases} \tag{8}$$
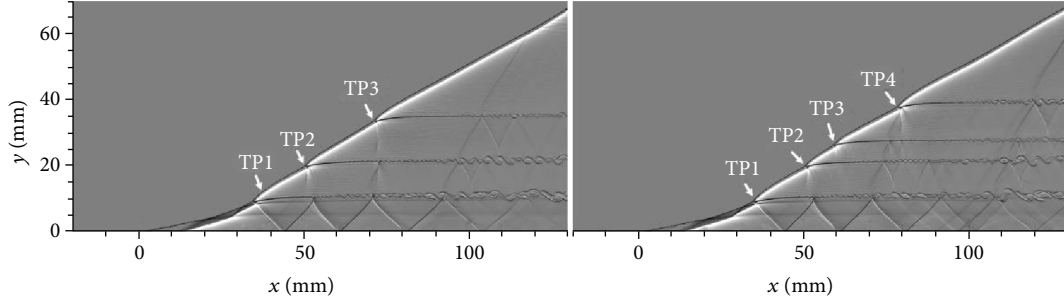
FIGURE 3: Grid convergence test at $\theta = 32°$. (a) Undisturbed steady flow field for 64 pts/ΔI and (b) steady flow field after UTHD for 64 pts/ΔI.

FIGURE 4: Evolution of the flow field after DJFD of $100\Delta t$ at $\theta = 32°$. (a) $t = 100\Delta t$ (the jet flow has just been turned off), (b) $t = 900\Delta t$, (c) $t = 2100\Delta t$, (d) $t = 5700\Delta t$, (e) $t = 16200\Delta t$, and (f) steady state after the disturbance.

Clearly, at any instant, the local heat release $\tilde{q}$ or q satisfies $\tilde{q} = \lambda \tilde{Q}$ or $q = \lambda Q$, where $\tilde{Q}$ and Q are the dimensionless and dimensional total heat released by the reactant ($\tilde{Q} = Q/RT_0$), respectively.

The governing equations above are numerically solved using an open-source adaptive mesh refinement computational fluid dynamic program called AMROC [34] which is based on the finite volume method. The block-structured adaptive mesh refinement technique of AMROC makes high-resolution capture of discontinuities in the flow field possible. Discretization is conducted using the MUSCL-Hancock scheme which is second-order accurate, together with the hybrid Roe scheme as the Riemann solver. In order to ensure total variation diminishing (TVD) properties, a van Albada slope limiter is employed. The Godunov splitting method is used to treat the source term so as to overcome the problem of stiff chemistry. The parameter setup is listed in Table 1. The AMROC program with the two-step induction-reaction kinetic model has also been used by Li et al. [35, 36] to investigate detonation reflection. The computational domain is shown in Figure 1. The left and top boundaries are the inflow boundaries, and the bottom

FIGURE 5: Evolution of the flow field after DJFD of $200\Delta t$ at $\theta = 32°$. (a) $t = 200\Delta t$ (the jet flow has just been turned off), (b) $t = 1200\Delta t$, (c) $t = 22800\Delta t$, and (d) $t = 36500\Delta t$.

boundary in the range of 0 mm ≤ x ≤ 130 mm is a fixed wall. The angle between the inflow direction and the horizontal direction, θ, represents the wedge angle. θ can vary so that different wedge angles can be tested. The right boundary and the bottom boundary in the range of −20 mm ≤ x < 0 mm are the outflow boundaries on which the flow field variants are extrapolated from the inside.

In this study, all the original steady flow fields are obtained through the following method: an inert shock wave is obtained by turning off the chemical reactions, and then an ODW is obtained by turning on the reactions in the cold flow. As introduced in Section 1, we will introduce different kinds of flow disturbances into the original steady flow fields. To be specific, the flow disturbances include an upstream transient high-pressure region (UTHD) and a downstream jet flow (DJFD). UTHD is within a rectangular zone of −10 mm ≤ x < 0 mm and 0 mm ≤ y < 20 mm where the local static pressure P is 10 times the inflow static pressure P_∞. DJFD is located in the range of 10 mm ≤ x ≤ 20 mm on the bottom boundary. The jet is a sonic flow normal to the bottom boundary, at a static pressure 10 times that of the inflow, and with other parameters the same as that of the inflow. In this study, the jet's lasting period is variable in different cases to check the effects, including 100 time steps, 200 time steps, and 500 time steps. The time step Δt is controlled by the Courant number. In this study, the Courant number of 0.95 is used, which is corresponding to a time step of approximately 10^{-7} seconds. All of the results in this study are presented in the form of numerical schlieren, $\partial\rho/\partial y$.

3. Results and Discussion

Three different wedge angles including $\theta = 32°$, $\theta = 31°$, and $\theta = 30°$ are tested in this study. In the following, the results

FIGURE 6: Pressure distributions on the bottom boundary of the steady flow fields after the DJFD of $100\Delta t$ and $200\Delta t$ at $\theta = 32°$.

of the $\theta = 32°$ case are given. Figure 2 shows the evolution of the flow field after UTHD. At $t = 0$, a high-pressure disturbance region of $P = 10P_\infty$ is introduced in the upstream of the leading shock of the original steady ODW at $\theta = 32°$, as shown in Figure 2(a). In Figure 2(a), the wave surface of the ODW has three steady triple points, indicated by TP1, TP2, and TP3, respectively. TP1 is the primary triple point. Since TP1, TP2, and TP3 are all steady, they differ from the unstable triple points of cellular structures that are
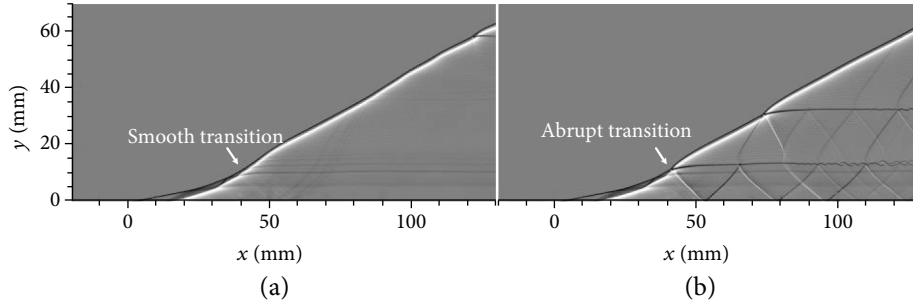
FIGURE 7: Steady flow fields before and after UTHD at $\theta = 31°$. (a) Before and (b) after.
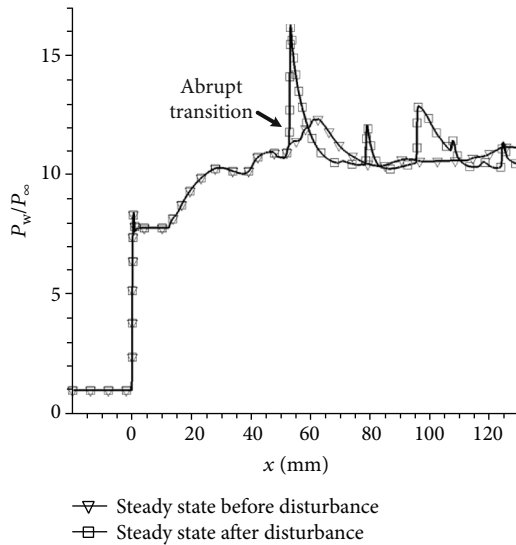
FIGURE 8: Pressure distributions on the bottom boundary of the steady flow fields before and after UTHD at $\theta = 31°$.

continuously oscillatory. After UTHD is introduced into the flow field, the pressure disturbance propagates downstream, and the flow field is disturbed significantly. A new triple point forms near the wedge tip (see Figure 2(c)) after the disturbance passes, and the ODW near this newly formed triple point is slightly bow-shaped. However, the triple point continuously moves downstream and the flow field finally recovers to very similar to its original state (compare Figure 2(a) and Figure 2(h)), except that the steady ODW after the disturbance has four steady triple points on its wave surface (denoted by TP1, TP2, TP3, and TP4, respectively, in Figure 2(h)). Thus, the primary triple point of the ODW is stable to the UTHD, but the wave surface is unstable to the UTHD.

To assess whether the aforementioned results are grid-independent, Figure 3 shows the steady ODWs before and after disturbed by UTHD for 64 pts/ΔI. In both the undisturbed and disturbed cases, the results of 64 pts/ΔI are almost the same as that of 32 pts/ΔI (compare Figure 3(a) with Figure 2(a) and Figure 3(b) with Figure 2(h)), except that the slip lines of the 64 pts/ΔI are slightly clearer. Thus, 32 pts/ΔI is sufficient to reach grid convergence in this study.

Considering that the primary triple point being stable to UTHD may be due to insufficient disturbance time, a

longer-term DJFD disturbance is introduced into the original steady flow field at $\theta = 32°$. Figure 4 shows the evolution of the flow field after DJFD that lasts for $100\Delta t$. Clearly, the evolution of the flow field takes longer compared to that of UTHD because the current disturbance is no longer transient. A significant bow shock together with a triple point forms immediately when the jet flow is introduced into the flow field (see Figure 4(a)). However, the triple point again moves continuously downstream. After sufficient time, the flow field becomes the same as that of the UTHD case (compare Figure 4(f) with Figure 2(h)). That is to say, for DJFD of $100\Delta t$, the primary triple point is still stable. This indicates that the jet flow time may be still insufficient to trigger instability of the primary triple point.

Figure 5 shows the evolution of the flow field after DJFD of $200\Delta t$ at $\theta = 32°$. A much stronger bow shock forms after the jet flow is introduced (compare Figure 5(a) with Figure 4(a)). After $36500\Delta t$, which is sufficiently long, the primary triple point remains located somewhere upstream (near the wedge tip) and cannot recover to its undisturbed state (compare Figure 5(d) with Figure 2(a)). Furthermore, the ODW itself presents more unsteady features, including the unsteady slip line with large-scale vortexes and another unsteady triple point on the wave surface. Thus, for this longer-term jet flow, the primary triple becomes unstable. It seems that the formation of a strong bow shock or ODW near the wedge tip is the precondition for triggering instability of the primary triple point. Therefore, the effect of the location and intensity of the disturbance can be further deduced. That is, the primary triple point is stable if the location of the disturbance is significantly far from the primary triple point or if the intensity of the disturbance is insufficient to form a strong bow shock or ODW near the wedge tip. Figure 6 compares the pressure distributions on the bottom boundary of the steady flow fields after the $100\Delta t$- and 200 Δt-DJFD. Clearly, after the $200\Delta t$-DJFD, there exists a remarkable pressure jump on the wedge surface, which indicates the reflection of the transverse shock. In the far downstream, the pressure on the wedge surface recovers at a similar level with the undisturbed case.

Now, we start to consider the case of $\theta = 31°$. Henceforth, the detailed evolution processes of the flow fields will not be provided since they are similar to the previous cases and we mainly focus on the steady flow fields before and after disturbances. Figure 7 shows the steady flow fields before and after UTHD of the $\theta = 31°$ case. Before UTHD, the ODW presents
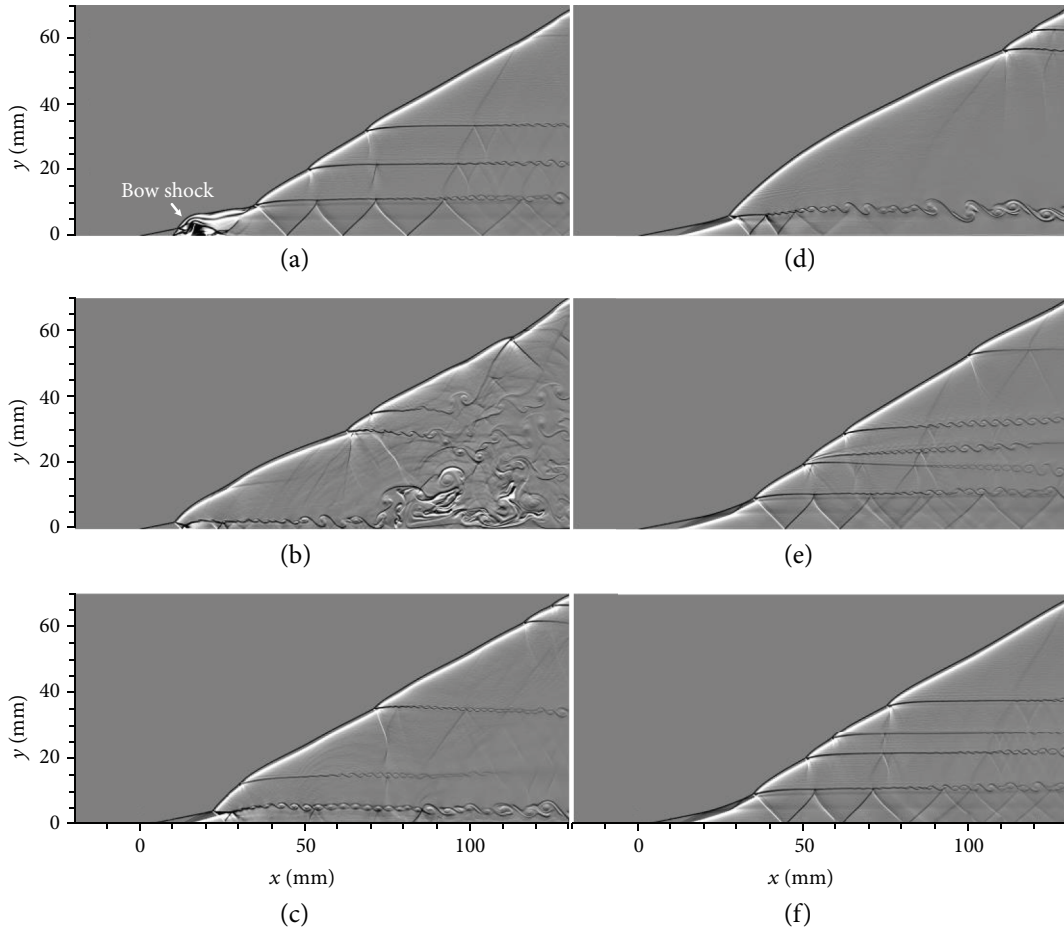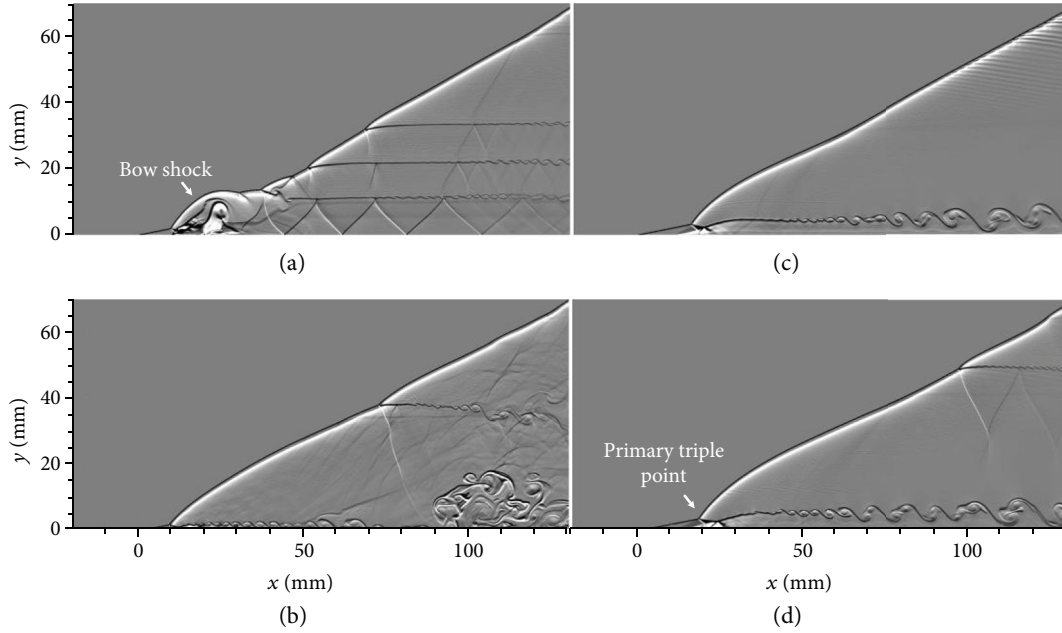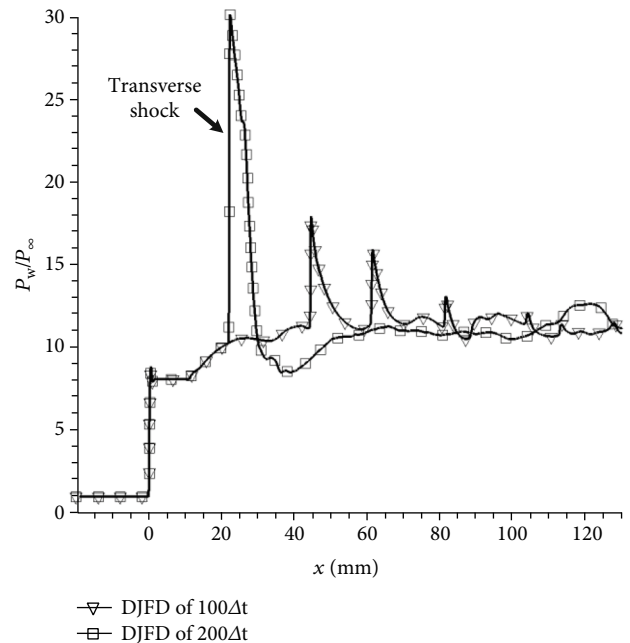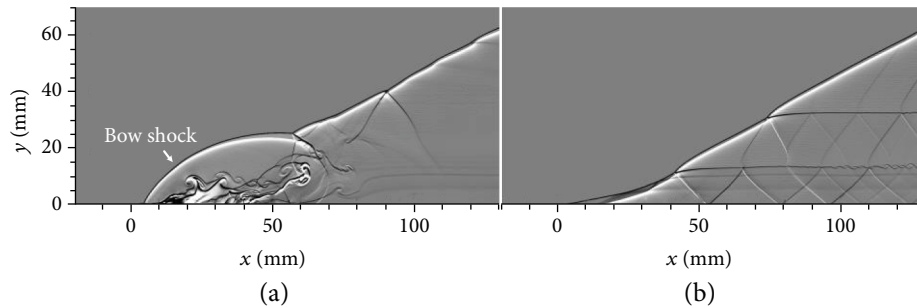
FIGURE 9: Evolution of the flow field after DJFD of $500\Delta t$ at $\theta = 31°$. (a) $t = 500\Delta t$ (the jet flow has just been turned off) and (b) steady state after the disturbance.
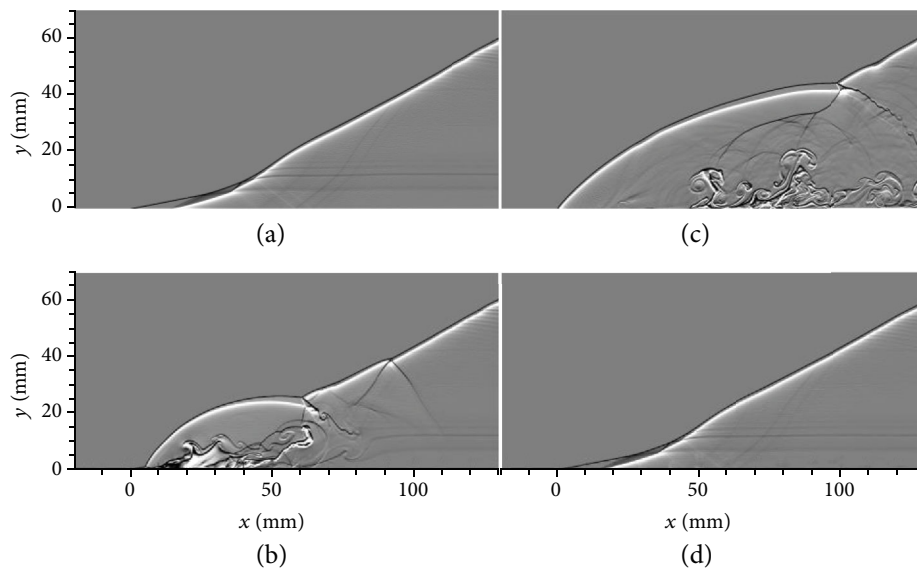
FIGURE 10: Evolution of the flow field after DJFD of $500\Delta t$ at $\theta = 30°$. (a) $t = 0$ (original steady state), (b) $t = 500\Delta t$ (the jet flow has just been turned off), (c) $t = 700\Delta t$, and (d) steady state after the disturbance.

a smooth transition pattern with no primary triple point or transverse shock. However, after UTHD, the transition pattern becomes abrupt, with the existence of the primary triple point and the transverse shock. Figure 8 compares the pressure distributions on the bottom boundary before and after UTHD. The transverse shock of the abrupt transition gives rise to a pressure jump on the wedge surface whereas the smooth transition has no sudden pressure jump.

Figure 9 shows the evolution of the flow field after DJFD that lasts for $500\Delta t$ at $\theta = 31°$. Although the ODW is highly locally detached and bow-shaped near the wedge tip after the jet flow is turned off, as shown in Figure 9(a), it finally becomes the same as that after UTHD (compare Figure 9(b) with Figure 7(b)). Thus, there is no upstream moving triple point for the $\theta = 31°$ case.

Finally, the case of $\theta = 30°$ is tested. Figure 10 shows the evolution of the flow field after DJFD of $500\Delta t$. It is seen that before and after the disturbance, the ODW keeps totally unchanged. Since the $500\Delta t$-DJFD is a much more intense disturbance than UTHD, it is reasonable to expect that the ODW will still be unchanged by UTHD. This means that the ODW is absolutely stable to disturbances at $\theta = 30°$.

The stability of the steady ODW flow field after the disturbance is also worth discussing. At $\theta = 32°$, the steady flow field after UTHD or DJFD of $100\Delta t$ (both can trigger wave surface instability) is stable to disturbance of the same type but remains unstable to DJFD of $200\Delta t$ that can further trigger the primary triple point instability. However, the steady flow field after DJFD of $200\Delta t$ is stable to any other kind of disturbances, suggesting that the ODW with an upstream primary triple point is absolutely stable, just like the case of $\theta = 30°$.

Although the ODW is unstable to flow disturbances in a certain wedge angle range, it can maintain standing stabilization on the wedge, which is beneficial to propulsive ODW applications.

4. Conclusions

The disturbance resistance of ODWs was numerically studied in this work using the two-dimensional reactive Euler equations with a two-step induction-reaction kinetic model. In contrast to previous studies by other researchers [4, 12, 24–26], the present work demonstrates that an ODW is not

stable or resistant to flow disturbances under certain conditions and is sensitive to the disturbance form. The ODW tends to be stable at a smaller wedge angle and unstable at a larger wedge angle. The unstable characteristics manifest themselves in the ODW structure and transition pattern. In the unstable wedge angle range, only the ODW surface and transition pattern change after UTHD and short-term DJFD, whereas the upstream moving of the primary triple point occurs after long-term DJFD because a local strong detached bow shock wave forms near the wedge tip via this kind of disturbance. Although the ODW presents unstable responses to disturbances, it maintains the standing stability after disturbances, which is desired for an oblique detonation engine.

Data Availability

The (numerical schlieren) and (pressure distribution) data used to support the findings of this study are included within the article.

Conflicts of Interest

The authors declare that there is no conflict of interest regarding the publication of this paper.

Acknowledgments

References

[1] D. T. Pratt, J. W. Humphrey, and D. E. Glenn, "Morphology of standing oblique detonation waves," *Journal of Propulsion and Power*, vol. 7, no. 5, pp. 837–845, 1991.

[2] K. Ghorbanian and J. D. Sterling, "Influence of formation processes on oblique detonation wave stabilization," *Journal of Propulsion and Power*, vol. 12, no. 3, pp. 509–517, 1996.

[3] S. A. Ashford and G. Emanuel, "Wave angle for oblique detonation waves," *Shock Waves*, vol. 3, no. 4, pp. 327–329, 1994.

[4] C. Li, K. Kailasanath, and E. S. Oran, "Detonation structures behind oblique shocks," *Physics of Fluids*, vol. 6, no. 4, pp. 1600–1611, 1994.

[5] L. Í. S. F. Figueria da Silva and B. Deshaies, "Stabilization of an oblique detonation wave by a wedge: a parametric numerical study," *Combustion and Flame*, vol. 121, no. 1-2, pp. 152–166, 2000.

[6] J. Y. Choi, D. W. Kim, I. S. Jeung, F. Ma, and V. Yang, "Cell-like structure of unstable oblique detonation wave from high-resolution numerical simulation," *Proceedings of the Combustion Institute*, vol. 31, no. 2, pp. 2473–2480, 2007.

[7] M. Gui and B. Fan, "Wavelet structure of wedge-induced oblique detonation waves," *Combustion Science and Technology*, vol. 184, no. 10-11, pp. 1456–1470, 2012.

[8] H. H. Teng and Z. L. Jiang, "On the transition pattern of the oblique detonation structure," *Journal of Fluid Mechanics*, vol. 713, pp. 659–669, 2012.

[9] J. Verreault, A. J. Higgins, and R. A. Stowe, "Formation and structure of steady oblique and conical detonation waves," *AIAA Journal*, vol. 50, no. 8, pp. 1766–1772, 2012.

[10] J. Verreault, A. J. Higgins, and R. A. Stowe, "Formation of transverse waves in oblique detonations," *Proceedings of the Combustion Institute*, vol. 34, no. 2, pp. 1913–1920, 2013.

[11] H. H. Teng, Z. L. Jiang, and H. D. Ng, "Numerical study on unstable surfaces of oblique detonations," *Journal of Fluid Mechanics*, vol. 744, pp. 111–128, 2014.

[12] Y. Liu, D. Wu, S. Yao, and J. Wang, "Analytical and numerical investigations of wedge-induced oblique detonation waves at low inflow Mach number," *Combustion Science and Technology*, vol. 187, no. 6, pp. 843–856, 2015.

[13] H. Teng, H. D. Ng, K. Li, C. Luo, and Z. Jiang, "Evolution of cellular structures on oblique detonation surfaces," *Combustion and Flame*, vol. 162, no. 2, pp. 470–477, 2015.

[14] P. Yang, H. Teng, Z. Jiang, and H. D. Ng, "Effects of inflow Mach number on oblique detonation initiation with a two-step induction-reaction kinetic model," *Combustion and Flame*, vol. 193, pp. 246–256, 2018.

[15] F. K. Lu, H. Fan, and D. R. Wilson, "Detonation waves induced by a confined wedge," *Aerospace Science and Technology*, vol. 10, no. 8, pp. 679–685, 2006.

[16] S. Bhattrai and H. Tang, "Formation of near-Chapman-Jouguet oblique detonation wave over a dual-angle ramp," *Aerospace Science and Technology*, vol. 63, pp. 1–8, 2017.

[17] P. G. Harris, R. Farinaccio, R. A. Stowe, R. Link, D. Alexander, and L. Donahue, "Structure of conical oblique detonation waves," in *44th AIAA/ASME/SAE/ASEE Joint Propulsion Conference & Exhibit*, p. 4687, Hartford, CT, USA, 2008.

[18] J. Verreault and A. J. Higgins, "Initiation of detonation by conical projectiles," *Proceedings of the Combustion Institute*, vol. 33, no. 2, pp. 2311–2318, 2011.

[19] J. Kasahara, T. Arai, S. Chiba, K. Takazawa, Y. Tanahashi, and A. Matsuo, "Criticality for stabilized oblique detonation waves around spherical bodies in acetylene/oxygen/krypton mixtures," *Proceedings of the Combustion Institute*, vol. 29, no. 2, pp. 2817–2824, 2002.

[20] S. Maeda, R. Inada, J. Kasahara, and A. Matsuo, "Visualization of the non-steady state oblique detonation wave phenomena around hypersonic spherical projectile," *Proceedings of the Combustion Institute*, vol. 33, no. 2, pp. 2343–2349, 2011.

[21] S. Maeda, J. Kasahara, and A. Matsuo, "Oblique detonation wave stability around a spherical projectile by a high time resolution optical observation," *Combustion and Flame*, vol. 159, no. 2, pp. 887–896, 2012.

[22] S. Maeda, S. Sumiya, J. Kasahara, and A. Matsuo, "Initiation and sustaining mechanisms of stabilized oblique detonation waves around projectiles," *Proceedings of the Combustion Institute*, vol. 34, no. 2, pp. 1973–1980, 2013.

[23] S. Maeda, S. Sumiya, J. Kasahara, and A. Matsuo, "Scale effect of spherical projectiles for stabilization of oblique detonation waves," *Shock Waves*, vol. 25, no. 2, pp. 141–150, 2015.

[24] G. Fusina, J. P. Sislian, and B. Parent, "Formation and stability of near Chapman–Jouguet standing oblique detonation waves," *AIAA Journal*, vol. 43, no. 7, pp. 1591–1604, 2005.

[25] H. H. Teng, W. Zhao, and Z. L. Jiang, "A novel oblique detonation structure and its stability," *Chinese Physics Letters*, vol. 24, pp. 1985–1988, 2007.

[26] S. Miao, J. Zhou, Z. Lin, X. Cai, and S. Liu, "Numerical study on thermodynamic efficiency and stability of oblique detonation waves," *AIAA Journal*, vol. 56, no. 8, pp. 3112–3122, 2018.

[27] Y. Fang, Z. Hu, H. Teng, Z. Jiang, and H. D. Ng, "Numerical study of inflow equivalence ratio inhomogeneity on oblique

detonation formation in hydrogen-air mixtures," *Aerospace Science and Technology*, vol. 71, pp. 256–263, 2017.

[28] P. Yang, H. D. Ng, and H. Teng, "Numerical study of wedge-induced oblique detonations in unsteady flow," *Journal of Fluid Mechanics*, vol. 876, pp. 264–287, 2019.

[29] P. Yang, H. D. Ng, H. Teng, and Z. Jiang, "Initiation structure of oblique detonation waves behind conical shocks," *Physics of Fluids*, vol. 29, no. 8, article 086104, 2017.

[30] K. Wang, Z. Zhang, P. Yang, and H. Teng, "Numerical study on reflection of an oblique detonation wave on an outward turning wall," *Physics of Fluids*, vol. 32, article 046101, 2020.

[31] Y. Liu, L. Wang, B. Xiao, Z. Yan, and C. Wang, "Hysteresis phenomenon of the oblique detonation wave," *Combustion and Flame*, vol. 192, pp. 170–179, 2018.

[32] H. D. Ng, M. I. Radulescu, A. J. Higgins, N. Nikiforakis, and J. H. S. Lee, "Numerical investigation of the instability for one-dimensional Chapman–Jouguet detonations with chain-branching kinetics," *Combustion Theory and Modelling*, vol. 9, no. 3, pp. 385–401, 2005.

[33] P. Yang, H. Teng, H. D. Ng, and Z. Jiang, "A numerical study on the instability of oblique detonation waves with a two-step induction-reaction kinetic model," *Proceedings of the Combustion Institute*, vol. 37, no. 3, pp. 3537–3544, 2019.

[34] R. Deiterding, "Parallel adaptive simulation of multi-dimensional detonation structures, [Ph.D. thesis]," Brandenburgischen Technischen Universität Cottbus, 2003.

[35] J. Li, J. Ning, and J. H. S. Lee, "Mach reflection of a ZND detonation wave," *Shock Waves*, vol. 25, no. 3, pp. 293–304, 2015.

[36] J. Li and J. H. S. Lee, "Numerical simulation of Mach reflection of cellular detonations," *Shock Waves*, vol. 26, no. 5, pp. 673–682, 2016.

Research Article

A Comparison Investigation on Cylinder Test in Different Ambient Media by Experiment and Numerical Simulation

Fan Zhang [ID],[1] Fei Shen,[1] Biaobiao Li,[1] Baohui Yuan,[1] and Bing Li [ID][2]

[1]*Xi'an Modern Chemistry Research Institute, Xi'an, Shaanxi 710065, China*
[2]*School of Aeronautics, Northwestern Polytechnical University, Xi'an, Shaanxi 710072, China*

Correspondence should be addressed to Fan Zhang; zhangfan3141@163.com

When the detonation reaction occurs after the charge in the warhead is ignited, the propagation of the detonation wave and the expansion of the detonation product will interact with the wrapped metallic shell and cause the shell material to accelerate, extremely deform, and eventually rupture, which is a typical strong fluid-structure interaction problem. In this paper, a comparison investigation on a cylinder test in different ambient media was implemented by experiment and numerical simulation, respectively. In the experimental test, the attention was paid to discussing the differences of the accelerating process of the cylinder metal wall, the expansion modes, and the fragment shape of the cylinder due to the medium with different shock wave impedance which surrounds the cylinder shell. For the numerical simulation, a coupling scheme of a meshless method and finite element method called the coupled finite element material point method was used to reproduce the cylinder expansion problem driven by explosive sliding detonation where the interaction between the cylinder wall and the explosive/detonation product is enforced by using a point-to-surface contact scheme to accurately achieve contact and separation between material particles and finite elements. Lastly, the macroscopic and microscopic states of the cylinder failure were compared and discussed for further discussion.

1. Introduction

The warhead is filled with high energetic materials and utilizes the detonation product, shock wave, and fragments to destroy the targets. The main factors affecting the damage efficiency consist of the density of the explosive, the detonation speed, the ability of acceleration, and the dynamical properties of the structure and material of the target. At present, the cylinder test is the simplest and the most feasible test method to evaluate the capability of an explosive and the dynamical properties of the cylinder material which was first proposed and applied by Kury et al. [1] of LLNL. In this test, the explosive is placed inside the metallic cylinder to be tested, and the charge is detonated at one end by a detonator or an explosive plane-wave lens. In the process of the detonation wave propagating to the other end of the cylinder, the high-speed scanning camera is used to record the cylinder wall expansion history. The image processing technology is used to obtain the expansion speed and the specific kinetic

energy and to characterize the characteristic quantity of the explosive capability. In the relevant fields including experimental design, testing, and data extraction of cylinder tests, a large number of research results can be referenced. Wang et al. [2] discussed the expansion, acceleration, and rupture process of cylindrical casing made of three types of material including TU1 copper, 50SiMnVB steel, and ANSI 1045 steel in the air medium by means of experimental tests and accurately measured the oscillation of velocity at the scanning slit of cylindrical casing by using the DPS (arrayed Doppler Photonic System). Goto et al. [3] studied the expansion and fracture process of cylinder and ring under the plane-strain and uniaxial-stress conditions by detonation load and gave the relevant coefficients of the Johnson-Cook damage model of cylindrical material based on the experimental data. Lindsay et al. [4] used the Shen-Castan edge detection algorithm to extract the expansion displacement curve of the cylinder wall from the slit expansion film more efficiently and accurately; meanwhile, a three-stage force formula model on the wall

expansion of the cylinder was proposed to capture the most prominent features of the expansion of the wall of the cylinder. In particular, it can commendably reproduce the peaks and valleys of the first reverberation of the velocity curve of the wall. In the existing researches, few papers have involved the expansion of the cylinder in the water medium. Yang et al. [5] investigated the detonation and postcombustion effects on the underwater explosion of an aluminized explosive which was not confined by any metallic shell with a meshless method, the MOC method. It focused on the nonisentropic flow due to postcombustion effect which affects the shock trajectory and gas-water interface. Hamashima et al. [6] obtained the JWL parameters of the detonation product of the cylindrical and spherical high explosives SEP which was not confined either by the shell through the nonideal detonation of the underwater explosion. Zhao et al. [7] researched the energy output characteristics of cyclotrimethylenetrinitramine- (RDX-) based aluminized explosives under the water with different aluminum content.

The cylinder test problem is a typical sliding detonation problem involving the propagation of detonation wave and the large deformation, fracture, and complicated phase changes of materials which are highly nonlinear. Meanwhile, the cylindrical metal, detonation product, and the outer cylinder medium form a complicated fluid-structure coupling system which increases the difficulty of numerical simulation. As one kind of meshfree particle method, the material point method [8] takes an advantage in the simulation of the dynamic response of materials under the initiation and the detonation of energetic materials. In particular, the solid material, the gas of the detonation product, and the detonation wave can be coupled under the uniform framework by the material point method which avoids the difficulty of the interface treatment. For example, Hu and Chen [9] studied the synergistic effects of concrete walls undergoing the action of the detonation of explosives and impact of fragments. Wang et al. [10, 11] used the material point method to evaluate the sliding detonation process of explosives and simulated the explosion welding between metal plates. Ma et al. [12] proposed an adaptive material point method to handle the numerical fracture problem in a one-dimensional shock tube; the method was also applied to solve the explosively driven metal flyer and the three-dimensional-shaped charge jet problem [13]. Yang et al. [14] introduced stochastic failure factors into the material model and successfully simulated the metal spherical shell rupturing process under the blast loading. Zhang et al. [15, 16] used the ignition growth equation to study the shock detonation process of solid explosives and further discussed the critical impact velocity of the flyer causing the explosion to detonate. Yang [17] studied the shock wave propagation problem and the dynamic response process of structure undergoing underwater explosion by using the generalized material point method. In order to avoid the numerical fracture problem of the material point method in simulating the propagation of detonation waves, Cui and Zhang [18, 19] established a coupling scheme of the material point method with the finite difference method for simulating the detonation wave propagation process and its coupling with the concrete target. Furthermore, the

material point method has achieved favorable applications in other fields such as hypervelocity impact [20, 21], incompressible fluid [22, 23], and molecular dynamics [24].

In this paper, the numerical method and experimental test will be used to investigate the cylinder expansion problem driven by sliding detonation of the explosive. Firstly, the cylinder expansion problem is introduced in Section 1. In Section 2, an improved version of the coupled finite element material point method and the contact algorithm is presented. In Section 3, the expansion process of the metal cylinder in the air medium is compared with that in the water medium by the test results and numerical methods. In Section 4, the rupture modes of the cylinder in the air/water medium are analyzed through the shock wave theory and microscanning technique. After the above research, it provides a reference for the explosion-driven problem of the underwater cylinder test.

2. Coupling of Finite Element Method with Material Point Method

The updated Lagrangian framework was applied in both the finite element method and the material point method; their weak form can be given as [8]

$$\int_V \delta u_i \rho \ddot{u}_i dV + \int_V \delta u_{i,j} \sigma_{ij} dV - \int_V \delta u_i \rho b_i dV - \int_{\Gamma_t} \delta u_i \bar{t}_i d\Gamma = 0,$$

(1)

where the subscripts i and j denote the components of the spatial coordinates following the Einstein summation convention, ρ is the density of the current state, b_i is the body force per unit mass, u_i is the displacement, δu_i is the corresponding virtual displacement, σ_{ij} is the Cauchy stress, Γ_t stands for the prescribed traction boundary of V, and $\bar{t}_i$ is the external traction.

2.1. Material Point Method. MPM is a hybrid method with Eulerian-Lagrangian description in which a material domain is represented by a collection of Lagrangian particles moving through a Eulerian background grid, as shown in Figure 1. The particles carry all state variables such as the mass, the position, the velocity, the acceleration, and the stress and strain, whereas the grid which carries no permanent information is used to solve the momentum equations and calculate the spatial derivative of physical variables. In this paper, the regular orthogonal grid is adopted for simplicity and high efficiency.

Since the whole domain is discretized by n_p particles, the spatial density can be approximated as follows:

$$\rho(x) = \sum_{p=1}^{n_p} m_p \delta(x - x_p),$$

(2)

where n_p is the sum of particles, m_p is the mass of particle p, δ is the Dirac delta function, and x_p is the location of particle p.
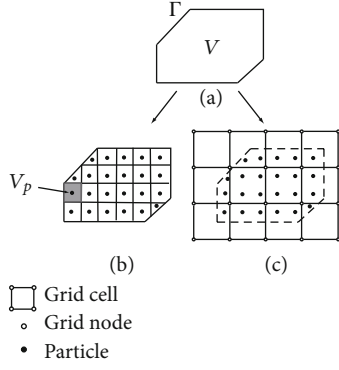
FIGURE 1: Material point method [8]: (a) material domain, (b) material represented by material points, and (c) discretization by material points.

When the momentum equations are solved in each time step, the background grid is attached rigidly to the particles and deforms with particles so that the grid can be viewed as a finite element discretization for the material domain. Consequently, the displacement $u_i(x)$ at any location can be approximated through

$$u_i(x) = \sum_{I=1}^{n_g} N_I(x) u_{iI}, \tag{3}$$

where n_g is the total number of grid nodes.

Substituting Equations (2) and (3) into the weak form Equation (1) and applying the lumped grid mass matrix yield

$$m_I \dot{v}_{iI} = f_{iI}, \quad I = 1, 2, \cdots, n_g, \tag{4}$$

where $\dot{v}_{iI}$ is the velocity of grid node I,

$$m_I = \sum_{p=1}^{n_p} N_{Ip} m_p \tag{5}$$

is the mass of grid node I and $N_{Ip} = N_I(x_p)$,

$$f_{iI} = f_{iI}^{ext} + f_{iI}^{int} \tag{6}$$

is grid nodal force, where

$$f_{iI}^{int} = -\sum_{p=1}^{n_p} N_{Ip,j} \sigma_{ijp} \frac{m_p}{\rho_p} \tag{7}$$

is the internal grid nodal force,

$$f_{iI}^{ext} = \sum_{p=1}^{n_p} m_p N_{Ip} b_{ip} \tag{8}$$

is the external grid nodal force and is the Cauchy stress and body force of particle p, respectively. The momentum Equation (4) in the background grid can be solved either by the explicit integration scheme or by the implicit integration scheme (readers can refer to the related references [8] for more details). From the above discretization and computational process, it is found that the weak form is equivalent to the momentum equation and the traction boundary condition is the same in MPM and FEM. The biggest difference is that the particle quadrature is used in the material point method in each time step and Gauss quadrature in the finite element method.

2.2. Coupled Finite Element Material Point Method. In the impact problem with low and moderate striking velocity, the deformation of the metallic projectile is smaller than that of the concrete target. For handling this problem, Lian et al. [25] proposed a coupling scheme named the coupled finite element material point method (CFEMP) based on the updated Lagrangian framework. Then, an improved CFEMP scheme, a particle-to-surface contact algorithm rather than the grid-based contact method, was presented by Chen et al. [26]. It drew on the idea of the particle-to-surface contact algorithm in FEM to satisfy the contact conditions exactly at the contact interface, and it is convenient to implement the contact/slip/split between material particles and the finite elements. The improved contact version is comprised of four steps: In the first step, the information of the FEM grid is acquired to extract the surface mesh of the finite element grid. In the second step, establishing the potential contact pairs between the material points and the surface elements is carried out based on the possible contact event. In the third step, according to the potential contact pairs, the exact contact position and the gap for each contact pair are calculated by using a local search. In the last step, the contact force resisting the penetration into another body is imposed for each contact pair. The contact force applied on the material point is mapped into the background grid nodes, and that applied on the surface grid element is distributed to finite element nodes.

The existing numerical investigations show that improved CFEMP with the particle-to-surface contact algorithm was stable in the problems such as the free falling of a wedge into water and water column collapse with elastic baffle [26], and the efficiency and precision are better than the material point method and original CFEMP. However, further verification is needed in the gas detonation case with local extreme deformation.

3. Cylinder Expansion Test in Different Media

The main purpose of the cylinder test is to evaluate the capacity of acceleration for explosives. Generally, the typical cylinder test is carried out in an air medium under standard atmospheric pressure. Due to the very low shock wave impedance of air, the impedance of air medium on the acceleration of cylinder explosives is negligible in the theoretical analysis and numerical simulation. If the air medium is replaced by the water medium in the cylinder test, the influence of the water medium on the propagation of detonation wave as well as the cylinder expansion must be considered, because it is a typical fluid-structure interaction problem. In
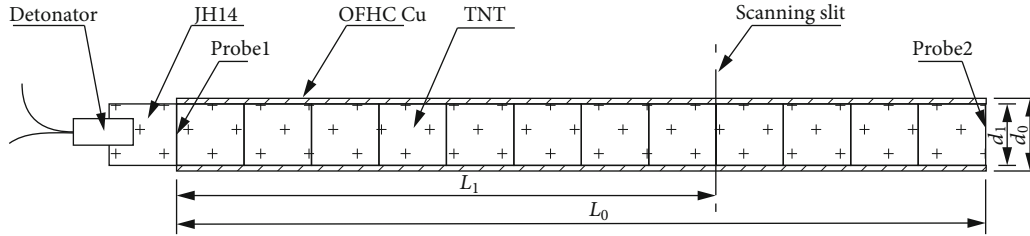
FIGURE 2: The configuration of cylinder with charges.

FIGURE 3: The photo of the underwater cylinder test.
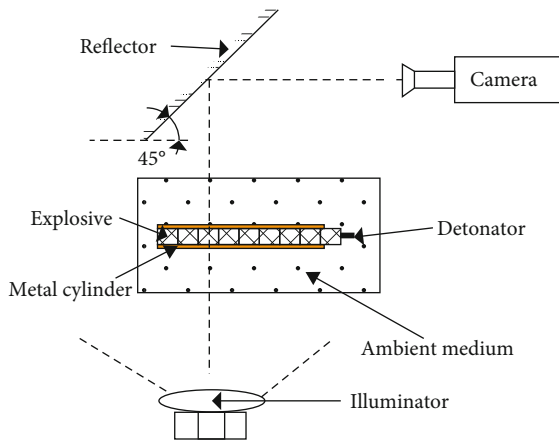
FIGURE 4: The whole experimental layout of explosively loaded metal cylinder test.
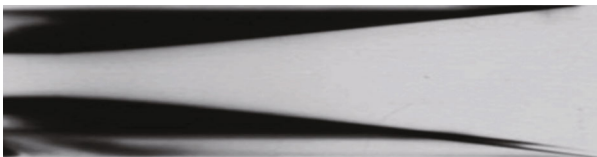
FIGURE 5: The wall-expanded negative in air medium.

this section, the cylinder tests in two different media were conducted and compared.

3.1. Cylinder Test Experiment and Its Layout. The cylindrical charges and configuration are shown in Figure 2. The main
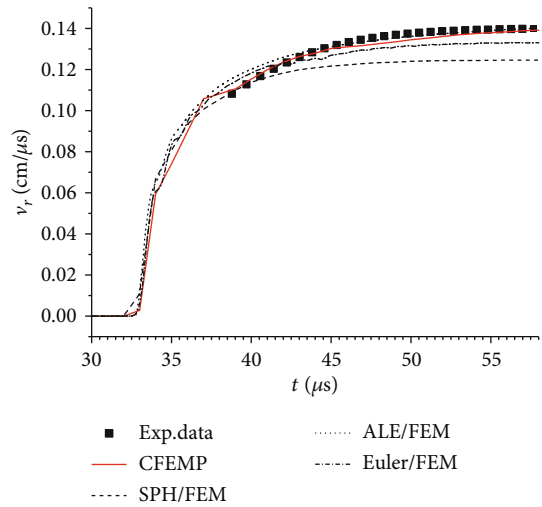
FIGURE 6: The wall-expanded speed-time curve at the slit.

charge is made of TNT explosive, which was connected one by one in series with a size of $\phi 25$ mm × 25 mm. The material of the cylinder is oxygen-free copper TU1 with an outer diameter of $d_0 = 30.12$ mm, an inner diameter of $d_0 = 25.0$ mm, and a length of $L_0 = 300$ mm. The detonation end was extended by one JH14 charge and ignited by a detonator, and the detonation velocity of the explosive was measured by an electric probe at each end of the copper cylinder. A SJZ-15 high-speed scanning camera was used for scanning slit during the test. In the process of test, the light source was provided by parallel backlight technology. The slit position was located at a position with a 200 mm distance from the detonation end, the camera speed was set to 6×10^4 r/min, and its corresponding scanning speed was 3 km/s.

The experimental device of the underwater cylinder test is shown in Figure 3; the tank made of wood and plexiglas which has a length of 400 mm, a width of 300 mm, and a height of 300 mm was filled with water. The light source and scanning camera can be used because the front and rear observation windows are transparent. In our test, the argon-jet spark light source was adopted to supply the illumination. For safety reasons, relevant tests were carried out in the explosion tower of the Xi'an Modern Chemistry Research Institute. The whole experimental layout of the explosively loaded metal cylinder test is illustrated in Figure 4.

When the cylinder expansion test was happening, the expansion trajectory negative at the slit can be obtained through the scanning camera. As shown in Figure 5, the horizontal axis represents the time variable and the vertical axis

TABLE 1: The parameters for TNT explosive.

ρ_0 (g/cm^3)	A (Mbar)	B (Mbar)	JWL EOS R_1	R_2	W	E_0 (kJ/cm^3)	C-J parameters D (cm/μs)	$P_{\text{C-J}}$ (Mbar)
1.589	3.712	0.0323	4.15	0.95	0.3	7.0	0.6874	0.21

TABLE 2: The material constants for TU1.

Material parameters ρ_0 (g/cm^3)	v	E (Mbar)	Johnson-Cook strength model A (MPa)	B (MPa)	n	c	m	$\dot{\varepsilon}_0$ (s^{-1})	T_{room} (K)	T_{melt} (K)
8.96	0.35	1.29	90	292	0.31	0.025	1.09	1.0	293	1356

represents one-dimensional image of the slit expansion at the corresponding time. A microscope was used to manually interpret the scanning negative of the cylinder expansion. First, the starting position of the cylinder wall is determined by manual visual inspection as the origin of coordinates. Next, the ordinate and abscissa of the point at the interface are identified along the expansion trace at the equal axial distance, and then, according to the image magnification and the scanning speed, the expansion distance $(R - R_0)$ of the cylinder wall and the corresponding expansion time t are calculated. Lastly, a series of $(R_j - R_0) - t_j$ data is obtained, and a curve can be fitted based on them. The above specific experimental data processing was described in the literature [1].

3.2. Cylinder Test and Numerical Result in Air Medium. The cylinder wall-expanded negative at the slit was obtained by a cylinder test in an air medium as shown in Figure 5. According to the data of $(R_j - R_0) - t_j$, the expansion speed-time curve of the outer wall of the cylinder can be obtained by the differential calculation as illustrated in Figure 6. The detail of data is supplemented in the supplemental file (available here).

In order to quantitatively investigate the propagation of detonation wave, the flow process of detonation products, and fluid-structure interaction between product gas as well as environmental medium and the cylinder shell, the improved CFEMP based on MPM3D (http://comdyn.hy .tsinghua.edu.cn/english/mpm3d) [27] software was used in this paper for numerical verification. Meanwhile, in order to compare the numerical accuracy with other numerical algorithms, the numerical results from the SPH/FEM, ALE/- FEM, and Euler/FEM coupling schemes based on Autodyn software were listed in this subsection. In the numerical model, the detonation speed of the booster charge is close to that of the main charges inside the copper tube, so all charges were simulated based on the equation of state of the JWL (Jones-Wilkins-Lee) reaction product of TNT which takes the form of

$$p = A\left(1 - \frac{\omega}{R_1 V}\right)e^{-R_1 V} + B\left(1 - \frac{\omega}{R_2 V}\right)e^{-R_2 V} + \frac{\omega E}{V}, \quad (9)$$

where $E = \rho_0 e$ is the internal energy per unit initial volume and ρ_0 is the reference density. ω, A, B, R_1, and R_2 are user-defined material constants. D is the C-J detonation velocity, $P_{\text{C-J}}$ is the C-J pressure. All parameters are listed in Table 1. For the copper TU1, the Johnson-Cook strength model is adopted as follows:

$$\sigma_y = \left(A + B\bar{\varepsilon}^n\right)\left(1 + C \ln \dot{\bar{\varepsilon}}^*\right)\left(1 - T^{*m}\right), \quad (10)$$

where A, B, n, C, and m are material constants, $\dot{\bar{\varepsilon}}^* = \dot{\bar{\varepsilon}}/\dot{\varepsilon}_0$ is the dimensionless effective plastic strain rate, $\dot{\varepsilon}_0$ is the effective plastic strain rate corresponding to the quasistatic test used to determine the yield and hardening parameters A, B, and n, and $\dot{\bar{\varepsilon}} = \sqrt{(2/3)\dot{\varepsilon}'_{ij}\dot{\varepsilon}'_{ij}}$ is the plastic strain rate. $T^* = (T - T_r)/(T_m - T_r) \in [0, 1]$ is the dimensionless temperature; T_r and T_m are the room temperature and melting temperature of the material. Its parameters are listed in Table 2 and the Mie-Grüneisen equation of state where $c_0 = 0.394$ cm/μs, $s = 1.49$, and $\gamma = 2.0$. In the CFEMP model, a quarter model was used in order to save the calculation cost and the effects of the air medium are ignored based on the previous analysis. The total length of cylinder charges is 325 mm which was discretized into 321099 particles with a space size of 0.5 mm, and the orthogonal cube grid is overlapped on the computational domain with a size of 1.0 mm × 1.0 mm × 1.0 mm. The copper tube with a length of 300 mm, an inner diameter of 25 mm, and an outer diameter of 30.12 mm was discretized by a finite element mesh which has 4848 nodes and 3000 elements. In SPH/FEM, ALE/FEM, and Euler/FEM coupling models, the two-dimensional axisymmetric model was used where the charges were discretized by SPH, ALE, or Euler, and all the copper tubes were discretized by the finite element method. Their sizes were consistent with those of the material particles and finite elements in CFEMP.

As shown in Figure 6, the numerical results of the expansion speed of the cylinder tube were compared with the experimental results at the slit ($L_1 = 200$ mm). It is found that the time when the cylinder wall at the slit simulated by several numerical methods started to expand was basically simultaneous at $t \approx 32.5\ \mu$s. In the beginning, the cylinder wall underwent a sharp radial expansion when the detonation wave front had passed the slit. When the explosive around the slit had completely reacted, the cylinder wall continued to expand under the action of the rarefaction wave and the reaction product. With the subsequent expansion
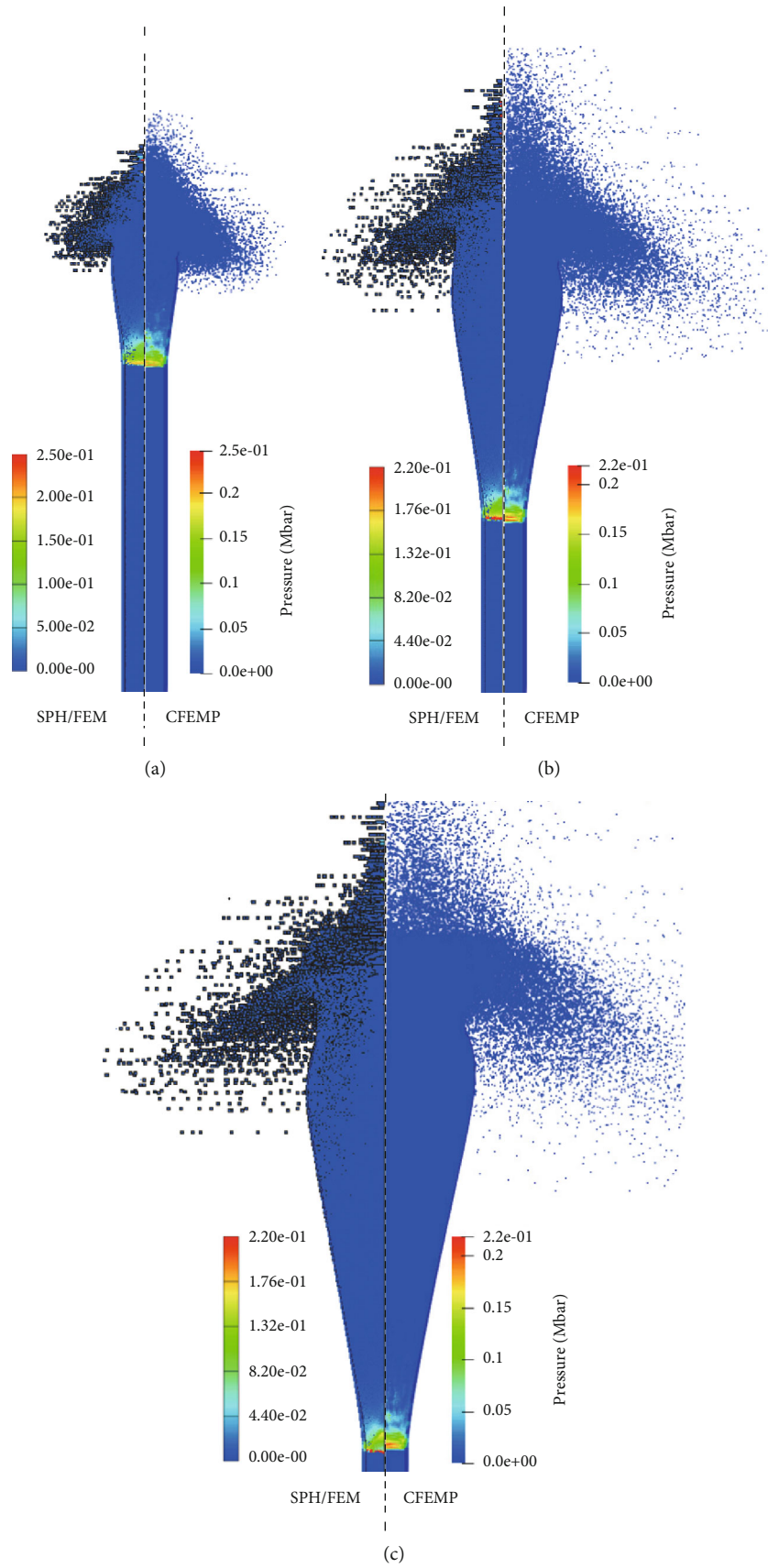
FIGURE 7: Comparisons of pressure contour by CFEMP and SPH/FEM schemes for cylinder test in air medium: (a) $t = 15\,\mu$s, (b) $t = 30\,\mu$s, and (c) $t = 45\,\mu$s.
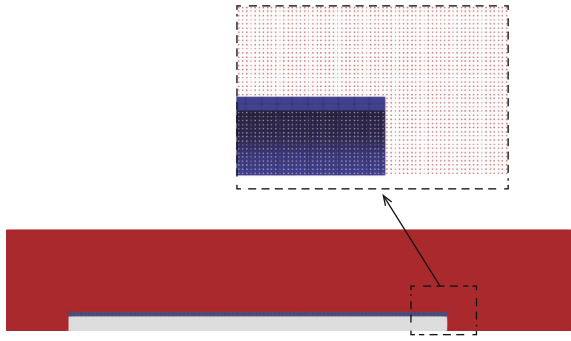
Figure 8: The configuration of the underwater cylinder test by CFEMP.

Figure 9: The wall-expanded negative in water medium.

of the detonation product, the expansion rate of the cylinder wall dropped significantly and tended to be a constant. Among these numerical methods, the numerical results of CFEMP are consistent with the results and trends of other numerical methods. However, two issues are found in the SPH/FEM scheme analogous to CFEMP. Firstly, the wave front region of the shock wave was widened to cause the copper wall to expand in advance, because the kernel function approximation was adopted in SPH and the influence domain of particle was enlarged. Secondly, the speed of cylinder wall expansion was significantly lower than the experimental value which is mainly due to the excessive numerical dissipation during the propagation process. On the other hand, the coupling scheme of the Euler method and the finite element method caused the contact force to decrease due to the penetration of the fluid-solid interface in the later stage. It led to the lower expansion speed of the cylinder wall than that of the experimental test. If the ALE/- FEM scheme was used to discrete charge and cylinder tube, respectively, it can simulate large deformation and guarantee the nonpenetration at the fluid-solid interface, whose results are consistent with the experimental test as illustrated in Figure 6.

As illustrated in Figure 7, the pressure contours obtained by two numerical simulation methods including SPH/FEM and CFEMP were compared at three different times. The result of SPH/FEM was placed on the left side and the result of CFEMP on the right side. It is observed that the location of shock wave propagation and the deformation of the cylinder tube from two methods were symmetric basically. However, there were some anomalous particles with excessive pressure in the SPH/FEM scheme due to the tensile instability, which did not happen in the CFEMP scheme. On the other hand, the expanding velocity of particles in CFEMP was higher than that in SPH/FEM at the top of the cylinder tube, which is caused mainly by the interface instability of the material point method in the CFEMP scheme. In conclusion, the

two meshless methods coupled with the finite element method are suitable to simulate the sliding detonation of the explosive and the expansion and deformation process of the cylinder wall in the cylinder test; in terms of quantitative comparison, the result of CFEMP is closer to the experimental result compared with the SPH/FEM scheme.

3.3. Cylinder Test and Numerical Result in Water Medium. Based on the standard cylinder test in the air medium, the air medium was replaced by the water medium as shown in Figure 3. The TU1 cylinder tube has an outer diameter of 30.12 mm, an inner diameter of 25 mm, and a length of 300 mm. In order to ensure the reliability of the installation of the detonator under the water, the length of the charge column is consistent with that of the cylinder tube, i.e., the detonation end and the left end of the cylinder tube are flush. In addition, other material parameters are consistent with the case in the air medium. The observation slit is also marked at the same position $L_1 = 200$ mm from the left end of the copper tube. The water tank is constructed by wooden and plexiglas plates, and the experimental device is suspended in the centre of the pool and fixed with iron wires as illustrated in Figure 3. In the numerical model of CFEMP, the TNT charges were discretized into 76224 material particles. The spacing length of each particle was set to 0.8 mm with a size of background grid of 1.6 mm × 1.6 mm. The TU1 tube was discretized by finite element mesh, and the finite element mesh in this case was consistent with that in the first case. The water domain was discretized into 4238869 material particles. The CFEMP model is shown in Figure 8. For the model of water, its viscosity was ignored in the strength model, and the Mie-Grüneisen polynomial was used in the equation of state. The formulation of EOS was given as follows:

$$p_H = \begin{cases} \rho_0 C_0^2 \left[\mu + (2s-1)\mu^2 + (s-1)(3s-1)\mu^3 \right], & \text{if } \mu \geq 0, \\ \rho_0 C_0^2 \mu, & \text{if } \mu < 0, \end{cases} \tag{11}$$

where $\mu = (\rho/\rho_0) - 1$ represents the compressibility of the material and c_0 and s are the relevant material parameters. These parameters related to water used in this paper are set as $\rho_0 = 1.0$ g/cm^3, $c_0 = 0.165$ cm/μs, and $s = 1.92$. In SPH/FEM and ALE/FEM models, a two-dimensional axisymmetric model was established. The charge and water were discretized by SPH or ALE, and the cylinder tube was discretized by finite element mesh whose size and material model were consistent with those of finite element mesh applied in CFEMP.

As shown in Figure 9, the velocity-time curve of cylinder wall expansion at the slit was extracted from the cylinder test whose data is supplied in the supplemental file, and it was found that the expansion curve of the cylinder in the water medium was significantly different from that in the air. First, on the velocity peak of the curve, the value of the cylinder wall expansion (about 770 m/s) under the water was obviously smaller than that (about 1399 m/s) in the air medium. Second, for the trend of the velocity-time curve, the expansion speed curve of the cylinder in the air medium shows a
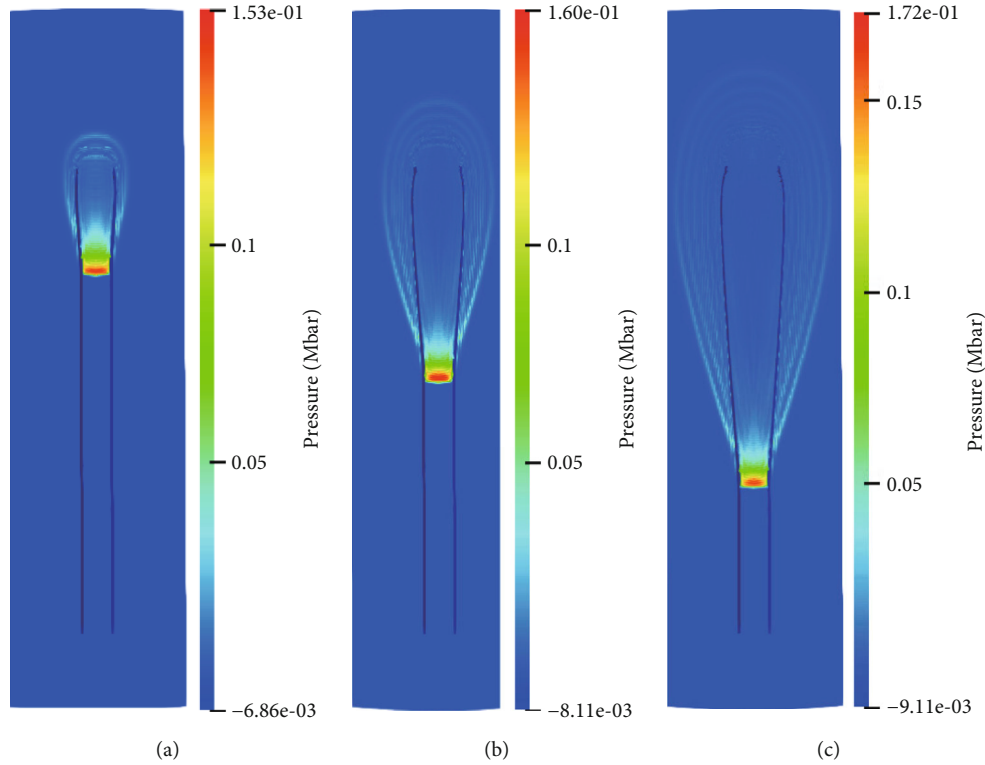
FIGURE 10: The pressure contour for cylinder test in water medium by CFEMP scheme: (a) $t = 10 \, \mu s$, (b) $t = 20 \, \mu s$, and (c) $t = 30 \, \mu s$.

monotonously increasing change. Oppositely, the curve of the cylinder in the water medium had a rapid increasing at the initial stage and then a slow decreasing. Compared with several numerical methods, the velocity-time curve simulated by the CFEMP method was basically the same as the experimental data at the beginning, the peak, and the latter stages. At the same time, by comparing the expansion negatives (Figures 5 and 9) of the cylinder tests and tests and the simulation configurations (Figures 7 and 10), it was found that the rate of the cylinder expansion under the water was smaller than that in the air medium. For the SPH/FEM method applied in this problem, due to the interface between the water and copper tube, the amplitude of the rarefaction wave which was reflected in the detonation product was greatly reduced, and then, the numerical energy dissipation in SPH/FEM was also reduced. According to the above analysis, the numerical results in the water medium by CFEMP and ALE/FEM schemes were closer to the experimental result than that in the air medium. The pressure contour by the CFEMP method is shown in Figure 10, from which the trajectory of the detonation wave front and the interface between the cylinder wall and the water can be clearly identified.

3.4. Investigation on the Propagation of Shock Wave in Different Media. The difference of shock wave impedance of the medium outside the cylinder wall leads to the distinguishing expanding pattern of the cylinder tube, which further changes the detonation energy and momentum transmission paths to cause the different distribution of detonation energy to the medium. In this subsection, the one-dimensional shock wave theory was used to explain the issue. The cylinder tube coupling with air or water can be regarded as a multimedium system; the combination of different shock wave impedance media with a cylinder tube will cause the shock wave at the interface to reflect and transmit according to different manners. In the process of shock wave propagation in the cylinder test, it is supposed that the attenuation in the thin-walled cylinder is neglected, so the type of the stress wave reflected at the interface of two media just depends on the shock wave impedance of the media based on the shock wave theory. When the shock wave propagates from medium I to medium II, if the impedance of medium I is greater than that of medium II, the rarefaction wave will be reflected at the interface. On the contrary, the reflected wave is the shock wave if the impedance of medium I is less than that of medium II.

The Hugoniot curve of the undisturbed material can be obtained by using the mass conservation equation, the momentum conservation equation, and the shock compression law in the solid after the incident shock wave reached the interface as follows:

$$p = \rho_0 u(c_0 + su), \tag{12}$$

where ρ_0 is the initial density of the material, c_0 and s are related material parameters, and u is the particle velocity at the deformed domain. The parameters of the Hugoniot curve which refer to the EOS of material are listed in Table 3.

When the shock wave propagates to the interface of two media, the values of the reflected wave and the transmitted wave can be calculated by using the shock Hugoniot curve

TABLE 3: The parameters of Hugoniot curve.

	ρ_0 (g/cm^3)	c_0 (cm/μs)	s
TU1	8.96	0.394	1.49
Water	1.0	0.165	1.92
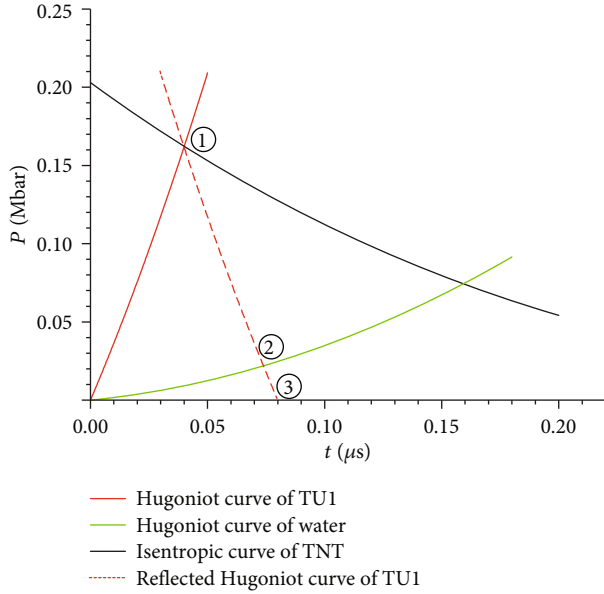
FIGURE 11: The analysis diagram of the stress wave propagation process.

or the isentropic p-u curve of the medium. As shown in Figure 11, the red and green solid curves represent the shock Hugoniot curve of different media (copper and water, respectively). The value of the slope from the original point to any point at the Hugoniot curve becomes large with increasing the shock wave impedance of the medium. The solid black curve indicates the isentropic curve of the TNT detonation product. According to the equation of state of the explosive, the parameters of the detonation wave at the C-J point, and the isentropic equation of the detonation product, the relationship between the lateral particle velocity and rarefaction wave pressure of detonation can be calculated as

$$u = \frac{2D\gamma}{\gamma^2 - 1}\left[1 - \left(\frac{p}{p_{\text{C-J}}}\right)^{(\gamma-1)/2\gamma}\right], \tag{13}$$

where u is the particle velocity and p is the pressure of incident shock wave at the interface, D is the explosive detonation wave speed and is set to be 0.6874 cm/μs, γ is the multi-index of the explosive and is set to be 2.727, and $p_{\text{C-J}}$ is the C-J detonation pressure of explosive and is set to be 0.21 Mbar. As shown in Figure 11, the red dotted line is the isentropic curve of copper. For the sake of simplicity, the isentropic rarefaction wave curve is approximated by the
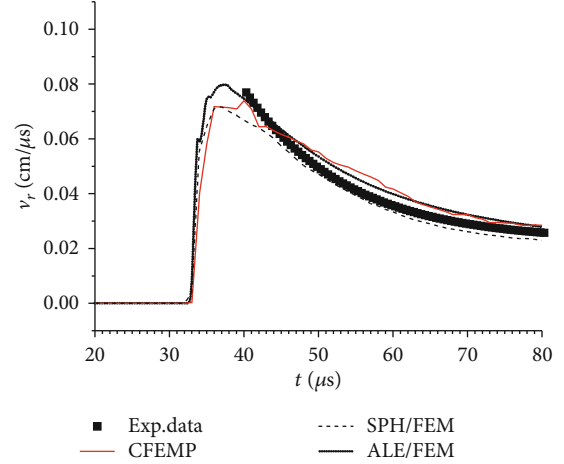
FIGURE 12: The wall-expanded velocity-time curve at the slit.

reflected Hugoniot curve; the specific form can be expressed as

$$p = \rho_0(2u_1 - u)[c_0 + s(2u_1 - u)]. \tag{14}$$

For the air medium, since its shock wave impedance is much lower than that of metal or water, it can be approximated as $p(u) = 0$. According to the illustration of Figure 11, when the detonation wave propagates along the copper tube, the intersection point ① between the Hugoniot curve of the copper and the isentropic curve of the detonation product represents the transmitted wave pressure and the particle velocity at the interface. When the shock wave in copper is transmitted into the water, since the shock wave impedance of copper is greater than that of water, the intersection point ② between the mirror symmetry of the Hugoniot curve of copper and the Hugoniot curve $p(u)$ of water represents the transmitted shock wave. Conversely, if the medium outside the copper is air, the intersection point ③ represents the transmitted shock wave at the interface below the intersection point ②. In the above two cylinder tests with different environmental media, the charge and copper materials were the same, so the time when the first shock wave peaks transmitted to the copper medium at the slit was consistent. As illustrated in Figure 11, the particle velocity at the interface when the shock wave is transmitted into the water medium is about 0.73 mm/μs (point ②) which is basically consistent with the initial expansion velocity peak of the outer wall of the cylinder in Figure 10, and the pressure of transmitted shock wave is about 2.0 GPa. In another case, when the shock wave is transmitted into the air medium, the particle velocity behind the shock wave front in the air is about 0.78 mm/μs (point③), and the pressure of transmitted shock wave is neglected compared with the pressure in the water medium.

4. Discussion on Microscopic Analysis of Cylinder Damage

Based on the shock wave theory, the propagation process of shock wave in the medium was analyzed theoretically in the

(a)   (b)
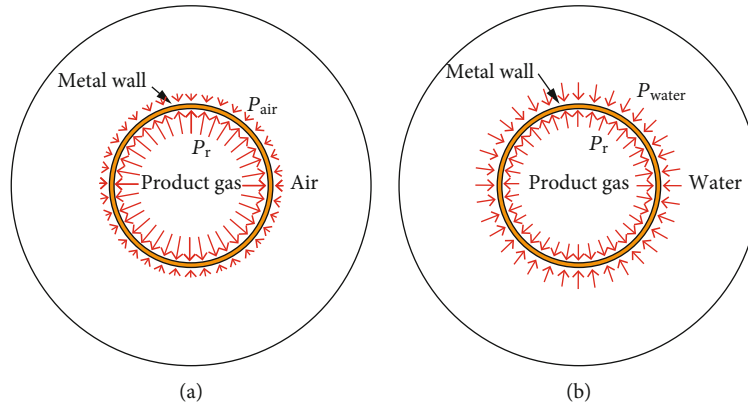
FIGURE 13: The schematic diagram on the resultant force applied on the cylinder wall at the second stage: (a) in air medium and (b) in water medium.

(a)   (b)

FIGURE 14: Recycled fragments in the experiment.

previous section, but it could not quantitatively evaluate the work done by the detonation product acting on the copper tube. Through further numerical simulations and experimental measurements, it is found that the cylinder which is surrounded by different environmental media has different loading history curves as shown in Figures 6 and 12. In the air medium, the cylinder wall undergoes a typical process including sharp loading ($33 \mu s \leq t \leq 34 \mu s$), slow loading ($34 \mu s < t \leq 55 \mu s$), and shell fracture ($t > 55 \mu s$). But in the water medium, another process was presented which includes a sharp loading ($33 \mu s \leq t \leq 34 \mu s$), slow unloading ($34 \mu s \leq t \leq 80 \mu s$), and shell fracture finally. The essential reason is ascribed to the change of the resultant force applied at the cylinder wall. For example, the first stage of sharp loading was completed quickly under the first transmitted shock wave from the detonation product. At the second stage, on account of the superposition of transmitted shock wave at the detonation product/cylinder wall interface and the reflected rarefaction wave at the cylinder wall/air or cylinder wall/water interface, the cylinder wall was pressed by outside and inside forces collectively. In the case of the air medium, P_r was far greater than P_{air} at the first stage; the cylinder wall was accelerated rapidly. At the second stage, P_{air} raised due to the transmitted shock wave, but it was far less than P_r as illustrated in Figure 13(a). In the case of the water medium, P_r was also far greater than P_{water} at the first stage. After the transmitted shock wave reached the interface between the

cylinder wall and the water for the first time, P_{water} exceeded P_r gradually at the second stage as illustrated in Figure 13(b). Finally, for both cylinder tests, the cylinder wall kept expanding along the radial direction due to the gas expansion and the inertia. When the deformation of the cylinder wall approached the limitation of fracture, the copper wall will undergo a circumferential and axial fracture up to breaking up. As shown in Figure 14, we recovered some of the copper tube fragments from two tests. For the cylinder test in the air medium, most of the fragments are slender with an average length of about 26 mm and average width of 10 mm. Conversely, the fragments have a flake shape with an average length of about 270 mm and an average width of 14.7 mm for the cylinder test in the water medium.

In order to further study the microscopic failure mechanism of the cylinder tube driven by explosive, a scanning electron microscope (SEM, JSM580) was used to observe the microscopic scale of the metal fragments recovered after the test. For the first case in the air medium, the surface of the recovered fragments presents successive waves along the axial direction and no obvious strip-shaped appearance as shown in Figure 15(a-1). After zooming it in, the obvious local bulges were visible which is called dimple due to the outer surface under tension as shown in Figure 15(a-2). When the medium around the cylinder is water, the surface of the recovered cylinder fragments generally showed a relatively regular parallel strip along its axial direction. As shown

(a-1)

(a-2)

(b-1)

(b-2)
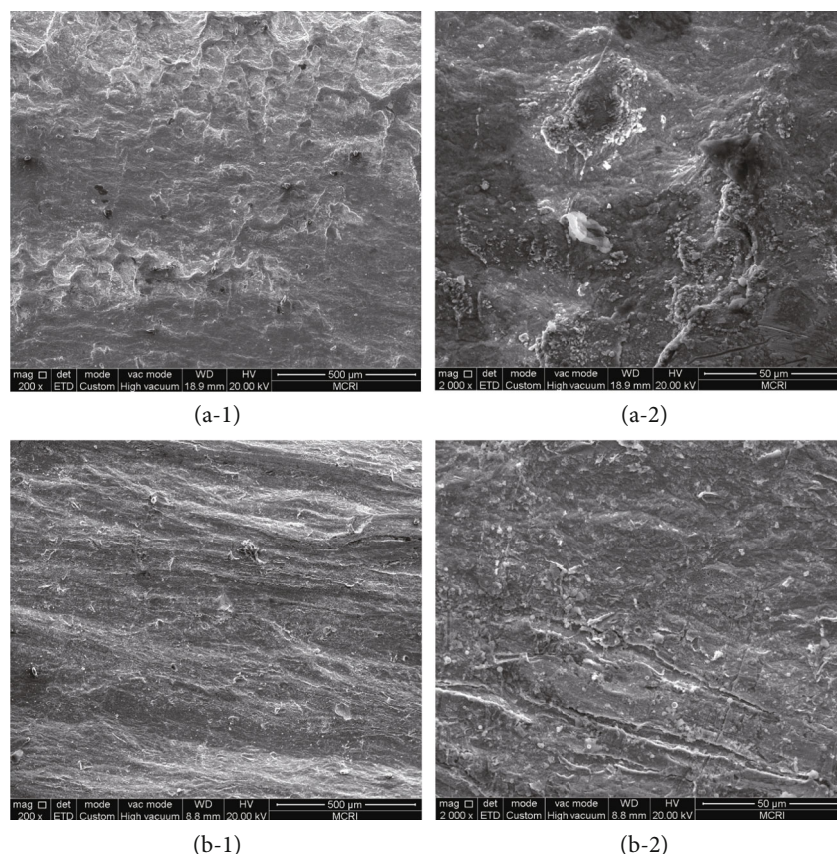
FIGURE 15: SEM photos of fragments in different media: (a-1) in the air (×200), (a-2) in the air (×2000), (b-1) in the water (×200), and (b-2) in the water (×2000).

in Figures 15(b-1) and 15(b-2), it shows obvious axial cracks without significant dimples.

5. Conclusions

In this paper, the sliding detonation law of the charging cylinder in different media was studied by numerical simulation and experimental methods. Firstly, an improved fluid-structure coupling numerical method, coupled finite element material point method, was applied to simulate the expansion process of the cylinder under sliding detonation. Secondly, the numerical accuracy of several different numerical methods was compared, and the accuracy of the coupled finite element material point method was verified by the experimental data. Numerical simulations and experimental tests have demonstrated the effect of different media on the expansion of the cylinder. The cylinder in the air medium has undergone three stages of sharp loading, slow loading, and shell rupture. In the water medium, the cylinder experienced a sharp loading, slow unloading, and final shell rupture. The cylinders have different expansion laws in different medium environments, mainly due to the difference of shock wave impedance, which causes the internal and external pressures acting on the cylinder to change. Finally, the macroscopic and microscopic states of the cylinder failure were compared and discussed, which provides a prelimi-

nary reference for the subsequent investigation of the failure of the material.

Data Availability

The image data used to support the findings of this study are included within the supplementary file. And the image data used to support the findings of this study are available from the corresponding author upon request.

Conflicts of Interest

The authors declare that they have no conflicts of interest.

Acknowledgments

Supplementary Materials

The file "Experiment data.doc" consists of two tables: Table 1 is the data of experimental data of the cylinder test in the air which is consistent with that in Figure 6; Table 2 is the data of experimental data of the cylinder test in the water which is consistent with that in Figure 12. *(Supplementary Materials)*

References

[1] J. Kury, H. Hornig, and E. Lee, "Metal acceleration by chemical explosive," in *Fourth Symposium (International) on Detonation*, pp. 3–13, White Oak, Mary land, USA, 1965.

[2] X. Y. Wang, S. S. Wang, and F. Ma, "Experimental study on the expansion of metal cylinders by detonation," *International Journal of Impact Engineering*, vol. 114, pp. 147–152, 2018.

[3] D. M. Goto, R. Becker, T. Orzechowski, H. Springer, A. Sunwoo, and C. Syn, "Investigation of the fracture and fragmentation of explosively driven rings and cylinders," *International Journal of Impact Engineering*, vol. 35, no. 12, pp. 1547–1556, 2008.

[4] C. M. Lindsay, G. Butler, C. Rumchik, B. Schulze, R. Gustafson, and W. R. Maines, "Increasing the utility of the copper cylinder expansion test," *Propellants Explosives Pyrotechnics*, vol. 35, no. 5, pp. 433–439, 2010.

[5] C. Yang, X. Li, H. Yan, X. Wang, and Y. Wang, "Numerical study of the postcombustion effects on the underwater explosion of an aluminized explosive by a novel nonisentropic model for the detonation products," *Journal of Energetic Materials*, vol. 37, no. 2, pp. 174–187, 2019.

[6] H. Hamashima, Y. Kato, and S. Itoh, "Determination of JWL parameters for non-ideal explosive," in *AIP Conference Proceedings*, vol. 706, pp. 331–334, Portland, OR, 2004.

[7] Q. Zhao, J. Nie, Q. Wang, Z. Zhou, and Q. Jiao, "Numerical and experimental study on cyclotrimethylenetrinitramine/aluminum explosives in underwater explosions," *Advances in Mechanical Engineering*, vol. 8, no. 10, 2016.

[8] X. Zhang, Z. Chen, and Y. Liu, *The Material Point Method: A Continuum-Based Particle Method for Extreme Loading Cases*, Academic Press, 2017.

[9] W. Q. Hu and Z. Chen, "Model-based simulation of the synergistic effects of blast and fragmentation on a concrete wall using the MPM," *International Journal of Impact Engineering*, vol. 32, no. 12, pp. 2066–2096, 2006.

[10] Y. X. Wang, Z. Chen, and M. Sun, "Numerical simulation of slippage detonation by material point method-MPM," *Mechanics in Engineering*, vol. 29, no. 3, pp. 20–25, 2007.

[11] Y. X. Wang, H. G. Beom, M. Sun, and S. Lin, "Numerical simulation of explosive welding using the material point method," *International Journal of Impact Engineering*, vol. 38, no. 1, pp. 51–60, 2011.

[12] S. Ma, X. Zhang, Y. P. Lian, and X. Zhou, "Simulation of high explosive explosion using adaptive material point method," *CMES-Computer Modeling in Engineering & Sciences*, vol. 39, no. 2, pp. 101–123, 2009.

[13] S. Ma and X. Zhang, "Adaptive material point method for shaped charge jet formation," *Chinese Journal of Solid Mechanics*, vol. 30, no. 5, pp. 504–508, 2009.

[14] P. F. Yang, Y. Liu, X. Zhang, X. Zhou, and Y. L. Zhao, "Simulation of fragmentation with material point method based on Gurson model and random failure," *CMES: Computer Modeling in Engineering & Sciences*, vol. 85, no. 3, pp. 207–236, 2012.

[15] Z. Zhang, W. D. Chen, and W. M. Yang, "The material point method for shock-to-detonation transition of heterogeneous solid explosive," *Explosion & Shock Waves*, vol. 31, no. 1, pp. 25–30, 2011.

[16] Z. Zhang, *Study on Material Point Method for Shock Initiation of Solid Explosive*, Harbin Engineering University, Harbin, Heilongjiang, China, 2010.

[17] W. M. Yang, *Research on material point method for underwater explosion and shock problems, [Ph.D. thesis]*, Harbin Engineering University, Harbin, Heilongjiang, China, 2013.

[18] X. X. Cui, X. Zhang, X. K. Sze, and X. Zhou, "An alternating finite difference material point method for numerical simulation of high explosive explosion problems," *CMES: Computer Modeling in Engineering & Sciences*, vol. 92, no. 5, pp. 507–538, 2013.

[19] X. X. Cui, X. Zhang, X. Zhou, Y. Liu, and F. Zhang, "A coupled finite difference material point method and its application in explosion simulation," *CMES: Computer Modeling in Engineering & Sciences*, vol. 98, no. 6, pp. 565–599, 2014.

[20] P. Liu, Y. Liu, X. Zhang, and Y. Guan, "Investigation on high-velocity impact of micron particles using material point method," *International Journal of Impact Engineering*, vol. 75, pp. 241–254, 2015.

[21] Y. Liu, H. K. Wang, and X. Zhang, "A multiscale framework for high-velocity impact process with combined material point method and molecular dynamics," *International Journal of Mechanics and Materials in Design*, vol. 9, no. 2, pp. 127–139, 2013.

[22] F. Zhang, X. Zhang, K. Y. Sze, Y. Lian, and Y. Liu, "Incompressible material point method for free surface flow," *Journal of Computational Physics*, vol. 330, pp. 92–110, 2017.

[23] F. Zhang, X. Zhang, and Y. Liu, "An augmented incompressible material point method for modeling liquid sloshing problems," *International Journal of Mechanics and Materials in Design*, vol. 14, no. 1, pp. 141–155, 2018.

[24] N. F. He, Y. Liu, and X. Zhang, "Seamless coupling of molecular dynamics and material point method via smoothed molecular dynamics," *International Journal for Numerical Methods in Engineering*, vol. 112, no. 4, pp. 380–400, 2017.

[25] Y. P. Lian, X. Zhang, and Y. Liu, "Coupling of finite element method with material point method by local multi-mesh contact method," *Computer Methods in Applied Mechanics and Engineering*, vol. 200, no. 47-48, pp. 3482–3494, 2011.

[26] Z. P. Chen, X. M. Qiu, X. Zhang, and Y. P. Lian, "Improved coupling of finite element method with material point method based on a particle-to-surface contact algorithm," *Computer Methods in Applied Mechanics and Engineering*, vol. 293, no. 15, pp. 1–19, 2015.

[27] Z. T. Ma, X. Zhang, and P. Huang, "An object-oriented MPM framework for simulation of large deformation and contact of numerous grains," *CMES: Computer Modeling in Engineering & Sciences*, vol. 55, no. 1, pp. 61–87, 2010.

Research Article

Investigation on Acoustic Properties of Thruster Chamber with Coaxial Injectors and Plenum Chamber

Dekun Gao,[1] Jianxiu Qin [ID],[2] and Huiqiang Zhang [ID][1]

[1]*School of Aerospace Engineering, Tsinghua University, Beijing 100084, China*
[2]*China Academy of Aerospace Aerodynamics, Beijing 100071, China*

Correspondence should be addressed to Jianxiu Qin; qinjianxiu@hotmail.com
and Huiqiang Zhang; zhanghq@mail.tsinghua.edu.cn

Based on the URANS equation, a numerical simulation is carried out for acoustic properties of the thruster chamber with coaxial injectors and plenum chamber in a liquid rocket engine. Pressure oscillations with multiacoustic modes are successfully excited in the chamber by using the constant volume bomb method. FFT analysis is applied to obtain the acoustic properties of eigenfrequencies, power amplitudes, and damping rates for each excited acoustic mode. Compared with the acoustic properties in the model chamber with and without an injector as well as with and without the plenum chamber, it can be found that the injector with one open end and one half-open end still can work as a quarter-wave resonator. The power amplitudes of the acoustic mode can be suppressed significantly when its eigenfrequency is close to the tuning frequency of the injector, which is achieved by Cutting down the pressure Peak and Raising up the pressure Trough (CPRT). Compared with the acoustic properties in the model chamber with and without the plenum chamber, it can be found that 1L acoustic pressure oscillation is inhibited completely by the plenum chamber and other acoustic pressure oscillations are also suppressed in a different extent. The injector and plenum chamber have a little effect on the eigenfrequencies and damping rate of each acoustic mode. For multimode pressure oscillation, it is better for tuning frequency of the injector closing to the lower eigenfrequency acoustic mode, which will be effective for suppression of these multiacoustic modes simultaneously.

1. Introduction

Gas-liquid coaxial injectors have been widely used in liquid rocket engines for their good properties on the mixing of fuel and oxygen, atomization of liquid propellant, and combustion stability of the thruster chamber. Many research works have been conducted on such injectors and related combustion chambers.

High-frequency combustion instability often occurs in liquid propellant engines and may be related to the geometry of the atomizing elements that are often used. Shear coaxial injector elements are particularly prone to such instability because the resonant acoustic frequencies of the LOX post are often close to the resonant frequencies of the combustion chamber [1]. A phenomenon on combustion instability in a subscale combustor for a LOX/methane rocket engine has been conducted by JAXA [2], in which the effects of five types

of single shear coaxial injector on the combustion instability were observed. The injection-coupled response of a LOX post was predicted by Lin et al. based on the finite element model (FEM) [3], in which the observed instability was a result of the interaction of combustion chamber resonance frequencies with injector resonance frequencies. Injector-driven combustion instabilities in a hydrogen/oxygen rocket combustor were investigated by Groening et al. [4]. It was found that the oscillation of the heat release rate was related to the injector acoustics but was not corresponding with the combustion chamber pressure oscillations. Urbano et al. analyzed the combustion instability by using large eddy simulation in a liquid rocket engine with multiple coaxial injectors [5]; it was shown that the overall acoustic activity was strongly coupled with the injector. It can be found that the coaxial injector and its acoustic properties have an important effect on the combustion in the chamber of the

(a) Model A chamber without injectors and plenum chamber

(b) Model B chamber with 7 injectors but without plenum chamber

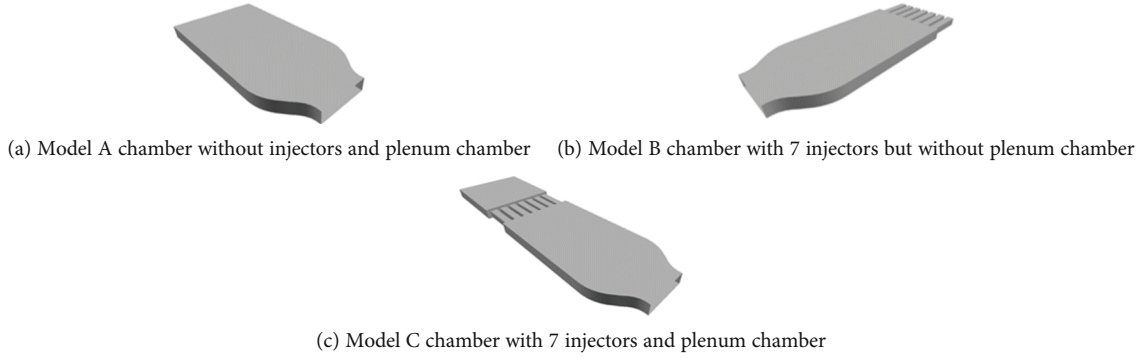(c) Model C chamber with 7 injectors and plenum chamber

Figure 1: Configurations of three model chambers.

liquid rocket engine. So, the acoustic properties and decay rate of coaxial injectors have got much investigation.

Acoustic characteristics and acoustic damping induced by gas-liquid scheme coaxial injectors were studied by Zhou et al. [6, 7]; it has been found that such injector can play a significant role in acoustic damping or absorption. Sohn et al. [8] examined combustion-stability characteristics of a coaxial injector by using a scaling method, in which similarity of acoustic, hydrodynamic, and combustion characteristics between a model test and an actual test was achieved. They [9] also studied acoustic fine-tuning of gas-liquid coaxial injectors by using linear acoustic analysis. Haksoon and Sohn [10] experimentally studied the gas-liquid coaxial injector as an acoustic resonator in the combustion chamber. Soller et al. [11] conducted a hot fire test in a thruster chamber with several coaxial swirl injectors under the condition of chamber pressures in the range of 4.0 MPa to 8.5 MPa and mixture ratios between 2.4 and 3.5, and the effects of the injector's parameters on the combustion instability were observed. Pomeroy et al. [12, 13] studied the response of combustion in a gas-centered swirl coaxial injector to high-amplitude, high-frequency, and transverse-mode pressure oscillation by using a high-speed camera. Kim and Heister [14] developed a homogeneous two-phase flow model to assess hydrodynamic instabilities of coaxial injectors, in which effects of the density ratio, gas-liquid velocity ratio, sheet thickness, channel length, and Reynolds number on such instabilities were discussed. The flame of a single coaxial injector was investigated by Zhukov and Feil [15]. And the spray characteristics of the gas-centered swirl coaxial injector were measured by Jeon et al. [16].

As shown above, many research works have been carried out to investigate the atomization, combustion, and acoustic properties of the gas-liquid coaxial injector. Indeed, such an injector is not like a typical acoustic resonator with one closed end, but it has one open end connected with the combustion chamber and one half-open end connected with the plenum chamber. Therefore, the acoustic properties of such an injector may be different from the typical acoustic resonator, and the plenum chamber may have a contribution to the decay of the pressure oscillation in the combustion chamber. But such contribution has never been evaluated till now. So, the acoustic properties of such an injector are investigated in this paper in a rocket engine combustor with a plenum

chamber by using a numerical constant volume bomb method, in which a nonlinear pressure oscillation with multi-acoustic modes is excited.

2. Numerical Methodology

2.1. Geometric Configurations. A model chamber sliced from a combustion chamber of a 100 kN LOX/kerosene rocket engine is adopted in this paper for its less cost of computational time, in which seven gas-liquid coaxial injectors are included. In order to observe the effects of such injectors and the plenum chamber on the decay of pressure oscillation in the combustion chamber, three kinds of model chambers are presented in this paper. One is Model A, which is comprised of a combustion chamber without injectors and a plenum chamber. For Model B, seven gas-liquid coaxial injectors are equipped at the head of Model A. For Model C, a plenum chamber is connected with those injectors in Model B. These three model chambers are shown in Figure 1. By comparing the decay processes of pressure oscillations in Models A and B, the effects of these injectors on the acoustic properties of the combustion chamber can be obtained, while by comparing the related processes in Model B and Model C, the role of the plenum chamber on the decay of pressure oscillations can be identified.

The geometry sizes of the model chambers are shown in Figure 2. The model chamber is a center slice of a full-scaled chamber, and it keeps the same geometrical parameters in transverse (x direction) and longitudinal (z direction) dimensions as a full-scaled chamber. The lengths from the injector plate to the nozzle entrance and throat are 130 mm and 180 mm, respectively. The transverse sizes of the model chamber and nozzle throat are 88 mm and 45.2 mm, respectively. The thickness (spanwise size) of this slice chamber is 12 mm. The transverse and spanwise (y direction) sizes of these injectors are 10 mm, while their length is set as 22, 32, 44, 62, 78, and 100 mm for different cases. The length and width of the plenum chamber are 100 mm and 88 mm, respectively. Compared with transverse size of the injector with 10 mm, there is a contraction with 5 mm at the inlet of the injector, which is shown in Figures 1 and 2. So, the injector's outlet is an open end, while its inlet is a half-open end; it is corresponding to that in engineering.
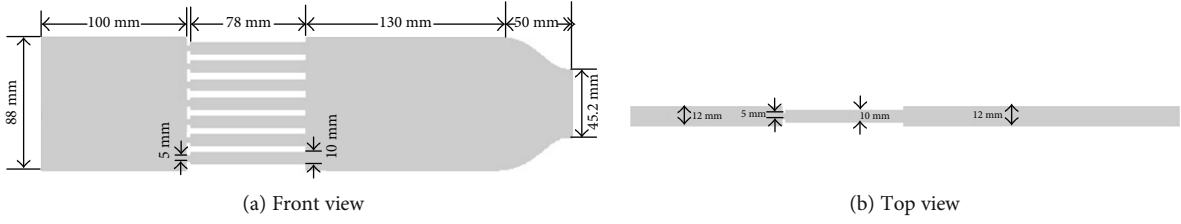
(a) Front view

(b) Top view

FIGURE 2: The geometry size of the thrust chamber, injector, and plenum chamber.

2.2. Governing Equation. Investigation on the acoustic performance of the combustion chamber under cold condition in normal temperature and pressure environment is generally adopted in engineering to evaluate the chamber's eigenfrequencies and decay rates [17]. So, the model chambers are initially filled with quiescent air with a pressure of 0.1 MPa and a temperature of 300 K. Instead of loudspeakers or bombs in engineering used as a stimulated source, a pressure pulse is imposed on a determined region in the model chambers in present works. The stimulated turbulent flow and pressure oscillations in these chambers are simulated by the URANS method and compared with each other, in which the turbulent is described by the k-ε model. The governing equations for turbulent flow in the model chambers can be written as follows:

$$\frac{\partial \rho}{\partial t} + \frac{\partial \rho u_j}{\partial x_j} = 0, \tag{1}$$

$$\frac{\partial (\rho u_i)}{\partial t} + \frac{\partial \left(\rho u_i u_j\right)}{\partial x_j} = -\frac{\partial p}{\partial x_j} - \frac{\partial}{\partial x_j}\left(\frac{2}{3}\rho k\right) + \frac{\partial \tau_{ij}}{\partial x_j}, \tag{2}$$

$$\frac{\partial (\rho e)}{\partial t} + \frac{\partial \left(\rho u_j e\right)}{x_j} = -p\frac{\partial u_j}{\partial x_j} - \frac{\partial}{\partial x_j}\left(-K\frac{\partial T}{\partial x_j} - \rho Dh\right) + \rho\varepsilon, \tag{3}$$

$$\frac{\partial (\rho k)}{\partial t} + \frac{\partial \left(\rho u_j k\right)}{\partial x_j} = -\frac{2}{3}\rho k\frac{\partial u_j}{\partial x_j} + \tau_{ij}\frac{\partial u_i}{\partial u_j} + \frac{\partial}{\partial x_j}\left(\frac{\mu_e}{\sigma_k}\frac{\partial k}{\partial x_j}\right) - \rho\varepsilon, \tag{4}$$

$$\frac{\partial (\rho\varepsilon)}{\partial t} + \frac{\partial \left(\rho u_j\varepsilon\right)}{\partial x_j} = -\left(\frac{2}{3}C_{\varepsilon 1} - C_{\varepsilon 3}\right)\rho\varepsilon\frac{\partial u_j}{\partial x_j} + \frac{\partial}{\partial x_j}\left(\frac{\mu_e}{\sigma_\varepsilon}\frac{\partial\varepsilon}{\partial x_j}\right)$$
$$+ \frac{\varepsilon}{k}\left(C_{\varepsilon 1}\tau_{ij}\frac{\partial u_i}{\partial x_j} - C_{\varepsilon 2}\rho\varepsilon\right), \tag{5}$$

where $\rho, p, u_j, e, T, h, k,$ and ε represent the density, pressure, velocity in the jth direction, total energy, temperature, enthalpy, turbulent kinetic energy, and its dissipation rate, respectively. D and K are diffusion coefficient and heat conduction coefficient, respectively. For effective viscosity μ_e and viscous stress tensor τ_{ij}, we have

$$\mu_e = \mu + \mu_t, \tag{6}$$

TABLE 1: Turbulence model coefficients.

Parameter	μ	$C_{\varepsilon 1}$	$C_{\varepsilon 2}$	$C_{\varepsilon 3}$	σ_k	σ_ε
Value	0.09	1.44	1.92	-1.0	1.0	1.3

$$\tau_{ij} = \mu_e\left(\frac{\partial u_i}{\partial x_j} + \frac{\partial u_j}{\partial x_i}\right) - \frac{2}{3}\mu_e\frac{\partial u_j}{\partial x_j}\delta_{ij}, \tag{7}$$

where

$$\mu_t = \frac{\rho C_\mu k^2}{\varepsilon}. \tag{8}$$

The turbulent model coefficients are shown in detail in Table 1, in which the standard coefficients are adopted in the present works.

2.3. Numerical Algorithm and Boundary Conditions. The semi-implicit method for pressure linked equations is adopted to solve the pressure field. And the forward-Euler difference method is employed for temporal difference. The finite volume method is adopted for spatial difference, in which the diffusion terms and convection terms are discretized by a second-order central difference scheme and second-order upwind scheme, respectively.

The injector face of the combustion chamber, as well as side walls of thruster chambers, injector, and plenum chamber, is set as wall boundary. The adiabatic condition and turbulent law-of-the-wall condition are adopted to wall boundary. In order to avoid setting as a closed end for the upstream boundary of injectors for Model B chamber and for the upstream boundary of the plenum chamber in Model C chamber, a small velocity and a given pressure are set at these upstream boundaries. The chamber exit is set as an outlet boundary, in which the pressure at the exit is set as ambient pressure and the velocity is set equal to that of the logical inside neighbor vertex. It means that the partial derivative in the streamwise direction is set to zero at the outlet. The boundary condition in the nozzle throat for the cold case is different from the real hot case. There is no reflection of the pressure wave at the throat in the real case, but in our case, the pressure wave may be reflected at the exit where the pressure is set as the ambient pressure, which may influence the longitudinal acoustic modes. However, the longitudinal acoustic modes are mainly dominated by the wall of the convergence section of the nozzle which is the same for the

present case and real case. So, the above boundary condition for the outlet is acceptable.

The grid scales are 2 mm, 1 mm, and 2 mm in the x, y, and z directions, respectively. The time step is set as 5×10^{-7} s, but it is 1×10^{-8} s during the period of the constant volume bomb imposed on the steady flow in the chamber.

The initial condition is that the model chambers are filled with air at 1 atm and 300 K. As shown in Figure 3, a region Ω (colored by red) is selected to impose the constant volume bomb; it is a $6 \, mm \times 6 \, mm \times 6 \, mm$ cube with the central coordinate (37 mm, 0, and 7 mm). It is 4 mm far from the injection panel and the upper wall of the chamber. At this region, the initial pressure, temperature, and density are detonated as P_0, T_0, and ρ_0, respectively. A gas with pressure γP_0, temperature αT_0, and density $\beta \rho_0$ is added into this region Ω from the initial time t_0 to time $t_0 + \Delta t$, which has the same components with the original gas in the imposed region Ω. Supposing that the imposed gas and the original gas are mixed quickly through a constant volume process, the pressure $P(x, y, z, t)$, temperature $T(x, y, z, t)$, and density $\rho(x, y, z, t)$ at the imposed region Ω after imposing are thereby obtained as follows:

$$P(x, y, z, t) = (1 + \gamma)P_0, \tag{9}$$

$$\rho(x, y, z, t) = (1 + \beta)\rho_0, \tag{10}$$

$$T(x, y, z, t) = \left(\frac{1 + \gamma}{1 + \beta}\right)T_0, \tag{11}$$

$$\gamma = \alpha\beta, \tag{12}$$

$$(x, y, z) \in \Omega, \tag{13}$$
$$t_0 \leq t \leq t_0 + \Delta t.$$

A pressure pulse is then achieved as a stimulated source by this method. α, γ, and β are model coefficients. The temperature of the imposed region usually keeps the same before and after the imposing process; thus, we have $\alpha = 1$ and $\gamma = \beta$. Only one model coefficient γ is required to be predetermined in this model, by which the peak value of such pressure pulse can be selected. In this paper, γ and Δt are taken as 19 and 10^{-6} s, and then, a pressure pulse as 20 times higher than the initial pressure is achieved in the model chambers with a period of 10^{-6} s to induce a pressure oscillation. For all model chambers, the location and intensity of the pressure pulse are the same. After the constant volume bomb is imposed in the chamber, several positions near the chamber wall and near the injector face are selected to observe the pressure oscillation. For the sliced chamber adopted in this paper, transverse (x direction) and longitudinal (z direction) acoustic modes recorded in these observation points are almost the same. In order to save space, the results for only one observation point are shown in the paper. This observation point locates at the opposite side of the bomb; its pressure is applied to study the acoustic properties of the chamber.
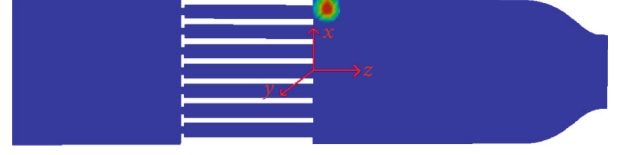
FIGURE 3: The imposed region of the constant volume bomb in the model chamber.

2.4. Quantification of Acoustic Damping Capacity. Half-power bandwidth Δf_n is adopted to evaluate the acoustic damping capacity of each model chamber in this paper. Pressure oscillations with large amplitude are achieved in the model chamber by using the above numerical constant volume bomb. FFT analysis is then carried out, and some power peaks in the frequency region can be obtained. For the n_{th} peak with power amplitude $P_{n,peak}$ at corresponding frequency f_n, half-power bandwidth Δf_n is calculated as the following:

$$\Delta f_n = (f_{n,2} - f_{n,1}), \tag{14}$$

where $f_{n,2}$ and $f_{n,1}$ are the frequencies at which the power amplitude of the pressure oscillation corresponds to $P_{n,peak}/\sqrt{2}$ with $f_{n,2} > f_{n,1}$. Once the half-power bandwidth has been determined, the damping rate α_n of the model chamber for this acoustic mode with the peak frequency f_n can be figured out by the following relation:

$$\alpha_n = \pi \Delta f_n. \tag{15}$$

Furthermore, the nondimensional damping factor η_n for a peak frequency f_n is defined by the half-power bandwidth method as follows:

$$\eta_n = \frac{\alpha_n}{\pi f_n} = \frac{\Delta f_n}{f_n}. \tag{16}$$

As shown in this equation, the bigger the half-power bandwidth is, the higher the damping rate is, which means that pressure oscillations of the corresponding acoustic mode decay faster. Hence, half-power bandwidth, which is dimensionless by eigenfrequency, is applied as a quantification parameter of the damping factor of the chamber in this paper.

3. Results and Discussion

The numerical method applied in this paper for acoustic properties of a combustion chamber has been validated for a small thrust liquid rocket engine chamber by experimental results [18]. So, the validation of the numerical method is no longer done again in this paper. On the other hand, there is a lack of experimental data for the cases in this paper.

3.1. Grid Convergence Study. Acoustic performances for three model chambers, including their acoustic-mode eigenfrequencies and damping capacities, are mainly considered in

(a) Eigenfrequency

(b) Amplitude

(c) Damping factor
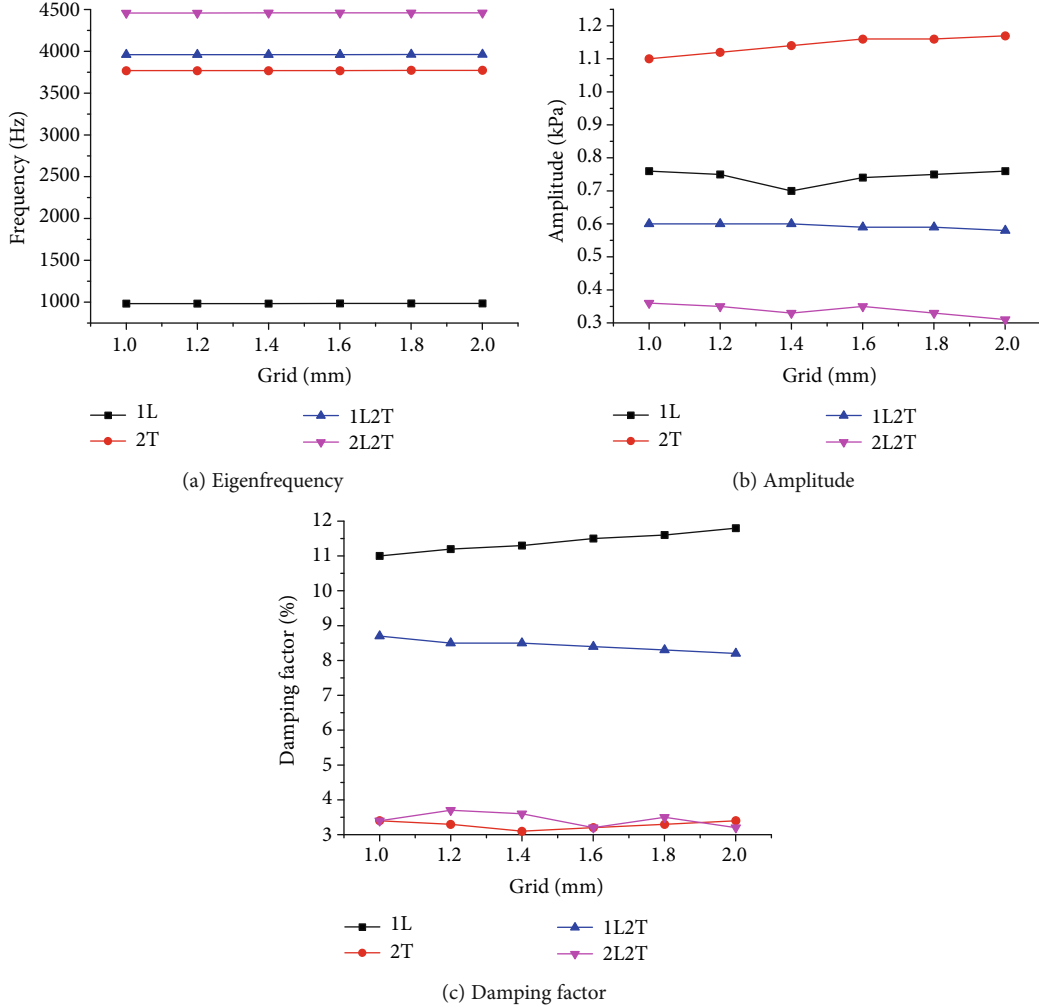
FIGURE 4: Acoustic performances of the chamber with different grid sizes.

this paper. So, grid convergences are examined based on these acoustic performances. Grid sizes varied from 1 mm to 2 mm in the x and z directions are employed in grid convergence study. The eigenfrequencies and damping factors of acoustic modes for the Model A chamber are shown in Figure 4. For grid sizes varied from 1 mm to 2 mm, the identified acoustic modes are the same, and the frequencies, amplitudes, and damping factors of these acoustic modes do not have any significant difference. In order to reduce the computation cost, 2.0 mm grid size is enough to predict the acoustic performances of the chamber used in this paper.

3.2. Acoustic Properties of Model A Chamber. The eigenfrequencies of acoustic modes of the Model A chamber are obtained by theoretical calculation, in which the combustion chamber with the nozzle convergence section is treated theoretically as a closed cylindrical chamber. The eigenfrequencies for a cylindrical chamber closed at both sides can be calculated with the following:

TABLE 2: Theoretical eigenfrequencies of acoustic modes in the model chamber.

Longitudinal (L)	Transverse (T)		
	0	1	2
0	—	1875 Hz	3750 Hz
1	1064 Hz	2155 Hz	3898 Hz
2	2128 Hz	2836 Hz	4311 Hz

$$f_{lmn} = \frac{c}{2\pi}\sqrt{\frac{\lambda_{mn}^2}{R_c^2} + \frac{l^2\pi^2}{L_c^2}}, \quad l, m, n = 0, 1, 2, \cdots, \quad (17)$$

where λ_{mn} is the transverse eigenvalue [17]. c is the speed of sound and taken as 340 m/s in the present cases. For combustion chambers as shown in Figure 1, L_c is the effective acoustic length, which is taken as the sum of chamber length and one-half of the converging nozzle length.

Based on Equation (17), the theoretical eigenfrequencies of acoustic modes of the Model A chamber are shown in Table 2. The 1L acoustic mode has the lowest eigenfrequency.

(a) Pressure oscillations
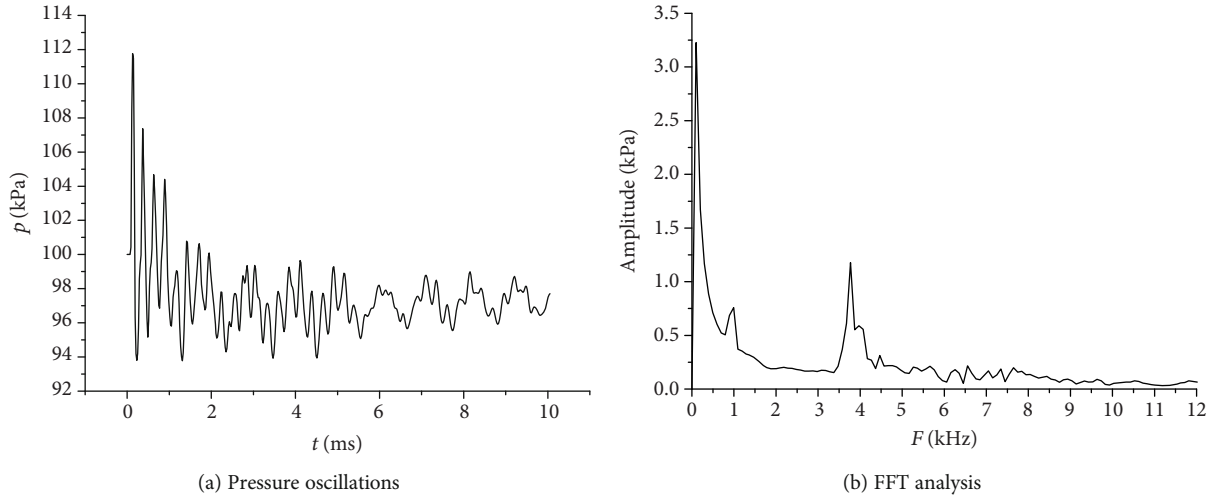
(b) FFT analysis

FIGURE 5: Pressure oscillations and their FFT analysis at the observation point for Model A chamber.

The 1T and 2T acoustic modes are very important for engineering; their eigenfrequencies are 1875 Hz and 3750 Hz. These eigenfrequencies are applied to identify the acoustic modes excited by the numerical constant volume bomb in the model chambers in the following analysis.

After imposing a constant volume bomb in the Model A chamber, the pressure oscillations at the observation point are shown in Figure 5(a), and their corresponding FFT analysis is shown in Figure 5(b). Four peak frequencies are observed as 985 Hz, 3771 Hz, 3961 Hz, and 4461 Hz. Compared with the theoretical eigenfrequencies of acoustic modes for this chamber as shown in Table 2, 985 Hz, 3771 Hz, 3961 Hz, and 4461 Hz of these four peak frequencies are identified as the first longitudinal (1L) acoustic mode, second transverse (2T) acoustic mode, 1L2T acoustic mode, and 2L2T acoustic mode, respectively. Furthermore, the eigenfrequencies, power amplitudes, and damping rate of these four acoustic modes are therefore obtained and shown in Table 3. For peak frequency 3961 Hz, though it is identified as the 1L2T acoustic mode, it is difficult to determine its half-power bandwidth for its peak is not isolated with a small peak value. Only frequency and amplitude are given for this peak, and its damping factor is not available.

Comparing the power amplitudes of these four acoustic modes, the 1L and 2T modes are the acoustic modes that can be excited most easily in this chamber for they have large power amplitudes. The other two acoustic modes of 1L2T and 2L2T may appear due to interaction of 1L and 2T acoustic modes, so they have small power amplitudes. Comparing the damping rate of these four acoustic modes, the 1L mode is the acoustic mode that can be decayed most rapidly for they have a large damping rate, while 2T and 2L2T modes are acoustic modes that can be decayed most difficulty for their small damping rates. The damping rate of 1L2T is between those of 1L acoustic mode and 2T acoustic mode. Though the eigenfrequency of 1L is smaller than those of the other three acoustic modes, it has the largest damping rate due to the open downstream condi-

TABLE 3: Eigenfrequency, power amplitude, and damping rate of acoustic modes in the Model A chamber.

Acoustic modes	Properties	Values
1L acoustic mode	Eigenfrequency (Hz)	985
	Amplitude (kPa)	0.76
	Damping factor	11.8%
2T acoustic mode	Eigenfrequency (Hz)	3771
	Amplitude (kPa)	1.17
	Damping factor	3.4%
1L2T acoustic mode	Eigenfrequency (Hz)	3961
	Amplitude (kPa)	0.58
	Damping factor	—
2L2T acoustic mode	Eigenfrequency (Hz)	4461
	Amplitude (kPa)	0.31
	Damping factor	3.2%

tions. So, the present results are reasonable. In general, based on theoretical acoustic modes and spatiotemporal evolution of instantaneous pressure distribution in the chamber, the peak frequencies obtained by the present simulation can be successfully identified. It can be concluded that multimode acoustic pressure oscillations are stimulated by the present numerical constant volume bomb model, and acoustic properties like eigenfrequencies, power amplitudes, and damping rate are given quantitively in the present work.

3.3. Acoustic Properties of Model B Chamber. The gas injector in the coaxial injector is not like a typical quarter-wave resonator for it has two open ends. However, the end of this injector at the plenum side is usually a half-open end for there is a contraction. So, the coaxial injector is usually considered as a quarter-wave resonator in engineering, which is widely used to suppress combustion instability in a liquid rocket engine. The tuning frequencies f_0 of such an injector are determined

TABLE 4: Eigenfrequency, power amplitude, and damping rate of acoustic modes in the Model B chamber.

		Length of the injector (cm)						
		0	2.2	3.2	4.4	6.2	7.8	10
Resonator's tuning frequency (f_0, Hz)		—	3750	2578	1875	1330	1057	825
1L acoustic mode	Eigenfrequency (Hz)	985	944	853	—	—	—	1126
	Amplitude (kPa)	0.76	1.1	1.1	—	—	—	0.58
	Damping factor	11.8%	11.2%	17.3%	—	—	—	11.5%
2T acoustic mode	Eigenfrequency (Hz)	3771	3777	3791	3798	3798	3842	3567
	Amplitude (kPa)	1.17	0.72	1.1	1.15	0.31	0.57	1.18
	Damping factor	3.4%	3.5%	2.5%	2.1%	—	3.5%	2.1%
1L2T acoustic mode	Eigenfrequency (Hz)	3961	4155	4076	3988	4178	4049	4131
	Amplitude (kPa)	0.58	1.1	1.65	0.65	0.8	0.89	0.61
	Damping factor	8.2%	2.4%	2.4%	3.2%	4.3%	2.0%	3.4%
2L2T acoustic mode	Eigenfrequency (Hz)	4461	4626	—	4368	4558	—	4507
	Amplitude (kPa)	0.31	0.8	—	0.33	0.49	—	0.44
	Damping factor	3.2%	3.7%	—	1.9%	4.6%	—	2.0%
Unidentified frequency peak	Eigenfrequency (Hz)	—	—	—	—	3323	—	—
	Amplitude (kPa)	—	—	—	—	0.59	—	—
	Damping factor	—	—	—	—	5.3%	—	—

by its length L_{inj}. As the following equation,

$$f_0 = \frac{c}{4\left(L_{inj} + \Delta L\right)}, \tag{18}$$

where f_0 denotes tuning frequency of the injector, c is the sound speed of gas in the injector, and ΔL is the length correction factor, which is neglected in this paper.

In order to cover the eigenfrequencies of acoustic modes shown in Table 2, which are possible to appear in the model chamber, a series of injector length are selected in this paper. The tuning frequencies for different length injectors are shown in Table 4, which vary from 825 Hz to 3750 Hz. The eigenfrequencies of 1L and 2T acoustic modes in the model chamber are exactly covered.

After imposing a constant volume bomb in the Model B chamber, FFT analysis of pressure oscillations at the observation point for cases with different injector lengths is shown in Figure 6. For the Model B chamber, it is difficult to obtain its eigenfrequencies of acoustic modes through theoretical calculation, so the peak frequencies that appeared in Figure 6 are also identified by the theoretical eigenfrequencies of acoustic modes for the Model A chamber. There are four peak frequencies among these results for the Model B chamber; they are located between 853 Hz and 1126 Hz, 3323 Hz and 3777 Hz, 4049 Hz and 4155 Hz, and 4368 Hz and 4626 Hz, respectively. And based on the theoretical eigenfrequencies of acoustic modes for the Model A chamber, they are therefore identified as eigenfrequencies of 1L, 2T, 1L2T, and 2L2T acoustic modes, respectively. So, the excited acoustic modes in the Model B chamber by the same numerical constant volume bomb are still those of 1L, 2T, 1L2T, and 2L2T modes. Compared with those in the Model A chamber,

there is no new acoustic mode that appeared in the Model B chamber. So, the acoustic modes excited by the same stimulated source do not change for the case with or without injectors. It mainly depends on the chamber configuration for the observed acoustic-mode pressure oscillation propagation in the chamber.

The eigenfrequencies, power amplitudes, and damping rate of 1L, 2T, 1L2T, and 2L2T acoustic modes observed through Figure 6 in the Model B chamber are listed in Table 4. In order to compare with those in the Model A chamber directly, the results for the Model A chamber are also listed in Table 4 and marked by zero length of the injector. The eigenfrequencies and damping rate of each acoustic mode for the Model B chamber are close to those of the corresponding acoustic mode for the Model A chamber. So, with or without an injector does not have a significant effect on the eigenfrequency of the acoustic mode. And the extra decay due to propagation of the pressure wave in the injector is not the main way to suppress the pressure oscillations.

However, injectors have a great effect on the power amplitudes of the acoustic modes which even decrease to zero for some cases. For the case of injector length with 2.2 cm, the tuning frequency of such injector is close to the eigenfrequency of the 2T acoustic mode. Compared with the amplitude of the 2T acoustic mode in the Model A chamber, it decreases obviously for this case with injectors. However, the pressure oscillation of 1L acoustic mode is enhanced due to the redistribution of oscillation energy among these acoustic modes. For the case of injector length with 3.2 cm, the tuning frequency is not close to either eigenfrequencies of 1L and 2T acoustic modes, so the pressure oscillations of these two acoustic modes are not restrained anymore. But the pressure oscillation of the 2L2T acoustic mode disappears for this case. The tuning frequency of the

(a) 2.2 cm

(b) 3.2 cm

(c) 4.4 cm

(d) 6.2 cm

(e) 7.8 cm

(f) 10.0 cm

FIGURE 6: FFT analysis of pressure oscillations at the observation point for the Model B chamber with different injector lengths.

injector is roughly half of the eigenfrequency of the 2L2T acoustic mode, so the injector may play as a half-wave resonator of the 2L2T mode. For the case of injector length with 4.4 cm, the tuning frequency closes to the eigenfrequency of 1L acoustic modes, and the pressure oscillation of the 1L acoustic mode is inhibited completely, while it does not work for the other acoustic modes. For the case of injector length with 6.2 cm, the tuning frequency is keeping close to the eigenfrequency of 1L acoustic modes much more, and the pressure oscillation of 1L acoustic modes is still repressed

completely, while the pressure oscillation of 2T also suppresses significantly. The peak value of the 2T acoustic mode is very small enough that its half-power bandwidth cannot be read, so the damping factor for this mode is not available in Table 4. However, there is a new peak at the frequency of 3323 Hz for this case. So, the energy of pressure oscillation of the 2T acoustic mode may transfer to this new-frequency mode which cannot be identified. For the case of injector length with 7.8 cm, it still restrains the 1L acoustic mode completely, and it is also effective for suppression of the
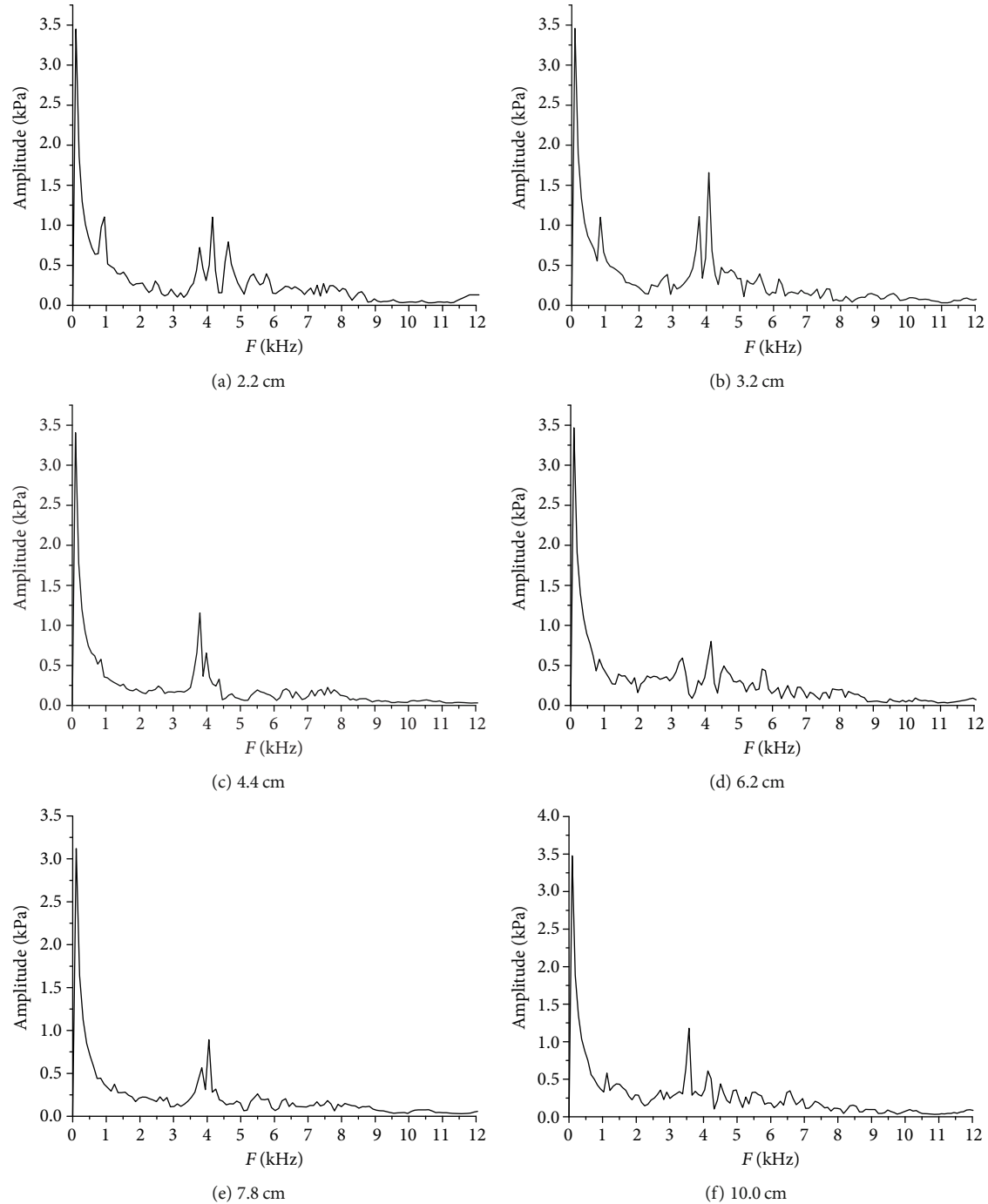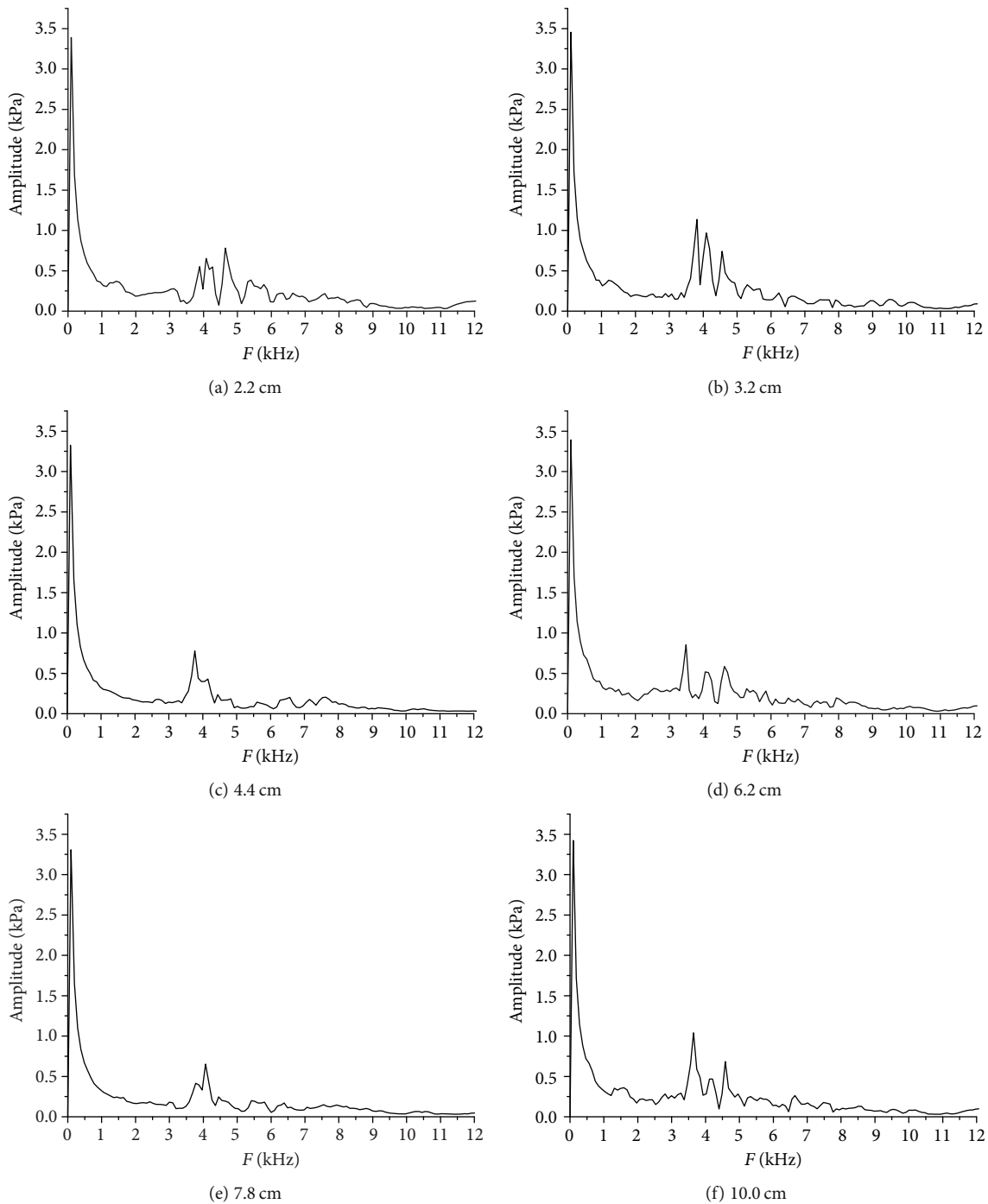
Figure 7: FFT analysis of pressure oscillations at the observation point for the Model C chamber with different injector lengths.

2T acoustic mode. The pressure oscillation of the 2L2T acoustic mode also disappears for this case. For the case of injector length with 10 cm, it has little effect on suppression of 1L and 2T acoustic modes for the tuning frequency of such injector is much less than the eigenfrequency of the acoustic modes.

For the 1L2T and 2L2T acoustic modes, their eigenfrequencies are larger or much larger than the tuning frequency, so suppression of injectors on these two acoustic modes has not been observed clearly. Compared with the case without

an injector, the power amplitudes of these two acoustic modes increase in most cases indeed due to the redistribution of pressure oscillation energy among these acoustic modes through the injectors. In general, for the Model B chamber, injectors with length from 6.2 cm to 7.8 cm are good at suppression of pressure oscillation. The 1L acoustic mode is inhibited completely for injectors are acting as quarter-wave resonators, and 2T is suppressed largely due to redistribution of pressure-oscillation energy through these injectors, while power amplitudes of 1L2T and 2L2T acoustic modes

TABLE 5: Eigenfrequency, power amplitude, and damping rate of acoustic modes in the Model C chamber.

		Length of the injector (cm)						
		0	2.2	3.2	4.4	6.2	7.8	10
Resonator's tuning frequency (Hz)		—	3750	2578	1875	1330	1057	825
1L acoustic mode	Eigenfrequency (Hz)	985	—	—	—	—	—	—
	Amplitude (kPa)	0.76	—	—	—	—	—	—
	Damping factor	11.8%	—	—	—	—	—	—
2T acoustic mode	Eigenfrequency (Hz)	3771	3886	3813	3756	3777	3771	3648
	Amplitude (kPa)	1.17	0.55	1.13	0.78	0.24	0.41	1.0
	Damping factor	3.4%	4.4%	2.2%	4.2%	—	3.8%	3.6%
1L2T acoustic mode	Eigenfrequency (Hz)	3961	4076	4092	4147	4060	4062	4160
	Amplitude (kPa)	0.58	0.65	0.97	0.42	0.52	0.66	0.47
	Damping factor	8.2%	2.5%	4.3%	4.0%	6.6%	2.5%	3.5%
2L2T acoustic mode	Eigenfrequency (Hz)	4461	4644	4558	—	4627	—	4583
	Amplitude (kPa)	0.31	0.78	0.74	—	0.58	—	0.68
	Damping factor	3.2%	2.0%	2.5%	—	3.3%	—	2.1%
Unidentified frequency peaks	Eigenfrequency (Hz)	—	—	—	—	3494	—	—
	Amplitude (kPa)	—	—	—	—	0.85	—	—
	Damping factor	—	—	—	—	2.5%	—	—

increase not dramatically. 1L and 2T acoustic modes, which are mostly concerned by engineering, are significantly controlled by coaxial injectors.

So, such a coaxial injector with one open end and another half-open end still can work as a quarter-wave resonator. For multimode pressure oscillation, it is better for tuning frequency of the injector closing to the lower eigenfrequency acoustic mode, which will be effective for suppression of these multiacoustic modes simultaneously.

3.4. Acoustic Properties of Model C Chamber. After imposing a constant volume bomb in the Model C chamber, FFT analysis of pressure oscillations at the observation point for cases with different injector lengths is shown in Figure 7. The peak frequencies that appeared in Figure 7 are also identified by the theoretical eigenfrequencies of acoustic modes for the Model A chamber. There are three peak frequencies among these results for the Model C chamber; they are located between 3459 Hz and 3886 Hz, 4060 Hz and 4160 Hz, and 4558 Hz and 4644 Hz, respectively. Based on the theoretical eigenfrequencies of acoustic modes for the Model A chamber, these peak frequencies are therefore identified as eigenfrequencies of 2T, 1L2T, and 2L2T acoustic modes, respectively. So, the excited acoustic modes in the Model C chamber by the same numerical constant volume bomb are those of 2T, 1L2T, and 2L2T modes. Compared with those in Model A and B chambers, there is no new acoustic mode that appeared in the Model C chamber. So, the acoustic modes excited by the same stimulated source do not change for the case with or without injectors as well as with or without the plenum chamber. It still mainly depends on the chamber configuration for the observed acoustic-mode pressure oscillation propagation in the chamber.

The eigenfrequencies, power amplitudes, and damping rate of 2T, 1L2T, and 2L2T acoustic modes observed through

Figure 7 in the Model C chamber are listed in Table 5. The eigenfrequencies of each acoustic mode for the Model C chamber are close to those of the corresponding acoustic mode for the Model B chamber. So, with or without the plenum chamber does not have a significant effect on the eigenfrequencies of the corresponding acoustic modes. Compared with cases in the Model B chamber, the pressure oscillation of the 1L acoustic mode is completely suppressed for all cases with different injector lengths when just the plenum chamber is considered in the Model C chamber. So, it can be concluded that the plenum chamber is very effective for suppression of 1L acoustic pressure oscillation. In general, the damping rate of 2T, 1L2T, and 2L2T acoustic modes is a little larger for cases in the Model C chamber than those in the Model B chamber; it means that the plenum chamber provides an extra decay for pressure oscillation of these acoustic modes, but such decay is not significant. However, the amplitudes of 2T and 1L2T acoustic modes for cases with the plenum chamber are smaller significantly than those without the plenum chamber. So, the plenum chamber decreases the amplitudes of the acoustic modes mainly by absorbing the pressure-oscillation energy of the combustion chamber, not just by extra decay of the propagation pressure wave. Amplitudes of 2L2T acoustic modes for cases in the Model C chamber are a little larger than those in the Model B chamber; it may be induced by redistribution of pressure-oscillation energy among these acoustic modes through injectors. The effects of injector length on the 2T acoustic pressure oscillation for the Model C chamber are like those for the Model B chamber. The tuning frequency of the 2.2 cm length injector is very close to eigenfrequency of the 2T acoustic mode; it can be found that the amplitudes of the 2T acoustic mode decrease significantly as compared with the cases without injectors. From then on, the amplitudes of the 2T acoustic mode increase with the length of injectors. It

(a) Pressure wave propagating into the injectors

(b) Pressure wave propagating into the chamber where pressure is in the lowest value

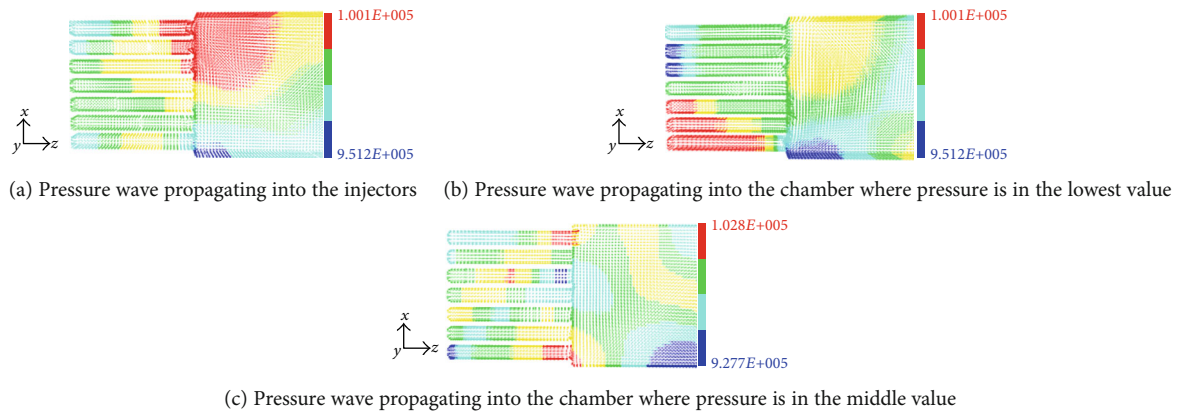(c) Pressure wave propagating into the chamber where pressure is in the middle value

FIGURE 8: Instantaneous velocity vector and pressure fields in injectors and chamber.

means that the injectors still can work as a quarter-wave resonator with the plenum chamber.

3.5. Effects of Injectors and Plenum Chamber on the Pressure Oscillation. Figure 8 shows the instantaneous velocity vector and pressure fields in the chamber and injector. As shown in Figure 8(a), pressure waves propagate into the injectors when pressures at the chamber zone adjacent to injectors are in high value. It means that some energies of pressure oscillation are absorbed by injectors from their peak. As shown in Figure 8(b), the pressure waves propagated into injectors from the chamber reflect at the end of the injectors and go towards the chamber. When it arrives at the exit of the injector, the pressure at the chamber zone adjacent to the injectors is just in its lowest value. So, the absorbed energy from the peak of pressure oscillation is added to a trough of pressure oscillation. In this way, which is called Cutting down the pressure Peak and Raising up the pressure Trough (CPRT), the power amplitudes of the acoustic mode, by which eigenfrequency is close to the tuning frequency of injectors, are suppressed significantly as shown in Model B and C chambers. As shown in Figure 8(c), when the pressure wave in injectors arrives at the exit of injectors, the pressure at the chamber zone adjacent to the injectors is in the middle value. It means that the pressure at this zone is controlled by other acoustic modes which are different from the acoustic mode that this pressure wave is induced. So, the energy of pressure oscillation is transformed from one acoustic mode to other acoustic modes through these injectors. So, as shown in Model B and C chambers, such redistribution of pressure oscillation energy leads to an increase of power amplitudes of some acoustic modes when injectors are considered and multimode pressure oscillations present in the chamber.

Figure 9 shows the instantaneous velocity vector and pressure fields in the plenum chamber and injector. For the lower four injectors, the pressure at the injector zone adjacent to the plenum chamber is in high value; pressure waves thereby propagate from injectors to the plenum chamber. Such propagations of pressure waves are easily and frequently observed in the numerical results. The pressure waves propagated from the plenum chamber to the injector can also be observed as upper three injectors, but its ampli-
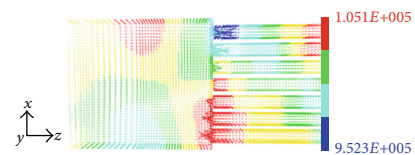

FIGURE 9: Instantaneous velocity vector and pressure fields in injectors and plenum chamber.

tude is obviously smaller than that propagated from injectors to the plenum chamber. That is the reason why the pressure oscillation of most acoustic modes can be suppressed significantly by the plenum chamber.

4. Conclusion

The effects of coaxial injectors and plenum chamber on the acoustic properties of the thruster chamber are numerically investigated, in which a numerical constant volume bomb is employed to excite multimode pressure oscillation. FFT analysis and half-power bandwidth method are applied to get the eigenfrequency, power amplitude, and damping rate of each excited acoustic mode. Under the same stimulated source, the excited acoustic modes are the same as 1L, 2T, 1L1T, and 2L2T for chambers with and without injectors as well as with and without plenum chamber, and their eigenfrequencies and damping rates do not have obvious changes. The injectors still act as a quarter-wave resonator under multimode pressure oscillations for they are very effective to suppress acoustic-mode pressure oscillation when its eigenfrequency is close to the tuning frequency of injectors. And it is better for tuning frequency of the injector closing to the lower eigenfrequency acoustic mode, which will be effective for suppression of these multiacoustic modes simultaneously. Comparing the pressure oscillation with and without the plenum chamber, the plenum chamber can inhibit 1L acoustic-mode pressure oscillation completely and also has obvious effects on other acoustic modes. For multimode pressure oscillation, it can be found that there is a redistribution of pressure-oscillation energy among those excited acoustic modes.

Data Availability

The data used to support the findings of this study are available from the corresponding authors upon request.

Conflicts of Interest

The authors declare that they have no conflicts of interest.

Acknowledgments

References

[1] J. J. Hutt and M. Rocker, "High-frequency injection-coupled combustion instability," *Progress in Astronautics and Aeronautics*, vol. 169, pp. 345–356, 1995.

[2] H. Kawashima, K. KOBAYASHI, T. Tomita, and T. Kaneko, "A combustion instability phenomenon on a LOX/methane subscale combustor," in *6th AIAA/ASME/SAE/ASEE Joint Propulsion Conference & Exhibit*, Nashville, TN, 2010.

[3] R.-S. Lin, F. Bertolotti, C. Eckett, T. Hinerman, and R. Jensen, "A study of the application of a finite element model to the predictions of the injection-coupled response of a LOX post," in *46th AIAA/ASME/SAE/ASEE Joint Propulsion Conference & Exhibit*, Nashville, TN, 2010.

[4] S. Gröning, J. S. Hardi, D. Suslov, and M. Oschwald, "Injector-driven combustion instabilities in a hydrogen/oxygen rocket combustor," *Journal of Propulsion and Power*, vol. 32, no. 3, pp. 560–573, 2016.

[5] A. Urbano, L. Selle, G. Staffelbach et al., "Exploration of combustion instability triggering using large eddy simulation of a multiple injector liquid rocket engine," *Combustion and Flame*, vol. 169, pp. 129–140, 2016.

[6] J. Zhou, X. Hu, Y. Huang, and Z. Wang, "Flowrate and acoustics characteristics of coaxial swirling injector of hydrogen/oxygen rocket engine," in *32nd Joint Propulsion Conference and Exhibit*, Lake Buena Vista, FL, U.S.A., 1996.

[7] J. Zhou, X. Hu, and Y. Huang, "An experimental study on acoustic characteristics of gas-liquid coaxial injector of liquid rocket engine," *Journal of Propulsion Technology-Beijing-*, pp. 37–41, 1996.

[8] C. H. Sohn, Y. J. Kim, Y.-M. Kim, and V. P. Pikalov, "A scaling method for combustion stability rating of coaxial gas-liquid injectors in a subscale chamber," *Journal of mechanical science and technology*, vol. 26, no. 11, pp. 3691–3699, 2012.

[9] C. H. Sohn, I. S. Park, S. K. Kim, and H. J. Kim, "Acoustic tuning of gas-liquid scheme injectors for acoustic damping in a combustion chamber of a liquid rocket engine," *Journal of Sound and Vibration*, vol. 304, no. 3-5, pp. 793–810, 2007.

[10] H. Kim and C. H. Sohn, "Experimental study of the role of gas-liquid scheme injector as an acoustic resonator in a combustion chamber," *Journal of Mechanical Science and Technology*, vol. 20, no. 6, pp. 896–904, 2006.

[11] S. Soller, R. Wagner, H.-P. Kau, P. Martin, and C. Maeding, "Combustion stability characteristics of coax-swirl-injectors for oxygen/kerosene," in *43rd AIAA/ASME/SAE/ASEE Joint Propulsion Conference & Exhibit*, Cincinnati, OH, 2007.

[12] B. Pomeroy, C. Morgan, and W. Anderson, "Response of a gas-centered swirl coaxial injector to transverse instabilities," in *47th AIAA/ASME/SAE/ASEE Joint Propulsion Conference & Exhibit*, San Diego, California, 2011.

[13] B. Pomeroy, J. Sisco, J. Eckstein, and W. Anderson, "Characterization of gas-centered swirl-coaxial injector stability in a subscale multi-element combustor," in *44th AIAA/ASME/SAE/ASEE Joint Propulsion Conference & Exhibit*, Hartford,CT, 2008.

[14] B. D. Kim and S. D. Heister, "Two-phase modeling of hydrodynamic instabilities in coaxial injectors," *Journal of Propulsion and Power*, vol. 20, no. 3, pp. 468–479, 2004.

[15] V. P Zhukov and M. Feil, "Numerical Simulations of the Flame of a Single Coaxial Injector," *International Journal of Aerospace Engineering*, vol. 2017, 11 pages, 2017.

[16] J. Jeon, M. Hong, Y. M. Han, and S. Y. Lee, "Experimental study on spray characteristics of gas-centered swirl coaxial injectors," *Journal of Fluids Engineering*, vol. 133, no. 12, p. 121303, 2011.

[17] W. E. Anderson and V. Yang, Eds., *Liquid rocket engine combustion instability*, American Institute of Aeronautics and Astronautics, 1995.

[18] J. Qin, H. Zhang, and B. Wang, "Numerical evaluation of acoustic characteristics and their damping of a thrust chamber using a constant-volume bomb model," *Chinese Journal of Aeronautics*, vol. 31, no. 3, pp. 470–480, 2018.

Research Article

Experimental Study on Pulse Detonation Engine with Two-Phase Inhomogeneous Mixture

Jishuang Gong [iD] [1] **and Hu Ma** [2]

[1]*School of Aeronautics and Astronautics, Sun Yat-sen University, Guangzhou, 510275, China*
[2]*School of Mechanical Engineering, Nanjing University of Science and Technology, Nanjing 210094, China*

Correspondence should be addressed to Jishuang Gong; gongjsh@mail.sysu.edu.cn

In order to investigate the effects of fuel distribution on the operation of two-phase pulse detonation engine (PDE), a series of cold flow and multicycle PDE experiments was carried out with 9 mixing schemes. Homogeneity degree with fuel distribution considered in terms of space and time was proposed to quantitatively evaluate the mixing of liquid fuel and air by particle image velocimetry (PIV) in cold flow experiments. Operation stability of multicycle PDE was presented by statistical analysis of peak pressure at the outlet of a detonation tube. The relationship between operation stability and homogeneity degree was quantitatively elaborated. These experimental results indicated that not only using mixing reinforcement devices (such as pore plate and reed valve) was fuel distribution improved but also the effect of inlet ways on the homogeneity degree was weakened. The homogeneity degree of fuel distribution $\zeta = 0.72$ was a critical value for stable working of multicycle PDE. When homogeneity degree was lower than 0.72, stable state was not maintained and detonation wave in some cycles was not established due to poor fuel distribution. Therefore, it is necessary to hold homogeneity degree larger than 0.72 to achieve stable operation of PDE. These results contribute to enhancing the operation stability and offering guidelines for the design of PDE's mixing scheme.

1. Introduction

Pulsed detonation engine (PDE) obtains thrust by intermittent detonation wave. Numerous theoretical, experimental, and numerical studies were carried out since PDE poses higher thermodynamic efficiency [1]. Gaseous fuels will be more easily applied to PDE because of the easier mixing with oxidants [2–5], but their energy density is lower than that of liquid fuel; then, the application to PDEs is not that promising. Liquid fuel has now been the focus in this field [6, 7]. Studies on spray detonation presented that PDE efficiency (check again!) is highly related to the droplet size and vaporization of liquid fuel [8, 9]; thus, atomization and vaporization of liquid fuel should be considered for liquid-fueled PDE.

Cheatham et al. conducted single-cycle performance estimations of an idealized liquid-fueled PDE by numerically simulating the detonation of JP-10 fuel droplets in oxygen

and in air [10]. Their results suggested that for small enough droplets or with sufficient prevaporization of the fuel, liquid-fueled PDE will provide comparably single-cycle propulsive performance to gaseous-fueled PDE. However, the performance would decrease when droplet sizes were too large that a self-propagating detonation wave cannot be obtained at the end of the tube. By comparing simulation results to experimentally observed trends, the conclusions were drawn that smaller droplet sizes and higher levels of heating and prevaporization are likely to increase the ease of detonation initiation of liquid-fuelled mixtures [11].

Simulations of a single ideal-tube PDE fueled with multiphase $JP10-O_2$ and JP10-air mixtures were reported by Tangirala et al. [12]. For the diameter ranges of the droplets ($3 \mu m$–$10 \mu m$ for fuel-air and $10 \mu m$-$20 \mu m$ for fuel-O_2 mixtures) and the equivalence ratio considered in their investigations, the predicted velocity defect was 5% of the quasisteady detonation velocity through gas-phase mixtures of
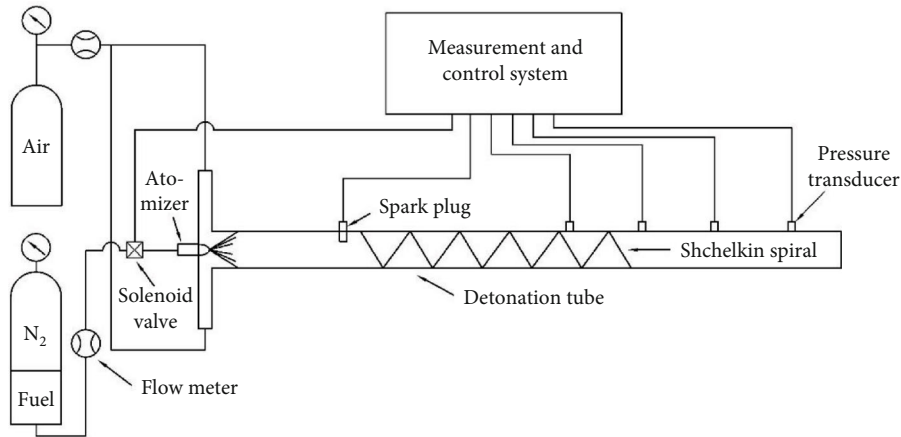
FIGURE 1: Schematic of PDE experimental setup.

JP10-O_2/air, and specific impulse I_{spf} of the PDE initially fueled with gaseous fuel was higher (1-5%) than the I_{spf} of a PDE initially fueled with a multiphase JP10-O_2/air mixture.

It has been demonstrated in these studies that improving initial atomization and vaporization levels of liquid fuel could provide a benefit to the performance of PDE. The atomization with a high-speed coaxial airflow was discussed by Lasheras et al. [13]. They stated that the high-speed airflow driven by stagnation pressures is required to atomize the injected fuel. Sauter mean diameter (SMD) values below $10\,\mu m$ can be achieved when gas-injection velocities were greater than $220\,m/s$. Wang et al. [14] investigated the influences of atomization on PDE by employing laser light scattering for the measurements of mean droplet size. It was observed that equivalence ratio limits turned wide and detonation wave velocity increased as the gasoline droplet size decreased.

Tucker et al. reduced the evaporation time of liquid fuel in a pulsed detonation engine through a fuel flash vaporization system [15, 16]. The results showed that the flash vaporization system quickly provides a detonable mixture for all of the fuels tested without coking the fuel lines, and ignition time has nearly no dependence on fuel injection temperatures. In their works, the successful detonation of flash vaporized JP-8 in air was achieved over a range of fuel temperatures and fuel-to-air ratios.

Miser et al. [17] built a concentric tube heat exchanger using the waste heat generated by a PDE to produce a flash vaporization of a JP-8/air mixture. The duration of the steady-state tests exceeded the operating time of any previous JP-8-fueled PDEs, which is higher than twenty minutes and limited only by fuel storage capacity.

Helfrich et al. [18] studied the effect of fuel temperature on PDE's performance with different liquid fuels by the concentric tube heat exchanger. In their works, for all fuels except JP-10, increasing the fuel injection temperature leads to the decrease of both DDT (deflagration-to-detonation transition) time (by 15%) and detonation distance (by up to 30%) but causes the increase of detonation percentage by up to 180% and barely affects the ignition time.

Fan et al. [19] discussed the beneficial effects of the fuel pretreatments on PDRE performance with five concentric-counter-flow heat exchangers. The outcomes showed that with the aid of fuel preheating, the time and distance of DDT for liquid kerosene were remarkably reduced and the operation time was greatly prolonged. With the increase of fuel temperature, the specific impulse rises from 97.3 s at 25°C to 115.4 s at 200°C.

Even fuel was vaporized from liquid to gas, the fuel distribution in detonation tube still largely influences PDE's performance, and this aspect is now attracting considerable attention from researchers [20, 21]. Tunable diode laser and absorption spectroscopy techniques had been applied to provide time-resolved fuel mass fraction measurements in PDE by Brophy et al. [22, 23]. It was found that the fuel mass fraction distribution within a PDE inherently affects the overall system performance in terms of both the initiation characteristics and the resulting fuel-based-specific impulse performance values. A stratified axial fuel distribution, where a near-stoichiometric mixture occurs near the initiation end of a combustor and a leaner mixture appears near the combustor exit, has significant operation benefits, such as promoting rapid ignition/DDT and increasing fuel-based specific impulse compared to uniform fuel distribution mixtures with the same aggregate fuel mass fraction.

Perkins and Sung [24] analyzed detonation cycles of nonuniform H_2-air mixtures using two-dimensional numerical simulation. The results presented that for an H_2-air system, good fuel-air mixing is not a prerequisite for optimal detonation tube performance. In order to investigate spray detonation, droplet diameter distribution and two-phase mixture homogeneity were considered by Brett [25]. In his research, Mie scattering was used to image two-phase mixture and the mixture homogeneity was ascertained by statistical analysis of these images. It can be concluded that small changes in homogeneity might have little impact on the detonation wave velocity.

As mentioned above, there are many existing studies on the influence of mixture heterogeneity on PDE performance, but those results are mostly concerned with gas phase conditions. Two-phase PDE's performance was influenced not
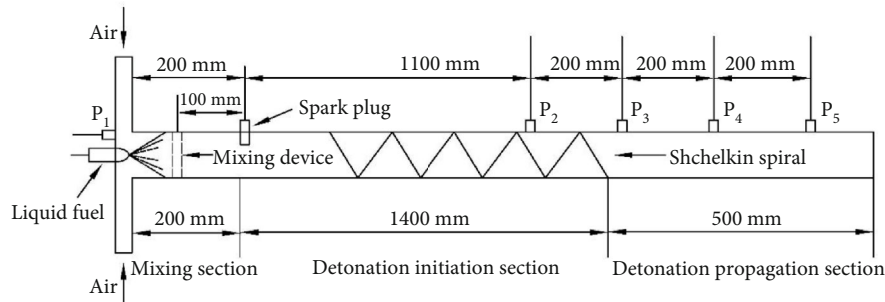
FIGURE 2: Detonation tube.

only by atomization and evaporation of liquid fuel but also by mixture homogeneity. This is a matter of great concern to practical PDE; however, there was little detailed research on this aspect. Therefore, a series of multicyclic two-phase PDE experiments was carried out with 9 mixing strategies to quantitatively investigate the effect of two-phase mixture homogeneity on two-phase PDE operation.

2. Experimental Setup

2.1. PDE Experimental Setup. PDE's experimental systems are set up to study multicyclic operation of two-phase air-breathing PDE. The experimental test rig is composed of a propellant supply system, a detonation tube, a measurement and control system, and an ignition system, as illustrated in Figure 1.

The propellant supply system consists of an oxidizer supply equipment and a fuel supply equipment. The fuel supply equipment provides liquid gasoline fuel (No. 97 in China) which contained 97% C_8H_{18} to the detonation tube by a pressure-swirl atomizer. The gasoline is stored in a cylinder, within which the upper part was full of nitrogen. The mass flow rate of gasoline is measured by a flow meter and is controlled by the pressure of nitrogen. Sauter mean diameter is measured by shadowgraph (71 μm in these experiments).

Air, as an oxidizer, is supplied to a detonation tube by an oxidizer supply equipment. A flow meter and a regulating valve are used to measure and control the mass flow rate of air. The solenoid valve in the fuel supply system is installed to ensure periodic detonations. The average equivalence ratio of 1.5 is fixed at all experiments.

The detonation tube is 50 mm in inner diameter and 2100 mm in length, which includes a mixing section of 200 mm, a detonation initiation section of 1400 mm, and a detonation wave propagation section of 500 mm, as shown in Figure 2. Mixing devices such as a pore plate or a reed valve are set in the mixing section to get a different fuel distribution. More details about the mixing devices are shown in Figures 3 and 4. Detonable mixture is ignited in detonation initiation section by an ignition system. The ignition system adopts spark plug discharge with a frequency of 14 Hz and delivers energy of 1 J. In order to decrease DDT run-up distance and time, a Shchelkin spiral with a blockage ratio of 0.422 is placed in the detonation initiation section. The length and outside diameter of Shchelkin spiral are
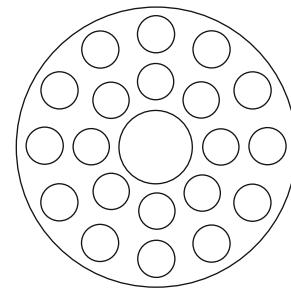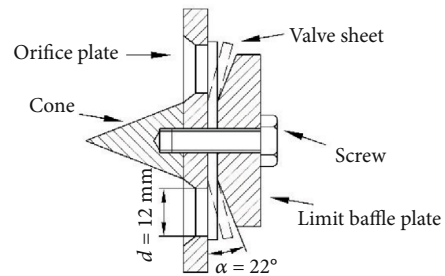

FIGURE 3: Pore plate.

FIGURE 4: Reed valve.

1300 mm and 50 mm, respectively, which has a wire diameter of 6 mm and 35 mm distance between coils. The blockage ratio of 0.422 is close to the optimum value of 0.43 given by Peraldi et al. [26].

To record the pressure history along the detonation tube, dynamic piezoelectric pressure transducers are flush-mounted in the detonation tube, as shown in Figure 2. Signals from these transducers are transmitted to a 6-channel simultaneous sampling module through a signal conditioner. The sampling frequency is 500 kHz in all experiments.

2.2. PIV Experimental Setup. For the two-phase mixture, it is very difficult to achieve a uniform mixture and regions with more gas or more liquid are likely to appear. Therefore, the homogeneity of the mixture must be considered in two-phase PDE. Particle image velocimetry (PIV) is employed to image the fuel distribution with time in the detonation tube, as shown in Figure 5, where an image analysis software, a high-speed CMOS camera, and a double-cavity Nd:YAG laser are implemented. A pulse laser sheet, which shoots from
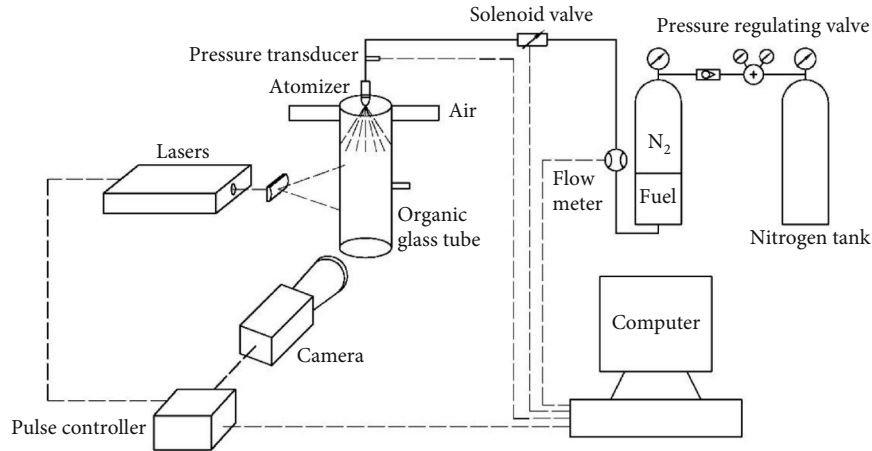
FIGURE 5: PIV experimental setup.

the double-cavity Nd:YAG laser with pulse energy of 30 mJ at 1 kHz, is arranged to illuminate the center plane near the spark plug. The high-speed CMOS camera is used to record particle distribution of the illuminated region with 1280∗ 800 pixels and 1 kHz. An organic glass tube with 50 mm inner diameter and 2 mm thickness is incorporated as the observation window.

2.3. Mixing Schemes. To get a different fuel distribution, 9 mixing schemes, as shown in Table 1, are carried out in the mixing section for these experiments. Tangential, axial, and radial air inlet ways, as shown in Figures 6(a)–6(c), respectively, are adopted to provide air to the detonation tube by four inlet branches. Mixing reinforcement devices, such as a pore plate and a reed valve, are installed in the mixing section to achieve different fuel distribution and mixture homogeneities. The structure of the pore plate which has 0.54 blockage ratio is plotted in Figure 3. The diameter is 14 mm for big pore and 7 mm for small pores.

The reed valve is composed of an orifice plate, a cone, a valve sheet, a limit baffle plate, and a screw, as illustrated in Figure 4. The left part of the reed valve is connected to the air inlet system and the right end goes to the detonation initiation section. The orifice plate has eight orifices which are evenly distributed along the circumference of the orifice plate. The diameter of orifices is $d = 12$ mm. The valve switches on (as shown in dashed line of Figure 4) in the filling process of combustible mixture driven by the pressure difference between left and right of the valve, the maximum opening angle of the valve sheet is $\alpha = 22°$, and the blockage ratio of the reed valve is 0.54.

3. Two-Phase Mixture Homogeneity

For PDE, whether the combustible mixture can be ignited or not depends largely on two-phase mixture homogeneity near the spark plug. Therefore, fuel distribution near spark plug with different mixing schemes is captured by PIV. Figure 7(a) shows the fuel distribution near spark plug for the tangential air inlet way without a mixing reinforcement

TABLE 1: Nine different mixing schemes.

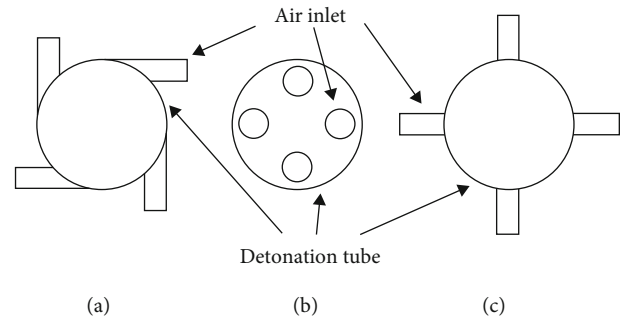| Air inlet ways	No-mixing reinforcement device	Mixing reinforcement device	
		Pore plate	Reed valve
Tangential	Case 1	Case 4	Case 7
Radial	Case 2	Case 5	Case 8
Axial	Case 3	Case 6	Case 9

FIGURE 6: Tangential (a), axial (b), and radial (c) air inlet ways.

device. Centrifugal forces are generated by the tangential airflow in the tube. The centrifugal forces lead to a spiral movement of fuel droplets along the tube wall, and there are a little fuel droplets near the axis of the tube. It can be seen from Figure 7(b) that the pore plate reduces the centrifugal forces of air and improves the fuel distribution near the spark plug.

Figure 7 only gives instantaneous spatial distribution of liquid fuel. A deserving notice is that the two-phase mixture homogeneity not just relates to spatial distribution but to time as well. To further quantitative study mixture homogeneity for 9 mixing schemes, the space and time are considered by the statistical analysis of these images from PIV. Digital information with gray value of each pixel points is contained in these images. The homogeneity degree of fuel distribution, ζ, can be calculated by following equation:

$$\zeta = 1 - \frac{S_G^2}{\bar{G}^2} = 1 - \frac{1/((n-1) \times (m-1)) \sum_{(i,t)=(1,1)}^{(n,m)} \left(G_{i,t} - \bar{G} \right)^2}{\bar{G}^2},$$

$$(1)$$

where $G_{i,t}$ is the gray value of pixel point i at time t, n is the sum of pixel points, and m is the total number of pictures. We set $m = 100$, $\bar{G}$ is the average gray value of pixel points for all pictures. The closer the homogeneity degree ζ is to 1, the more homogeneous the liquid fuel distribution is.

Figure 8 shows homogeneity degree for nine mixing schemes. It can be seen from Figure 8 that the homogeneity degree changes from 0.32 to 0.87 for different mixing schemes. The air inlet ways have larger effects on the homogeneity degree without mixing reinforcement devices than those arrangements with the pore plate or reed valve. The homogeneity degree of axial inlet way is larger than that of tangential inlet way for all cases. In comparison with tangential inlet way, the homogeneity degree of axial inlet way has been increased by 103% for the test with no mixing reinforcement devices, but by 20.8% for the one with the pore plate and 4.88% for the reed valve incorporated case. The mixing reinforcement devices, such as the pore plate and reed valve, in addition to improve the homogeneity degree near spark plug, reduce the effect of inlet ways on the homogeneity degree as well and the reed valve outperforms the pore plate.

4. Effect of Homogeneity Degree on PDE

4.1. Multicycle PDE Experiments. To investigate the effect of mixing homogeneity on PDE operating characteristics, a series of multicycle two-phase detonation experiments is carried out with nine different mixing schemes. In these experiments, the filling velocity of air is about 30 m/s, the equivalence ratio of fuel/air mixture is 1.5, the ignition frequency of spark plug was 14 Hz, and the ambient pressure and temperature are 1 atm and 280 K, respectively.

Figure 9(a) shows the pressure history of Case 1 where tangential inlet way is utilized and no mixing reinforcement device is employed. It can be seen from Figure 9(a) that the two-phase mixture is ignited only once during the period of 1 s with an ignition frequency of 14 Hz and the deflagration flame dose not translate to detonation wave. This is because centrifugal forces generating from rotating airflow cause a bad homogeneity degree, which becomes seriously fuel-rich near the spark plug and fuel-lean near the axis in the detonation tube. Its homogeneity degree is 0.32 for case 1, making the ignition hard.

Figures 9(b) and 9(c) show the pressure history along the detonation tube for Case 2 and Case 3, respectively. Compared with Case 1, achieving successful ignition is significantly improved due to the improvement of the mixture homogeneity degree, but detonation wave is still not obtained in several cycles. This indicates that the homogeneity degrees for Case 2 and Case 3 still could not meet the requirement of PDE, which means it is difficult to establish detonation wave even if ignition succeeds in some cycles.

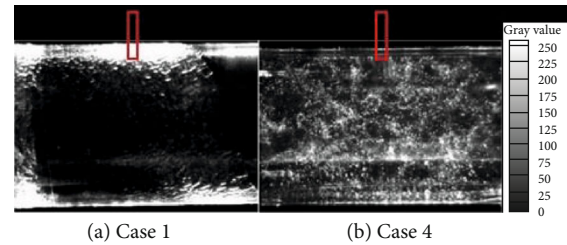(a) Case 1   (b) Case 4

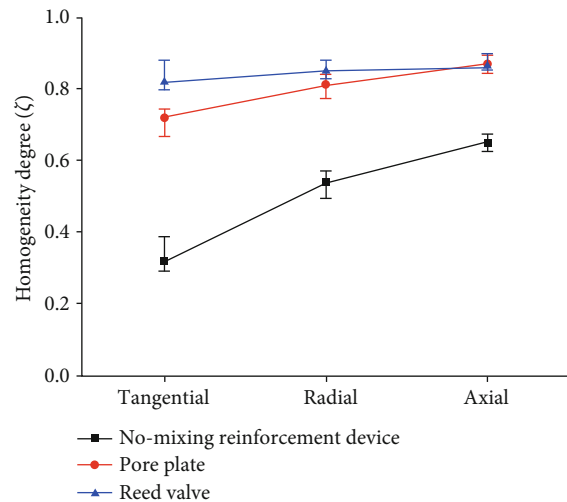FIGURE 7: Fuel distribution recorded by PIV.

FIGURE 8: Homogeneity degree with 9 mixing schemes.

To improve fuel distribution and operation stability of PDE, the pore plate is installed 100 mm upstream to the spark plug in Case 4, Case 5, and Case 6.

Figure 10(a) shows the pressure history for Case 4. It can be seen that the detonation wave is established under all states except one throughout the period of 1 s with an ignition frequency of 14 Hz. It is found that the pore plate is able to reduce the negative impact of centrifugal forces from rotating airflow on fuel distribution. Compared with that for Case 1, the operation stability of PDE for Case 4 significantly gets enhanced as the pore plate improves the homogeneity degree of fuel-air mixture from 0.32 for Case 1 to 0.72 for Case 4.

Figures 10(b) and 10(c) show the pressure histories for Case 5 and Case 6, respectively. It can be seen from these figures that successful detonation wave initiation is always reached for Case 5 and Case 6. These indicate that the homogeneity degrees for Case 5 and Case 6 can satisfy the requirement of PDE. Compared with Figure 9, the pore plate can improve operation stability of PDE for all different air inlet ways.

Figure 11 shows the pressure history along the detonation tube with the reed valve implemented. As shown in Figure 11, PDE with the reed valve can operate more steadily for different air inlet ways. It indicates that besides improving the homogeneity to meet the requirements of PDE, the reed valve also reduces the effect of air inlet ways on PDE.
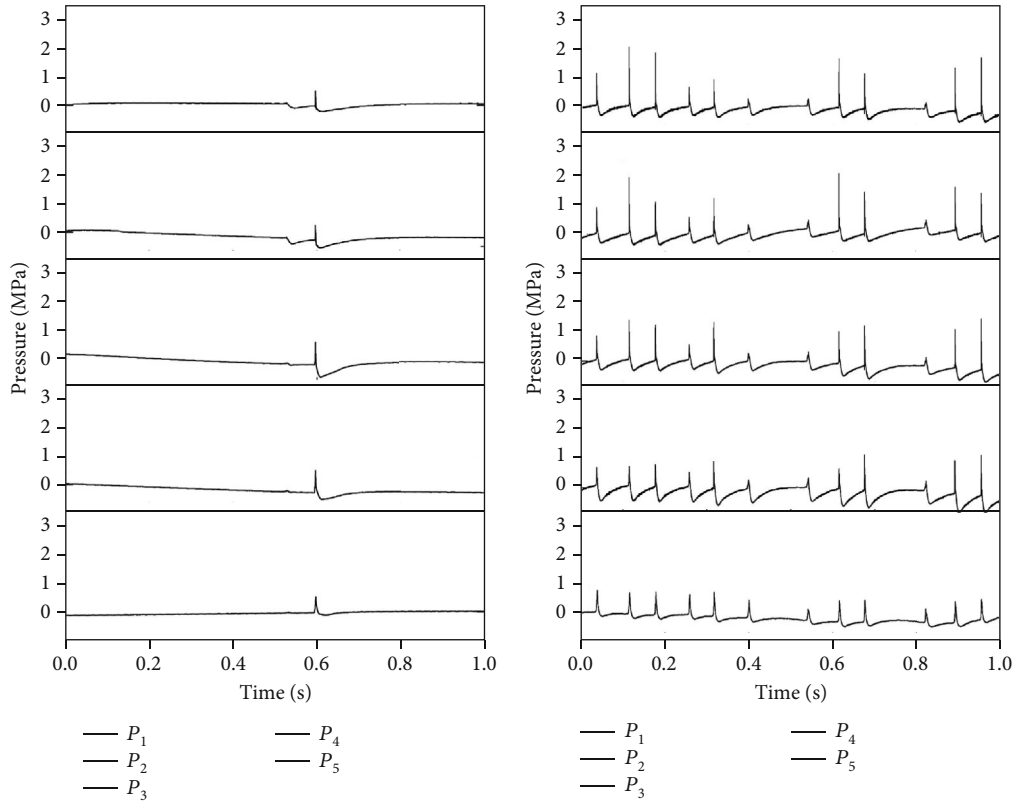
(a) Case 1

(b) Case 2
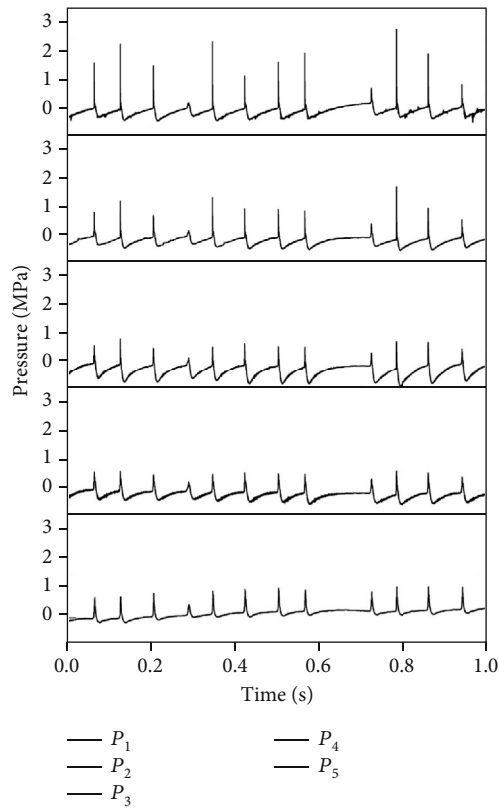
(c) Case 3

FIGURE 9: Pressure history for no-mixing reinforcement device.

(a) Case 4

(b) Case 5

(c) Case 6

Figure 10: Pressure history for the pore plate.

(a) Case 7

(b) Case 8

(c) Case 9

FIGURE 11: Pressure history for the reed valve.

FIGURE 12: Operation stability of multicycle PDE for different homogeneity degrees.

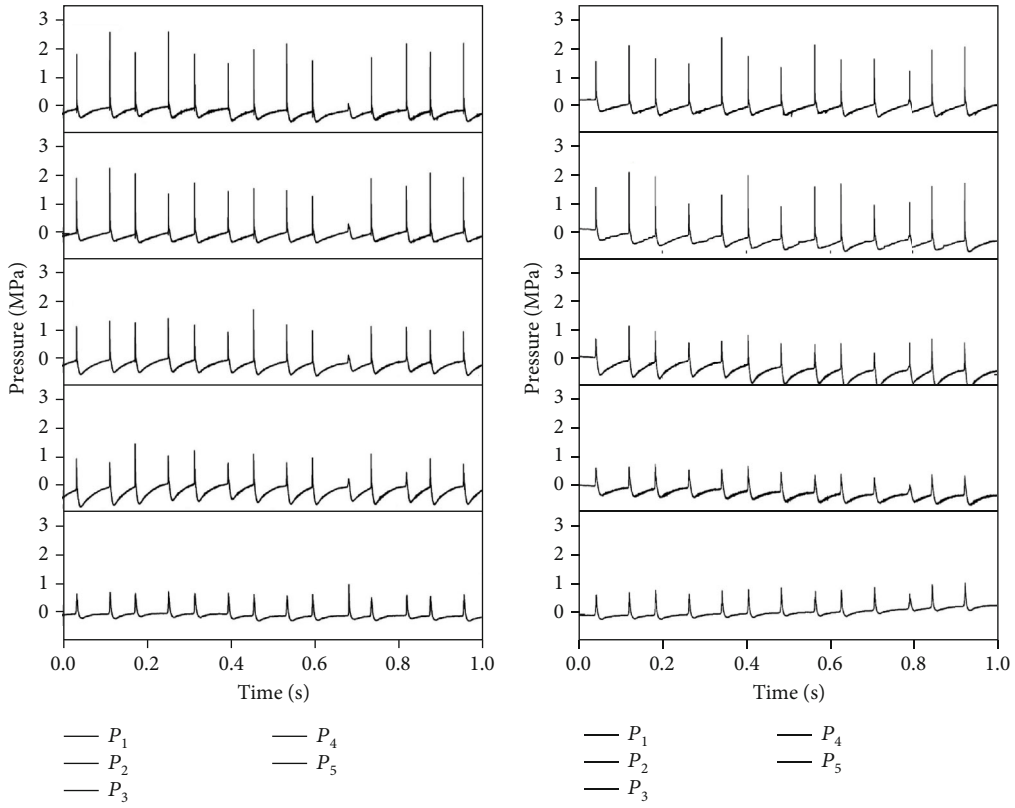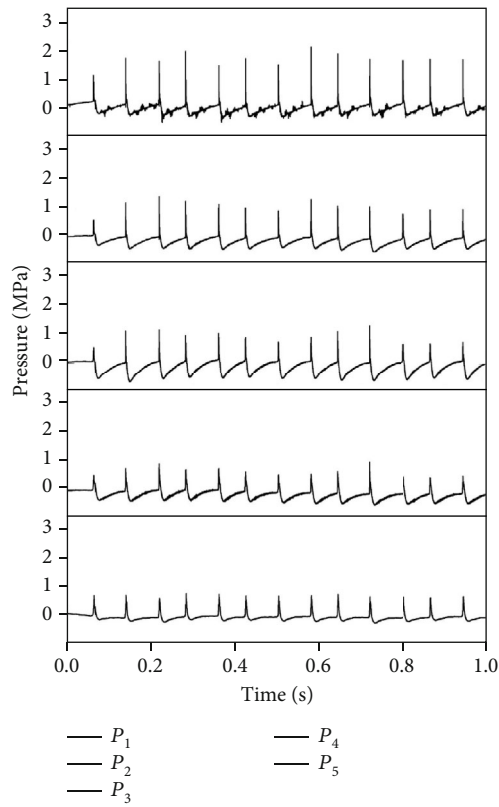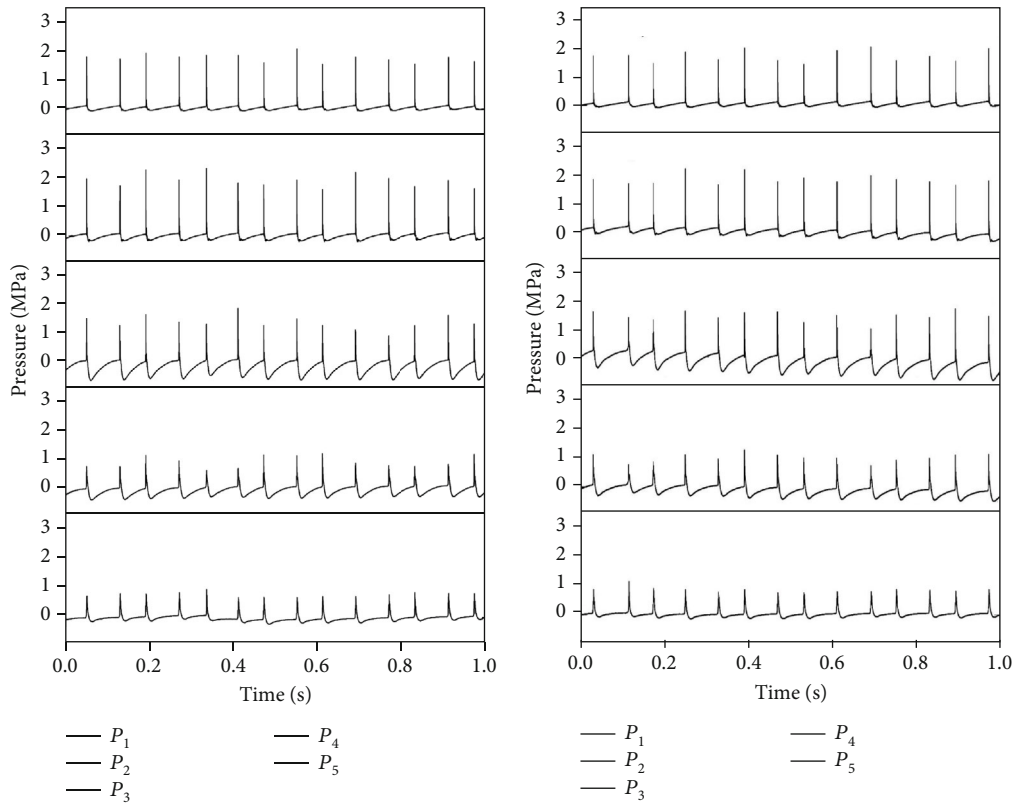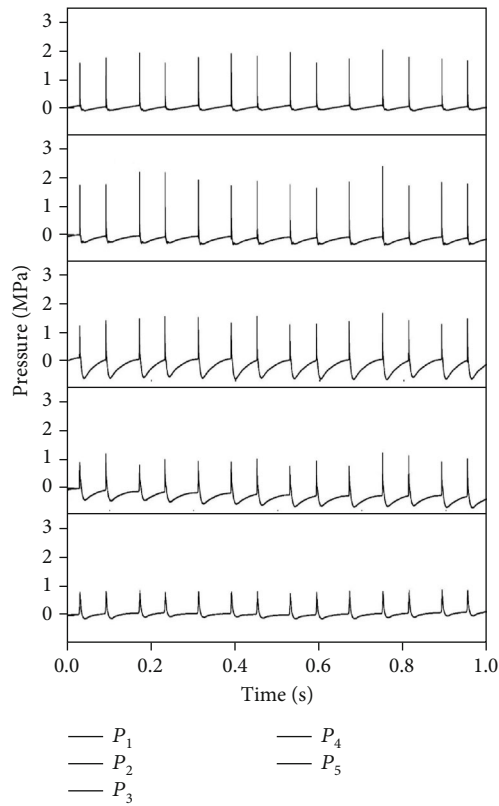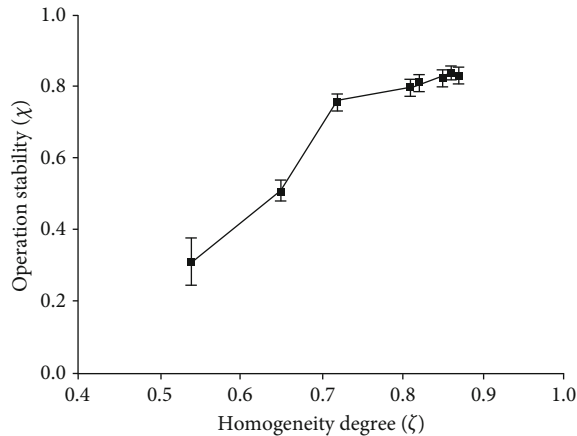Furthermore, compared with Figure 10, the detonation waves are achieved ahead of the P4 position in Figure 11. The DDT distance of PDE with the reed valve is shorter than that with the pore plate.

4.2. Operation Stability of PDE. To further study the relation between operation stability of PDE and homogeneity degree of two-phase mixture, the operation stability is ascertained by the statistical analysis of peak pressure at P_5. It can be calculated using the following equation:

$$\chi = 1 - \frac{S_p^2}{\bar{p}^2} = 1 - \frac{1/(N-1)\sum_{i=1}^{N}(p_i - \bar{p})^2}{\bar{p}^2}, \qquad (2)$$

where p_i is the peak pressure of cycle i at P_5, N is the number of cycle used in the average, and $\bar{p}$ is the average of peak pressure. The closer the operation stability χ is to 1, the more stable the multicyclic working of PDE is.

The operation stability of multicycle PDE χ for different homogeneity degree ζ is plotted in Figure 12. It can be seen from the figure that the operation stability of multicycle PDE increases when the homogeneity degree improves. The highest gained operation stability χ is 0.841 when ζ is 0.86 at case 9. When homogeneity degree ζ is larger than 0.72, ζ has a small impact on the operation stability of multicycle PDE, and the operation stability slightly increases with the increase of ζ, whereas as ζ is lower than 0.72, ζ has a significant influence and the operation stability rapidly declines with the decrease of ζ. This is attributed to the ignition fails or detonation wave is not achieved in some cycles for the lower homogeneity degree. Therefore, the homogeneity degree $\zeta = 0.72$ is a critical value of stable working of multicycle two-phase PDE. For the higher homogeneity degree, the operation stability χ is influenced by both the homogeneity degree and turbulence Therefore, the operation stability χ presents a small decline as ζ increases from 0.86 to 0.87.

5. Summary and Conclusions

This work first quantitatively investigated the effect of the homogeneity degree of mixture on the operation stability of multicycle PDE by PIV with 9 mixing schemes. Based on the experimental results, it can be concluded as follows:

(1) Homogeneity degree, which takes fuel distribution with space and time into account, was proposed to quantitatively assess the mixture of liquid fuel and air. The homogeneity degree of axial inlet way was better than that of tangential and radial inlet way. Centrifugal forces produced from rotating airflow led to a spiral movement of fuel droplets along the tube wall, and just a few fuel droplets are present near the axis for tangential air inlet way without mixing reinforcement devices. The mixing reinforcement devices, such as pore plate and reed valve, not only improved fuel distribution near spark plug but also reduced the effect of inlet ways on the homogeneity degree. As for the arrangement, the reed valve performs better than the pore plate

(2) Operation stability of multicycle PDE was presented by the statistical analysis of peak pressure at the outlet of the detonation tube. The relationship between operation stability of PDE and homogeneity degree of mixture was quantitatively analyzed. The homogeneity degree of $\zeta = 0.72$ was a critical value for stable working of multicycle two-phase PDE. When homogeneity degree ζ was lower than 0.72, it had significant influences on the operation stability of multicycle PDE and detonation waves in some cycles were not achieved due to poor homogeneity degree. The homogeneity degree ζ could have a small impact on the operation stability of multicycle PDE if ζ was larger than 0.72. Therefore, it was necessary to achieve a homogeneity degree ζ of above 0.72 to ensure PDE works steadily. These generated results were expected to improve the operation stability and to offer guidelines for the design of PDE's mixing scheme

(3) Since detonation wave is the complex of shock wave and flame, the stability of detonation wave is preliminarily discussed by using pressure wave time curve in this paper, which is not enough. The future research plan is that Schlieren technology will be used to specifically study the shock-flame structure under the condition of nonuniform mixed detonating mixture

Nomenclature

d: Diameter
DDT: Deflagration-to-detonation transition
$G_{i,t}$: Gray value of pixel point i at time t
$\bar{G}$: Average gray value
I_{spf}: Specific impulse based on fuel
m: Total number of pictures

n: Sum of pixel points
N: Number of operation cycle
P_i: Mounted position of transducers i
p_i: Peak pressure of cycle i at P_5
$\bar{p}$: Average of peak pressure
PDE: Pulse detonation engine
α: Maximum opening angle of valve sheet
ζ: Homogeneity degree of fuel distribution
χ: Operation stability of PDE.

Data Availability

The data is all in the article. There is no additional data.

Conflicts of Interest

The authors declare no competing financial interest.

Acknowledgments

References

[1] V. F. Nikitin, V. R. Dushin, Y. G. Phylippov, and J. C. Legros, "Pulse detonation engines: technical approaches," *Acta Astronautica*, vol. 64, no. 2-3, pp. 281–287, 2009.

[2] J. E. Shepherd, "Detonation in gases," *Proceedings of the Combustion Institute*, vol. 32, no. 1, pp. 83–98, 2009.

[3] R. Driscoll, A. St George, D. Munday, and E. J. Gutmark, "Optimization of a multiple pulse detonation engine-crossover system," *Applied Thermal Engineering*, vol. 96, pp. 463–472, 2016.

[4] M. Shimo and S. D. Heister, "Multicyclic-detonation-initiation studies in valveless pulsed detonation combustors," *Journal of Propulsion and Power*, vol. 24, no. 2, pp. 336–344, 2008.

[5] F. Y. Zhang, T. Fujiwara, T. Miyasaka et al., "Experimental study of key issues on pulse detonation engine development," *Transactions of The Japan Society for Aeronautical and Space Sciences.*, vol. 45, no. 150, pp. 243–248, 2003.

[6] Z. Wang, Z. Liang, Y. Zhang, and L. Zheng, "Direct-connected experimental investigation on a pulse detonation engine," *Proceedings of the Institution of Mechanical Engineers, Part G: Journal of Aerospace Engineering*, vol. 231, no. 7, pp. 1338–1346, 2016.

[7] Y. Huang, H. Tang, J. Li, and J. Wang, "Deflagration to detonation transition of kerosene–air mixtures in a small-scale pulse detonation engine," *Proceedings of the Institution of Mechanical Engineers Part G: Journal of Aerospace Engineering*, vol. 225, no. 4, pp. 441–448, 2011.

[8] E. K. Dabora, K. W. Ragland, and J. A. Nicholls, "Drop-size effects in spray detonations," *Symposium (International) on Combustion*, vol. 12, no. 1, pp. 19–26, 1969.

[9] Z. C. Lin, J. A. Nicholls, M. J. Tang, C. W. Kauffman, and M. Sichel, "Vapor pressure and sensitization effects in detonation of a decane spray," *Symposium (International) on Combustion*, vol. 20, no. 1, pp. 1709–1716, 1985.

[10] S. Cheatham and K. Kailasanath, "Single-cycle performance of idealized liquid-fueled pulse detonation engines," *AIAA Journal*, vol. 43, no. 6, pp. 1276–1283, 2005.

[11] S. Cheatham and K. Kailasanath, "Numerical modelling of liquid-fuelled detonations in tubes," *Combustion Theory and Modelling*, vol. 9, no. 1, pp. 23–48, 2005.

[12] V. Tangirala, A. Dean, O. Peroomian, and S. Palaniswamy, "Investigations of two-phase detonations for performance estimations of a pulse detonation engine," in *45th AIAA Aerospace Sciences Meeting and Exhibit*, p. 1173, Reno, NV, 2007.

[13] J. Lasheras, B. Varatharajan, C. Varga, and F. Williams, "Studies of fuel distribution and detonation chemistry for pulse detonation engines," in *ISOABE, ISABE- International Symposium on Air Breathing Engines, 15th*, p. 1174, Bangalore, India, 2001.

[14] Z. Wang, C. Yan, W. Fan, and L. Zheng, "Experimental study of atomization effects on two-phase pulse detonation engines," *Proceedings of the Institution of Mechanical Engineers Part G: Journal of Aerospace Engineering*, vol. 223, no. 6, pp. 721–728, 2009.

[15] C. Tucker, P. King, R. Bradley, and F. Schauer, "The use of a flash vaporization system with liquid hydrocarbon fuels in a pulse detonation engine," in *42nd AIAA Aerospace Sciences Meeting and Exhibit*, p. 0868, Reno, Nevada, 2004.

[16] K. C. Tucker, P. I. King, and F. R. Schauer, "Hydrocarbon fuel flash vaporization for pulsed detonation combustion," *Journal of Propulsion and Power*, vol. 24, no. 4, pp. 788–796, 2008.

[17] C. Miser, P. King, and F. Schauer, "PDE flash vaporization system for hydrocarbon fuel using thrust tube waste heat," in *41st AIAA/ASME/SAE/ASEE Joint Propulsion Conference & Exhibit*, p. 3511, Tucson, Arizona, 2005.

[18] T. M. Helfrich, P. I. King, J. L. Hoke, and F. R. Schauer, "Effect of supercritical fuel injection on cycle performance of pulsed detonation engine," *Journal of Propulsion and Power*, vol. 23, no. 4, pp. 748–755, 2007.

[19] Z. C. Fan, W. Fan, H. Tu, J. L. Li, and C. J. Yan, "The effect of fuel pretreatment on performance of pulse detonation rocket engines," *Experimental Thermal and Fluid Science*, vol. 41, pp. 130–142, 2012.

[20] E. Barbour, L. Ma, J. Jeffries, R. Hanson, C. Brophy, and J. Sinibaldi, "Real-time measurements of C2H4 concentration with application to PDEs operating on oxygen and air," in *41st AIAA/ASME/SAE/ASEE Joint Propulsion Conference & Exhibit*, p. 4376, Tucson, Arizona, 2005.

[21] L. Ma, J. Jeffries, R. Hanson, K. Hinckley, P. Pinard, and A. Dean, "Characterization of the fuel fill process in a multicycle pulse detonation engine using a diode-laser sensor," in *41st AIAA/ASME/SAE/ASEE Joint Propulsion Conference & Exhibit*, p. 3834, Tucson, AZ, 2005.

[22] C. M. Brophy and R. K. Hanson, "Fuel distribution effects on pulse detonation engine operation and performance," *Journal of Propulsion and Power*, vol. 22, no. 6, pp. 1155–1161, 2006.

[23] C. M. Brophy, J. O. Sinibaldi, and L. Ma, "Effects of non-uniform mixture distributions on pulse detonation engine performance," in *43rd AIAA Aerospace Sciences Meeting and Exhibit*, p. 1304, Reno, Nevada, 2005.

[24] H. D. Perkins and C. J. Sung, "Effects of fuel distribution on detonation tube Performance," *Journal of Propulsion and Power*, vol. 21, no. 3, pp. 539–545, 2005.

[25] M. K. Brett, *Spray Detonation in a Well-Characterized Homogeneous Mixture*, Stanford University, Stanford, California, 2003.

[26] O. Peraldi, R. Knystautas, and J. H. Lee, "Criteria for transition to detonation in tubes," *Symposium (International) on Combustion*, vol. 21, no. 1, pp. 1629–1637, 1988.

Research Article

Droplet Size Spatial Distribution Model of Liquid Jets Injected into Subsonic Crossflow

Luhao Liu,[1] **Lijun Yang** ⬤,[1,2] **and Qingfei Fu**[1,2]

[1]*School of Astronautics, Beijing University of Aeronautics and Astronautics, 100083, China*
[2]*Beijing Advanced Innovation Center for Big Data-Based Precision Medicine, Beihang University, 100083, China*

Correspondence should be addressed to Lijun Yang; yanglijun@buaa.edu.cn

Liquid jet injected into transverse subsonic gaseous flow has been widely utilized in many industrial applications. It is useful to determine the spatial distribution of generated droplets in the near-field region for high-efficiency combustion. In this paper, we propose a simplified model to predict droplet spatial distribution in transverse subsonic gaseous flow. Linear stability analysis has been used to determine the disturbance growth rate on the surface of a liquid column. When the amplitude of disturbance is of the same order of magnitude as jet radius, the liquid jet breaks up into ligaments. We can make an assumption that the generation rate of small droplet equals to liquid breakup rates, which varies with a spatial location under this circumstance. Combining these relations with the definition of SMD (Sauter mean diameter), a semitheoretical relation to evaluate droplet spatial distribution along the liquid column can be established. The present model has been compared with empirical relation based on experiments under different conditions. Results indicate that in the surface breakup region, the current model shows great consistency with experimental observations while there exists a relatively large discrepancy between the current model and experimental observation in the column breakup region because of its strong nonlinear effect near the breakup point. In addition, the effects of flow parameters on droplet size spatial distribution have been investigated.

1. Introduction

Liquid jet injected into a transverse gaseous flow is widely used in many industrial applications like scramjet in hypersonic vehicles [1–6]. Compared with the traditional injection method, the transverse injection system has many advantages such as rapid atomization and relatively simple structure. In general, atomization processes can be divided into two parts which are primary breakup and secondary breakup, respectively. The present paper concentrates on the characteristics of the primary breakup of liquid injected into a transverse gaseous flow.

In this research field, an earlier study focuses on liquid jets exposed to supersonic crossflow [7, 8]. When a liquid jet is in a high-speed transverse gaseous flow, an aerodynamic force stimulates a strong disturbing wave on the liquid surface. The breakup process is quite rapid because of the high gaseous speed. In their experiments, high frequency, large amplitude waves controlled by an aerodynamic force

were observed. When the airstream Mach number is large enough, the liquid column goes through a strong atomization process that disturbing wave cannot be observed on the jet surface. In order to solve this problem, Xiao et al. [9], and Li et al. [10], utilized high-quality numerical simulation to investigate primary breakup processes of a liquid jet exposed into supersonic crossflow, which agrees well with experimental results. In addition, under supersonic airflow condition, it generates a detached bow shock wave before the injection point [11], which transforms supersonic airstream into the subsonic airstream. Therefore, research focus has shifted to subsonic transverse gaseous crossflow in the last few decades.

For nonturbulent round jet injected into gaseous crossflow, there existed numerous empirical graphs to classify the primary breakup regime. It can be found that We_G (gaseous Weber number) is the most commonly used parameter to define breakup regime [12, 13]. Wu et al. [14] firstly used $We_G - q$ (q is the liquid-gas momentum ratio) map to classify the primary breakup regime, which can be mainly divided

into two parts: column breakup regime and surface breakup regime. Sallam et al. [15] used $We_g - (\lambda_s/d_j)$ map to show the correlation between λ_s/d_j and breakup regime where λ_s is the wavelength of instability waves developing on the windward side of a liquid jet. It could be found that surface wavelength decreases with the increase of gas Weber number.

Recently, many investigators studied the trajectory of a liquid column, penetration height, and distribution of droplet with advanced experimental equipment. Rezaei et al. [16] used laser sheet planar imaging technology to get instantaneous spatial spray images and obtained the correlation of primary breakup length with different fuel temperatures in a pressure swirl injector. Amighi and Ashgriz [17] provided plenty of experimental data of atomization processes and determined the correlation between trajectories of water jet injected into subsonic crossflow air and different flow parameters. In addition, they utilized the laser light sheet illumination technique and shadowgraphy to establish a relation between global droplet size and various parameters like jet velocity, air temperature, and injector diameter [18]. Broumand and Birouk [19] summarized these correlations between breakup distance or height of a liquid jet exposed to subsonic gaseous crossflow and various physical parameters.

It is well known that a liquid jet goes through a series of atomization processes and finally became a group of tiny droplets. Hence, it is quite significant for a subsequent combustion process to determine the distribution of Sauter mean diameter (SMD) in a flow field. Nevertheless, the existed SMD prediction methods mainly concentrate on empirical correlations related to experimental data [20]. It is quite obvious that these correlations depend strongly on experimental conditions, which cannot explain the physical nature hidden in related breakup phenomenons. Therefore, some theoretical models have been established to evaluate SMD. For instance, Varga et al. [21], developed a dual-instability mode to explain the breakup process of liquid film exposed to a high-speed gaseous flow, which agreed well with experiments.

It should be noticed that in the flow field, the value of SMD measured by the Malvern system in the experiment is full-field SMD distribution which is not precise enough for further optimum design. Therefore, droplet size spatial distribution which means SMD is a function of spatial locations is significant for deeper investigation. Unfortunately, there has rarely related research about how to determine SMD spatial distribution by a theoretical or semitheoretical method, which has a great meaning of optimum design for a next-generation engine.

In this paper, we utilize linear stability analysis based on full-wavelength assumption to obtain a surface instability wave growth rate, and then, it can be combined with the nonturbulent round liquid jet breakup rate observed by Sallam et al. [15] in experiments. A semitheoretical spatial SMD distribution prediction model can be determined in the near-field region. This prediction model coincides quite well to the present empirical correlation obtained by plenty of experiments in the surface breakup region. In addition, the effect of flow parameters like injection velocity and transverse gaseous velocity on droplet size spatial distribution will be investigated as well.

2. The Droplet Size Spatial Distribution Model

Many papers have justified that unstable wave exists on the surface of the liquid column [22, 23]. The initial unstable wave propagates along the liquid jet direction while strong interaction between transverse gas and liquid column makes the amplitude of unstable wave larger. In order to simplify the present problem, a series of assumptions have been made as follows. The transverse gaseous flow is incompressible and irrotational. According to Amini [23], jet bending and deformation processes are negligible when the gas-liquid momentum ratio is not sufficiently high; therefore, liquid jet preserves its cylindrical shape before the breakup point. In addition, the geometry effect of the injector and gravity force has been neglected. The initial stage of breakup process is schematically showed in Figure 1, where u_G denotes the velocity of transverse gaseous flow, u_L is the velocity of the liquid jet, d_j is the initial diameter of the liquid column, which is equal to the diameter of an injector in the present analysis, and λ is the wavelength of surface instability wave.

There has an assumption that unstable wave within one wavelength will be shed from a cylindrical surface by an aerodynamic force and then form as a small ligament, i.e.,

$$D_{\text{lig}} \propto \lambda. \tag{1}$$

The scale of primary droplets formed at the tip of small ligaments is given by the following expression, i.e.,

$$D_{\text{pri}} = \beta D_{\text{lig}}, \tag{2}$$

where D_{pri} is the diameter of droplets formed by a primary breakup, D_{lig} is the diameter of ligaments, and β is the constant related to form small droplets in a regime of Rayleigh breakup which equals to 1.2 suggested by Sallam et al. [15].

When a liquid jet is injected into a transverse gaseous flow, a tangential aerodynamic force around a liquid column makes ligaments detached from the liquid column. There exists an assumption that ligaments shedding from the interface of a liquid jet per unit wavelength equal to a liquid breakup rate which is a small droplet generation rate as well. Therefore, we can establish the mass conservation relation, i.e.,

$$m_{\text{rate}}(\lambda)d\lambda \propto \rho_l D_{\text{pri}}^3 n_{\text{rate}}(\lambda)d\lambda, \tag{3}$$

where $n_{\text{rate}}(\lambda)$ represents the formation number of small droplets per unit wavelength of a column surface. The mass flow rate induced by surface instability wave per unit wavelength is proportional to reduced shedding velocity, i.e., λ/τ, where τ is the characteristic time that instability wave reaches sufficient amplitude compared with the radius of a liquid column (Mayer [24]). It can be related to the growth rate of instability wave on the liquid surface caused by
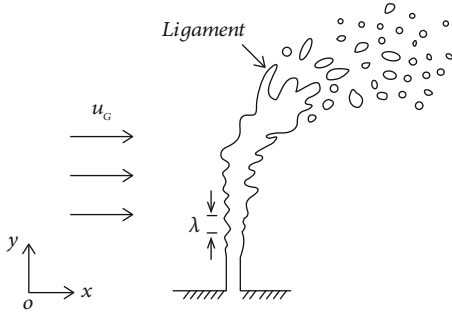
FIGURE 1: Schematic diagram of a liquid jet in transverse crossflow.

transverse airflow. Hence, the characteristic time is inversely proportional to the instability growth rate of surface wave, i.e.,

$$\tau \propto \frac{1}{\omega_R}, \qquad (4)$$

where ω_R is the growth rate of instability wave. Therefore, the mass flow rate of shedding surface waves per unit wavelength gives

$$m_{\mathrm{rate}}(\lambda)d\lambda \propto \rho_L \lambda \omega_R d\lambda. \qquad (5)$$

Combining Equations (3) and (5), we can obtain

$$D_{\mathrm{pri}}^2 n_{\mathrm{rate}}(\lambda)d\lambda \propto \frac{\lambda \omega_R}{D_{\mathrm{pri}}}d\lambda. \qquad (6)$$

By integrating Equation (6) from minimum to maximum wavelength of surface instability wave and then substituting Equations (1) and (2) into Equation (6), we can obtain

$$\int_{\lambda_{\min}}^{\lambda_{\max}} D_{\mathrm{pri}}{}^2 n_{\mathrm{rate}}(\lambda)d\lambda \propto \int_{k_{\min}}^{k_{\max}} \frac{2\pi}{\beta} \frac{\omega_R}{k^2}dk. \qquad (7)$$

It is clear that the definition of Sauter mean diameter is

$$\mathrm{SMD} = \frac{\int_{\lambda_{\min}}^{\lambda_{\max}} D_{\mathrm{pri}}{}^3 n_{\mathrm{rate}}(\lambda)d\lambda}{\int_{\lambda_{\min}}^{\lambda_{\max}} D_{\mathrm{pri}}{}^2 n_{\mathrm{rate}}(\lambda)d\lambda}. \qquad (8)$$

Substituting Equations (3) and (7) into Equation (8), we can obtain

$$\mathrm{SMD}(y) = C\frac{\beta}{2\pi}\frac{m_{\mathrm{rate}}(y)}{\int_{k_{\min}}^{k_{\max}}\left(\omega_R/k^2\right)dk}, \qquad (9)$$

where $k_{\min}$ and $k_{\max}$ are the minimum and maximum wave number, respectively. Because previous relationship such as Equation (1) to Equation (7) is not a strict equation, it is necessary to introduce an integral constant C, which depends on the structure of injector and physical properties of fluids. When we settle down the value of C, it cannot be changed under different flow rates [25]. m_{rate} is the liquid breakup

rate, for round nonturbulent liquid jets injected into a transverse gaseous flow; m_{rate} can be expressed as follows (Sallam et al. [15]):

$$m_{\mathrm{rate}}(y) = 6.89 \times 10^{-4} \rho_L u_P \exp\left(\frac{5.43y}{y_b}\right), \qquad (10)$$

where u_P is the liquid droplet velocity flowing in the transverse crossflow that can be expressed as

$$u_P = 6.7u_\infty \sqrt{\frac{\rho_G}{\rho_L}}, \qquad (11)$$

where u_∞ is the transverse gaseous velocity and y_b is the breakup height of the liquid column, which can be expressed as $y_b = 8.05q^{0.5}D_0$ where D_0 is the diameter of the injector. We should notice that it depends on various parameters such as liquid-gas momentum ratio, injector diameter, and Ohnesorge number. The expressions of y_b under different circumstances can be found in Broumand and Birouk [19]. It should be noticed that on the upstream side of the liquid jet, an aerodynamic force tends to accelerate gas toward the liquid jet in transverse stream direction near the upstream stagnation point, which makes liquid column compressed and develops Rayleigh-Taylor wave on the surface of the liquid column.

Wang et al. [22] utilized the linear instability analysis to obtain dispersion relation of surface waves on the round nonturbulent liquid jets injected into transverse subsonic gaseous airflow. Therefore, we can make some necessary simplifications and dispersion equation reduces to

$$\omega_R^2 = \frac{(ku_L)^2}{1+\bar{\rho}} - \frac{(ku_L)^2}{(1+\bar{\rho})^2} - \frac{\sigma k^3}{\rho_L(1+\bar{\rho})} + \frac{k\rho_G u_G^2}{2h(1+\bar{\rho})\rho_L}, \qquad (12)$$

where a is the radius of the liquid jet, $h = a/8$ is the reduced thickness because of the compressive effect of an aerodynamic force, $\bar{\rho} = \rho_G/\rho_L$ is the density ratio, and σ is the surface tension.

In the expression of SMD, the range of integration needs to be determined before calculation. $k_{\min}$ corresponds to the minimum value of unstable wavenumber; before the breakup of the liquid jet, surface wave develops noticeably and its wavelength is assumed to be equal to the diameter of the injector. After that point, the liquid column would not hold its cylindrical shape and breakup into ligaments and large droplets. Therefore, the minimum wavenumber can be expressed as follows, i.e.,

$$k_{\min} = \frac{2\pi}{d_j}. \qquad (13)$$

Subsequently, we should determine the value of $k_{\max}$. We set $\omega_R = 0$ and obtain the cutoff wavenumber. However, in order to make sure the convergence of calculation, we should set minimum wavelength equals to $0.1d_j$ according to Ashgriz and Mashayek [26]. Therefore, the maximum wavenumber in the present calculation is

$$k_{\max} = \frac{2\pi}{0.1 d_j}. \tag{14}$$

During the theoretical derivation, the relation between primary droplet and ligaments has been established by Rayleigh breakup. Then, the total number of primary droplets can be connected with the liquid breakup rate measuring by existed experiments. Finally, we can substitute Equations (10) and (12) into Equation (9); then, a semitheoretical relation based on linear stability analysis can be expressed as follows, i.e.,

$$\text{SMD}(y) = C \frac{\beta}{2\pi} \exp\left(\frac{5.43y}{y_b}\right) \times \frac{6.89 \times 10^{-4} \rho_L u_P}{\int_{k_{\min}}^{k_{\max}} \sqrt{\left(u_L^2/\left(k^2(1+\bar{\rho})\right)\right) - \left(u_L^2/\left(k^2(1+\bar{\rho})^2\right)\right) - \left(\sigma/\left(\rho_L k(1+\bar{\rho})\right)\right) + \left(\rho_G u_G^2/\left(2k^3 h(1+\bar{\rho})\rho_L\right)\right)} \, dk}. \tag{15}$$

In reality, the precise primary breakup phenomenon of liquid jet injected into a transverse gaseous flow includes column breakup, which characteristics are quite different from a surface breakup. To be more specific, within the column breakup regime, the liquid column breakups to large ligaments entirely and the cylindrical shape of the liquid jet would not be maintained. More significantly, surface instability wave will disappear and linear instability analysis will not adjust to the present condition. Therefore, the related phenomenon considered and discussed in this paper just simplifies some breakup processes and obtains SMD spatial distribution in the surface breakup regime near the exit of the injector.

3. Results and Discussion

In this section, we will first verify the correction and application scope of the present model and then investigate the effect of different flow parameters on the maximum growth rate of surface instability wave and spatial distribution of droplet size in a transverse gaseous flow.

3.1. Verification of Model. In order to verify the validness of the present semitheoretical relation, experimental conditions in Kihm et al. [27] are utilized as basic parameters. Water was injected through an injector which diameter equals to 0.5 mm. Other conditions have presented here, which includes three different transverse gas Reynolds number of 50000, 60000, and 70000, respectively. The air-liquid ratio has been set as 25, 30, and 35, and the liquid flow rate varies between 1.58 and 4.21 ml/s. In addition, in their experiments, the value of SMD has been measured by the Malvern detector at the x location of 10 mm and 20 mm downstream from the center of the injector exit.

Based on these experimental results, an empirical relation of SMD spatial distribution can be obtained by the Buckingham-PI theorem, which is shown as follows:

$$\frac{\text{SMD}}{D_0} = 1.015 \times 10^{19} \, \text{Re}_g^{-3.5998} \, \text{Re}_f^{-1.8094} \text{We}_g^{2.2474} \left(\frac{x}{D_0}\right)^{-0.6867} \left(\frac{y}{D_0}\right)^{1.9718}, \tag{16}$$

where D_0 is the diameter of the injector, We_g is the gas Weber number, and Re_g and Re_f are gas Reynolds number and liquid Reynolds number, respectively. x is the horizontal distance between breakup point and injector exit while y is the vertical distance between them. Because the liquid breakup rate is independent of the horizontal direction, we can measure the value of SMD at breakup point, i.e., $x = x_b$. The correlation of liquid column breakup distance with injector diameter can be found in Broumand and Birouk [19], which has been shown previously. We choose four groups of different flow rates in order to compare it with our present model.

According to experimental observations, breakup time can be calculated by

$$t_b = \frac{y_b}{v_j}, \tag{17}$$

where y_b is the breakup height and v_j is the liquid injection velocity. Results show that regardless of injection velocity, breakup time is about 3 ms. It indicates that the existence time of liquid column in crossflow is quite short and the surface instability wave development process is quite rapid. The comparison of SMD spatial distribution between the present model and an empirical relation is shown in Figure 2.

It should be noticed that the unit of x-coordinate is y/D_0 and the unit of y-coordinate is SMD/D_0, which indicates the relative size between breakup height or SMD and diameter of injector, respectively. It shows that the overall tendency of SMD increases synchronously with the development of liquid column. Because limited injectors and flow rates were tested in experiments of Kihm et al. [27], the integral constant C is set to an optimum value, i.e., $C = 3 \times 10^{-6}$ according to calculation result and previous attempts. The changes in temperature and pressure of transverse airflow are reflected in physical properties like gas density, which do not vary noticeably in experiments. According to the experimental conditions, we set temperature and pressure of airflow as constant in our analysis.
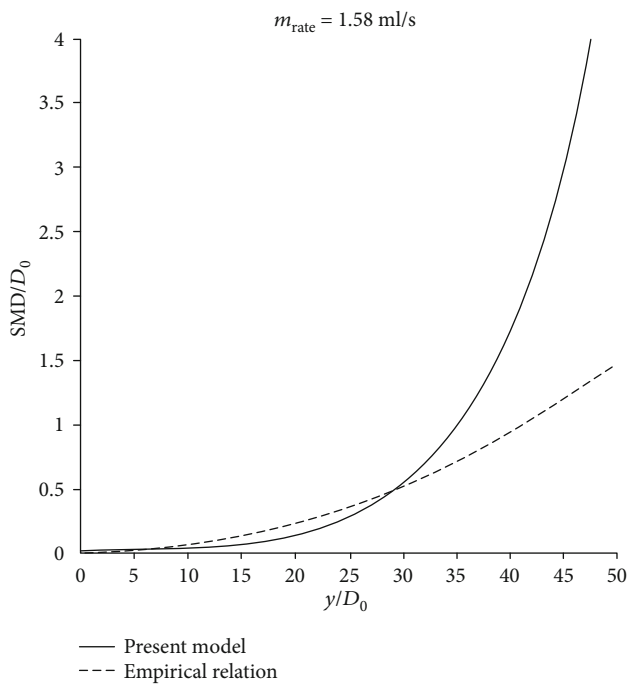
(a)
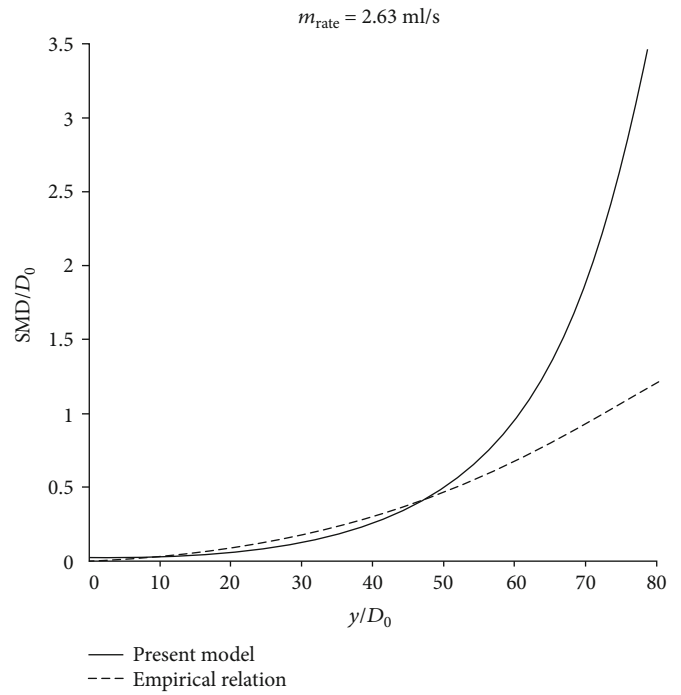
(b)
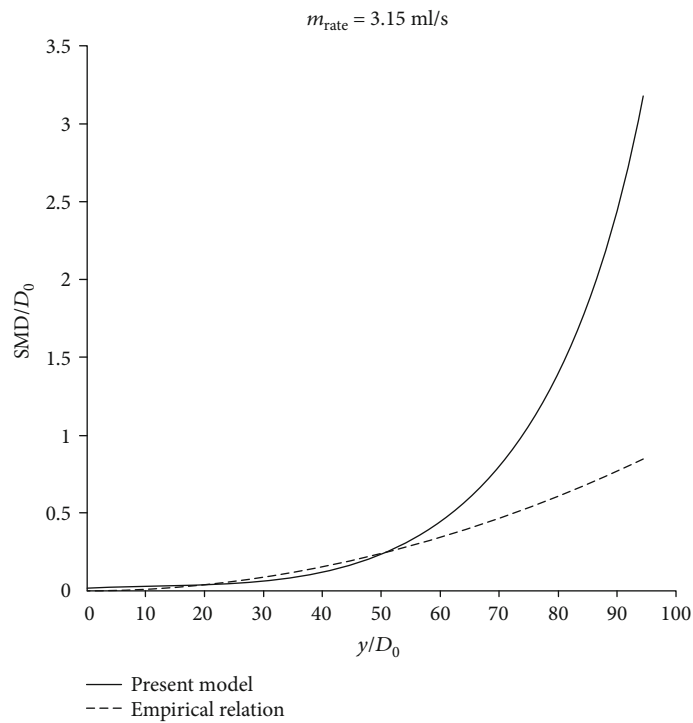
(c)

FIGURE 2: Continued.

(d)

Figure 2: Comparison of the SMD spatial distribution between present model predictions and empirical relation by Kihm et al. [27]. (a) $m_{rate} = 1.58$ ml/s. (b) $m_{rate} = 2.63$ ml/s. (c) $m_{rate} = 3.15$ ml/s. (d) $m_{rate} = 4.21$ ml/s.
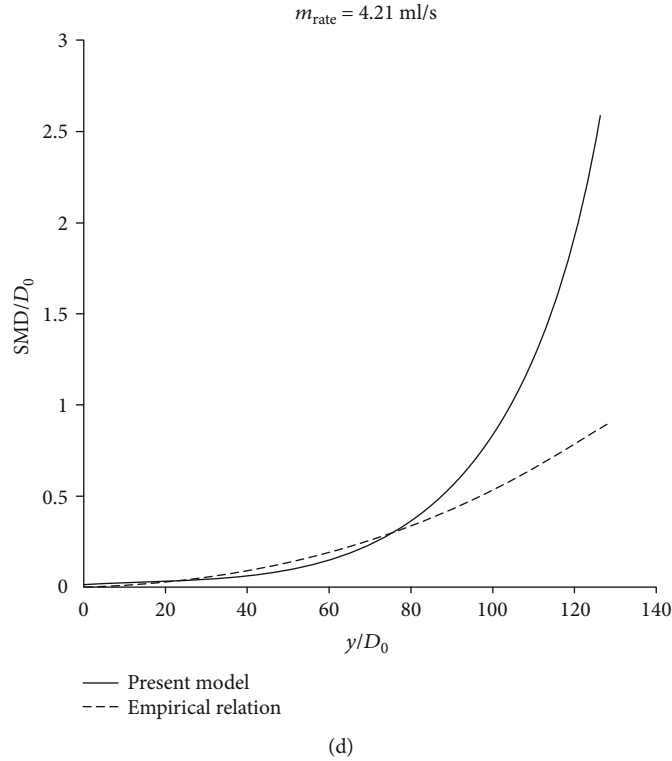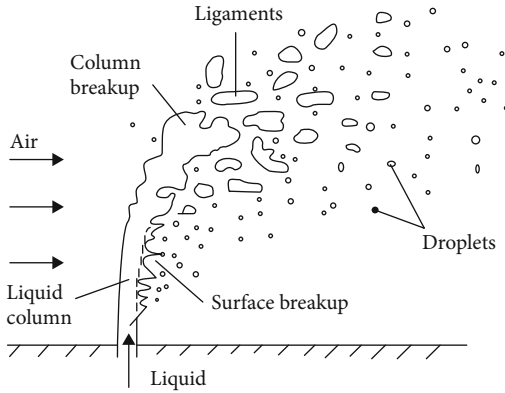

Figure 3: Schematic diagram of the breakup region of liquid jet injected into transverse airflow.

It is straightforward that breakup height increases monotonously with the increase of liquid flow rate. As shown in Figure 2 that small droplets are generated after leaving the exit of the injector which is the effect of tangential force acting on the surface of the liquid column. In the present model, it indicates that for short-wavelength disturbance near the exit of the injector, it produces relatively small droplets and droplet size spatial distribution predicted by the present semitheoretical model coincides quite well with empirical relation; the deviation between empirical relation and present model is small in surface breakup region. In addition, at the same height under different liquid flow rates, it indicates that SMD decreases with the increase of liquid flow rate. It

means that surface breakup intensifies with the increase of liquid-gas momentum ratio, which results in smaller SMD correspondingly. This tendency has also been observed by Tambe et al. [28], in their experiments. According to what we have mentioned above, it justifies the correctness of the present model in the surface breakup region.

Nevertheless, the increase of the liquid-gas momentum ratio can also change the breakup region, i.e., from the surface breakup region to the column breakup region. As shown in Figure 3 [14], in the column breakup region, liquid column and surface wave do not exist and liquid column breakups into large ligaments near the breakup point. We should notice that the present model is based on linear stability analysis and the development process of surface wave existed on a liquid column. When it approaches the breakup point, present simplified dispersion Equation (12) is not acceptable because of its strong nonlinear effect and the disappearance of surface waves. Therefore, the present model has a relatively large discrepancy with empirical relations in the column breakup region. In order to obtain more comprehensive and precise data, we can refer to some high-quality simulation such as Liu et al. [29], to understand the spray characteristics or breakup mechanism of a liquid jet in crossflow.

3.2. Effect of Flow Parameters. Flow parameters have significant effects on the instability characteristics and breakup processes of a liquid jet in a transverse gaseous flow. In the present investigation, we set the gas-liquid momentum ratio as a constant which confines breakup length and breakup
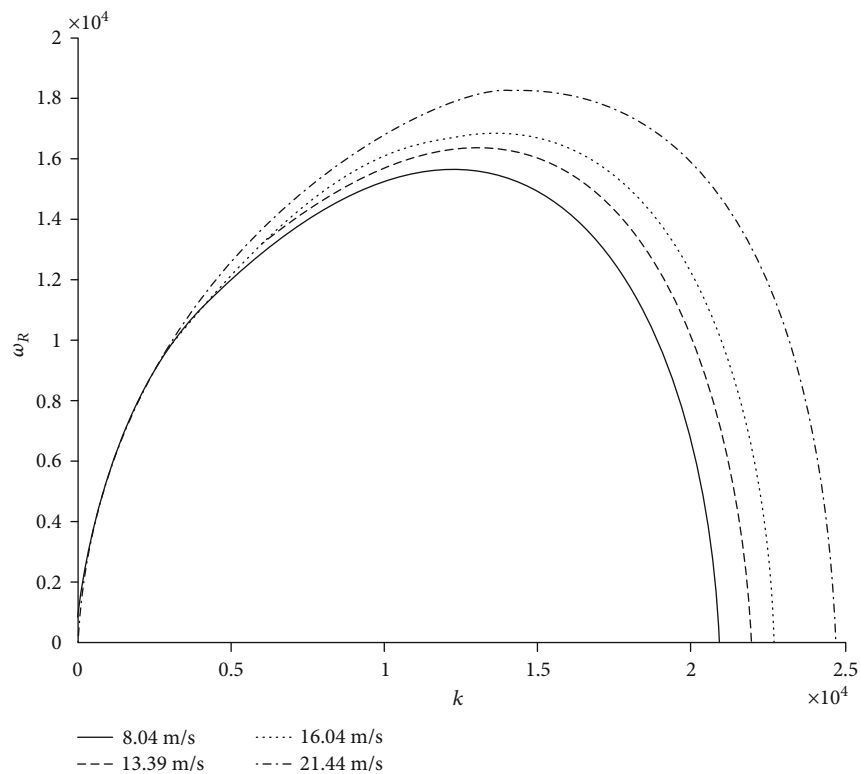
(a)
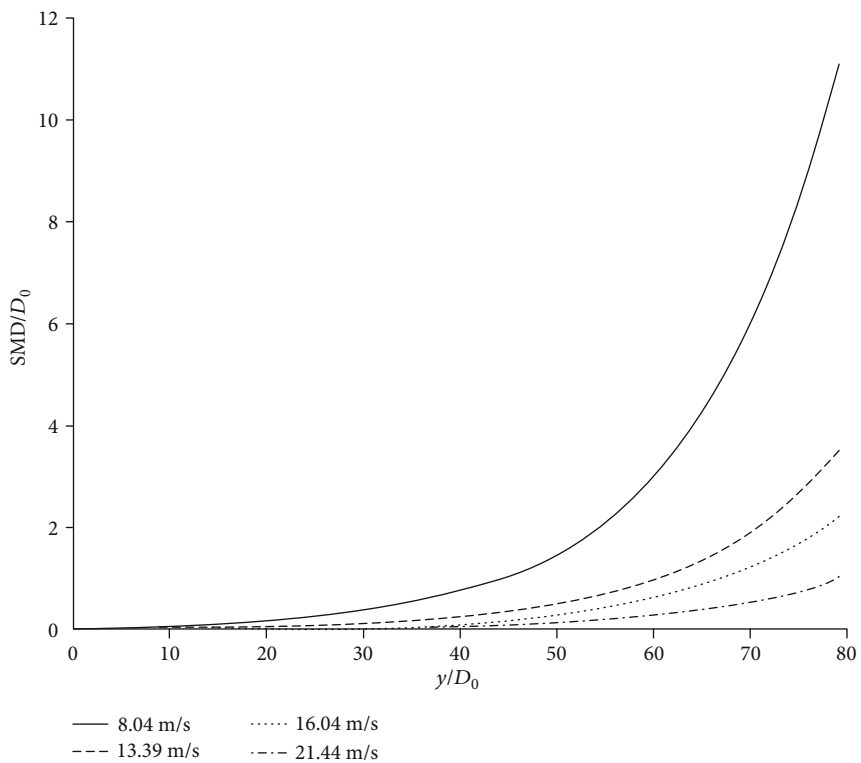
(b)

Figure 4: Effect of injection velocity to (a) surface wave growth rate and (b) droplet size distribution ($\sigma = 0.0728$ N/m^2, $\rho_G = 1.29$ kg/m^3, $\rho_L = 1000$ kg/m^3, and $q = 96.35$).

mode which are the same under different conditions and changes other flow parameters like injection velocity, liquid density, transverse gaseous velocity, and density to investigate the variation trends of maximum growth rate and cutoff wavenumber of surface instability wave. In addition, by changing flow parameters, we can obtain the droplet spatial distribution curve under various conditions. Through this way, we can predict SMD spatial distribution and its variation tendency with different flow parameters as well. The size distribution of droplets can be evaluated by comparing the value of SMD at the same height in the effective range of the present model.

3.2.1. Effect of Injection Velocity. The injection velocity is related to injector geometry, liquid mass flow rate, and pressure drop of the injector. The maximum growth rate and droplet distribution under different injection velocities are shown in Figure 4.

It should be noticed that these four injection velocities are not set randomly. These velocities correspond to the mass flow rate of the injector in related experiments. As shown in Figure 4(a), the maximum growth rate and cutoff wavenumber increase with the increase of injection velocity, which indicates that the liquid column is easier to break up and the wavelength of surface instability wave is smaller with larger injection velocity. These have been verified by previous researchers [23]. As shown in Figure 4(b), the droplet size distribution shows that SMD will be smaller for larger injection velocity. Physically, it can be explained that with larger injection velocity, smaller wavelength generated at the onset of liquid column shrinks into smaller droplets according to Rayleigh breakup mechanism. Furthermore, for larger injection velocity, the development of disturbing wave is insufficient, which also generates smaller droplets.

3.2.2. Effect of Liquid Density. Liquid density is a physical property which is independent to the injector. The effect of liquid density on the maximum growth rate and droplet distribution is shown in Figure 5.

It shows that in Figure 5(a), the maximum growth rate increases with the increase of liquid density while cutoff wavenumber rarely varies with liquid density, which means that initial wavelength on column surface is the same for different kinds of liquids. In Figure 5(b), it shows that SMD increases with denser liquid. It can be explained that the expression of droplet size distribution is inverse proportional to liquid density. And denser liquid refers to a smaller maximum growth rate that makes SMD larger. Hence, the value of SMD at specified height increases with the increase of liquid density, correspondingly.

3.2.3. Effect of Transverse Gaseous Velocity. Transverse gaseous velocity is related to the upstream condition. The effect of transverse gaseous velocity is shown in Figure 6.

Similar to Figure 4, these four transverse gaseous velocities refer to the corresponding gaseous Reynolds number in experiments. It shows in Figure 6(a) that increasing transverse gaseous flow promotes the wave development process on the surface of the liquid column. And the wavelength of the surface wave decreases with larger gaseous velocity, which can be represented by cutoff wavenumber. It indicates that in Figure 6(b) larger gaseous velocity makes SMD smaller. In physics, it can be explained that increasing gaseous velocity enlarges the aerodynamic force that could promote instability of jet, which has been observed in experiments by Behzad et al. [30]. Furthermore, similar to the effect of injection velocity, Rayleigh breakup would occur near the injector exit. It forms smaller droplets at the onset of the liquid column with larger gaseous velocity and smaller wavelength of surface wave.

3.2.4. Effect of Transverse Gaseous Density. The transverse gaseous pressure can be represented by gaseous density that pressure of transverse flow increases with gaseous density. The effect of transverse gaseous density is presented in Figure 7.

It shows in Figure 7(a) that different from the effect liquid density, the increase of gas density makes the maximum growth rate and cutoff wavenumber larger, which means denser gas induces a stronger aerodynamic force on the surface of the liquid column and promotes the breakup of the liquid jet. It can be indicated in Figure 7(b) that in a high pressure environment, denser gas suppresses the occurrence of column breakup and generation process of ligaments, which makes the value of SMD smaller. It is verified by high precision simulations [31].

3.2.5. Effect of Surface Tension. Surface tension is a physical parameter which is related to temperature and pressure. In the present investigation, we assume that surface tension does not vary with other parameters and only changes the value of surface tension to explore its impact. The effect of surface tension is presented in Figure 8.

It shows in Figure 8(a) that the increase of surface tension makes maximum growth rate and cutoff wavenumber smaller, which means surface tension has an effect to keep the cylindrical shape of the liquid jet, which restrains the breakup process. As shown in Figure 8(b), the value of SMD enlarges with the increase of surface tension. It can be explained that surface tension makes the maximum growth rate smaller and surface tension term is located in the denominator of expression of SMD spatial distribution. Therefore, increasing surface tension makes SMD larger.

4. Conclusion

This paper established a semitheoretical model to predict droplet size spatial distribution along the liquid column in the surface breakup region of liquid jet exposed to subsonic transverse crossflow. Linear stability analysis was utilized to describe the characteristic length scale and instability growth rate of the surface wave. Empirical relation obtained by other researchers has been used to verify the validness of the present model which shows great consistency in the surface breakup region. In the column breakup region, it has a large discrepancy because of its strong nonlinear effect near the breakup point.

(a)

(b)

FIGURE 5: Effect of liquid density to (a) surface wave growth rate and (b) droplet size distribution ($\sigma = 0.0728 \, \text{N/m}^2$, $\rho_G = 1.29 \, \text{kg/m}^3$, $u_L = 13.39 \, \text{m/s}$, and $q = 96.35$).

(a)

(b)

Figure 6: Effect of transverse gaseous velocity to (a) surface wave growth rate and (b) droplet size distribution ($\sigma = 0.0728\,\text{N/m}^2$, $\rho_L = 1000\,\text{kg/m}^3$, $\rho_G = 1.29\,\text{kg/m}^3$, and $q = 96.35$).

(a)
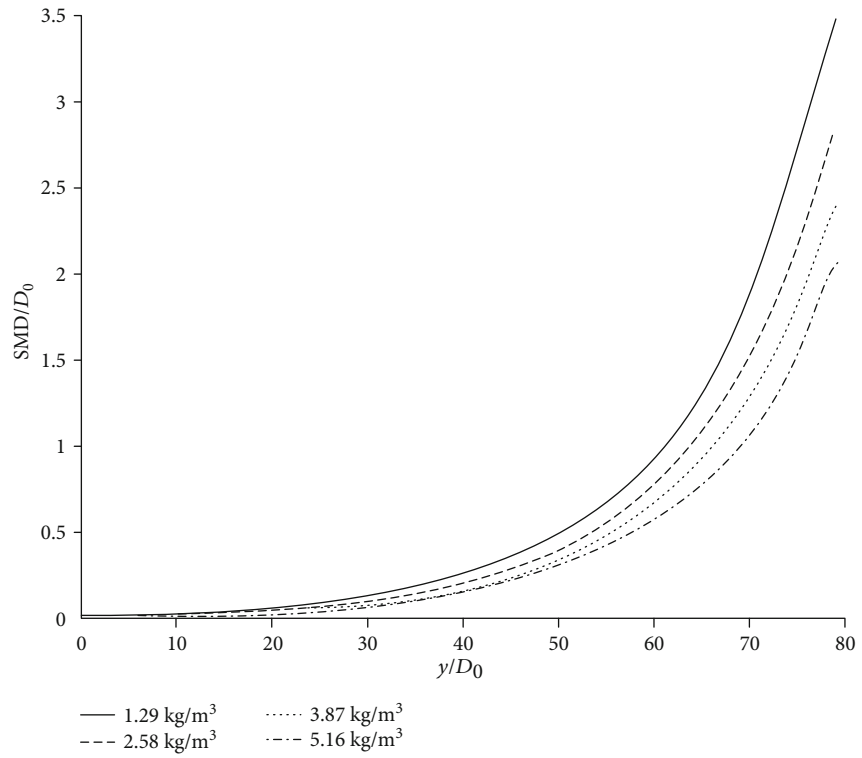
(b)

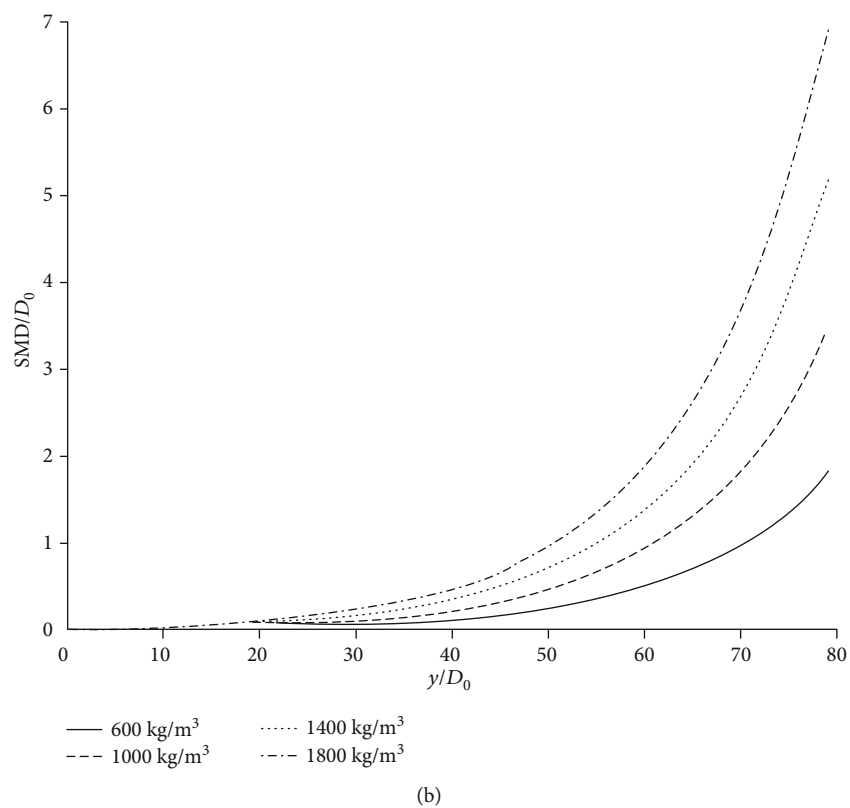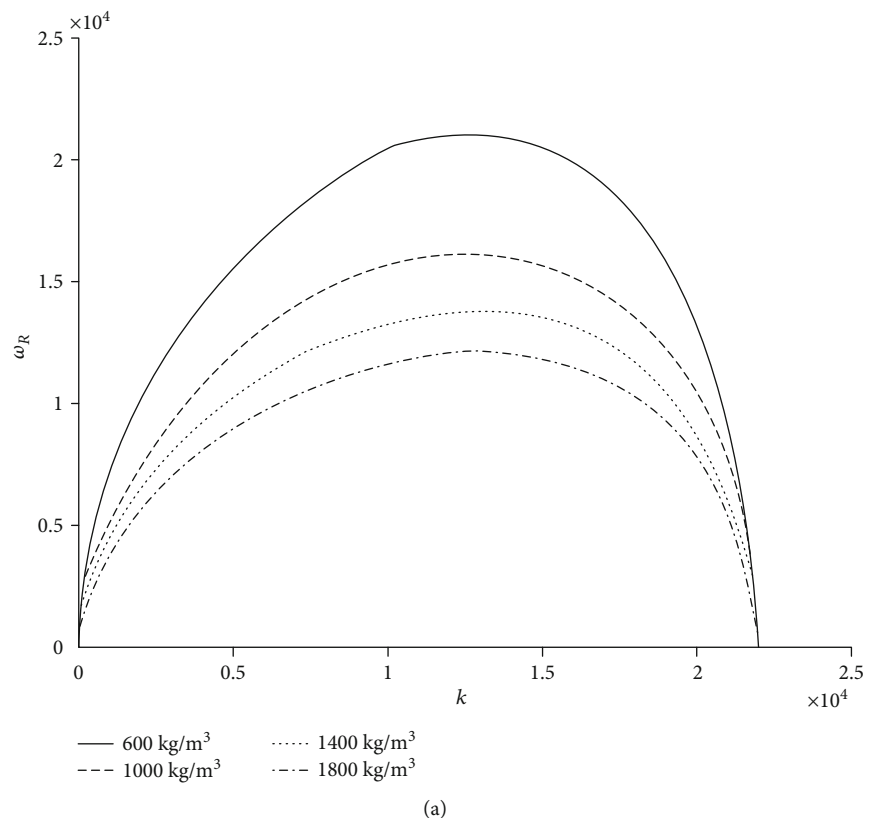FIGURE 7: Effect of transverse gaseous density to (a) surface wave growth rate and (b) droplet size distribution ($\sigma = 0.0728$ N/m^2, $\rho_L = 1000$ kg/m^3, $u_L = 13.39$ m/s, and $q = 96.35$).

(a)

(b)

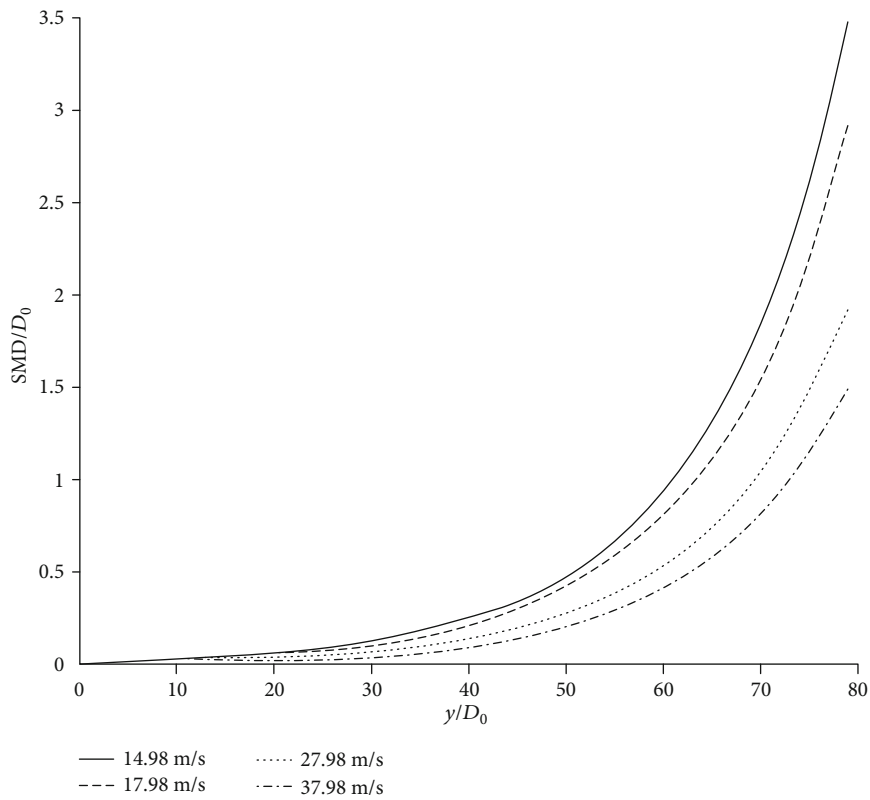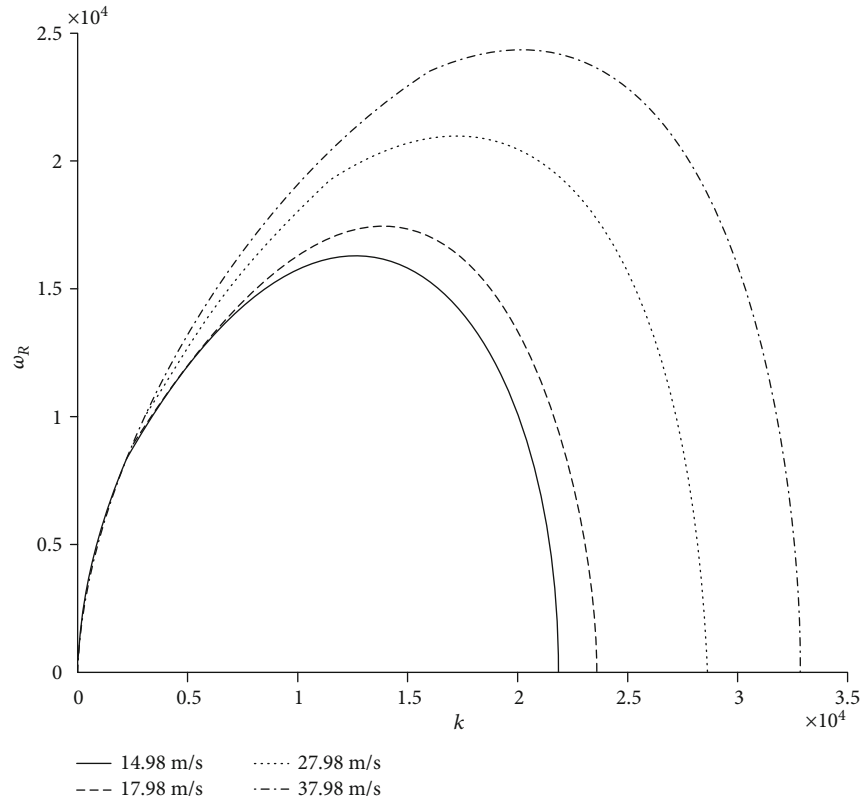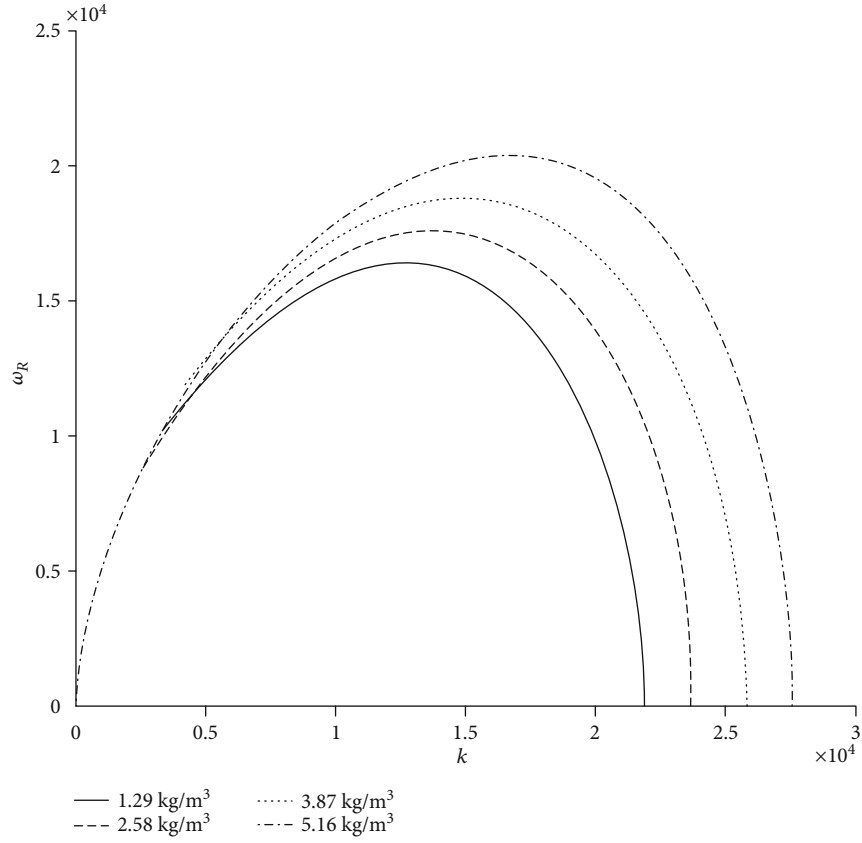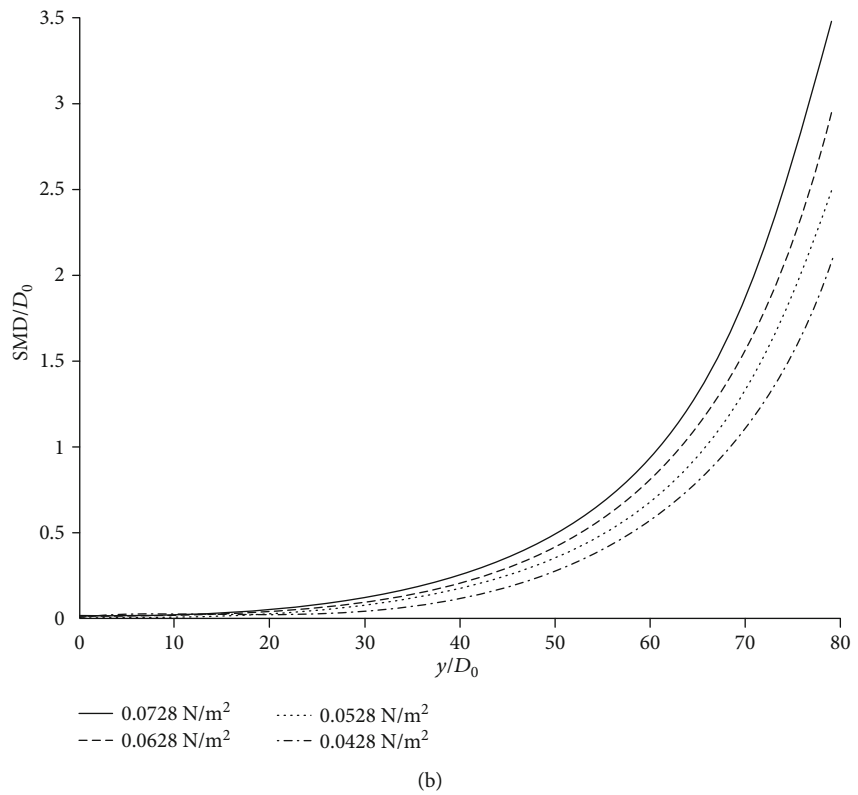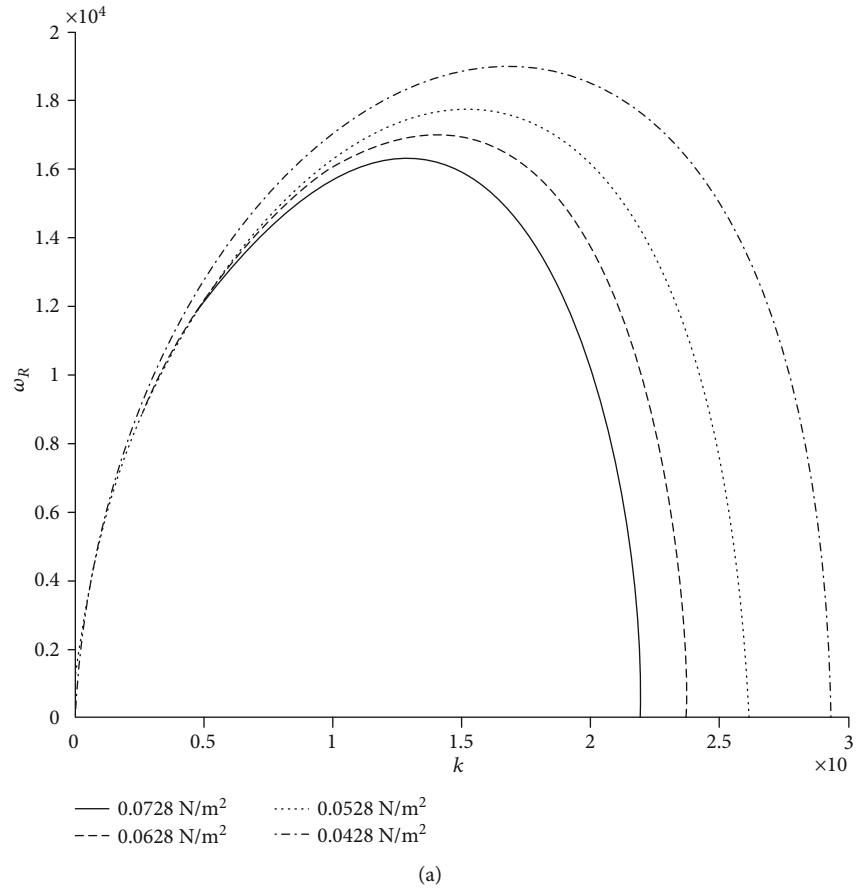FIGURE 8: Effect of surface tension to (a) surface wave growth rate and (b) droplet size distribution (ρ_g = 1.29 kg/m^3, ρ_L = 1000 kg/m^3, u_G = 37.98 m/s, u_L = 13.39 m/s, and q = 96.35).

The effects of various flow parameters on the maximum growth rate and droplet size spatial distribution have been investigated. At the same height of the liquid column, it will generate more tiny droplets near the exit of the injector with the increase of injection velocity, transverse gaseous velocity, and liquid density. Pressurized transverse gaseous flow promotes surface breakup that smaller droplets appear at the onset of the liquid column. However, increasing surface tension makes ligaments and droplets more difficult to shed from the liquid jet and generates more large droplets.

In the future, the present model can be modified to satisfy characteristics in the column breakup region and related results can be extended to high pressure and temperature environment. In addition, we can consider the effect of heat and mass transfer on the breakup process of liquid jets and droplet size spatial distribution in transverse gaseous flow, which is closer to real working conditions in the thrust engine.

Data Availability

The data used to support the findings of this study are available from the corresponding author upon request.

Conflicts of Interest

The authors declare that there is no conflict of interest regarding the publication of this paper.

Acknowledgments

References

[1] H. Wang, Z. Wang, M. Sun, and H. Wu, "Combustion modes of hydrogen jet combustion in a cavity-based supersonic combustor," *International Journal of Hydrogen Energy*, vol. 38, no. 27, pp. 12078–12089, 2013.

[2] W. Huang and L. Yan, "Numerical investigation on the ram-scram transition mechanism in a strut-based dual-mode scramjet combustor," *International Journal of Hydrogen Energy*, vol. 41, no. 8, pp. 4799–4807, 2016.

[3] M. Sun, Z. Zhong, J. Liang, and H. Wang, "Experimental investigation on combustion performance of cavity-strut injection of supercritical kerosene in supersonic model combustor," *Acta Astronautica*, vol. 127, pp. 112–119, 2016.

[4] H. Wang, Z. Wang, M. Sun, and N. Qin, "Large eddy simulation of a hydrogen-fueled scramjet combustor with dual cavity," *Acta Astronautica*, vol. 108, pp. 119–128, 2015.

[5] Z. Wang, M. Sun, H. Wang, J. Yu, J. Liang, and F. Zhuang, "Mixing-related low frequency oscillation of combustion in an ethylene-fueled supersonic combustor," *Proceedings of the Combustion Institute*, vol. 35, no. 2, pp. 2137–2144, 2015.

[6] M. B. Sun, Z. G. Wang, J. H. Liang, and H. Geng, "Flame characteristics in supersonic combustor with hydrogen injection

upstream of cavity flameholder," *Journal of Propulsion and Power*, vol. 24, no. 4, pp. 688–696, 2008.

[7] M. A. Kolpin, K. P. Horn, and R. E. Reichenbach, "Study of penetration of a liquid injectant into a supersonic flow," *AIAA Journal*, vol. 6, no. 5, pp. 853–858, 1968.

[8] N. Nejad, A. Schetz, and A. Jakubowski, "Mean droplet diameter resulting from atmoization of a transverse liquid jet in a supersonic airstream," in *International Meeting and Technical Display on Global Technology 2000*, pp. 1–16, USA, May 1980.

[9] F. Xiao, Z. G. Wang, M. B. Sun, J. H. Liang, and N. Liu, "Large eddy simulation of liquid jet primary breakup in supersonic air crossflow," *International Journal of Multiphase Flow*, vol. 87, pp. 229–240, 2016.

[10] P. Li, Z. Wang, M. Sun, and H. Wang, "Numerical simulation of the gas-liquid interaction of a liquid jet in supersonic crossflow," *Acta Astronautica*, vol. 134, pp. 333–344, 2017.

[11] L. Y. Wu, *Breakup and atomization mechanism of liquid jet in supersonic crossflow*, Doctoral degree paper, National University of Defense Technology, Changsha, 2016.

[12] J. Becker and C. Hassa, "Breakup and atomization of a kerosene jet in CROSSFLOWAT elevated pressure," *Atomization and Sprays*, vol. 12, no. 1-3, pp. 49–68, 2002.

[13] G. Vich and M. Ledoux, "Investigation of a liquid jet in a subsonic cross-flow," *International Journal of Fluid Mechanics Research*, vol. 24, no. 1-3, pp. 1–12, 1997.

[14] P. K. Wu, K. A. Kirkendall, R. P. Fuller, and A. S. Nejad, "Breakup processes of liquid jets in subsonic crossflows," *Journal of Propulsion and Power*, vol. 13, no. 1, pp. 64–73, 1997.

[15] K. A. Sallam, C. Aalburg, and G. M. Faeth, "Breakup of round nonturbulent liquid jets in gaseous crossflow," *AIAA Journal*, vol. 42, no. 12, pp. 2529–2540, 2004.

[16] S. Rezaei, F. Vashahi, G. Ryu, and J. Lee, "On the correlation of the primary breakup length with fuel temperature in pressure swirl nozzle," *Fuel*, vol. 258, pp. 1–10, 2019.

[17] A. Amighi and N. Ashgriz, "Trajectory of a liquid jet in a high temperature and pressure gaseous cross flow," *Journal Engineering Gas Turbine and Power*, vol. 141, no. 1, pp. 1–11, 2019.

[18] A. Amighi and N. Ashgriz, "Global droplet size in liquid jet in a high-temperature and high-pressure crossflow," *AIAA Journal*, vol. 57, no. 3, pp. 1–15, 2019.

[19] M. Broumand and M. Birouk, "Liquid jet in a subsonic gaseous crossflow: recent progress and remaining challenges," *Progressive of Energy and Combustion Science*, vol. 57, no. 1, pp. 1–29, 2016.

[20] M. Eslamian, A. Amighi, and N. Ashgriz, "Atomization of liquid jet in high-pressure and high-temperature subsonic crossflow," *AIAA Journal*, vol. 52, no. 7, pp. 1–13, 2014.

[21] C. M. Varga, J. C. Lasheras, and E. J. Hopfinger, "Initial breakup of a small-diameter liquid jet by a high-speed gas stream," *Journal of Fluid Mechanics*, vol. 497, pp. 405–434, 2003.

[22] S. L. Wang, Y. Huang, and Z. L. Liu, "Theoretical analysis of surface waves on a round liquid jet in a gaseous crossflow," *Atomization and Sprays*, vol. 24, no. 1, pp. 23–40, 2004.

[23] G. Amini, "Linear stability analysis of a liquid jet in a weak crossflow," *Physics of Fluids*, vol. 30, no. 8, pp. 1–11, 2018.

[24] E. Mayer, "Theory of liquid atomization in high velocity gas streams," *ARS Journal*, vol. 31, pp. 1783–1785, 1961.

[25] L. Z. Qin, R. Yi, and L. J. Yang, "Theoretical breakup model in the planar liquid sheets exposed to high-speed gas and droplet

size prediction," *International Journal of Multiphase Flow*, vol. 98, pp. 158–167, 2018.

[26] N. Ashgriz and A. Mashayek, *Handbook of Atomizaton and Sprays Theory and Application*, Springer, New York, 2011.

[27] K. D. Kihm, G. M. Lyn, and S. Y. Son, "Atomization of cross-injecting sprays into convective air stream," *Atomization and Sprays*, vol. 5, no. 4-5, pp. 417–433, 1995.

[28] S. Tambe, S. Jeng, H. Mongia, and G. Hsiao, "Liquid jets in subsonic crossflow," in *43rd AIAA aerospace sciences meeting and exhibit meeting papers*, pp. 1–17, Reno, USA, January 2005.

[29] N. Liu, Z. Wang, M. Sun, R. Deiterding, and H. Wang, "Simulation of liquid jet primary breakup in a supersonic crossflow under adaptive mesh refinement framework," *Aerospace Science and Technology*, vol. 91, pp. 456–473, 2019.

[30] M. Behzad, N. Ashgriz, and A. Mashayek, "Azimuthal shear instability of a liquid jet injected into a gaseous cross-flow," *Journal of Fluid Mechanics*, vol. 767, pp. 146–172, 2015.

[31] M. Behzad, N. Ashgriz, and B. W. Karney, "Surface breakup of a non-turbulent liquid jet injected into a high pressure gaseous crossflow," *International Journal of Multiphase Flow*, vol. 80, no. 1, pp. 100–117, 2006.

Research Article

Numerical Analysis of Self-Excited Combustion Instabilities in a Small MMH/NTO Liquid Rocket Engine

Jianxiu Qin [1] **and Huiqiang Zhang** [2]

[1]*China Academy of Aerospace Aerodynamics, China*
[2]*School of Aerospace Engineering, Tsinghua University, China*

Correspondence should be addressed to Huiqiang Zhang; zhanghq@tsinghua.edu.cn

Combustion instabilities in a small MMH/NTO liquid rocket engine used for satellite attitude and course control are numerically investigated. A three-dimensional Navier-Stokes code is developed to simulate two-phase spray combustion for cases with five different droplet Sauter Mean Diameters. As the droplet size increases from 30 microns to 80 microns, pressure oscillations are stronger with larger amplitudes. But an increase of the droplet size in the range of 80 microns to 140 microns indicates a reduction in the amplitudes of pressure oscillations. This trend is the same as the Hewitt criterion. The first tangential (1T) mode and the first longitudinal (1L) mode self-excited combustion instabilities are captured in the 60-micron and 80-micron cases. Abrupt spikes occur in the mass fraction of MMH and coincide with abrupt spikes in the mass fraction of NTO at the downstream regions just adjacent to the impinging points. Thus, local combustible high-dense mixtures are formed, which result in quasiconstant volume combustion and abrupt pressure spikes. The propagation and reflection of pressure waves in the chamber stimulate the combustion instability. When the droplet size is too small or too large, it is difficult to form local high-dense premixtures and combustion is stable in the chamber.

1. Introduction

A small MMH/NTO liquid rocket engine (LRE) is developed for the purpose of attitude control and course corrections for tactical missiles and artificial satellites. High-frequency combustion instability has plagued the development of LRE since the 1940s, in which organized oscillations with high amplitude greater than 10% of mean chamber pressure would be induced [1, 2]. Such oscillations may result in poor performance, unacceptable vibrations, or even catastrophic events. Thus, combustion instability must be considered in a priori. Because of the complexity of this problem and limited computational power to capture all the physical processes in the numerical simulations, combustion instability is still a challenge to the development of a rocket engine.

Hot fire tests were conducted to study combustion instability in the chamber [3–6]. But the quantity of tests is needed due to the notoriously probability and uncertainty of combustion instability. Thus, the prediction of combustion instability by numerical simulation is a major issue. Various levels of models have been developed to deal with combustion instability in the chamber. Wave equations [7–10], Finite Element Method (FEM) [11], and Linear Euler Equations (LEE) [12, 13] have been used to predict combustion instability. But transfer functions [14, 15] need to be provided and calibrated with high fidelity data. Computational Fluid Dynamics (CFD) method is regarded as an effective way to investigate combustion instability, which can provide insight into more detailed physical processes. Large Eddy Simulation (LES) is a good candidate, and it has been used to predict combustion instability successfully [16–21]. Detached Eddy Simulation (DES) featuring little demands on computational resources has been developed to investigate combustion instability [22–24]. However, liquid droplet dynamic was not considered and the propellants were gasified when they left the injectors in these simulations. For two-phase turbulent reactive flow, Unsteady Reynolds-Averaged Navier-Stokes (URANS) is always employed

[25, 26] and has been applied to study combustion instability in LRE [27–29]. Tucker et al. [30, 31] compared LES and URANS simulations of a combustor. The results showed the highest-fidelity LES and URANS best predicted the instantaneous temperature, vorticity fields, and wall heat flux, while the two lower-order LES provided a poor prediction. Therefore, URANS is employed in this paper due to the enormous demands of computer resources for DES or LES considering two-phase interactions.

As is well known, high-frequency combustion instability results from the coupling between unsteady heat release and acoustic pressure oscillations. Many researches focused on the simulation of unsteady heat release [17–20, 22, 32] and a heat release response function [33]. Raleigh index [34] was used to quantitatively evaluate the coupling between unsteady heat release and acoustic pressure oscillations, which represented a source term in the balance of acoustic energy [17]. When combustion instability occurs, the Raleigh index is greater than 0. But when the Raleigh index is greater than 0, there are cases shown that combustion instability does not occur. Moreover, it says nothing about how the initial heat release oscillation is produced and what is the source of pressure oscillation. High-frequency combustion instabilities can be classified as intrinsic and injection-coupled instabilities [2]. Injection-coupled instabilities arise when injected flow fluctuations couple with chamber acoustic modes, which mainly occur in LRE equipped with coaxial injectors. Mass flow rate oscillations in the injectors are the sources of heat release oscillations [35]. It was found that the acoustic mode of the chamber was coupled with that of injectors when combustion instability occurred [36–38]. For the cases in this work, like-doublet injectors are used and the mass flow rate is constant without oscillation. Intrinsic instabilities are governed by the subprocesses that occur following propellant injection, atomization, vaporization, mixing, and chemical reaction, in which injectors are passively involved. Sirignano and Duvvur [39, 40] summarized that the vaporization process was a key factor in combustion instability in the liquid rocket chamber. Lei and Turan [41] declared the evaporation process had a great influence on the nonlinear and intensity behavior of combustion instability. The vaporization rate depends on the flow field around the droplet and droplet size. Hewitt criterion [42, 43] was used to predict the highest mode of combustion instability in the chamber equipped with impinging injectors. Combustion instability is related to a stability correlating parameter d_0/U_j, where d_0 is the injector's orifice diameter and U_j is the injection velocity of the least volatile propellant. A reduction in d_0/U_j, indicating decreased stability margin, coincides with a reduction in the droplet size. Therefore, the droplet size may be a key factor in combustion instability. Few studies focused on the effects of droplet sizes on combustion instability in small thrust LREs. On the other hand, in previous studies, how the initial pressure oscillation is produced and what is the source of pressure oscillation are still not clearly explained.

In this paper, a robust three-dimensional two-phase reaction flow model based on URANS is developed. The spray combustion process for cases with different droplet sizes in

a small MMH/NTO LRE are investigated. Combustion instabilities are captured, and how the initial disturbance is induced and evolved combustion instability is analyzed. The effects of droplet sizes on combustion instability are discussed. The structure of this paper is in the following manner. First, a numerical model is described briefly in the next section followed by numerical method and boundary conditions. Then, physical model and calculation cases are given. Finally, the results of these cases are presented, in which the instability phenomenon is performed. The instability mechanism is analyzed further. And the effects of droplet sizes on combustion instability are discussed later.

2. Numerical Model

In a small MMH/NTO LRE, the propellants undergo injection, atomization, vaporization, mixing, chemical reaction, and expansion process. The Eulerian-Lagrangian method is employed to solve two-phase reactive flow in the combustion chamber, in which the Navier-Stokes (N-S) equations and the Lagrangian equations are for the gas phase and the liquid particles, respectively. The interactions between the two phases are mathematically expressed in source terms in the gas phase equations.

2.1. Continuous Phase Model. Three dimensional, multispecies gas-phase Navier-Stokes equations are used to describe the flow in the chamber. The standard $k - \varepsilon$ two-equation turbulence model is used. The governing equations of mass, momentum, energy, species mass fraction, turbulence kinetic energy, and turbulent dissipation can be expressed in the unified form [44]:

$$\frac{\partial(\rho\varphi)}{\partial t} + \frac{\partial(\rho\varphi u_j)}{\partial x_j} = \frac{\partial}{\partial x_j}\left(\Gamma_\varphi \frac{\partial\varphi}{\partial x_j}\right) + S_\varphi + S_{p\varphi} + S_{c\varphi}, \quad (1)$$

where φ, Γ_φ, S_φ, and u_j represent conservation variables, diffusion coefficients, convective source terms, and the velocity in three directions. $S_{p\varphi}$ and $S_{c\varphi}$ are the source terms determined by droplet vaporization and chemical reaction. The detailed variables are presented in Reference [44].

2.2. Atomization Model. The atomization of a liquid impinging jet is considered through a correction formula, by which spray properties are directly determined [45]. The droplets are introduced into the chamber with a N-T distribution [45] at given locations, where are the locations of impinging points of the like-doublet injectors. Initial velocities, mass flow rates, and Sauter Mean Diameters (SMD) of the droplets are given as boundary conditions. The droplets are injected in a fan or cone angle in spatial distribution. The initial velocity vector of droplets is determined by a random process. The number of parcel injected in each time step is obtained by the mass flow rate dividing the mass of droplet particle.

2.3. Droplet Phase Model. The Discrete Droplet Model (DMD) is used to describe the trajectories of droplets with the assumption that the droplets are enough diluted so that the interactions of droplets are ignored. The interaction of
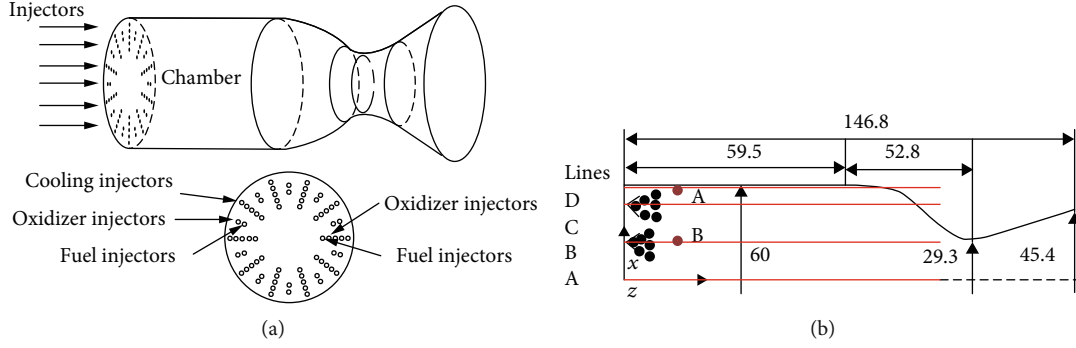
FIGURE 1: The schematic diagram and configuration parameters of the combustor and the injectors. (a) The schematic diagram of the combustor and the injectors. (b) The configuration parameters of the combustor (unit : mm).
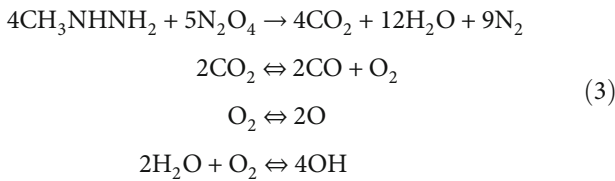
droplets and the surrounding gas are included in the source terms in gas-phase equations. The trajectories of discrete droplets are predicted by integrating the force balance on the droplets in a Lagrangian frame. The droplet gravity and other forces are neglected. Only the drag force is considered. The momentum equations for a droplet are as follows:

$$\frac{d\vec{u}_{p,j}}{dt} = \frac{3}{8} \frac{\rho}{r_j \rho_{p,j}} C_{D,j} \left| \vec{u} + \vec{u}' - \vec{u}_{p,j} \right| \left(\vec{u} + \vec{u}' - \vec{u}_{p,j} \right), \quad (2)$$

where the subscript p represents the droplet. The subscript j denotes droplet species. $C_{D,j}$ is the drag coefficient of the droplets. $\vec{u}$ is the mean gas velocity; $\vec{u}_{p,j}$ is the velocity of the j droplet. $\vec{u}'$ is the turbulence velocity fluctuation.

The source terms for the two-phase interactions are described in detail in Reference [44].

2.4. Chemical Reaction Model. To make this problem simple, only the gas-phase chemical reaction is considered, while the liquid-phase reaction is neglected. The kinetically chemical reaction rate is calculated by the Arrhenius expression of four-step chemical reactions. The MMH-NTO four-step chemical reactions are expressed:

$$4CH_3NHNH_2 + 5N_2O_4 \rightarrow 4CO_2 + 12H_2O + 9N_2$$
$$2CO_2 \Leftrightarrow 2CO + O_2$$
$$O_2 \Leftrightarrow 2O \quad (3)$$
$$2H_2O + O_2 \Leftrightarrow 4OH$$

3. Computational Methodology

The numerical methods employed to solve this problem include a temporal discretization and a spatial discretization. The finite volume method is employed to discrete Equation (1) in space, while the Euler scheme is used for the time terms. The diffusion terms and convection terms are approximated by a central difference scheme and a second-order upwind scheme, respectively. First, the source terms due to evaporation and two-phase interaction are calculated in a Lagrangian phase. Then, the field coupling pressure with velocity is solved by the Semi-Implicit Method for Pressure

Linked Equations (SIMPLE) method. The convection fluxes are calculated due to the movement of mesh in the Euler phase finally. This is the so-called Arbitrary Lagrangian-Eulerian (ALE) technique [46]. The grid size is 2 mm. Further refined grid does not improve the results significantly.

Adiabatic wall conditions are applied for the chamber walls including the injector face. Wall function treatment [47] is employed to the zone near the wall. The characteristic boundary (outflow boundary) is used at the exit, where the back pressure is specified and the velocity components are set equal to those of the logical inside neighbor vertexes due to supersonic flow at the exit.

4. Results and Discussion

4.1. Physic Model. The schematic diagram of the small MMH/NTO thrust chamber is presented in Figure 1. The diameter of the chamber is 60 mm, while the diameter of the throat is 29.3 mm. The length of the cylindrical part is 59.5 mm, while the total length of the chamber is 146.8 mm. The nozzle expansion ratio is 1.55. There are 60 like-doublet injectors and 10 cooling injectors shown as Figure 1(a). The like-doublet injectors are in the pattern of fuel-oxidizer-fuel-oxidizer. The atomization process is neglected, and the droplets are injected in the impinging points shown as Figure 1(b). The like-doublet injectors (impinging points) are distributed in two rings. The first ring is located at $r = 10.3$ mm, while the second ring is located at $r = 19.4$ mm. 20 like-doublet injectors are uniformly distributed in the first ring every 18 degrees in the circumference direction, while 40 like-doublet injectors are uniformly distributed in the second ring every 9 degrees. The cooling injectors are located at $r = 23$ mm and distributed every 36 degrees. 30% of the fuel injected by the cooling injectors are used to cool the chamber wall. The mixture ratio of NTO to MMH (O/F ratio) is 1.65, and the total mass flow rate is 484.5 g/s. The initial temperature of MMH and NTO droplets is 300 K. The spray cone angle is 75 degrees. The injection velocities of MMH and NTO are 23.5 m/s and 28.5 m/s, respectively. The mean chamber pressure is 1.09 MPa. At the initial time, the chamber is filled with N_2, while the chamber pressure and chamber temperature are 1.09 MPa and 3000 K, respectively.

TABLE 1: The theoretical characteristic frequencies of the chamber.

Acoustic mode	1L	2L	1T
Frequency (Hz)	5280	10560	9773

The theoretical characteristic frequencies of the chamber can be estimated by simplifying the chamber as a cylinder with the same diameter and equivalent length, which equals the sum of the length of the cylindrical part and two-thirds of the contraction part of the chamber [5]. The detailed values are presented in Table 1. The sound speed is taken as 1020 m/s according to the NASA-CEA.

4.2. *The Hewitt Criterion.* The stability correlating parameter d_o/U_j had been successfully used to predict combustion instability in the combustor with impinging jet injectors. The Hewitt Stability Correlation shown as Figure 2 presented the stability margin with d_o/U_j. d_o is the injector's orifice diameter, while U_j is the velocity of the least volatile propellant. A reduction in d_o/U_j indicates a decreased stability margin. It can be concluded that when fd_o/U_j is less than 0.1, combustion instability may occur.

Hot fire tests for the small MMH/NTO thrust chamber shown as Figure 1 are conducted to study whether the Hewitt criterion is suitable for the combustor. The parameters of the combustor and injectors are the same as those in Section 4.1, while the mass flow rate and parameter of propellant droplets are different. The parameters $d_0/U_{o(f)}$ are controlled by adjusting velocities of fuel (oxidizer). Thus, different $d_0/U_{o(f)}$ and the mass flow rate of fuel (oxidizer) are obtained. Pressure oscillations are monitored at the head of the chamber. The stable and unstable cases are performed in Figure 3 with different d_o/U_j. It can be found that the Hewitt criterion is applicable to this combustor. When the parameter d_o/U_j is less than a determined value, combustion instability occurs.

Anderson et al. [42, 43] declared that an increase in d_o/U_j implied an increase in the mean droplet size. In the atomization test for like-doublet injectors with water, it can be concluded that the SMD of the droplets can be expressed as follows:

$$D_{32} = \frac{1.73\sigma^{0.25}}{\rho_p^{0.25}\rho^{0.1}} \times \frac{d_0}{U_j} \times (-10.14\sin\theta + 28.763), \quad (4)$$

where the parameter σ is surface tension and θ is the spray cone angle. The parameter ρ_p is the density of the droplet. The SMD is proportional to d_o/U_j. Thus, when the SMD is less than a determined value, combustion instability may occur.

According to the Hewitt criterion, the first longitudinal (1L) and the first tangential (1T) combustion instabilities would occur when d_o/U_j is less than 1e-5. It can be estimated that when d_o/U_j equals to 1e-5 according to Equation (4), the SMD is about 80 microns. Thus, the SMD of droplet sizes investigated for MMH and NTO are 30 μm, 60 μm, 80 μm,

100 μm, and 140 μm. The detailed cases are presented in Table 2.

4.3. *The Instability Phenomenon.* In the hot test, pressure oscillations are monitored at Point A (28 mm, 0 mm, and 2 mm), which is near the chamber sidewall and shown in Figure 1(b). This point is located at the antinode of 1T mode and 1L mode. The test condition is the same as the simulation condition in Section 4.1, while the mean diameter and distribution of droplets are unknown. The FFT analysis of pressure oscillations is shown in Figure 4. There are two peak frequencies 4800 Hz and 10780 Hz.

Pressure oscillations in Case 1-Case 5 monitored at the same position (Point A) with the hot test are presented in Figure 5, which give an indication of the trends of time histories of pressure oscillations in the chamber including any growth or decay. The pressure data over time slice 5 ms to 10 ms are taken as FFT analysis, which are performed in Figure 6. The resonant frequencies of pressure oscillations are obtained by FFT analysis. There are also two peak frequencies around 4800 Hz and 9800 Hz in Case 1-Case 3. Compared with theoretical acoustics frequencies of the chamber, these resonant frequencies in the hot test and simulation results can be identified. The peak frequency around 4800 Hz is identified as 1L mode, while the peak frequency around 9800 Hz is identified as 1T mode. It is shown that the acoustic modes excited in the numerical simulation are in agreement with those in the hot test, which indicates the numerical method can predict acoustic modes of excited pressure oscillations in this paper. There are obvious differences in the amplitudes of acoustic modes due to some differences in the numerical simulation and hot test. Firstly, the atomization process is neglected in the numerical simulation. Secondly, no every droplet can be traced due to the limit of computational resources. Droplet parcels are employed to represent the quantity of droplets with the same trajectory. Thirdly, a global one-step chemical reaction is used in the simulation, while it is multistep complicated chemical reactions in the hot test. Moreover, it is a challenge for accurate measurements under a high-pressure and high-temperature condition in the hot test. In this paper, it focuses on whether combustion instability is acoustic combustion instability (high-frequency combustion instability). Therefore, the acoustic modes of pressure oscillations and the frequencies of excited acoustic modes are compared in the validation. It is difficult to compare their amplitudes quantitatively.

There are several features to note in Figure 5. The value of pressure oscillations is less than 0 at the initial time, although the initial chamber pressures are set as the mean chamber pressure 1.09 MPa. Because there is a time lag between the time when the propellant enters into the chamber and the time when they are burned and release their chemical energy, the pressure will drop at the initial time, which is the first feature of pressure oscillations. Upon initial, pressure oscillations rise to 0.3 MPa due to autoignition in Case 1, which is higher than that in Case 2. However, pressure oscillations drop to lower values in Case 3-Case 5. The pressure firstly declines to a lower value and then rises to a higher value from
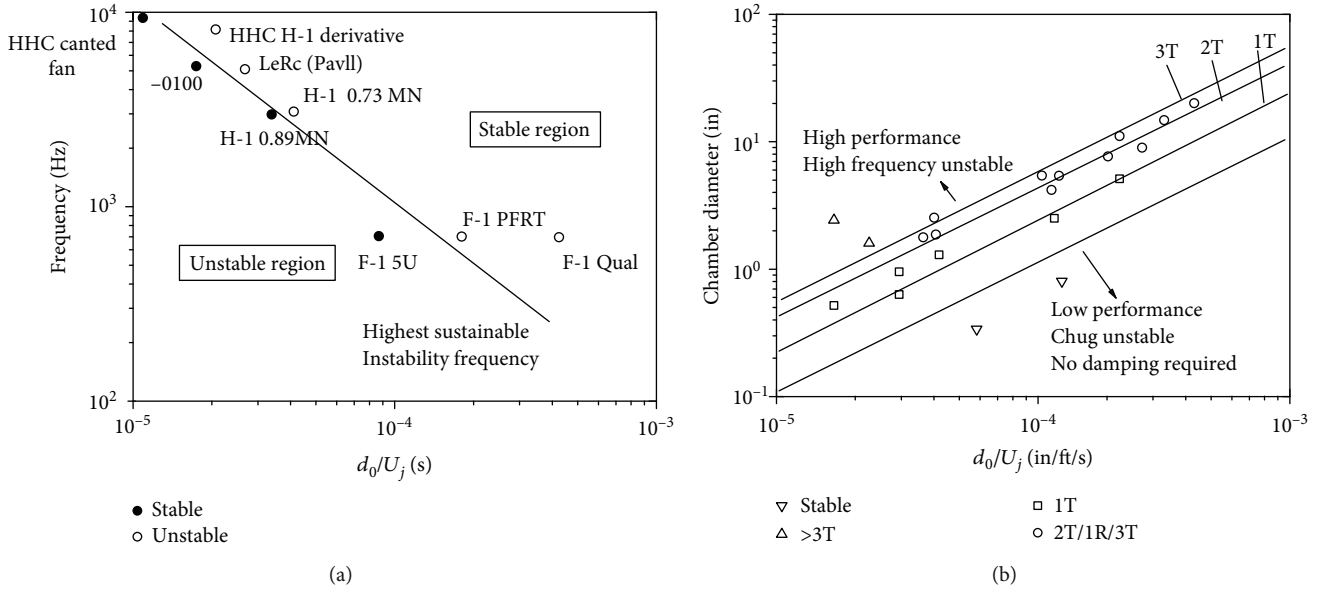
(a)

(b)

FIGURE 2: The Hewitt Stability Correlation [42]. (a) The eigenfrequency of the combustor. (b) Chamber diameter.
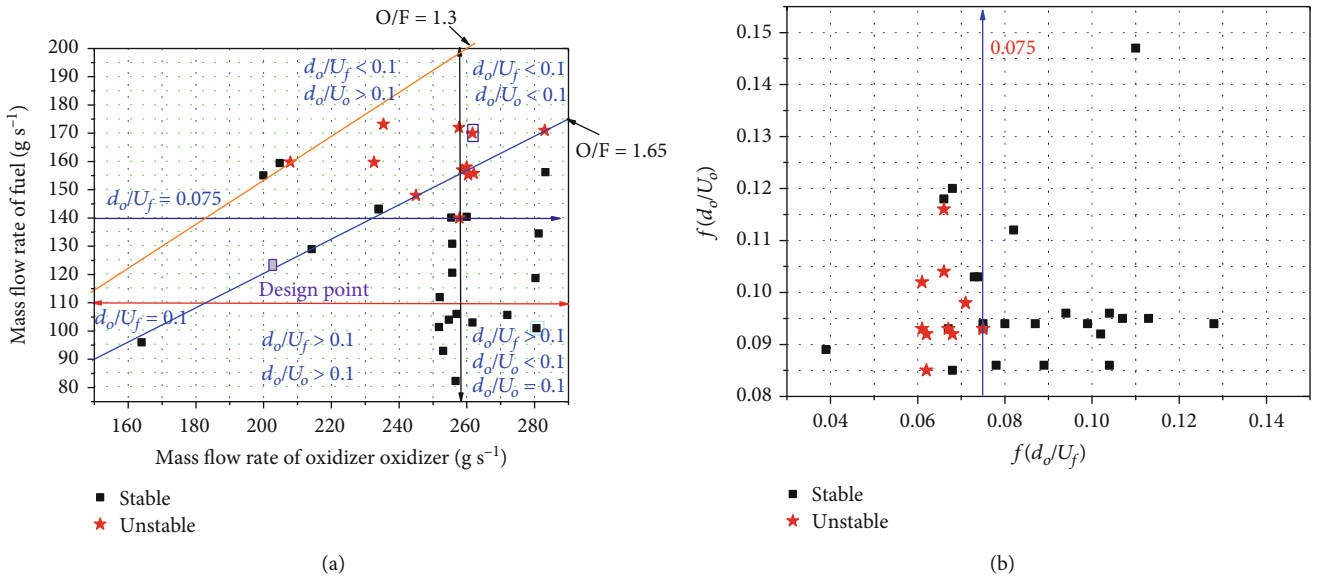

(a)

(b)

FIGURE 3: The stable and unstable cases in the hot tests. (a) Mass flow rate. (b) $f d_o / U_j$.

TABLE 2: The simulated cases.

Case	Case 1	Case 2	Case 3	Case 4	Case 5
SMD of droplet size (μm)	30	60	80	100	140

Case 3 to Case 5. Because the time lag becomes larger with the increase of the droplet size, it is important to note that pressure spikes due to the autoignition behavior may produce enough disturbances to trigger combustion instability. However, it is not a reason to induce combustion instability in this paper, because pressure oscillations decay and keep stable in Case 1 and Case 4, while high-amplitude pressure oscillations are excited in Case 2 and Case 3.

In Case 1, pressure oscillations decay within the amplitude of 10% of mean chamber pressure. The combustion is considered stable. For Case 2, the peak-to-peak amplitude of pressure oscillations steadies out approximately 0.7 MPa (64.2% of mean chamber pressure). Pressure waves are steep-fronted and not symmetric due to the nonlinear effect, which is the second feature of pressure oscillations. For Case 3, the peak-to-peak amplitude of pressure oscillations is 0.8 MPa (73.4% of mean chamber pressure). There exist many abrupt pressure spikes. For Case 4, pressure oscillations decline to -0.3 MPa at 0.5 ms and rise to 2.74 MPa at 1.75 ms. At 5.0 ms, pressure oscillations damp out to the steady mean chamber pressure. Thus, combustion instability is not triggered. In Case 5, the pressure drops to 0.55 MPa
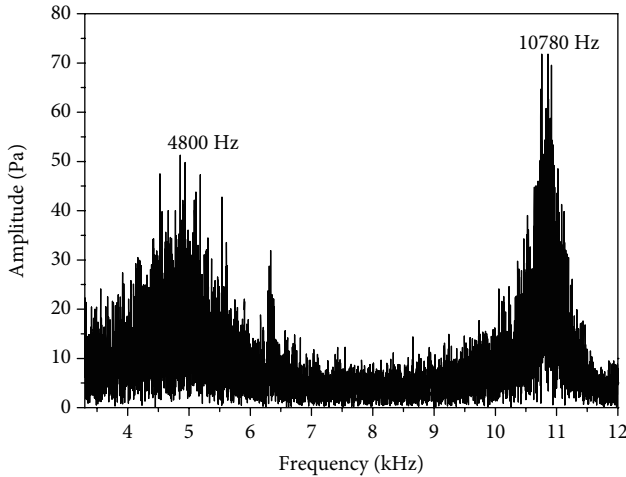
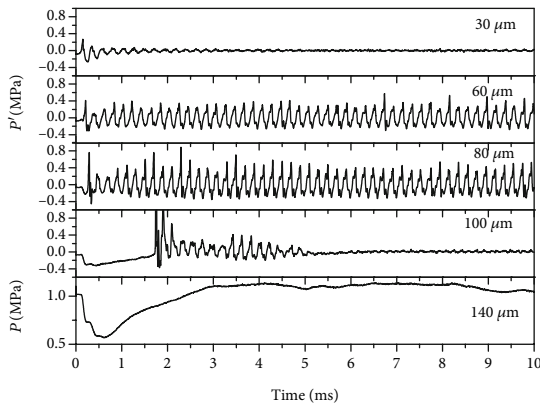Figure 4: FFT analysis of pressure oscillations in the hot test.

Figure 5: The time histories of pressure oscillations in Case 1-Case 5.

and then rises to 1.1 MPa at 3.0 ms. Mean chamber pressure varies slightly with time. There not exist high-amplitude pressure peaks. In Case 2 and Case 3, pressure oscillations are organized and periodic, which is the third feature of pressure oscillations. And the amplitudes are greater than 10% of mean chamber pressure. The 1T mode and 1L mode are excited. The amplitudes of 1L mode and 1T mode in Case 3 are the largest. Thus, combustion instability occurs in these two cases. Although the 1L mode and 1T mode are also excited in Case 1, the amplitudes of pressure oscillations are less than 10% of mean chamber pressure. Therefore, combustion instability is not excited in this case.

As the droplet size varies from 30 μm to 140 μm, combustion varies from stable to unstable, and to stable again. The 30 μm and 100 μm cases initially display high amplitude of pressure oscillations which damp over time and then keep stable. The 140 μm case displays no instability over 10 ms run time. There are obvious periodic high-amplitude pressure oscillations in 60 μm and 80 μm cases, and those in 80 μm are most violent. The amplitudes of pressure oscillations increase firstly and then decrease in the calculated range of droplet size. And the same trends are for the amplitude of 1L mode and 1T mode. Similar results were also provided by

Keenan et al. [48] and Kim et al. [49]. It indicates the results are reasonable in this paper. Keenan et al. [48] investigated the effects of 20 μm, 60 μm, 100 μm, and 140 μm droplet sizes of LOX and RP-1 on stability. The 20 μm and 60 μm displayed transverse instability, while the 100 microns initially displayed transverse instability but damped over time. The 140 microns showed no instability. Kim et al. [49] found that droplets on the order of 10 microns were stable to bombing, while 50-micron droplets were not stable. But the 100-micron droplets were stable to a simulated triggering mechanism.

4.4. Abrupt Pressure Spikes and Instability Mechanism. In order to reveal how combustion instability occurs, Case 2 is analyzed in detail. Figure 7 shows several instants of pressure contours of the chamber in Case 2, which perform the propagation of pressure waves in the chamber. The transverse sections are 2 mm, 4 mm, 6 mm, and 20 mm away from the injector face, respectively. The acoustic modes of oscillations can be revealed by the patterns of time evolution of pressure field. Small local high-pressure regions appear at the head of the chamber shown as Figure 7(a). Pressure waves propagate from a high-pressure region to a low-pressure region. In the transverse section, the center of the section becomes a low-pressure region, while the region near the sidewall becomes a high-pressure region shown in Figure 7(b). And the pressure at the right part is high than that at the left part, which is the typical pressure distribution of the 1T mode. Pressure waves reach the contraction section. The head region of the chamber becomes a low-pressure region, while the contraction section becomes a high-pressure region shown as Figure 7(c). Pressure waves are reflected and propagate to the head region of the chamber. And the head region of the chamber becomes a high-pressure region shown as Figure 7(d). It can be concluded that the 1L mode is excited. Therefore, the 1T mode and 1L mode are stimulated in Case 2, which indicates the identification of the peak frequencies of the FFT results is correct. Moreover, it is worth noting that small local high-pressure regions appear at the transverse sections 2 mm and 4 mm occasionally shown as Figures 7(a) and 7(d), where are at the downstream region just adjacent to impinging points, which may be the source of pressure oscillations.

In order to reveal how the small local high-pressure regions are formed, a monitored point named Point B is set there. Point B is at the location (10 mm, 0 mm, and 2 mm) shown as in Figure 1(b), where is the downstream region just adjacent to the first ring like-doublet injectors' impinging point. Point A is at the location (28 mm, 0 mm, and 2 mm), at the same transverse section with Point B, but near the sidewall. Figure 8 shows pressure oscillations at Point B are obviously stronger than those at Point A. The peak-to-peak amplitudes of pressure oscillations are approximately 1.7 MPa at Point B, but only 0.6 MPa at Point A. Furthermore, pressure peaks at Point B appear earlier than those at Point A shown as Figure 8(b). Pressure oscillations at Point A may result from the propagation of pressure waves produced at Point B. Pressure peaks at Point B may be the sources of pressure oscillations in the chamber.
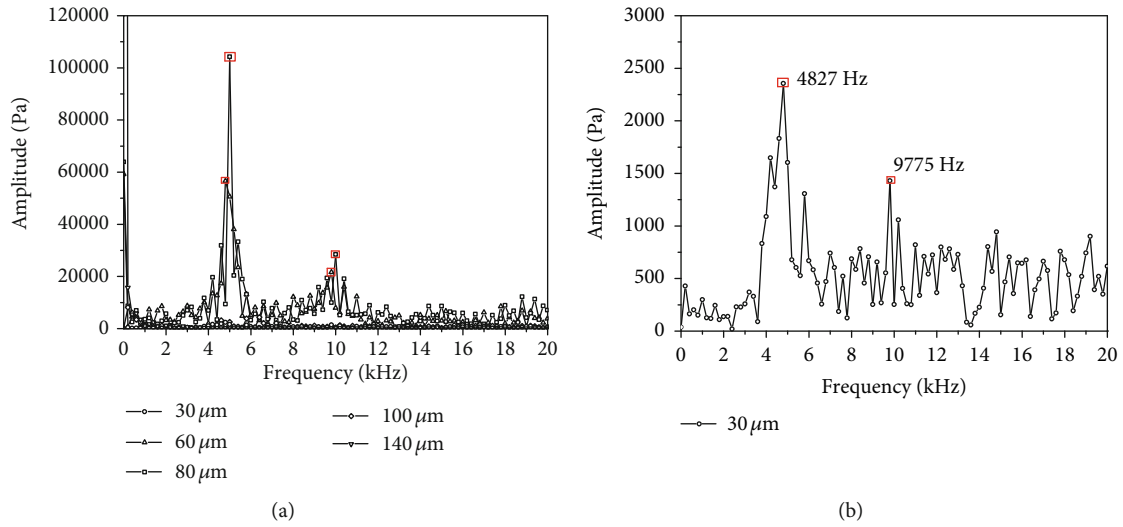
FIGURE 6: The FFT analysis of pressure oscillations in Case 1-Case 5. (a) FFT analysis in Case 1-Case 5. (b) FFT analysis in Case 1.
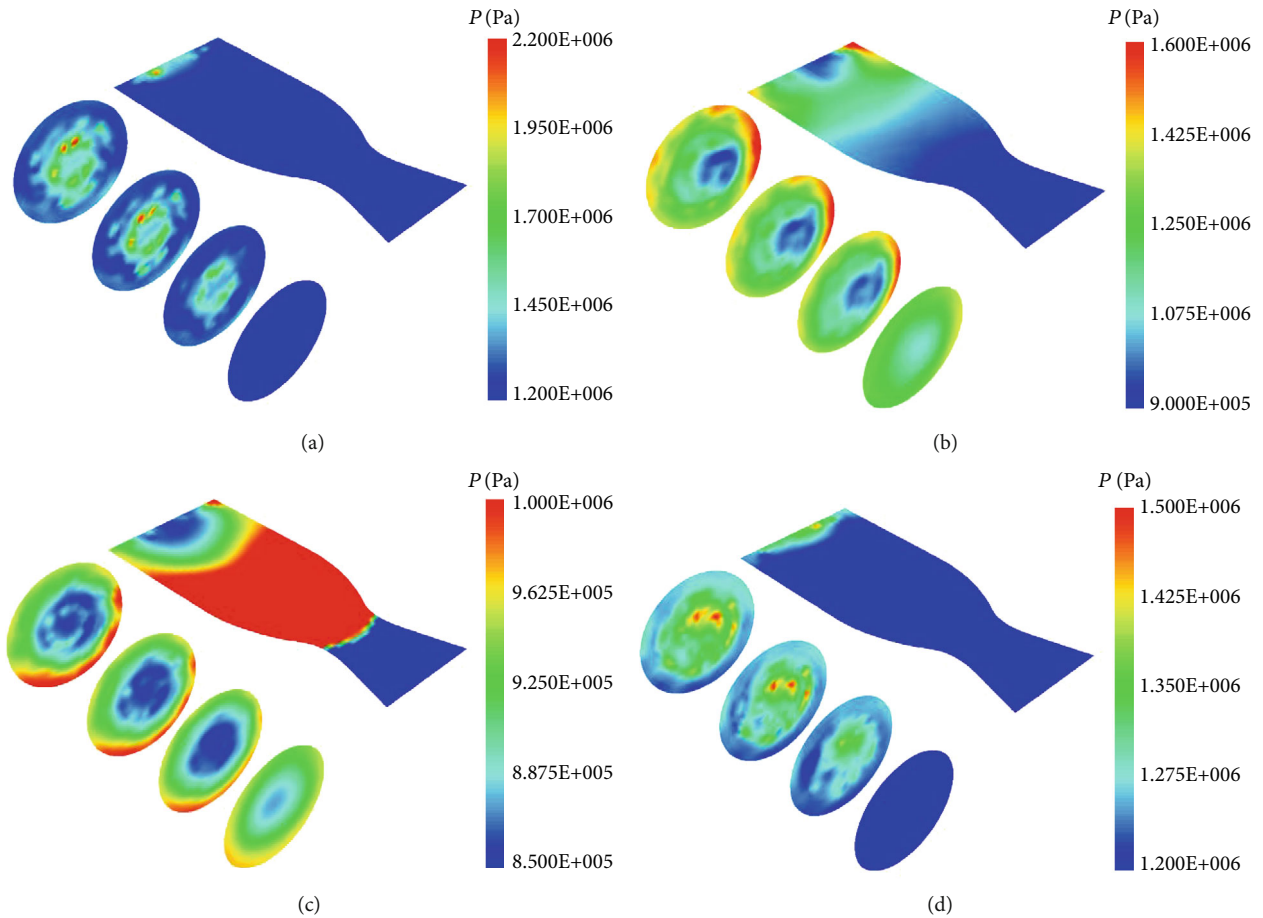
FIGURE 7: The time evolution of pressure contours in Case 2. (a) 6.70327 ms. (b) 6.73222 ms. (c) 6.78189 ms. (d) 6.90357 ms.

Then, the time histories of pressure oscillations of the surrounding points of Point B are observed. Figure 9 presents pressure oscillations from the time 8.320 ms to the time 8.360 ms, which give an indication of that where the pressure spike is induced. The back point is at the injector face, not presented. The amplitude of pressure oscillation at Point B is the highest. An abrupt pressure peak is observed in a period from $t_1 = 8.33830$ ms to $t_2 = 8.33906$ ms at Point B. The t_1 and t_2 are marked by squares in Figure 9. For the short interval $\Delta t = 0.76\,\mu$s, the pressure rises from 3.14 MPa to 4.58 MPa in this control volume. The pressure increase in the observed control volume is 1.44 MPa, and it is nearly

FIGURE 8: Pressure traces at Point A and Point B. (a) Pressure oscillations. (b) Pressure oscillations from 8 ms to 9 ms.

FIGURE 9: Pressure oscillations in the surrounding vertexes of a monitored point.

50% of the pressure at t_1, which indicates a pressure spike occurs. The pressure, temperature, density, density of MMH, evaporation amount of MMH, and combustion amount of MMH at the two instants in the Point B control volume and surrounding control volumes are shown in Table 3. The combustion amount of MMH at t_2 is the largest in the observed control volume B, whi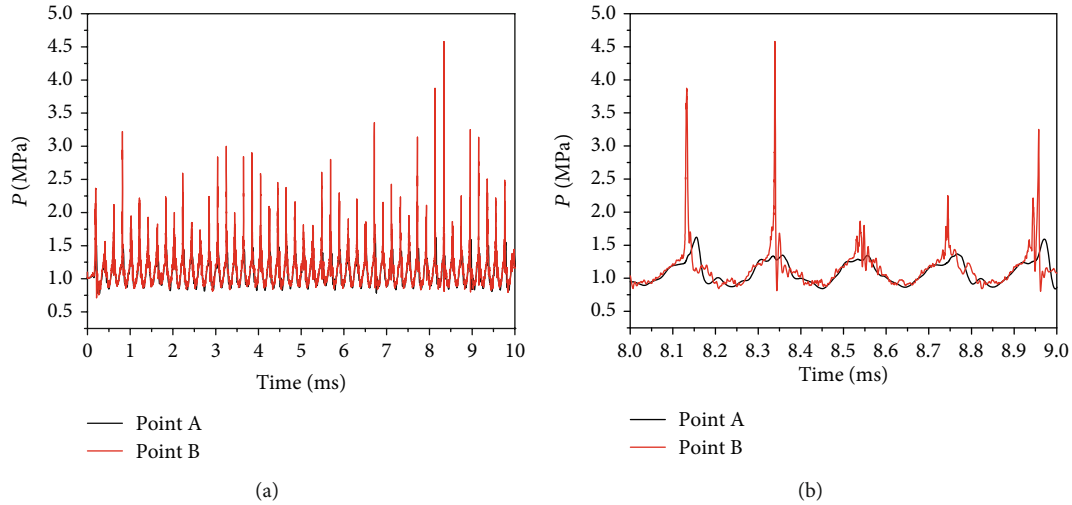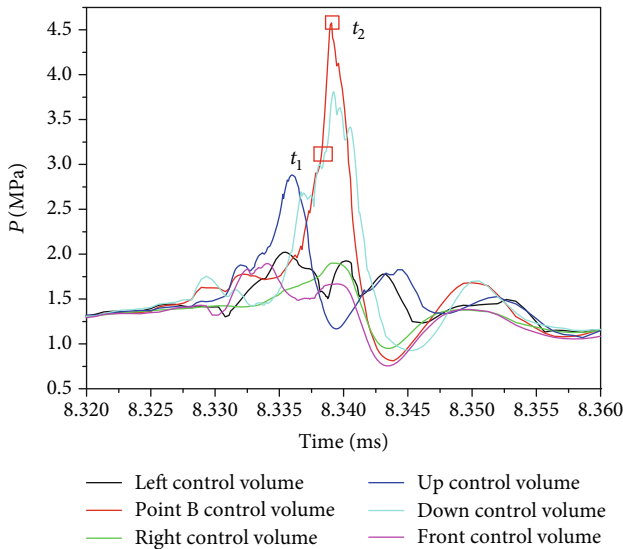le the evaporation amount of MMH at t_1 is the largest. This means violent combustion occurs from t_1 to t_2. In conclusion, the pressure peak at Point B in this period cannot result from the propagation of pressure waves of surrounding points. It may be caused by violent combustion.

The total heat release produced by a chemical reaction is 0.85 J, and the heat release rate is about $1.12e6$ w. The flow velocity in the control volume is 93 m/s. During the short interval, the corresponding propagation distance of fluid flow is 0.078 mm. Compared with the characteristic size of the

control volume 2 mm, convection fluxes with the surrounding vertexes can be neglected. The heat release due to combustion is consumed by the temperature rise of mixture, evaporation process, and two-phase interactions in the control volume. Base on the constant volume combustion theory, the temperature rise of the mixture in the control volume is 585 K, while that predicted by the numerical simulation is 538 K. In the theoretical calculation, the energy used for two-phase interactions is not considered. Thus, the temperature increase of the mixture is a little higher than that in the numerical simulation. The average molecular weight varies from 34.6 to 29.7. According to the constant volume combustion theory, the pressure at t_2 can be estimated. It is 4.47 MPa, which is comparable to the result of 4.58 MPa in the numerical simulation. The comparison of results obtained by constant-volume combustion theory and numerical simulation results is shown in Table 4. For the short interval $\Delta t = 0.76 \mu$s, the propagation distance of pressure waves is about 0.875 mm with sound speed 973 m/s. The pressure peaks cannot propagate to surrounding control volumes in this short interval. The density in the control volume is $4.93e$-3 g/cm^3 at t_1, while it is $5.14e$-3 g/cm^3 at t_2. Therefore, the density can be regarded unchanged, while the rise of pressure is proportional to the rise of temperature. The above analysis shows that quasiconstant volume combustion happens in a short period, which causes the abrupt rise of the pressure.

The consumed amount of MMH due to combustion is greater than the amount of MMH at t_1. Considering the propagation distance in this short interval, the fuel gas and oxidizer gas cannot flow from the surrounding control volumes. Thus, the evaporation amount has a great influence on combustion. Figure 10 shows the evaporation amount and consumed amount of MMH in the period from 8.335 ms to 8.345 ms. The abrupt enhancement of evaporation is followed by the enhancement of combustion. The abrupt rise of MMH consumed amount in the short interval means that violent combustion occurs. The time histories of mass fraction of fuel and oxidizer are given in Figure 11.

TABLE 3: Typical physical variables in the observed control volume and its surrounding control volumes in a time period Δt.

Control volume	t (ms)	P (MPa)	T (K)	ρ (g cm^{-3})	ρ_{MMH} (g cm^{-3})	evap$_{MMH}$ (g cm^{-3})	combustion$_{MMH}$ (g cm^{-3})
	$t_1 - \Delta t$	2.62	2755	3.85e-3	2.72e-4	3.22e-4	2.57e-4
Observed control volume B	t_1	3.14	2646	4.93e-3	4.83e-4	6.49e-4	3.60e-4
	t_2	4.58	3185	5.14e-3	1.32e-4	3.33e-4	6.08e-4
Left control volume	t_1	1.59	2631	2.18e-3	3.92e-4	2.41e-4	3.49e-5
	t_2	1.65	2509	2.74e-3	3.54e-4	1.12e-4	6.76e-5
Right control volume	t_1	1.78	3152	1.92e-3	1.58e-5	0	2.68e-5
	t_2	1.90	3219	1.96e-3	2.35e-6	0	3.72e-5
Up control volume	t_1	1.46	1715	4.29e-3	8.63e-4	1.54e-5	4.40e-5
	t_2	1.20	1514	4.41e-3	7.03e-4	4.88e-5	2.07e-5
Down control volume	t_1	2.96	2611	5.29e-3	4.49e-5	3.12e-4	2.80e-4
	t_2	3.71	2930	5.13e-3	1.25e-4	5.06e-4	4.08e-4
Front control volume	t_1	1.61	3074	1.92e-3	8.74e-6	1.60e-5	3.48e-5
	t_2	1.66	3057	2.01e-3	1.09e-6	0	2.48e-5

TABLE 4: The comparison of constant-volume combustion theory results and CFD simulation results.

	t_1	t_2 (constant-volume combustion theory)	t_2 (CFD simulation)
P (MPa)	3.14	4.47	4.58
T (K)	2646	3231	3185
ρ (g cm^{-3})	4.93e-3	4.93e-3	5.14e-3

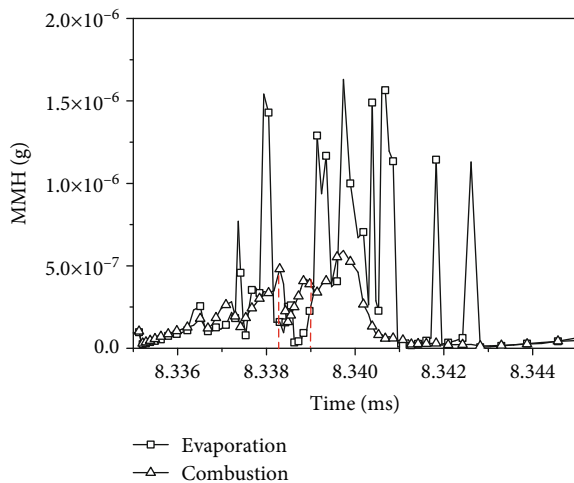FIGURE 11: The mass density of MMH and NTO.

FIGURE 10: The evaporation amount and consumed amount due to the combustion of MMH.

The oscillations of mass fraction of the oxidizer are in phase with those of mass fraction of the fuel. The mass fraction of fuel gas and oxidizer gas increases first from 8.335 ms to 8.338 ms. The enhancement of evaporation of fuel and oxidizer droplets leads to the accumulation of fuel and oxidizer gas. The mass fraction of fuel gas and oxidizer gas decreases sharply from 8.338 ms to 8.339 ms, which indicates that violent combustion occurs and the reactant gas is burned. Thus, violent combustion occurs in the period t_1 to t_2. Pressure waves cannot propagate to the surrounding control volumes in this short period, which leads to a high-amplitude increase of pressure, namely, pressure spikes.

These results are also supported by the work of Keenan et al. [48], Zhang et al. [44], Grenda et al. [50], and Daimon et al. [51], which indicates violent combustion (bombing) may occur in LRE. Keenan et al. [48] found that injecting the LOX and RP-1 droplets along the same vector in a given angel to mimic fan atomization may trigger self-excited instabilities, because the LOX and RP-1 droplets can interact more rapidly. Zhang et al. [44] found that quasiconstant volume combustion resulted in bombing, which induced self-excited combustion instability. Grenda et al. [50] found that the simulated bombing occurred when the droplets were

(a)

(b)

(c)

(d)

FIGURE 12: The time histories of pressure oscillations. (a) Slong line A. (b) Along line B. (c) Along line C. (d) Along line D.

on the order of 100 microns and 200 microns. Daimon et al. [51] investigated the explosion mechanism of hypergolic propellant and found that the instantaneous gasification of the propellant resulted in the explosion.
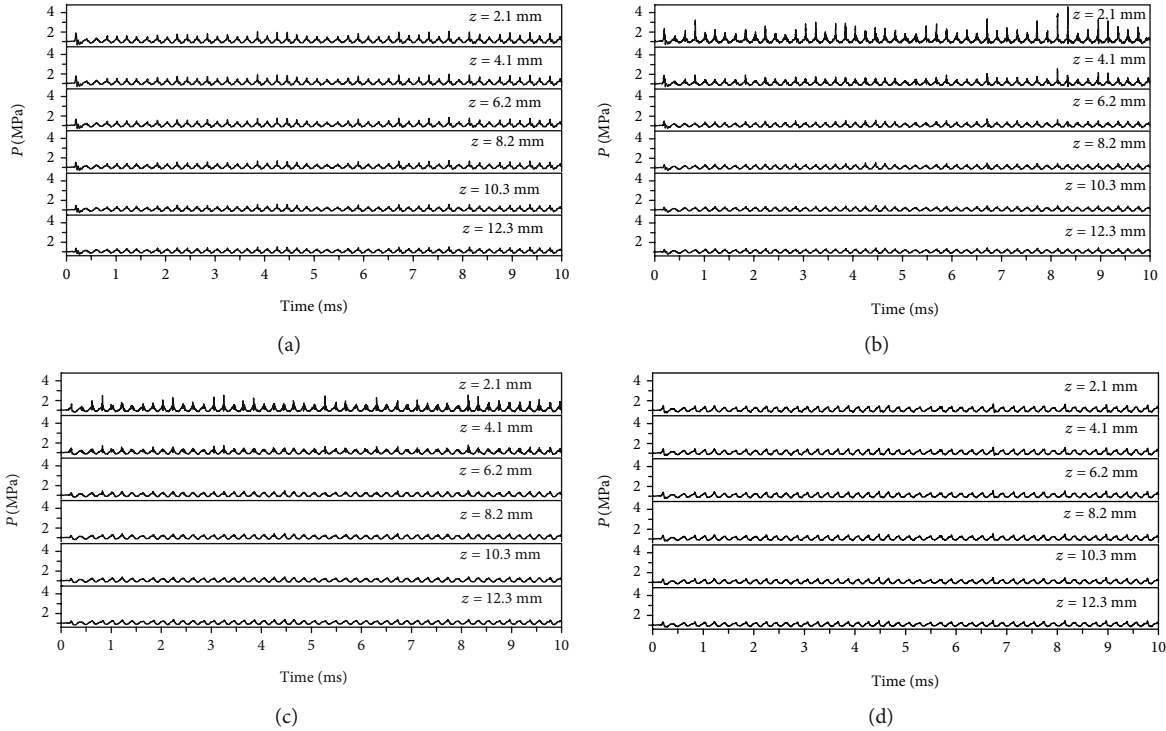
As Figure 7 shows, the local bombing phenomenon and abrupt pressure spikes appear in the chamber, mainly the downstream region just adjacent to the like-doublet injectors impinging points. Furthermore, the spatial and temporal distribution of pressure spikes is analyzed. Four lines A, B, C, and D parallel with the axis of the chamber are selected, which locate near the axis of the chamber, the inner like-doublet injector impinging points, the outer like-doublet injector impinging points, and the chamber sidewall, shown as red lines in Figure 1(b). The time histories of the pressure of six control volumes with space about 2 mm in the axial direction are presented in Figure 12. For spatial distribution, the pressure spikes mainly appear at line B and line C within 4.1 mm away from the injector face, where are the corresponding downstream regions just adjacent to the like-doublet injectors impinging point. The fuel and oxidizer droplets almost disappear at the head of the chamber in the 60-microns case. The combustion mainly occurs at the head of the chamber, where are the downstream region just adjacent to the impinging points. For temporal distribution, the pressure spikes come up frequently and stochastically over the 10 ms run time. Thus, pressure spikes occur at the downstream region just adjacent to the like-doublet injectors frequently and occasionally. The propagation and reflection of pressure waves would stimulate periodical pressure oscillations. And the characteristic frequencies of pressure oscillations are equal to the theoretical characteristic frequencies

of the chamber. Thus, combustion instability would be stimulated in the chamber.

4.5. Effects of Droplet Sizes on the Distribution of Abrupt Pressure Spikes. As shown in Section 4.3, the droplet size has a great influence on the amplitudes of pressure oscillations, which increase firstly and then decrease from $30 \, \mu m$ to $140 \, \mu m$. Self-excited combustion instabilities are stimulated in the cases with $60 \, \mu m$ and $80 \, \mu m$, while other cases are stable. In the detailed analysis of $60 \, \mu m$ case, it is found that quasiconstant volume combustion causing abrupt pressure spikes is the source to drive and sustain combustion instability. Therefore, the effects of droplet sizes on the distribution of abrupt pressure spikes are discussed in this section. Figures 13–17 show the acoustic pressure contours at two instants during 8 ms-10 ms in Case 1-Case 5, which provide an insight into the distribution of abrupt pressure spikes in the cases with different droplet sizes. The transverse sections are successively 2 mm, 4 mm, and 6 mm away from the injector face from left to right in Figures 13–17. The distribution of MMH and NTO droplets is shown in Figures 13(a)–17(a) and Figures 13(b)–17(b), respectively.

There are several features in these figures. Firstly, the MMH and NTO droplets are evaporated and disappear at the head of the chamber in Case 1-Case 3. The droplets go through the cylindrical part of the chamber in Case 4, while the droplets reach the throat of the thrust chamber in Case 5. As the droplet size increases, the distances the droplets go through are longer, because more time is needed to heat up the droplets and the evaporation rate is smaller with the increase of the droplet size.

FIGURE 13: The acoustic pressure contours in Case 1. (a) 8.26919 ms, MMH. (b) 9.43105 ms, NTO.

FIGURE 14: The acoustic pressure contours in Case 2. (a) 7.51051 ms, MMH. (b) 8.33989 ms, NTO.

FIGURE 15: The acoustic pressure contours in Case 3. (a) 8.32259 ms, MMH. (b) 9.72029 ms, NTO.

Furthermore, the pressure is almost uniform in the chamber in Case 1, Case 4, and Case 5, while there are large pressure gradients in Case 2 and Case 3. The pressure at the head of the chamber is obviously higher than that at the downstream region of the chamber, which implies that 1L mode combustion instability may occur. For transverse sec-

tions, there are small high-pressure regions (pressure spikes) in Figures 14 and 15, whose amplitudes are greater than 50% of mean chamber pressure. The pressure spikes mainly occur at the head of the chamber. They come up at the downstream region of the impinging points shown as the transverse section in Figures 14 and 15. Violent chemical reactions happen
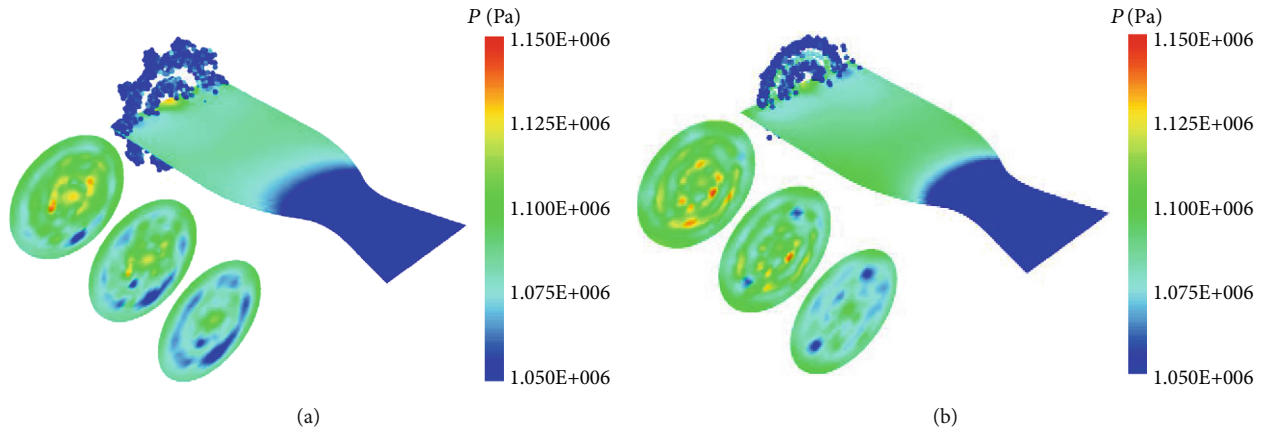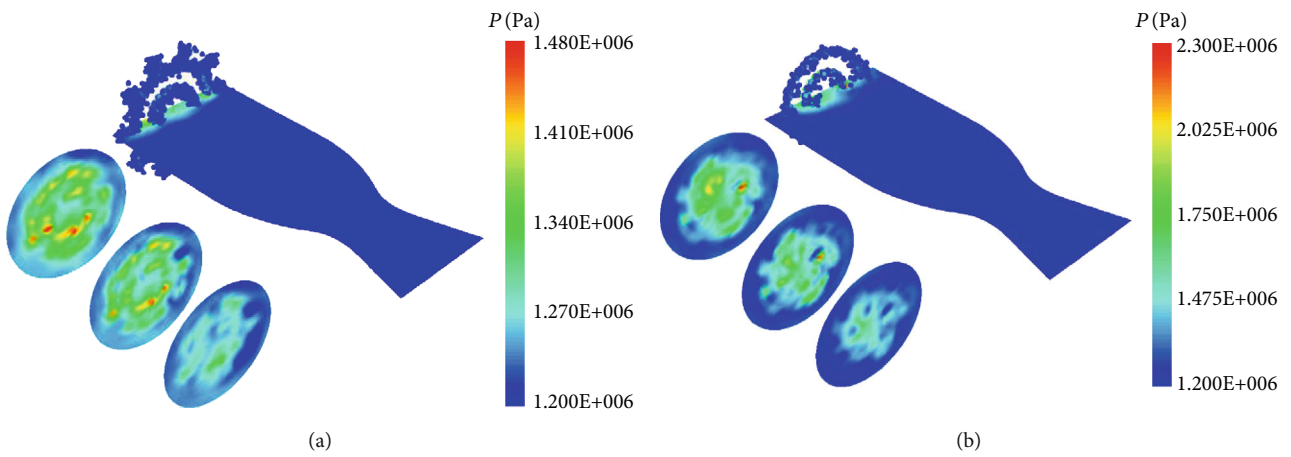
Figure 16: The acoustic pressure contours in Case 4. (a) 8.0647 ms, MMH. (b) 9.27406 ms, NTO.

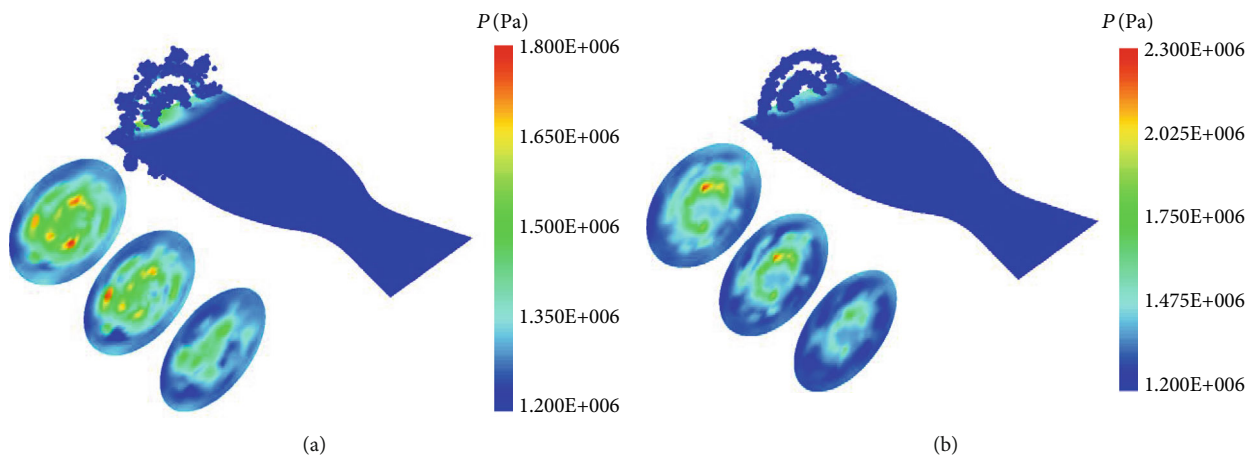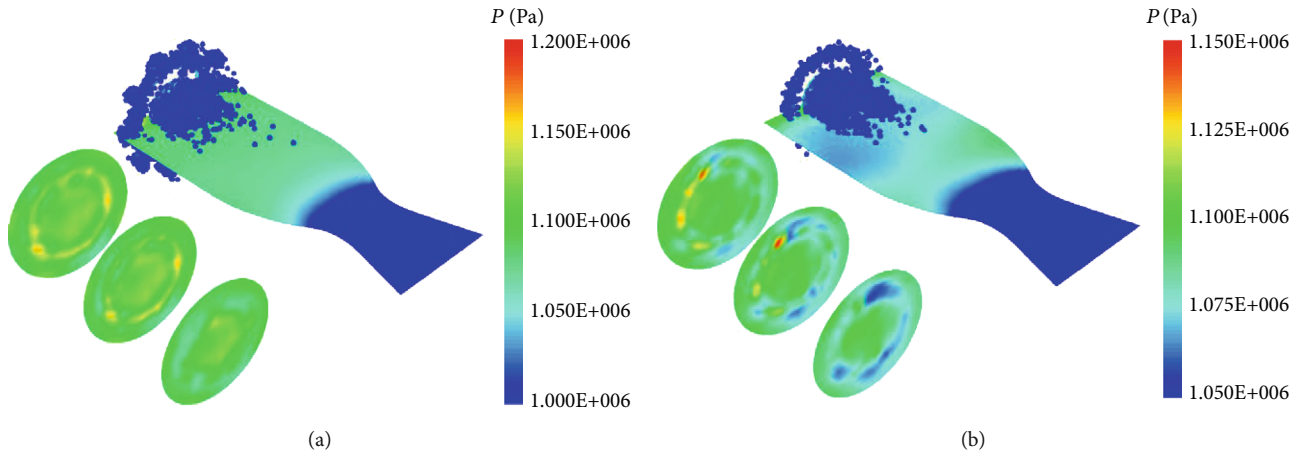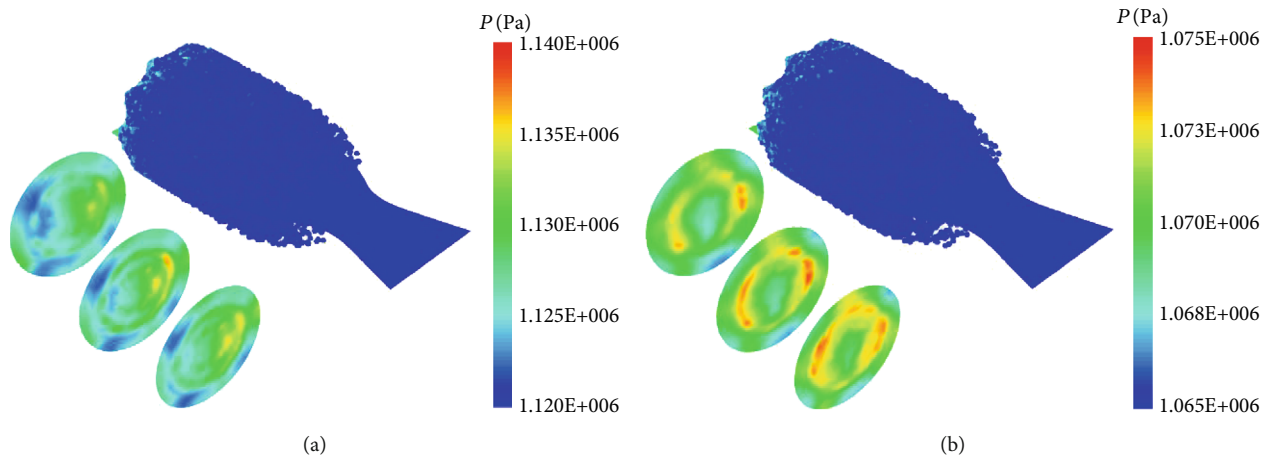Figure 17: The acoustic pressure contours in Case 5. (a) 8.19025 ms, MMH. (b) 8.84402 ms, NTO.

in these regions. For Case 1, the amplitudes of the red regions (high-pressure regions) are less than 10% of mean chamber pressure. It can be considered that there are not pressure spikes after the pressure spikes due to autoignition decay. There no exist obvious pressure spikes in Case 4. For Case 5, the pressure keeps stable without abrupt pressure spikes. The propellant droplets may go through the throat, which makes that mass flow rate of the throat section is not constant. Thus, mean chamber pressure changes slightly without strong pressure oscillations. Abrupt pressure spikes appear at the head of the chamber and combustion instabilities are induced with SMD $60\,\mu$m and $80\,\mu$m. When the SMD of droplets is too small or too large, abrupt pressure spikes are not observed and combustion is stable. It indicates combustion instabilities are involved with abrupt pressure spikes. And only when pressure spikes occur, combustion instabilities are excited. This conclusion is consistent with the instability mechanism. Pressure spikes may be the sources to drive and sustain combustion instability.

4.6. The Condition of the Formation of Abrupt Pressure Spikes. According to Section 4.5 in the results and discussions part, it can be known that combustion instabilities are related

to the occurrence of pressure spikes, which are sensitive to droplet sizes. In order to reveal how droplet sizes affect the occurrence of pressure spikes, the mass fraction of fuel and oxidizer gas at different radius with the distance of 2 mm away from the injection face is presented in Figures 18–22. The red lines represent the NTO mass fraction, while the black lines represent the MMH mass fraction. At $r = 6$ mm, the mass fraction of MMH is greater than that of NTO, while at $r = 10$ mm-18 mm, the mass fraction of NTO is greater. It is fuel rich for $r = 22$ mm, because the cooling injectors are located there and spray MMH. Moreover, the quantity of mass fraction peaks of MMH and NTO occurs at $r = 10$ mm and $r = 18$ mm, where are the downstream regions just adjacent to impinging points.

In Case 1, the oscillations of the mass fraction of MMH and NTO are not ordered with a small amplitude. For Case 2 and Case 3, the oscillations of mass fraction of MMH and NTO are organized and periodic especially at $r = 10$ mm, 18 mm, and 22 mm. From $r = 22$ mm, it can note that the frequencies of the mass fraction of MMH and NTO are both estimated as 5000 Hz by counting the number of peaks, about five, over 1 ms time slice. The oscillations of mass fraction of MMH are in phase with those of mass fraction of NTO.
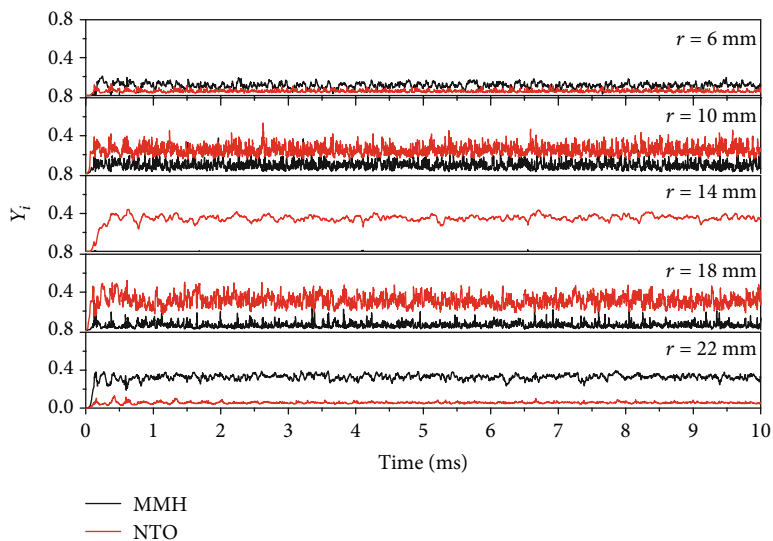
FIGURE 18: The time histories of mass fraction of MMH and NTO in Case 1.
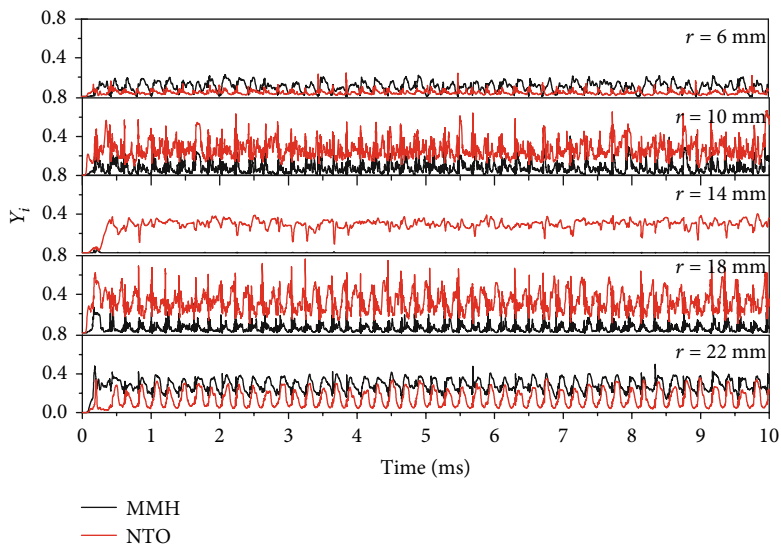

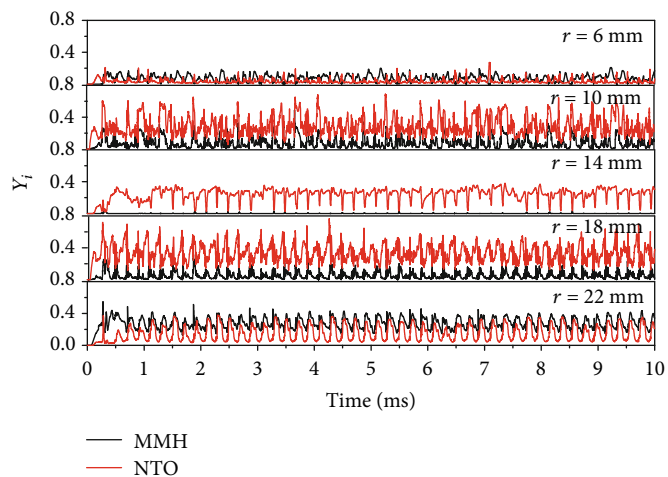FIGURE 19: The time histories of mass fraction of MMH and NTO in Case 2.

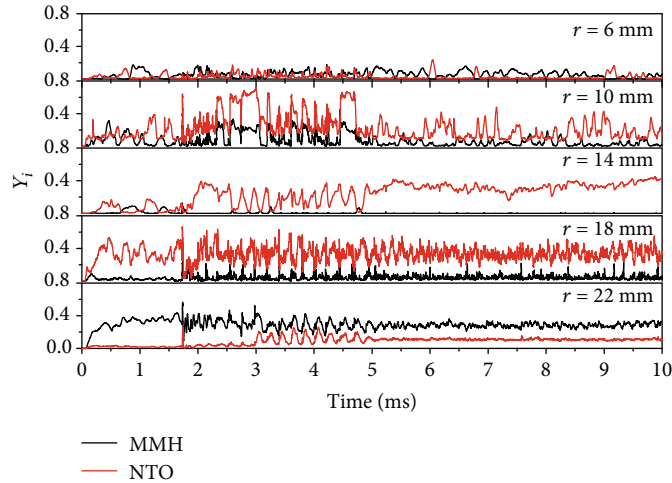FIGURE 20: The time histories of mass fraction of MMH and NTO in Case 3.

Figure 21: The time histories of mass fraction of MMH and NTO in Case 4.
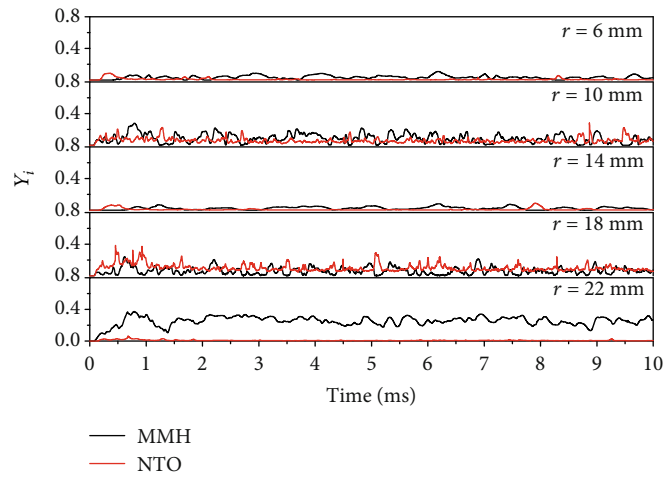
Figure 22: The time histories of mass fraction of MMH and NTO in Case 5.

Abrupt spikes arise at the time series of mass fraction of MMH accompanied with abrupt spikes at the time series of mass fraction of NTO. Thus, local premixtures are formed with a high density of reactant gas. Quasiconstant volume combustion happens there, which results in a high-amplitude rise of pressure. The abrupt pressure peaks arise frequently and stochastically. For Case 4, the oscillations of mass fraction of MMH and NTO are ordered over time slice 2 ms to 5 ms. Pressure oscillations over this time slice also display organized shown as in Figure 5. After 5 ms, the oscillations of mass fraction of MMH are out of phase with those of mass fraction of NTO. For Case 5, there no exist abrupt peaks in Figure 22. The mass fraction of MMH and NTO changes slowly with time.

Abrupt spikes occur in the mass fraction of MMH and NTO at the same time frequently and stochastically at the downstream regions just adjacent to impinging points. Local combustible mixtures are formed there, which lead to quasi-constant volume combustion and abrupt pressure peaks. Their propagation and reflection in the chamber wall may excite self-triggered combustion instability.

4.7. Effects of Droplet Sizes on Combustion Instability. In Case 1 to Case 3, abrupt pressure spikes come up more frequently with a higher amplitude, as the propellant droplet size increases. The evaporation of the droplets is faster with smaller diameters. The diffusion combustion is performed. The local mixed fuel and oxidizer gas are formed less frequently with smaller density. There are more abrupt peaks of the mass fraction of fuel and oxidizer with an increase in the droplet size in Case 1 to Case 3 shown in Figures 18–20. However, pressure spikes occur less frequently with a lower amplitude in Case 4. The vaporization of propellant droplets is slow because of large diameters. The peaks of the mass fraction of fuel and oxidizer occur less frequently. The mixture ratio O/F is large and it is hard to form local high-dense premixtures. No pressure spike exists after 5 ms. For Case 5, the fuel droplets appear at the throat part of thrust chamber. The densities of reactant gas are low at the head of the chamber, and local high-dense premixtures cannot be formed.

The trend is the same as the Hewitt Stability Correlation. A reduction in the droplet size of the range of 140 microns to

80 microns, indicating an increased tendency towards instability, implies a reduction in the stability parameter d_o/U_j in the Hewitt Stability Correlation. In the actual test, the mean droplet size is greater than 30 microns. The 30-microns droplet size case does not conclud in hot test.

The fuel and oxidizer droplets are injected along the same vector in a given angle, which result in that they are distributed in the chamber similarly. When the evaporation of fuel and oxidizer droplets is enhanced and mass fraction of fuel and oxidizer rise to a peak at the same time, local premixtures are formed easily with high density. This results in pressure spikes. The spikes in fuel and oxidizer mass fractions are formed by a combination of three factors of rapid evaporation, high density of droplets, and well mixing of fuel and oxidant. The droplet sizes determine the evaporation rate and number density of the propellant droplets, which further affect the formation of the local premixtures. When the droplet size is too small, the evaporation rate and initial number density are large. The fuel and oxidizer gas are burned out as soon as they are gasified from the fluid phase. And fuel and oxidant do not mix very well for a short existing time of fuel droplet and oxidant droplet. Therefore, the abrupt peaks of mass fraction of reactant gas would not exist. It is difficult to form high-dense premixture. When the droplet size is too large, the evaporation rate and initial number density are small and mass fraction of reactant gas will not vary greatly. It is also difficult to form high-dense premixture. Only when the droplet size is in a definite range, the abrupt peaks of mass fraction of reactant gas will occur stochastically and frequently at the same time. And it is easy to form high-dense premixture, which results in quasiconstant volume combustion and pressure spikes.

5. Conclusions

Combustion instabilities in a small MMH/NTO LRE are investigated numerically in this paper. A three-dimensional two-phase reaction turbulent flow is predicted by the Eulerian-Lagrangian method, in which the URANS equations are for the gas-phase flow and the DDM are for the trajectories of droplets. The two-phase interactions are modeled by the mass, momentum, and energy source terms in the gas-phase equations. The droplets are injected with given velocities and SMD at the determined positions. The 30 μm, 60 μm, 80 μm, 100 μm, and 140 μm cases are calculated.

As the droplet size increases from 30 microns to 140 microns, peak-to-peak pressure oscillations increase firstly and then decrease. Pressure oscillations are the strongest in 80-micron case. The amplitude and FFT analysis of pressure oscillations show that the 1L and 1T mode self-excited combustion instabilities occur in 60-micron and 80-micron cases. This shows when the droplet size is less than a value in a determined range, combustion instability would occur. This trend is the same as the Hewitt Stability Correction. But if the droplet size is too small such as 30 microns, pressure oscillations would decay and combustion keeps stable.

Further analysis shows that abrupt peaks occur in the mass fraction of MMH and NTO frequently at the downstream region just adjacent to impinging points. The oscillations of mass fraction of MMH are in phase with those of NTO, which are organized and periodic. The local combustible mixtures are formed, and violent combustion arises. The chemical reaction is faster than pressure expansion. Thus, quasiconstant volume combustion and abrupt pressure spikes are induced, which are the sources of pressure oscillations. The propagation and reflection of pressure waves in the chamber stimulate combustion instability. The droplet size affects the mass fraction of MMH and NTO by evaporation rate and initial number density. When the droplet size is too small, the fuel and oxidizer gas are consumed as soon as they are transformed from the fluid phase because of fast evaporation. Local high-dense combustible premixture is hard to be formed. When the droplet size is too large, the evaporation rate is small and there are less abrupt peaks in the mass density of fuel and oxidizer. Local bombing phenomenon appears frequently within a definite range of droplet size.

This study shows where the initial disturbances that induced combustion instability are from and how combustion instabilities are triggered. Furthermore, it reveals that propellant droplet sizes have a great influence on combustion instability and provide guidelines on the atomization of propellant.

Data Availability

The data used to support the findings of this study are available from the corresponding author upon request.

Conflicts of Interest

The authors declare that they have no conflicts of interest.

Acknowledgments

References

[1] D. T. Harrje and F. H. Reardon, *Liquid propellant rocket combustion instability*, NASA, Washington, DC, 1972.

[2] V. Yang and W. E. Anderson, *Liquid Rocket Engine Combustion Instability*, AIAA, Washington, DC, 1995.

[3] F. Richecoeur, P. Scouflaire, S. Ducruix, and S. Candel, "High-Frequency transverse acoustic coupling in a multiple-injector cryogenic combustor," *Journal of Propulsion and Power*, vol. 22, no. 4, pp. 790–799, 2006.

[4] K. Miller, J. Sisco, N. Nugent, and W. Anderson, "Combustion instability with a single-element swirl injector," *Journal of Propulsion and Power*, vol. 23, no. 5, pp. 1102–1112, 2007.

[5] B. Pomeroy and W. Anderson, "Transverse instability studies in a subscale chamber," *Journal of Propulsion and Power*, vol. 32, no. 4, pp. 939–947, 2016.

[6] C. Ruan, F. Chen, W. Cai, Y. Qian, L. Yu, and X. Lu, "Principles of non-intrusive diagnostic techniques and their applications for fundamental studies of combustion instabilities in gas turbine combustors: A brief review," *Aerospace Science and Technology*, vol. 84, pp. 585–603, 2019.

[7] A. P. Dowling and S. R. Stow, "Acoustic analysis of gas turbine combustors," *Journal of Propulsion and Power*, vol. 19, no. 5, pp. 751–764, 2003.

[8] J. Portillo, J. Sisco, Y. Yu, V. Sankaran, and W. Anderson, "Application of a generalized instability model to a longitudinal mode combustion instability," in *43rd AIAA/ASME/SAE/ASEE Joint Propulsion Conference & Exhibit*, Cincinnati, OH, 2007, July.

[9] W. A. Sirignano and P. P. Popov, "Two-dimensional model for liquid-rocket transverse combustion instability," *AIAA Journal*, vol. 51, no. 12, pp. 2919–2934, 2013.

[10] M. Sliphorst, S. Gröning, and M. Oschwald, "Theoretical and experimental identification of acoustic spinning mode in a cylindrical combustor," *Journal of Propulsion and Power*, vol. 27, no. 1, pp. 182–189, 2011.

[11] S. K. Kim, D. Kim, and D. J. Cha, "Finite element analysis of self-excited instabilities in a lean premixed gas turbine combustor," *International Journal of Heat and Mass Transfer*, vol. 120, pp. 350–360, 2018.

[12] Y. C. Yu, J. C. Sisco, V. Sankaran, and W. E. Anderson, "Effects of mean flow, entropy waves, and boundary conditions on longitudinal combustion instability," *Combustion Science and Technology*, vol. 182, no. 7, pp. 739–776, 2010.

[13] R. Smith, M. Ellis, G. Xia, V. Sankaran, W. Anderson, and C. L. Merkle, "Computational investigation of acoustics and instabilities in a longitudinal-mode rocket combustor," *AIAA Journal*, vol. 46, no. 11, pp. 2659–2673, 2008.

[14] X. Han, J. Li, and A. S. Morgans, "Prediction of combustion instability limit cycle oscillations by combining flame describing function simulations with a thermoacoustic network model," *Combustion and Flame*, vol. 162, no. 10, pp. 3632–3647, 2015.

[15] J. Li, Y. Xia, A. S. Morgans, and X. Han, "Numerical prediction of combustion instability limit cycle oscillations for a combustor with a long flame," *Combustion and Flame*, vol. 185, pp. 28–43, 2017.

[16] R. Garby, L. Selle, and T. Poinsot, "Simulation aux grandes echelles des instabilites de combustion dans un bruleur de longueur variable," *Comptes Rendus Mécanique*, vol. 341, no. 1-2, pp. 220–229, 2013.

[17] S. Matsuyama, J. Shinjo, S. Ogawa, and Y. Mizobuchi, "LES of high-frequency combustion instability in a single element rocket combustor," in *50th AIAA Aerospace Sciences Meeting including the New Horizons Forum and Aerospace Exposition*, p. 1271, Nashville, Tennessee, January 2012.

[18] S. Matsuyama, J. Shinjo, and Y. Mizobuchi, "LES of high-frequency combustion instability in a rocket combustor," in *51st AIAA Aerospace Sciences Meeting including the New Horizons Forum and Aerospace Exposition*, p. 0564, Grapevine (Dallas/Ft. Worth Region), Texas, January 2013.

[19] S. Srinivasan, R. Ranjan, and S. Menon, "Flame dynamics during combustion instability in a high-pressure, shear-coaxial injector combustor," *Flow, Turbulence and Combustion*, vol. 94, no. 1, pp. 237–262, 2015.

[20] C. Umphrey, M. E. Harvazinski, S. A. Schumaker, and V. Sankaran, "Large-eddy simulation of single-element gas-centered swirl-coaxial injectors for combustion stability prediction," in *53rd AIAA/SAE/ASEE Joint Propulsion Conference* p. 4698, Jul 2017.

[21] C. Kraus, L. Selle, and T. Poinsot, "Coupling heat transfer and large eddy simulation for combustion instability prediction in a swirl burner," *Combustion and Flame*, vol. 191, pp. 239–251, 2018.

[22] M. E. Harvazinski, W. E. Anderson, and C. L. Merkle, "Analysis of self-excited combustion instabilities using two- and three-dimensional simulations," *Journal of Propulsion and Power*, vol. 29, no. 2, pp. 396–409, 2013.

[23] M. E. Harvazinski, C. Huang, V. Sankaran et al., "Coupling between hydrodynamics, acoustics, and heat release in a self-excited unstable combustor," *Physics of Fluids*, vol. 27, no. 4, pp. 045102–045127, 2015.

[24] T. M. Nguyen, P. P. Popov, and W. A. Sirignano, "Longitudinal combustion instability in a rocket engine with a single coaxial injector," *Journal of Propulsion and Power*, vol. 34, no. 2, pp. 354–373, 2018.

[25] M. J. Nusca, "Utility of computational modeling for the study of combustion instability in small MMH-NTO liquid rocket engines," in *43rd AIAA/ASME/SAE/ASEE Joint Propulsion Conference & Exhibit*, p. 5562, Cincinnati, OH, July 2007.

[26] L. B. Zhang, M. Chu, and X. Xu, "Performance prediction of apogee attitude and orbit control thruster for MMH/NTO hypergolic bipropellant," in *50th AIAA/ASME/SAE/ASEE Joint Propulsion Conference*, p. 3572, Cleveland, OH, July 2014.

[27] M. Habiballah, D. Lourme, and F. Pit, "PHEDRE - Numerical model for combustion stability studies applied to the Ariane Viking engine," *Journal of Propulsion and Power*, vol. 7, no. 3, pp. 322–329, 1991.

[28] O. Knab, D. Preclik, and D. Estublier, "Flow field prediction within liquid film cooled combustion chambers of storable bi-propellant rocket engines," in *34th AIAA/ASME/SAE/ASEE Joint Propulsion Conference and Exhibit*, p. 3370, Cleveland,OH,U.S.A., July 1998.

[29] F. Zhuang, W. Nie, and Q. Zou, "Numerical simulation of MMH/NTO rocket engine combustion instability.," in *35th Joint Propulsion Conference and Exhibit*, p. 2779, Los Angeles,CA,U.S.A., June 1999.

[30] P. Tucker, S. Menon, C. Merkle, J. Oefelein, and V. Yang, "An approach to improved credibility of CFD simulations for rocket injector design," in *43rd AIAA/ASME/SAE/ASEE Joint Propulsion Conference & Exhibit*, p. 5572, Cincinnati, OH, July 2007.

[31] P. Tucker, S. Menon, C. Merkle, J. Oefelein, and V. Yang, "Validation of high-fidelity CFD simulations for rocket injector design," in *44th AIAA/ASME/SAE/ASEE Joint Propulsion Conference & Exhibit*, p. 5226, Hartford,CT, July 2008.

[32] R. Smith, G. Xia, W. A. Anderson, and C. L. Merkle, "Computational simulations of the Effect of backstep height on nonpremixed combustion instability," *AIAA Journal*, vol. 48, no. 9, pp. 1857–1868, 2010.

[33] M. L. Frezzotti, F. Nasuti, C. Huang, C. L. Merkle, and W. E. Anderson, "Quasi-1D modeling of heat release for the study of longitudinal combustion instability," *Aerospace Science and Technology*, vol. 75, pp. 261–270, 2018.

[34] J. Rayleigh, "The explanation of certain acoustical phenomena[1]," *Nature*, vol. 18, no. 455, pp. 319–321, 1878.

[35] V. G. Bazarov and V. Yang, "Liquid-propellant rocket engine injector dynamics," *Journal of Propulsion and Power*, vol. 14, no. 5, pp. 797–806, 1998.

[36] S. Gröning, J. S. Hardi, D. Suslov, and M. Oschwald, "Injector-driven combustion instabilities in a hydrogen/oxygen rocket combustor," *Journal of Propulsion and Power*, vol. 32, no. 3, pp. 560–573, 2016.

[37] A. Urbano, L. Selle, G. Staffelbach et al., "Exploration of combustion instability triggering using large eddy simulation of a multiple injector liquid rocket engine," *Combustion and Flame*, vol. 169, pp. 129–140, 2016.

[38] W. Armbruster, J. S. Hardi, D. Suslov, and M. Oschwald, "Experimental investigation of self-excited combustion instabilities with injection coupling in a cryogenic rocket combustor," *Acta Astronautica*, vol. 151, pp. 655–667, 2018.

[39] A. Duvvur, C. H. Chiang, and W. A. Sirignano, "Oscillatory fuel droplet vaporization-driving mechanism for combustion instability," *Journal of Propulsion and Power*, vol. 12, no. 2, pp. 358–365, 1996.

[40] W. A. Sirignano and G. Wu, "Multicomponent-liquid-fuel vaporization with complex configuration," *International Journal of Heat and Mass Transfer*, vol. 51, no. 19-20, pp. 4759–4774, 2008.

[41] S. Lei and A. Turan, "Chaotic modelling and control of combustion instabilities due to vaporization," *International Journal of Heat and Mass Transfer*, vol. 53, no. 21–22, pp. 4482–4494, 2010.

[42] W. E. Anderson, H. M. Ryan, and R. J. Santoro, "Combustion instability mechanisms in liquid rocket engines using impinging jet injectors," in *1st Joint Propulsion Conference and Exhibit*, p. 2357, San Diego,CA,U.S.A., July 1995.

[43] W. E. Anderson, K. L. Miller, H. M. Ryan, S. Pal, R. J. Santoro, and J. L. Dressler, "Effects of periodic atomization on combustion instability in liquid-fueled propulsion systems," *Journal of Propulsion and Power*, vol. 14, no. 5, pp. 818–825, 1998.

[44] H. Q. Zhang, Y. J. Ga, B. Wang, and X. L. Wang, "Analysis of combustion instability via constant volume combustion in a LOX/RP-1 bipropellant liquid rocket engine," *Science China Technological Sciences*, vol. 55, no. 4, pp. 1066–1077, 2012.

[45] W. S. Nie and S. J. Feng, *Chemical Kinetics Model and Numerical Simulation of Liquid Rocket Engine*, National Defense Industry Press, Beijing, 2011.

[46] C. W. Hirt, A. A. Amsden, and J. L. Cook, "An arbitrary Lagrangian-Eulerian computing method for all flow speeds," *Journal of Computational Physics*, vol. 135, no. 2, pp. 203–216, 1997.

[47] T. S. Wang and Y. S. Chen, "Unified Navier-Stokes flowfield and performance analysis of liquid rocket engines," *Journal of Propulsion and Power*, vol. 9, no. 5, pp. 678–685, 1993.

[48] J. A. Keenan, M. Z. Pindera, and M. G. Giridharan, *Simulation of spray combustion instability in liquid rocket engines*, AIAA Paper, 1997.

[49] Y. Kim, C. Chen, J. Ziebarth, and Y. CHEN, "Prediction of high frequency combustion instability in liquid propellant rocket engines," in *28th Joint Propulsion Conference and Exhibit*, p. 3763, Nashville,TN,U.S.A., July 1992.

[50] J. M. Grenda, S. Venkateswaran, and C. L. Merkle, "Mutidimensional analysis of combustion instabilities in liquid rocket motors," in *8th Joint Propulsion Conference and Exhibit*, p. 3764, Nashville,TN,U.S.A., July 1992.

[51] W. Daimon, Y. Gotoh, and I. Kimura, "Mechanism of explosion induced by contact of hypergolic Liquids," *Journal of Propulsion and Power*, vol. 7, no. 6, pp. 946–952, 1991.

Research Article

Comprehensive Performance Analysis for the Rotating Detonation-Based Turboshaft Engine

Zifei Ji,[1,2] **Ruize Duan,**[1] **Renshuai Zhang,**[1] **Huiqiang Zhang,**[1] **and Bing Wang** ⓘ[1]

[1]*School of Aerospace Engineering, Tsinghua University, Beijing 100084, China*
[2]*Shenyang Engine Research Institute, Aero Engine Corporation of China, Shenyang 110015, China*

Correspondence should be addressed to Bing Wang; wbing@tsinghua.edu.cn

Academic Editor: Wei Lin

The potential advantages of rotating detonation combustion are gradually approved, and it is becoming a stable and controllable energy conversion way adopted to the propulsion devices or ground-engines. This study focuses on the rotating detonation-based turboshaft engine, and the architecture is presented for this form of engine with compatibility between the turbomachinery and rotating detonation combustor being realized. The parametric performance simulation model for the rotating detonation-based turboshaft engine are developed. Further, the potential performance benefits as well as their generation mechanism are revealed, based on the comprehensive performance analysis of the rotating detonation-based turboshaft engine. Comparisons between the rotating detonation turboshaft engine and the conventional one reveal that the former holds significant improvements in specific power, thermal efficiency, and specific fuel consumption at lower compressor pressure ratios, and these improvements decrease with the increase of compressor pressure ratio and increase as turbine inlet temperature increases. The critical compressor pressure ratio corresponding to the disappearance of specific power improvement is higher than that corresponding to the disappearance of thermal efficiency and specific fuel consumption. These critical compressor pressure ratios are positively correlated with flight altitude and negatively correlated with flight velocity. The conductive research conclusion is guidable for the design and engineering application of rotating detonation-based engines.

1. Introduction

The helicopters have promising development and application foreground in both military and civil fields, owing to their superior performance operating at low altitude, low velocity, and maneuvering flight conditions. The turboshaft engine is the unique powerplant for the helicopter; therefore, advanced technologies for turboshaft engines have attracted significant interest in both academia and industry. The regenerative cycle and variable capacity technologies have the potential for improving the overall performance of the turboshaft engine, but the low technical maturity and poor technical versatility currently may be unacceptable. The turboshaft engine with simple cycle is still the first choice of advanced technology programs at present [1, 2].

For the conventional turboshaft with simple cycle, the key to enhancing the overall performance is to improve the total pressure ratio and temperature ratio [3]. After several

decades of developments, the performance improvement of conventional turboshaft engine has entered a bottleneck period, as shown in Figure 1 [2]. Pressure-gain combustion is a prospective technology for the further performance improvement of the turboshaft with simple cycle [4]. Rotating detonation is a form of pressure-gain combustion, and it holds many potential advantages, such as high intensity of reaction, high thermal efficiency, and low entropy increase [5–7], which are helpful to improve the thrust and fuel consumption performance and reduce the structural weight. In the past decades, numerous studies relating to the ignition and detonation initiation performance, the operating diagram, and the unstable modes and their generation mechanism of the rotating detonation combustor (RDC) are experimentally performed, and the detailed flowfield structure and cellular structure information are revealed by multidimensional numerical methods [8–12]. The above studies have made the rotating detonation technology being
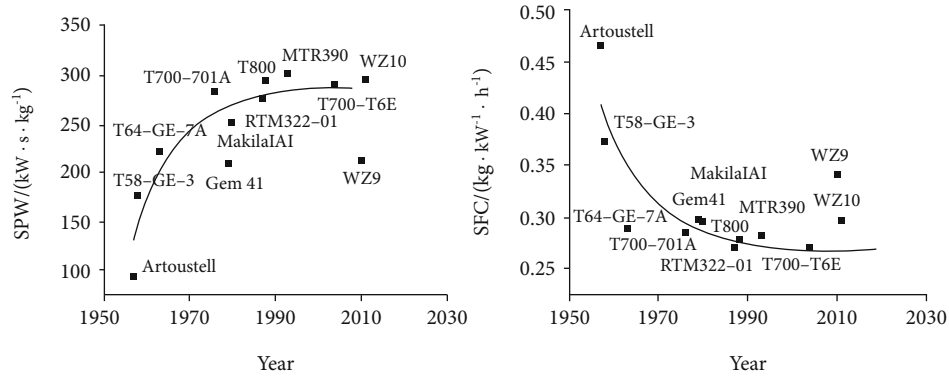
Figure 1: Technical trend of representative conventional turboshaft engines [2].

regarded as a stable and controllable energy conversion way. Naples et al. [13, 14] studied the interaction between the RDC and conventional turbine elements by the integration system of the T63 turboshaft engine embedded with an RDC. With the main combustor of GTD-350 engine being replace by an RDC, the feasibility of the RDC being applied to turboshaft engine has been confirmed by Wolański [15]. George et al. [16, 17] experimentally investigated the axial turbine performance operating under pulsating flows, which hold the similar features with the detonation chamber exhaust, and approved that the pressure oscillations may lead to undesirable turbine performance degradation. With the performance of the supersonic turbine being characterized by the power extraction and total pressure loss parameters, Liu et al. [18, 19] numerically studied the effects of unsteady inlet conditions on the operating characteristics of the supersonic turbine and revealed that leading edge shock waves were the main factor for the unsteady loss mechanism. Sousa et al. [20] analyzed the thermodynamic performance of the gas turbine with an RDC with the T-MATS software coupled with the MOC solver of RDC model; the result showed that the thermal efficiency of the rotating detonation turbine engine could be 5% higher than that of the conventional one at low compressor pressure ratios, but the performance benefits decreased as the compressor pressure ratio increased. With the accumulation of the achievements on rotating detonation turbine engine, the feasibility and potential advantages of this new form of engine are gradually approved [20–23]. However, studies regarding the overall performance characteristics and the potential performance benefits as well as their generation mechanism of the turboshaft engine embedded with an RDC are quite scarce. Compared to the conventional turboshaft engine, the study of rotating detonation-based turboshaft engine is still in its infancy.

This study aims at revealing the potential performance benefits of the rotating detonation-based turboshaft engine and promoting further application of RDC in propulsion systems. Firstly, the parametric cycle analysis model of the rotating detonation-based turboshaft engine is developed based on the low-order analytical model of RDC and the compatibility relationship between the turbomachinery and RDC. Then, the overall performance characteristics of the new form of engine are achieved. Finally, a performance comparison between the rotating detonation-based turboshaft engine and the conventional one is performed, and the performance benefits as well as their generation mechanism are revealed.

2. Mathematical and Physical Model

2.1. System Formulation. With the compatibility between RDC and turbomachinery under consideration, the isolator and mixer chamber are arranged upstream and downstream from RDC, respectively, in the dual-duct rotating detonation aeroturbine engine (DRDATE) [22]. With the power turbine and power shaft arranged downstream from the turbine of the DRDATE (which is used as the gas generator), a configuration for the rotating detonation-based turboshaft engine is proposed, as shown in Figure 2(a). Figure 2(b) further displays the ideal thermodynamic cycle process comparison between the rotating detonation-based turboshaft engine and the conventional one. For the rotating detonation-based turboshaft engine, air flows into the engine at state 0; the process 0-3 is the integrated compression process proceeding in the intake, isolator, and compressor; the processes $3'$-$3.5'$ and $3.5'$-$4'$ represent the shock compression and heat release due to combustion, respectively; the process $4'$-$9'$ represents the integrated expansion process proceeding in the turbine, power turbine, and nozzle; and the thermodynamic cycle is closed via the imaginary exothermic process $9'$-0. The thermodynamic cycle processes of the conventional turboshaft engine can be analyzed in exactly the same manner.

The final temperature of the heating process in rotating detonation-based turboshaft engine is higher than that in the conventional turboshaft engine with the same heat addition, as the specific heat capacity of detonation process is lower than that of the deflagration process. Therefore, the former corresponds less entropy production, which implies the heat loss owing to exhaust (which can be estimated with the projected area of the exothermic process to *s*-axis, as shown in Figure 2(b)) of the rotating detonation-based turboshaft engine is higher than that of the conventional one. The above has revealed the thermal efficiency benefit of the rotating detonation turbine engine conceptually.
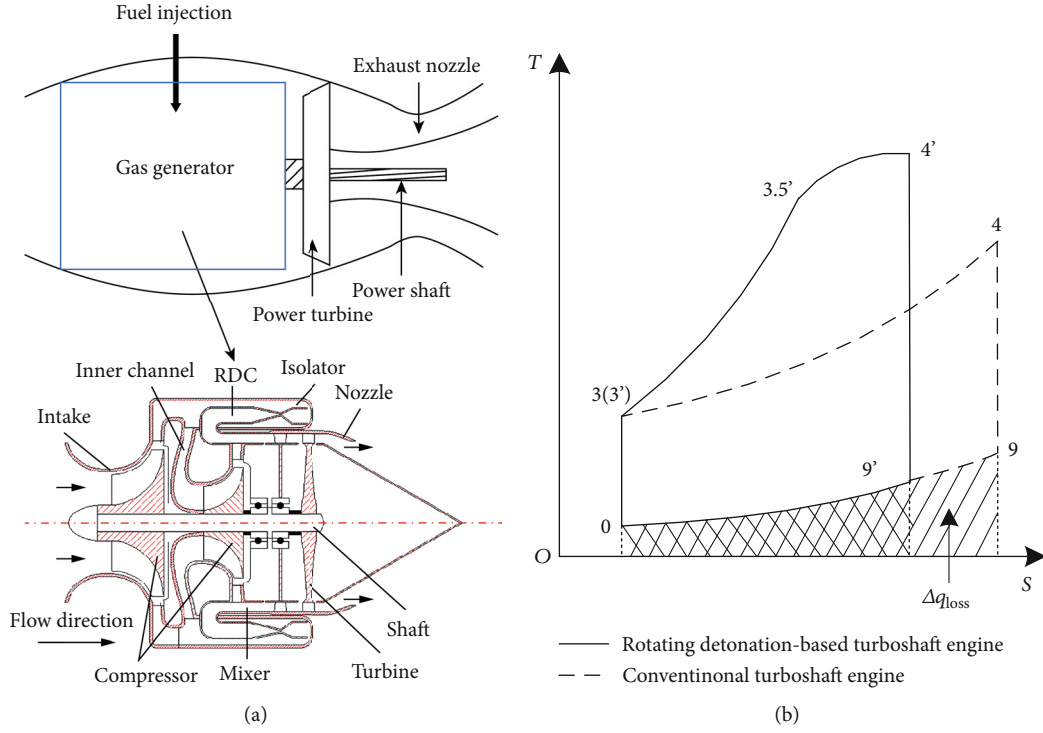
FIGURE 2: (a) Configuration and (b) ideal thermodynamic cycle processes of the rotating detonation-based turboshaft engine.

2.2. Parametric Cycle Analysis Model. The thermodynamic processes proceeding in the rotating detonation-based turbo-shaft engine can be simplified as "polytropic compression-rotating detonation-adiabatic mixing-polytropic expansion," and the reduced order model which was developed based on the matching relationship between the injection process and pressure decay after the detonation front [22] is adopted in this study for the estimation of the rotating detonation process. The RDC is fueled by kerosene, and the reaction mechanism is taken from [24]. The models of the remaining processes are consistent with the conventional turboshaft engine. The thermodynamic process in the conventional compressor can be regarded as nonisentropic polytropic compression, and the mathematical model can be expressed as follows:

$$p_3^* = \pi_c p_1^*, \tag{1}$$

$$\int_{T_1^*}^{T_3^*} c_p \frac{dT}{T} = R_0 \ln \pi_c, \tag{2}$$

$$h_3^* = h_1^* + \int_{T_1^*}^{T_3^*} c_p dT, \tag{3}$$

$$\eta_c = \frac{h_{3i}^* - h_1^*}{h_3^* - h_1^*}. \tag{4}$$

where h_{3i}^* is the total enthalpy corresponding to the isentropic compression with a compression pressure ratio π_c. The thermodynamic process in the turbine can be modeled in exactly the same way.

The gas properties are a function of the gas temperature. In this study, the parametric performance simulation model of the engine is developed based on the "variable-γ" strategy. Firstly, the gas properties of the single component can be calculated by polynomial fitting of temperature (the polynomial coefficients are referred to NASA [25]); then, the gas properties of working medium can be obtained by mass flow average.

$$c_{pi} = R_i \left(a_{0i} + a_{1i} T + a_{2i} T^2 + a_{3i} T^3 + a_{4i} T^4 \right), \tag{5}$$

$$c_p = \sum_{i=1}^{N} c_{pi} Y_i, \tag{6}$$

$$\gamma = \frac{\sum_{i=1}^{N} c_{pi} Y_i}{\sum_{i=1}^{N} Y_i \left(c_{pi} / \gamma_i \right)}. \tag{7}$$

Similar to the conventional turboshaft engine, specific power P_s, thermal efficiency η_{th}, and specific fuel consumption sfc are used as metrics to characterize the overall performance of the rotating detonation-based turboshaft engine. According to the parametric cycle analysis model and component matching equations, the performance metrics can be calculated by Equations (4)–(6). And α represents the air split parameter, which is the ratio of the mass flow rate of the inner duct to that of the outer duct in DRDATE. κ is the power split parameter, which is adopted to characterized the power split between the power turbine and the nozzle. According to the representative turboshaft engines, the value of κ is taken as 0.96.

TABLE 1: Uncertainty analysis of the performance metrics of the rotating detonation-based turboshaft engine.

| Performance metrics | P_s | | η_{th} | | sfc | |
Cycle parameters	p_4^*	T_4^*	p_4^*	T_4^*	p_4^*	T_4^*
ε	10%	10%	10%	10%	10%	10%
u_i $(i = 1, 2)$	0.96%	3.31%	2.14%	9.39%	2.09%	9.37%
u		4.19%		9.63%		9.60%

The subscripts 6 and 9 represent the parameters of power turbine inlet and exhaust nozzle outlet sections, respectively.

$$P_s = \left(1 + \frac{f}{1 + \alpha}\right) \kappa h_6^* \left[1 - \left(\frac{p_9}{p_6^*}\right)^{(\gamma - 1)/\gamma}\right], \qquad (8)$$

$$\eta_{th} = P_s / [f \cdot H_f / (1 + \alpha)], \qquad (9)$$

$$sfc = 3600 f / [P_s(1 + \alpha)]. \qquad (10)$$

The utilization of reduced order model of RDC can introduce calculation errors, owing to the assumptions. Compared to the 2D CFD solver, the calculation error of the reduced order model is below 10% [22, 23]. The overall uncertainty of the performance metrics of the rotating detonation-based turboshaft engine can be estimated by the sensitivity analysis of the calculation errors of RDC outlet parameters on overall performance of the engine. Assuming that Ψ is the performance metric; then, the overall uncertainty of Ψ can be calculated by

$$u_1 = [\Psi(p_4^* + \varepsilon p_4^*) - \Psi(p_4^*)] / \Psi(p_4^*), \qquad (11)$$

$$u_2 = [\Psi(T_4^* + \varepsilon T_4^*) - \Psi(T_4^*)] / \Psi(T_4^*), \qquad (12)$$

$$u = \sqrt{\sum u_i^2} = \sqrt{u_1^2 + u_2^2}, \qquad (13)$$

where ε is the model error of RDC, u_i represents the uncertainty component, and u represents the overall uncertainty. Table 1 summarizes the uncertainty components and overall uncertainty of the P_s, η_{th}, and sfc, which are generated by the calculation errors of the RDC model. It shows that the overall uncertainties of performance metrics remain at a relatively low level (<10%). In addition, the uncertainty of P_s is lower than that of η_{th} and sfc.

3. Results and Discussions

3.1. Sensitivity Analysis of Component Parameters on Overall Performance of the Engine. A sensitivity analysis is conducted below to reveal the variation in overall performance of the rotating detonation-based turboshaft engine versus the component parameters. The compressor pressure ratio π_c and turbine inlet temperature T_4^* play a major role in the overall performance of the engine. The variations in P_s, η_{th}, and sfc with respect to π_c and T_4^* under standard sea-level and high altitude cruise conditions are, respectively, illustrated in Figures 3 and 4. In the figures, the coordinate values of each points are determined by the P_s and sfc of the cases with the

corresponding values of π_c and T_4^*, and the values of η_{th} are presented by the color scales. The sensitivity of performance metrics to the π_c and T_4^* can be presented intuitively by the trends of curves and color scales. It can be seen that, with an increase in π_c, P_s and η_{th} first increase but then decrease, and sfc first decreases but then increases. As π_c increases, on the one hand, the power turbine pressure ratio π_t increases, and the sensitivity of π_t to changes in π_c decreases, as the pressure-gain of the RDC is negatively correlated with π_c [22]. On the other hand, the cycle heat addition decreases owing to the increase of combustor inlet temperature T_3^* and air split parameter α. In addition, the increase of α can weaken the potential benefits relating to the pressure gain of the RDC. At low values of π_c, the increase of π_t is the main factor influencing P_s, and P_s increases with the increase of π_c. As π_c increases, the increase of T_3^* and α becomes the dominant factor influencing P_s, and P_s decreases as π_c increases. The thermal efficiency η_{th} is positively correlated with P_s, so the variation of η_{th} is consistent with that of P_s. In addition, η_{th} is positively correlated with α according to Equation (9), so the unfavorable impact of T_3^* can be weakened. Therefore, the downward trend of η_{th} at high values of π_c is less obvious than that of P_s. On the basis of Equation (10), sfc is actually determined by P_s, α, and fuel-air ratio f. When T_4^* remains constant, α is positively correlated with π_c, and f is negatively correlated with π_c. At low values of π_c, the increase of P_s and α and the decrease of f are all favorable factors for reducing sfc. When the value of π_c is relatively high, the favorable effects due to the increase of α and decrease of f are not sufficient to overcome the effect unfavorable effect from the decrease in P_s, and the variation of sfc shows opposing trend. As shown in Figures 3 and 4, the isopleths of η_{th} run nearly parallel to the horizontal ordinate, which implies that there is a strong correction between the variation of η_{th} and that of sfc.

When the compressor pressure ratio π_c remains constant, P_s and η_{th} exhibit positive correlation with T_4^*, and sfc exhibits negative correlation with T_4^*. Furthermore, the performance metrics are less sensitive to changes in T_4^* than them to changes in π_c. As T_4^* increases, the cycle heat addition increases, resulting in the proportion of heat loss owing to exhaust decreases, which is favorable for the improvement of η_{th}. In addition, η_{th} is positively correlated with α, and α decreases with the increase of T_4^*. Therefore, the improvement of η_{th} due to the increase of cycle heat addition is weakened by the effect of α. In summary, η_{th} increases with an increase in T_4^*, and the sensitivity of η_{th} to changes in T_4^* decreases with an increase in T_4^*. The variation sfc can be explained in exactly the same manner. For a constant value
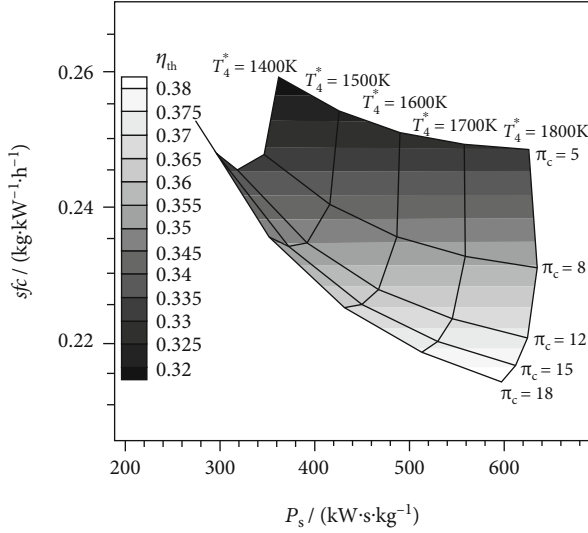
FIGURE 3: Variations in performance metrics with cycle parameters under standard sea-level condition.
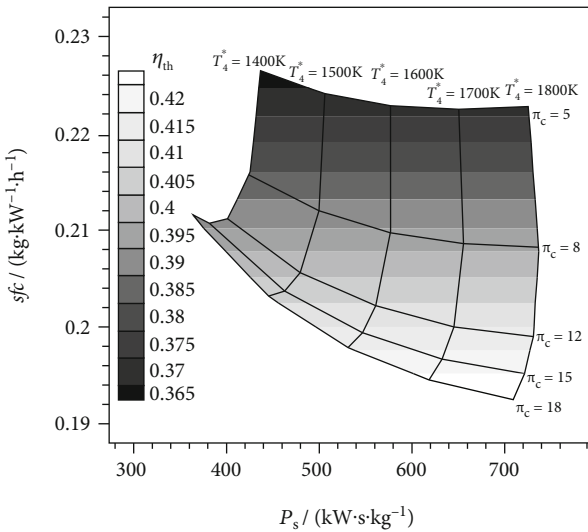

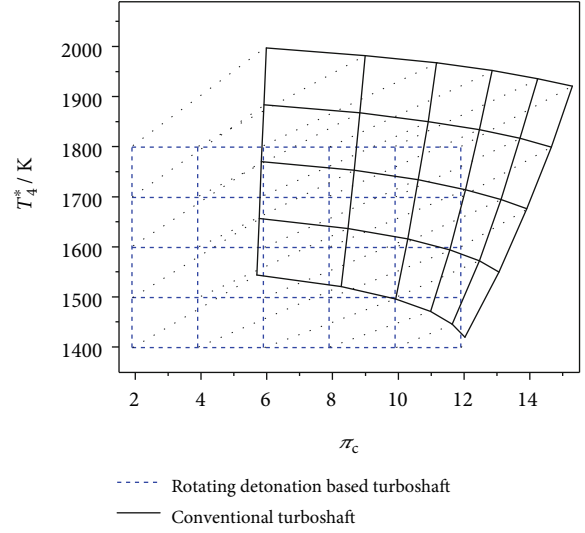FIGURE 4: Variations in performance metrics with cycle parameters under high altitude cruise condition.

FIGURE 5: Cycle parameters mapping between the rotating detonation turboshaft engine and the conventional one with the same performance metrics.

of π_c, P_s is actually determined by the cycle heat addition. Therefore, P_s increases monotonically with the increase of T_4^*. Generally, the application of rotating detonation technology does not change the variation trends of performance metrics of the turboshaft engine versus cycle parameters.

There is strong agreement between the variation trends of performance metrics under high-altitude cruise condition and those under standard sea-level condition versus cycle parameters. Under cruise condition, the total pressure ratio improves owing to the ram compression, and so do the performance metrics. As H increases, the freestream temperature T_0 as well as the combustor inlet temperature T_3^* decreases, which is favorable for the total pressure gain in the RDC. Therefore, the high-altitude cruise condition corresponds to higher P_s and η_{th} and lower sfc.

The cycle parameter comparison between the rotating detonation-based turboshaft engine and the conventional one with the same performance metrics is displayed in Figure 5. It can be seen that the former corresponds to a lower π_c and T_4^*. The reduction in π_c is conducive to improving the structural compactness and power weight ratio, and the reduction in T_4^* is a benefit for increasing the service life of the turbine. Furthermore, the benefits of reducing π_c and T_4^* exhibit a positive correlation with T_4^* and a negative correlation with π_c, and the internal mechanism is consistent with the variations in performance benefits versus π_c and T_4^*, which have been expressed above.

The feedback pressure perturbation generated by the RDC can be reduced effectively by the isolator, but it cannot be eliminated thoroughly [22]. The weakened pressure perturbation may result in reduction in compressor efficiency. Similarly, the turbine inlet parameter distribution can be improved owing to the mixing process in the mixer, but the turbine inlet parameter distribution of the rotating detonation-based turboshaft engine, which has a direct relationship with the turbine efficiency, is still less uniform than that of the conventional one. Therefore, the sensitivity analysis of turbomachinery efficiency and the total pressure recovery of the isolator on overall performance of the rotating detonation-based turboshaft engine is of significance. As the turbomachinery polytropic efficiency e_c and e_t is hardly dependent on the pressure ratios π_c and π_t [3], e_c and e_t are utilized to characterize the turbomachinery efficiency in this study. Figure 6 displays the effects of compressor polytropic efficiency e_c, turbine polytropic efficiency e_t and total pressure recovery coefficient of isolator σ_{is} on the overall performance of the engine. As π_c remains constant, the increase of e_c and e_t could improve the overall performance of the engine. And the performance metrics are more sensitive to changes in e_c and e_t at higher values of π_c. Furthermore, P_s and sfc are more sensitive to changes in e_c than to changes
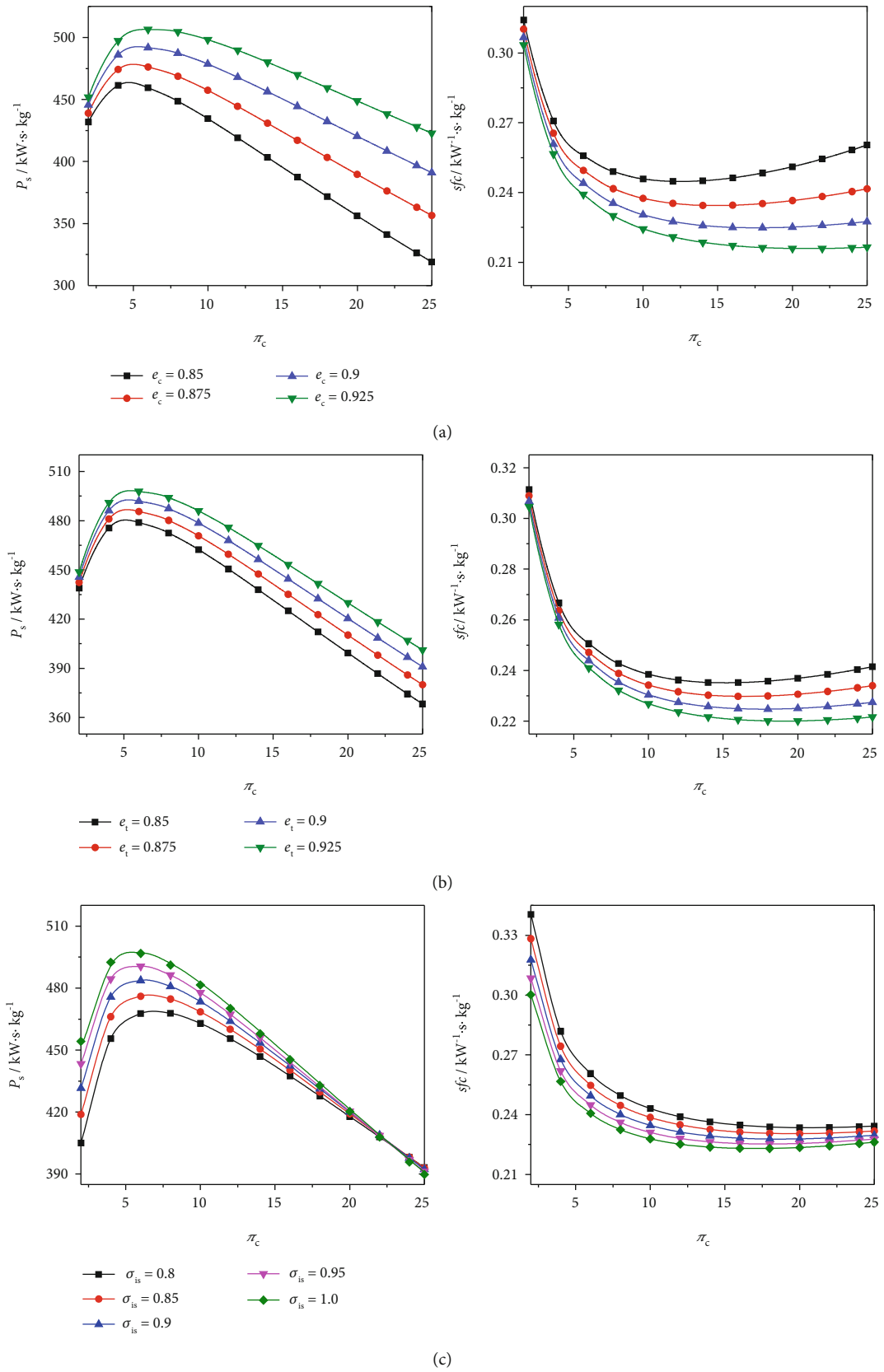
FIGURE 6: Variations in performance metrics with (a) compressor polytropic efficiency e_c, (b) turbine polytropic efficiency e_t, and (c) total pressure recovery coefficient of isolator σ_{is}.
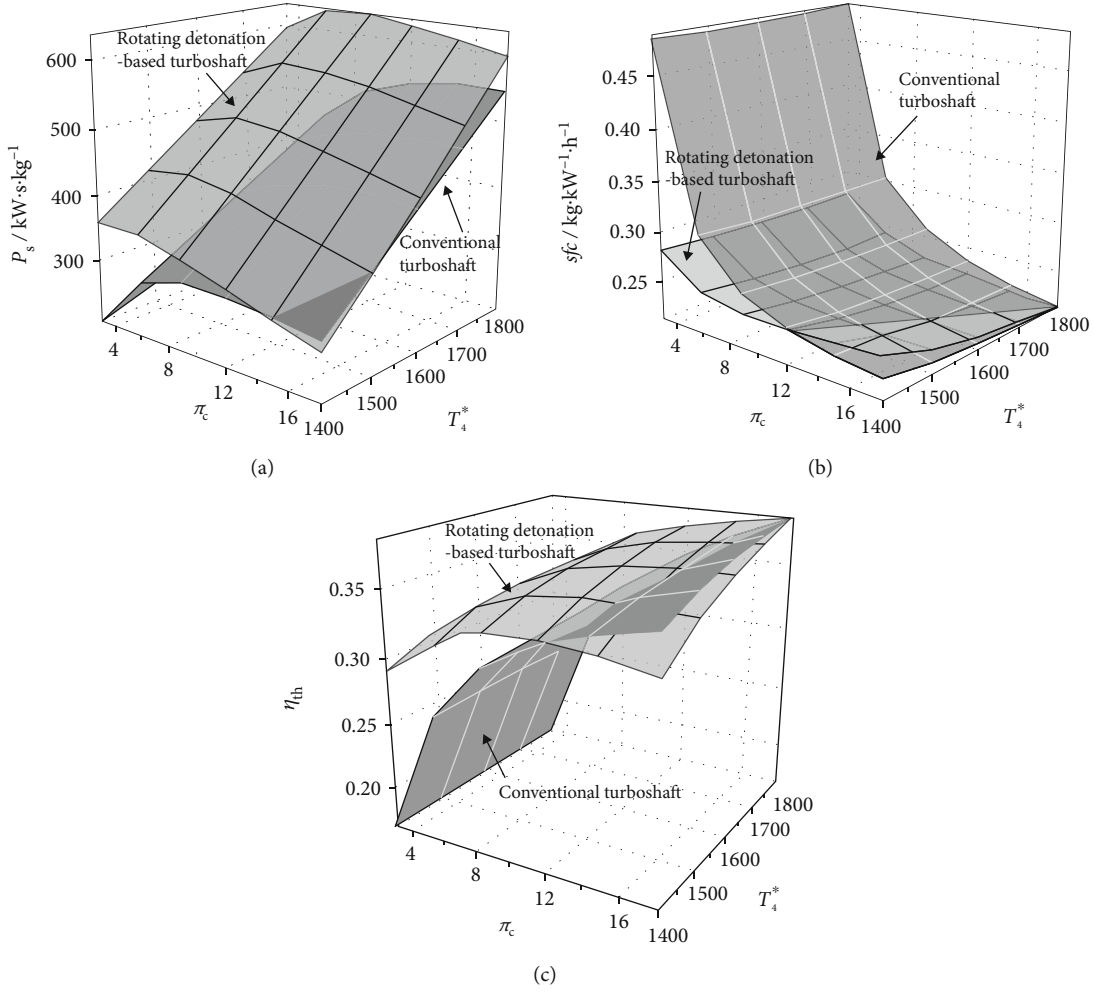
(a)

(b)

(c)

Figure 7: Performance comparison of turboshaft engine based on rotating detonation and the conventional one for different cycle parameters. (a) P_s, (b) sfc, and (c) η_{th}.

in e_t, as the compressor pressure ratio is normally higher than the turbine pressure ratio. Unlike the influence mechanism of e_c and e_t, the increase of σ_{is} has the same impact as improving the total pressure ratio of the engine. According to the sensitivity analysis of cycle parameters on overall performance of the engine, as π_c increases, P_s first increases but then decreases, and sfc first decreases but then increases. At low values of π_c, the higher the value of σ_{is}, the higher the value of P_s. When the value of π_c is relatively high, the situation is the opposite. As the optimum compressor pressure ratios corresponding to the maximum η_{th} and minimum sfc are higher than that corresponding to the maximum P_s, when the values of π_c are not quite high, the higher the value of σ_{is}, the higher the value of η_{th} and the lower the value of sfc.

3.2. Comparison Between the Rotating Detonation-Based Turboshaft Engine and the Conventional One. Figure 7 shows the variations in performance difference between the rotating detonation-based turboshaft engine and the conventional one with the same component parameters versus cycle parameters under the standard sea-level condition at take-off. It can be seen that, at low values of π_c, the rotating

detonation-based turboshaft engine exhibits significant potential benefits in P_s, η_{th}, and sfc. As π_c increases, the potential benefits decrease and tend to disappear. Furthermore, the compressor pressure ratio range corresponding to the rotating detonation-based turboshaft engine exhibiting benefit in P_s is wider than that corresponding to the engine exhibiting benefit in η_{th} and sfc. The fuel-air ratio f of the rotating detonation-based turboshaft engine is higher than that of the conventional one with the same cycle parameters. Then, the total pressure gain of the RDC is significant at low values of π_c, resulting in a higher power turbine pressure ratio π_{pt} of the rotating detonation-based turboshaft engine compared to the conventional one. As the total pressure gain of the RDC decreases with an increase in π_c, so does the benefit of π_{pt}. For the η_{th} and sfc of turboshaft engines, the higher value of f is an unfavorable factor, and the higher value of π_{pt} is a favorable factor. The potential benefits of η_{th} and sfc can be achieved by the rotating detonation-based turboshaft engine under the premise that the favorable effects generated by π_{pt} are sufficient to overcome the unfavorable effects of a higher value of f. Therefore, there is a strong agreement between the variations of the potential benefits in η_{th} and sfc and the variation of

the benefit of π_{pt}. The higher value of f and the higher value of π_{pt} are all favorable factors for the improvement of P_s. Therefore, the rotating detonation-based turboshaft engine exhibits significant benefit in P_s at low values of π_c. In addition, the power turbine inlet total enthalpy h_6^* of the rotating detonation-based turboshaft engine is lower than that of the conventional one, owing to the rear stage of compressor. Therefore, the benefit in P_s tends to disappear at high values of π_c. It is not difficult to draw the conclusion that the critical compressor pressure ratio π_{crit1} corresponding to the disappearance of P_s improvement is higher than that corresponding to the disappearance of η_{th} and sfc, according to the above explanation.

When the value of π_c remains constant, as T_4^* increases, the potential performance benefits of the rotating detonation-based turboshaft engine increase continuously. And the potential benefits in η_{th} and sfc are more sensitive to changes in T_4^* compared to the potential benefit in P_s. Although the total pressure gain of the RDC is independent of T_4^*, the effect of the total pressure gain of the RDC can be enlarged owing to the decrease of α. Therefore, the performance differences between the rotating detonation-based turboshaft engine and the conventional one increase with an increase in T_4^*. In addition, the fuel-air ratio difference increases as T_4^* increases owing to the decrease of α. As η_{th} is positively correlated with P_s and negatively correlated with f, the potential benefits in η_{th} is more sensitive to changes in T_4^*. According to the explanation in Section 3.1, there is a strong correction between the variation of η_{th} and that of sfc, so do the variations of performance benefits in η_{th} and sfc. The variations in critical compressor pressure ratio π_{crit1} corresponding to the disappearance of P_s improvement and the critical compressor pressure ratio π_{crit2} corresponding to the disappearance of sfc improvement of the rotating detonation-based turboshaft engine versus T_4^* are displayed in Table 2. It can be seen that π_{crit1} and π_{crit2} exhibit positive correlation with T_4^*, and π_{crit1} is normally larger than π_{crit2}.

As the value of π_c remains constant at 12 and the value of T_4^* remains constant at 1600 K, the variations in performance differences between the rotating detonation-based turboshaft engine and the conventional one versus flight parameters are shown in Figure 8. As V_0 increases, P_s and η_{th} of the two forms of engines increase, and sfc decreases monotonically. And the performance differences between the two forms of engines decreases with an increase in V_0. And the performance differences of η_{th} and sfc are more sensitive to changes in V_0 compared to the performance difference of P_s. As V_0 increases, the total pressure ratio of the engine increases owing to the ram compression, which is favorable for improving the overall performance. The performance benefits of the rotating detonation-based turboshaft engine compared to the conventional one are mainly contributed by the total pressure gain of the RDC. As V_0 increases, the combustor inlet temperature T_3^* increases, which is detrimental to the total pressure gain of the RDC [22, 23]. In addition, α increases with an increase in V_0, owing to the decrease of cooling capacity of the compressed

TABLE 2: Variations in critical compressor pressure ratios π_{crit1} and π_{crit2} with T_4^*.

T_4^*, K	π_{crit1}	π_{crit2}
1400	14.20	12.37
1500	18.23	13.87
1600	23.52	15.26
1700	30.69	16.5
1800	40.87	17.71

air. Then, the effect of the total pressure gain of the RDC can be weakened. In summary, the potential performance benefits of the rotating detonation-based turboshaft decrease with an increase in V_0. P_s and η_{th} of the two forms of engines exhibit a positive correlation with H, and sfc exhibits a negative correlation with H. And the performance differences between the two forms of engines exhibit a positive correction with H. With the increase of H, the freestream temperature T_0 decreases monotonically, which is favorable for the improvement of the overall performance. T_3^* decreases with an increase in H, resulting in the improvement of the total pressure gain of the RDC. In addition, α decreases with an increase in H, and the effect of the total pressure gain of the RDC can be enlarged. With the combined effects of these two factors, the potential performance benefits of the rotating detonation-based turboshaft increase with an increase in H. The effects of flight parameters on π_{crit1} and π_{crit2} are displayed in Tables 3 and 4. According to the calculation results, π_{crit1} and π_{crit2} are positively correlated with H and negatively correlated with V_0.

3.3. Optimum Pressure Ratios. On the basis of the variations in P_s and sfc of the rotating detonation-based turboshaft engine versus π_c, there exist an optimum compressor pressure ratio π_{opt1} that maximizes the specific power and an optimum compressor pressure ratio π_{opt2} that minimizes the specific fuel consumption. Table 5 shows the variations in π_{opt1} and π_{opt2} versus T_4^*. It can be seen that π_{opt1} and π_{opt2} increase with an increase in T_4^*, as P_s exhibits a positive correlation with T_4^* and sfc exhibits a negative correlation with T_4^*. The variations in π_{opt1} and π_{opt2} versus flight parameters V_0 and H are listed in Tables 6 and 7. With the increase of V_0, the optimum compressor pressure ratios decrease continuously owing to the ram compression. As H increases, the RDC inlet temperature decreases, and the pressure gain of the RDC increases monotonically. In addition, α decreases as the freestream temperature decreases with an increase in H. For the effects of the above factors, sfc performance improves with H as does π_{opt2}.

4. Conclusion

In this study, a configuration of the rotating detonation-based turboshaft engine with the compatibility between the turbomachinery and RDC under consideration is presented. Then, the performance characteristics of this new form of engine are investigated based on the parametric
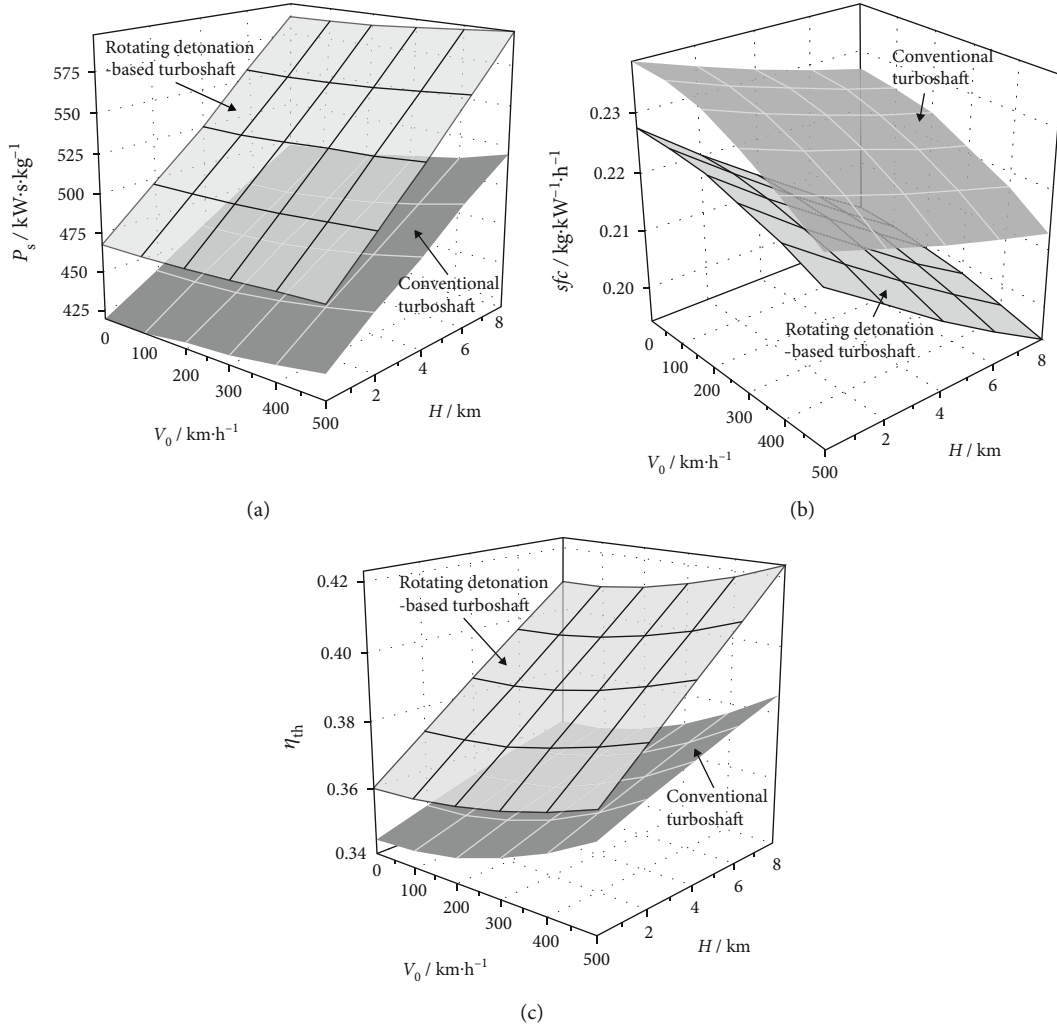
(a)

(b)

(c)

FIGURE 8: Performance comparison of turboshaft engine based on rotating detonation and the conventional one for different cycle parameters. (a) P_s, (b) sfc, and (c) η_{th}.

TABLE 3: Variations in critical compressor pressure ratios π_{crit1} and π_{crit2} with V_0.

V_0, km h^{-1}	π_{crit1}	π_{crit2}
0	23.52	15.26
150	23.32	15.1
300	22.72	14.63
450	21.77	13.89

TABLE 4: Variations in critical compressor pressure ratios π_{crit1} and π_{crit2} with H.

H, km	π_{crit1}	π_{crit2}
0	21.77	13.89
2	23.72	15.4
4	25.94	17.17
6	28.45	19.27
8	31.35	21.77

TABLE 5: Variations in optimum compressor pressure ratios π_{opt1} and π_{opt2} with T_4^*.

T_4^*, K	π_{opt1}	π_{opt2}
1400	4.18	11.04
1500	4.95	14.07
1600	5.79	17.67
1700	6.68	21.93
1800	7.71	26.52

TABLE 6: Variations in optimum compressor pressure ratios π_{opt1} and π_{opt2} with V_0.

V_0, km h^{-1}	π_{opt1}	π_{opt2}
0	5.79	17.67
150	5.73	17.56
300	5.55	17.28
450	5.31	16.81

TABLE 7: Variations in optimum compressor pressure ratios π_{opt1} and π_{opt2} with H.

H, km	π_{opt1}	π_{opt2}
0	5.40	16.98
2	5.66	18.73
4	5.94	20.76
6	6.25	23.13
8	6.60	25.92

thermodynamic cycle analysis model. In order to reveal the potential performance benefits and their generation mechanism, the performance comparison between the rotating detonation-based turboshaft engine and the conventional one is performed. The major conclusions are summarized as follows.

(1) When the flight parameters remain constant, as the compression ratio π_c increases, the specific power P_s and thermal efficiency η_{th} of the rotating detonation-based turboshaft engine first increase but then decrease, and the specific fuel consumption sfc first decreases but then increases. As the turbine inlet temperature T_4^* increases, P_s and η_{th} increase, and sfc decreases continuously. When the component parameters remain constant, with the increase in flight velocity V_0 and flight altitude H, P_s and η_{th} increase, and sfc decreases monotonically. There exist optimum compressor pressure ratios π_{opt1} and π_{opt2} which maximizes the specific power and minimizes the specific fuel consumption, respectively, and π_{opt1} is nominally larger than π_{opt2}. Furthermore, π_{opt1} and π_{opt2} are positively correlated with T_4^* and H and are negatively correlated with V_0.

(2) Compared to the conventional turboshaft engine, the thermal efficiency of the rotating detonation-based turboshaft engine can be improved above 7% at lower values of π_c, and the benefits decrease with an increase in π_c. As π_c remains constant, the performance improvements increase with the increase of T_4^*. As T_4^* remains constant at 1600 K, the value of π_{crit1} is about 23.5 corresponding to the disappearing of benefit in P_s, and value of π_{crit2} is about 15.3 corresponding to the disappearing of benefit in η_{th} and sfc. The critical compressor pressure ratios are positively correlated with T_4^* corresponding to the disappearance of performance benefits.

(3) When the value of π_c is not quite high and the value of T_4^* is not relatively low, the rotating detonation-based turboshaft engine exhibits competitive potential benefits within the typical flight envelope of helicopters (i.e., $V_0 < 450$ km/h and $H < 8$ km). The potential benefits of the rotating detonation-based turboshaft engine exhibit a positive correlation with H and exhibit a negative correlation with V_0. Fur-

thermore, the values of π_{crit1} and π_{crit2} increase with the increase in H and decrease with an increase in V_0.

Nomenclature

c_p: Specific heat at constant pressure
f: Fuel-air mass flow ratio
H_f: Fuel heating value
h: Enthalpy
Ma: Mach number
$\dot{m}$: Mass flow rate
P_s: Specific power
p: Pressure
R: Universal gas constant
sfc: Specific fuel consumption
T: Temperature
u: Overall uncertainty
V: Velocity
γ: Ratio of specific heats
η_0: Overall efficiency
η_{th}: Thermal efficiency
κ: Power split parameter
π_c: Compressor pressure ratio.

Superscripts

*: Total or stagnation parameters.

Subscripts

0: Freestream at the intake entrance
1: Compressor inlet section
3: Combustor inlet section
4: Turbine inlet section
6: Power turbine inlet section
9: Nozzle outlet section.

Abbreviations

DRDATE: Dual-duct rotating detonation aeroturbine engine
RDC: Rotating detonation combustor.

Data Availability

The data used to support the findings of this study are available from the corresponding author upon request.

Conflicts of Interest

The authors declare that there is no conflict of interest regarding the publication of this paper.

Acknowledgments

References

[1] E. T. Johnson and H. Lindsay, "Advanced technology programs for small turboshaft engines: past, present, future," *Journal of Engineering for Gas Turbines and Power*, vol. 113, no. 1, pp. 33–39, 1991.

[2] N. Ge, "Development and technical trend of turbo shafts engine," *Journal of Nanjing University of Aeronautics & Astronautics*, vol. 50, no. 2, pp. 145–156, 2018.

[3] S. Farokhi, *Aircraft Propulsion*, John Wiley & Sons, New York, NY, USA, 2nd edition, 2014.

[4] G. A. Richards, *New Developments in Combustion Technology - Part II: Step Change in Efficiency*, Princeton-CEFRC Summer School on Combustion, Princeton, NJ, US, 2012.

[5] F. A. Bykovskii, S. A. Zhdan, and E. F. Vedernikov, "Continuous spin detonations," *Journal of Propulsion and Power*, vol. 22, no. 6, pp. 1204–1216, 2006.

[6] P. Wolański, "Detonative propulsion," *Proceedings of the Combustion Institute*, vol. 34, no. 1, pp. 125–158, 2013.

[7] F. K. Lu and E. M. Braun, "Rotating detonation wave propulsion: experimental challenges, modeling, and engine concepts," *Journal of Propulsion and Power*, vol. 30, no. 5, pp. 1125–1142, 2014.

[8] J. Kindracki, P. Wolański, and Z. Gut, "Experimental research on the rotating detonation in gaseous fuels–oxygen mixtures," *Shock Waves*, vol. 21, no. 2, pp. 75–84, 2011.

[9] V. Anand and E. Gutmark, "Rotating detonation combustors and their similarities to rocket instabilities," *Progress in Energy and Combustion Science*, vol. 73, pp. 182–234, 2019.

[10] B. A. Rankin, D. R. Richardson, A. W. Caswell, A. G. Naples, J. L. Hoke, and F. R. Schauer, "Chemiluminescence imaging of an optically accessible non-premixed rotating detonation engine," *Combustion and Flame*, vol. 176, pp. 12–22, 2017.

[11] D. Schwer and K. Kailasanath, "Fluid dynamics of rotating detonation engines with hydrogen and hydrocarbon fuels," *Proceedings of the Combustion Institute*, vol. 34, no. 2, pp. 1991–1998, 2013.

[12] N. Tsuboi, S. Eto, A. K. Hayashi, and T. Kojima, "Front cellular structure and thrust performance on hydrogen-oxygen rotating detonation engine," *Journal of Propulsion and Power*, vol. 33, no. 1, pp. 100–111, 2017.

[13] A. Naples, J. Hoke, R. T. Battelle, M. Wagner, and F. R. Schauer, *Rotating Detonation Engine Implementation into an Open-Loop T63 Gas Turbine Engine*, AIAA Paper, 2017.

[14] A. Naples, J. Hoke, R. Battelle, and F. Schauer, "T63 turbine response to rotating detonation combustor exhaust flow," *Journal of Engineering for Gas Turbines and Power*, vol. 141, no. 2, article 021029, 2019.

[15] P. Wolański, "Application of the continuous rotating detonation to gas turbine," *Applied Mechanics and Materials*, vol. 782, pp. 3–12, 2015.

[16] A. S. George, R. B. Driscoll, D. E. Munday, and E. J. Gutmark, "Experimental comparison of axial turbine performance under pulsed air and pulsed detonation flows," AIAA Paper, 2013.

[17] A. S. George, R. Driscoll, E. Gutmark, and D. Munday, "Experimental comparison of axial turbine performance under steady and pulsating flows," *Journal of Turbomachinery*, vol. 136, no. 11, article 111005, 2014.

[18] Z. Liu, J. Braun, and G. Paniagua, *Three dimensional optimization for subsonic axial turbines operating at high unsteady inlet Mach number*, AIAA Paper, 2018.

[19] Z. Liu, J. Braun, and G. Paniagua, "Characterization of a supersonic turbine downstream of a rotating detonation combustor," *Journal of Engineering for Gas Turbines and Power*, vol. 141, no. 3, article 031501, 2019.

[20] J. Sousa, G. Paniagua, and E. C. Morata, "Thermodynamic analysis of a gas turbine engine with a rotating detonation combustor," *Applied Energy*, vol. 195, pp. 247–256, 2017.

[21] Z. Ji, H. Zhang, Q. Xie, and B. Wang, "Thermodynamic process and performance analysis of the continuous rotating detonation turbine engine," *Journal of Tsinghua University (Science and Technology)*, vol. 58, no. 10, pp. 899–905, 2018.

[22] Z. Ji, H. Zhang, and B. Wang, "Performance analysis of dual-duct rotating detonation aero-turbine engine," *Aerospace Science and Technology*, vol. 92, pp. 806–819, 2019.

[23] Z. Ji, H. Zhang, B. Wang, and W. He, "Comprehensive performance analysis of the turbofan with a multi-annular rotating detonation duct burner," *Journal of Engineering for Gas Turbines and Power*, vol. 142, no. 2, 2020.

[24] F. Ladeinde, X. Cai, B. Sekar, and B. Kiel, *Application of combined LES and flamelet modeling to methane, propane, and Jet-A combustion*, AIAA Paper, 2001.

[25] B. J. McBride, M. J. Zehe, and S. Gordon, "NASA Glenn coefficients for calculating thermodynamic properties of individual species," NASA Technical Report, NASA TP, USA, 2002.

Research Article

Simulation of Elliptical Liquid Jet Primary Breakup In Supersonic Crossflow

Yao-zhi Zhou [iD],[1,2] **Feng Xiao** [iD],[1,2] **Qing-lian Li** [iD],[1,2] **and Chen-yang Li** [iD][1,2]

[1]*Science and Technology on Scramjet Laboratory, National University of Defense Technology, Changsha 410073, China*
[2]*College of Aerospace Science and Technology, National University of Defense Technology, Changsha 410073, China*

Correspondence should be addressed to Qing-lian Li; peakdreamer@163.com

The study of elliptical liquid jets in supersonic flow in a Mach 2.0 is performed numerically. The primary breakup process of the elliptical liquid jet is simulated for a Weber number 223, liquid/gas flux momentum 4.0. The aspect ratios of elliptical geometries are set to be 0.25, 0.5, 1, 2, and 5. The results show a remarkable difference in liquid jet disintegration morphology at different aspect ratios. Under supersonic crossflow conditions, the elliptical liquid jet shows more breakup characteristics than the round liquid jet. As the aspect ratio grows, the penetration depth decreases. The elliptical liquid jet with AR = 0.25 has the largest penetration depth in all cases. Moreover, the round jet has a maximum spreading angle of 50.2°. The changing trends of the column breakup length both x direction and y direction are similar. The elliptical jet at a lower aspect ratio has a shorter breakup length due to the narrower windward area. The liquid jet has a pair of larger horseshoe vortex structure and a wider wake region at a higher aspect ratio. Two pairs of reversal vortex pairs with obvious characteristics can be observed in all the simulations.

1. Introduction

Liquid fuel is directly injected into a supersonic flow in a scramjet engine normally; it must atomize fully and mix well in milliseconds [1–3]. A lot of experiments about liquid jet breakup in high-speed gas have been studied in recent years [4–7]. It is a significant phenomenon that the atomization of liquid jet in a gaseous crossflow had a wide application in fields such as combustion in liquid rocket engine, gas turbine engines, or scramjets [8–13].

Obviously, there are three important physical processes that control atomization characteristics, the deformation of liquid column, the formation of surface waves, and the primary breakup [14–17]. To study these physical processes, one of the most convenient ways is to change the geometry of liquid orifices. The breakup mechanisms of liquid jets in still air of different orifice geometries have been studied in the last three decades [18–22]. An interesting conclusion been found that the liquid jets injected from a noncircular orifice had a shorter breakup time than a round orifice in a same orifice area. Among the many noncircular orifices, the

elliptical orifices have attracted plenty of attentions. Compared with the round liquid jets, the surface energy of elliptical liquid jets is smallest normally in a same orifice area. After the study of trajectories of elliptical jets in a gas flow, a theoretical model was developed in the works of [23]. In this model, as the aspect ratio increases, the penetration depth decreases. The spatial distribution of elliptical jets was studied using an empirical correlation experimentally in [24]. The deformation of the liquid column has some significant differences at different aspect ratios. A hybrid model was improved to apply a liquid jet in gas flow in [25]. The cross-section of the liquid column underwent a process from a circle to an ellipse, and the liquid mass is converted to discrete droplets at the same time.

Though many researchers referred to the improvement of spray efficiency through a process from a circle to an ellipse in elliptical jets, the elliptical liquid jet in a supersonic crossflow has not been studied so far. The speed of the crossflow is usually supersonic in a scramjet. There are many complex surface waves ahead of the liquid column; the flow field near the liquid column is very chaotic. The significance of
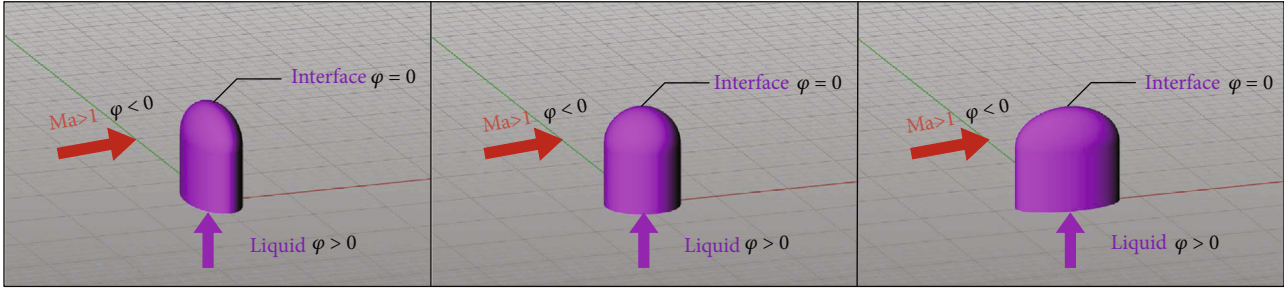
FIGURE 1: Initialization schematic between the round and elliptical jet.

TABLE 1: Supersonic crossflow conditions and liquid jet condition.

Supersonic crossflow			
Mach number	2.0	Gas velocity, U_G (m/s)	517.2
Static pressure, P_G (kPa)	17.2	Gas density, ρ_G (kg/m^3)	0.3
Static temperature, T_G (K)	167	Viscosity coefficient, μ_G (Pa·S)	1.1×10^{-5}
Liquid jet			
Injection velocity, U_L (m/s)	17.9	Water density, ρ_L (kg/m^3)	1000
Water pressure, P_L (kPa)	160.2	Momentum ratio, $q = \rho_L U_L^2 / \rho_G U_G^2$	4.0
Surface tension coefficient, σ (N/m)	0.072	Viscosity coefficient, μ_L (Pa·S)	1×10^{-3}

(a)   (b)
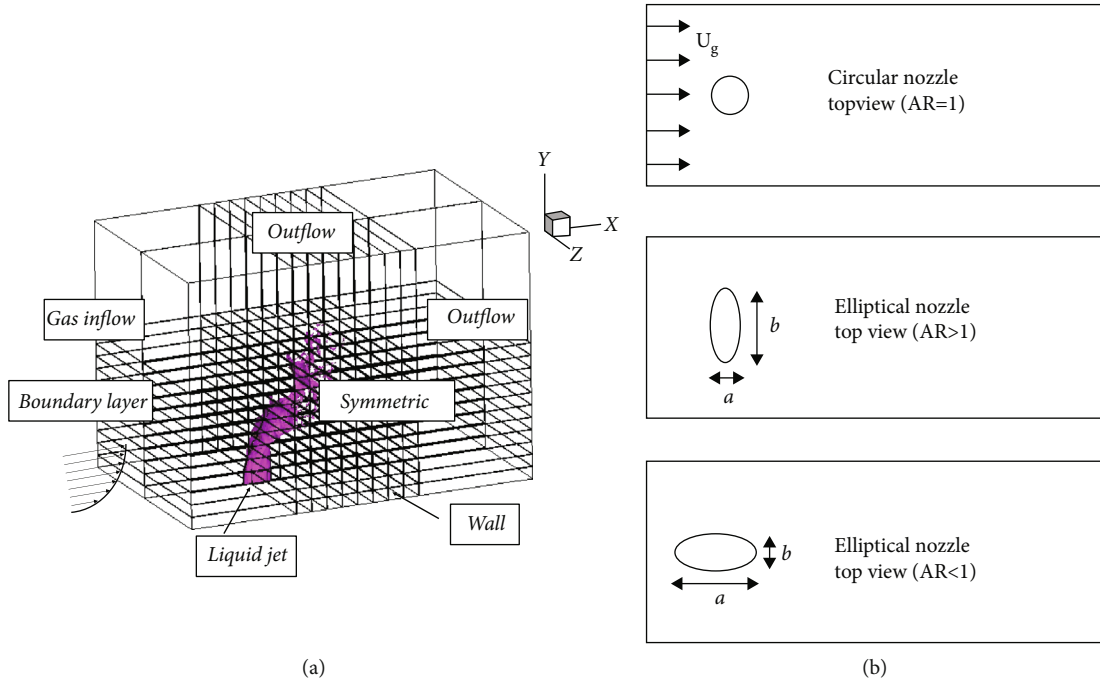
FIGURE 2: Simulation domain of elliptical liquid jet and top view of different orifice types.

this investigation focuses on the breakup processes of the elliptical jet, spatial distribution, and flow field characteristics presented in a supersonic crossflow which has not been fully investigated by previous studies.

Numerical research can obtain more flow field details than experimental research are applied in [26]. The detailed breakup process of a droplet in a supersonic flow has been studied numerically in [27–29]. The secondary atomization of a liquid jet has been predicted numerically in Ref. [30, 31]. Under the Euler-Lagrange framework, a two-phase simulation scheme was proposed in [32]. Under the Eulerian-Lagrangian framework, the liquid trailing phenomenon of a liquid jet in a supersonic crossflow was captured using large eddy simulation (LES) in [33, 34]. Using the CLSVOF method, the breakup process of a pulsed liquid jet in high-speed gas flow was studied in the works of [35].

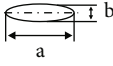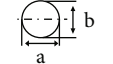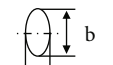TABLE 2: Geometries of injection nozzles (crossflow is from left to right).
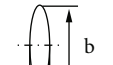
Configuration		Orifice Geometry	a (mm)	b (mm)	AR	A(mm²)	We_G
Case 1	Elliptical		0.4	0.1	0.25	0.0314	223
Case 2	Elliptical		0.2828	0.1414	0.5	0.0314	223
Case 3	Circular		0.2	0.2	1	0.0314	223
Case 4	Elliptical		0.1414	0.2828	2	0.0314	223
Case 5	Elliptical		0.1	0.4	4	0.0314	223

TABLE 3: Minimum mesh size under three kinds of meshes.

Grid-A	Grid-C	Grid-F
0.045D	0.09D	0.03D

This paper is organized as follows. The governing equations and numerical methods are described in Section 2. The breakup processes of the elliptical liquid jet in a supersonic crossflow are presented in Section 3.1; the spatial distribution of the elliptical liquid jet including the penetration depth, spreading angle, and breakup length is presented in Section 3.2. Then, Section 3.3 analyzes the flow field characteristics of the elliptical jet and round jet. Finally, a conclusion is presented in Section 4.

2. Governing Equations and Numerical Method

We adopted the CLSVOF method to track the liquid/gas interface. It absorbs the advantages of the LS method and the VOF method, which can capture the interface exactly and keep quality conservation for the two-phase flow in [36, 37]. The VOF is defined as the volume fraction of liquid in every cell. The LS ϕ is a distance function; ϕ represents the signed distance from the interface. The isosurface $\phi = 0$ represents the interface, with $\phi > 0$ in liquid and $\phi < 0$ in gas. Figure 1 depicts that the round jet has an initial liquid column during the initialization, while an elliptical jet has an initial elliptical cylinder, respectively. The detailed information about interface advection equations, liquid governing equations, and gas governing equations has been presented in Ref. [38, 39]. The spatially filtered LES formulation is employed in our solver, and the subgrid-scale (SGS) stress tensor arising from SGS eddies is modelled by the Smagorinsky eddy viscosity model. The temporal discretization and pressure gradient discretization can be referred to Ref. [38,
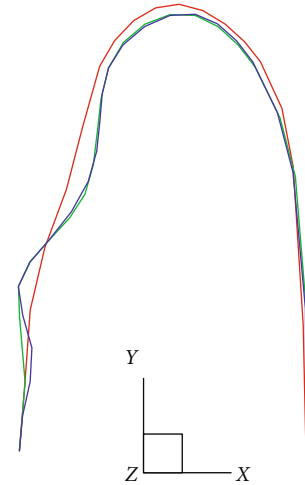

FIGURE 3: Simulated initial column shapes on Grid-C (red line), Grid-A (green line), and Grid-F (blue line) for Case 1.

40–42]. Our solver has been validated with experimental results of a sphere in our previous works [38].

To study the effects of the elliptical orifice, five geometries of elliptical orifices have been run. And the gas conditions and liquid condition are given in Table 1. The simulation domain is divided into 240 blocks as shown in Figure 2(a), which is $[0, 26D] \times [0, 15D] \times [-8D, 8D]$ in the x, y, and z directions. The equivalent diameter of the orifice outlet is represented by D, which is 0.2 mm in all the cases. A uniform Cartesian mesh is used in the region $[7.5D, 16D] \times [0, 10D] \times [3.5D, 3.5D]$. The top and right faces are defined as outflow boundary conditions, and the front and back faces are defined as symmetric boundary conditions. Figure 2(b) shows the geometry shapes and the top view of different orifices. The geometries of injection orifices are given in Table 2.
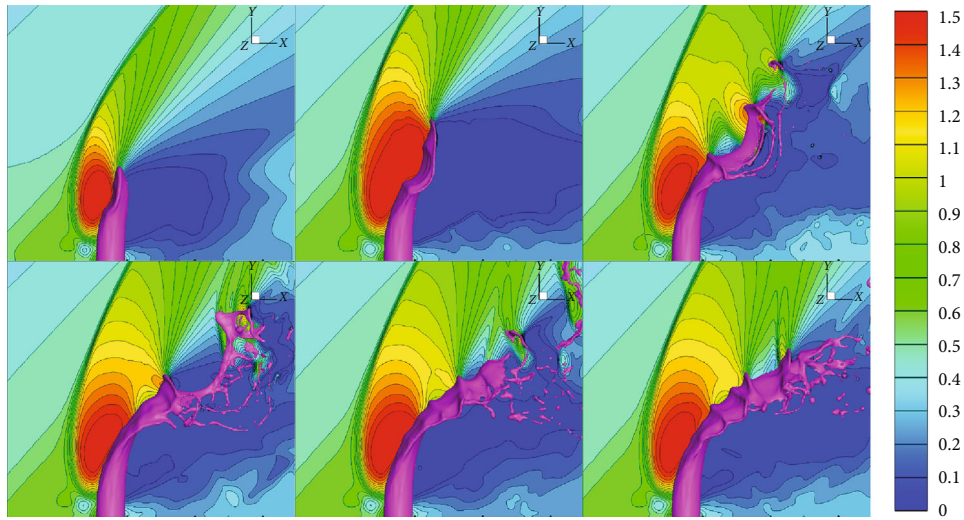
(a) Case 1
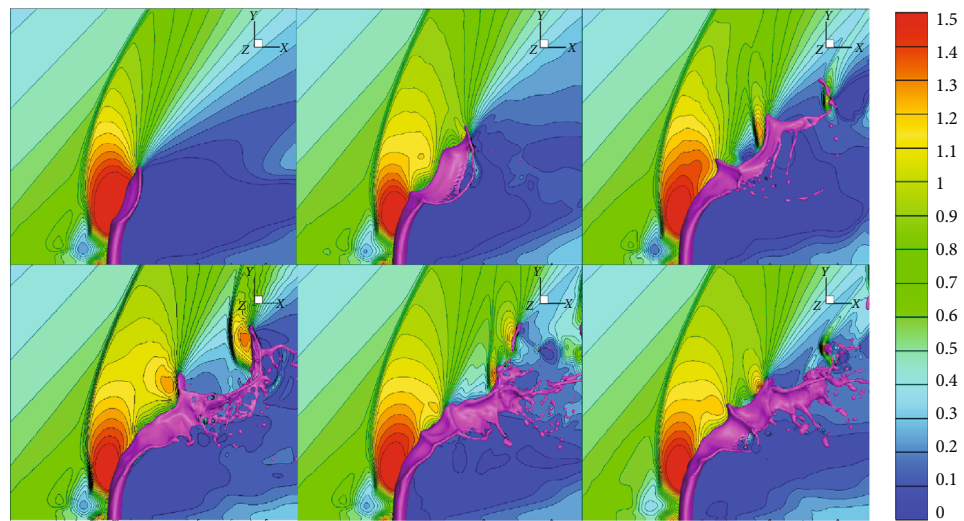
(b) Case 3
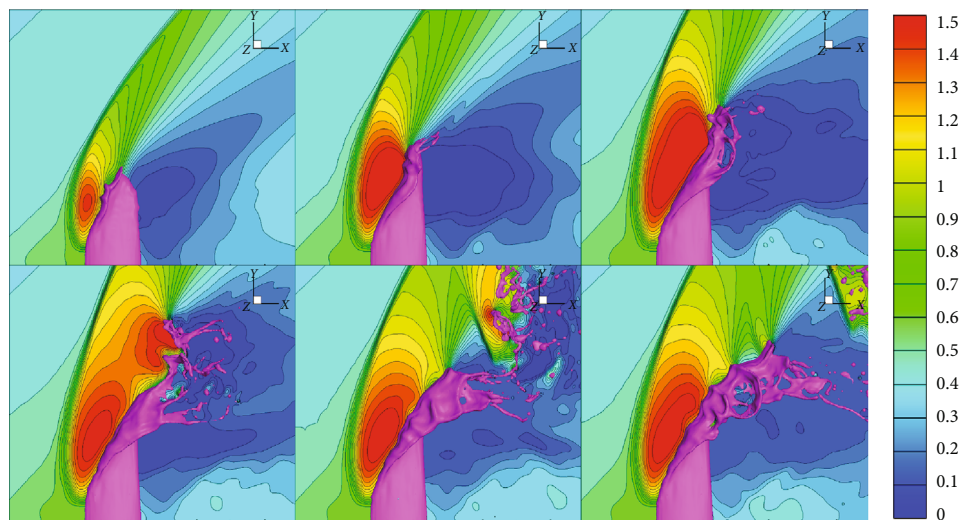
(c) Case 5

FIGURE 4: Morphology of liquid jet primary breakup with P^* contours in slice $z = 0$ for three AR, $\Delta t = 8\,\mu$s.
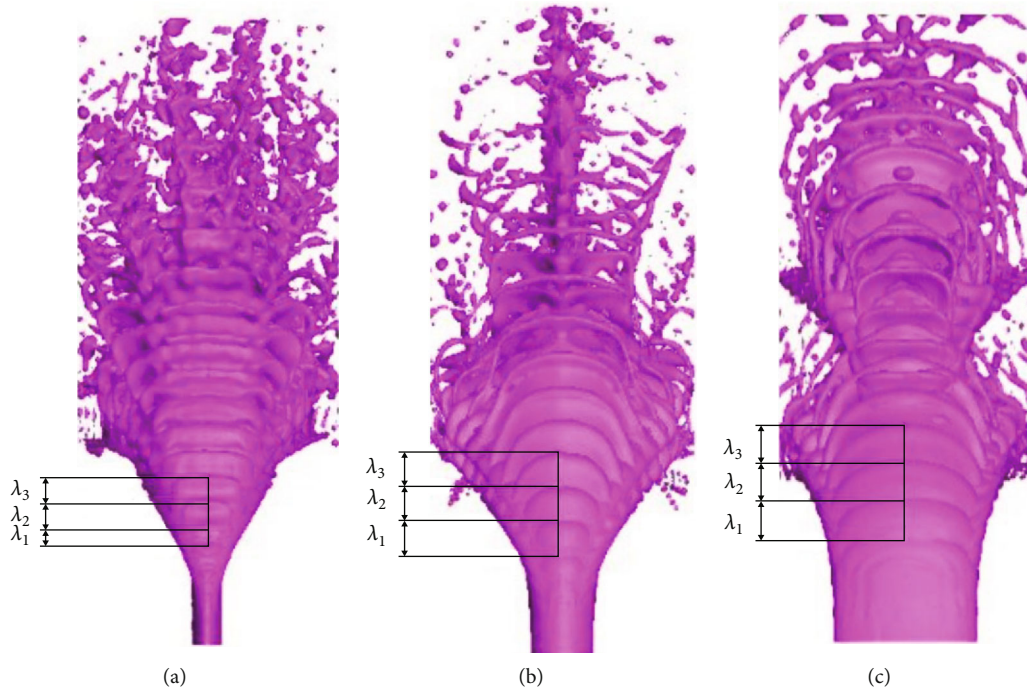
FIGURE 5: Measurement of surface wavelength for Case 1, Case 3, and Case 5.

Accordingly, a similar method has been used to check the grid resolution in Ref [38]. We used three different resolutions of the grid to simulate the cases in Table 3. There is a subtle difference between Grid-A and Grid-F in Figure 3. However, Grid-C predicts a significant interface shape compared with Grid-A and Grid-F. At last, the current grid (Grid-A) is chosen to be applied for all the cases in our works.

3. Results

3.1. Breakup Processes of Elliptical Liquid Jet in Supersonic Crossflow. Figure 4 shows the evolution of liquid jet breakup and the contours of the nondimensionalized pressure (P^*) in the gas crossflow at the AR of 0.25, 1, and 4. The difference of liquid column breakup process under these three aspect ratios is obvious, which will be taken as the main comparison condition in this paper. There is a bow shock wave forming ahead of the column. The primary breakup of the liquid jet includes two basic breakup modes: column breakup and surface breakup [2]. There are lots of ligaments stripping from the column in surface breakup mode. The liquid jet fractures on the central axis directly in column breakup mode. The length of a becomes shorter with the increase of the AR, while the length of b becomes longer with the increase of the AR at the same time, because of the same orifice area in all cases. Figure 5 shows that the wavelength of the initial surface waves becomes shorter with the decrease of the aspect ratio.

Figure 6 shows the cross-section of the jet at different locations, i.e., $y/D = 1, 2, 2.5, 3$, and 3.5. It can be seen that the liquid on the windward side pushes against both sides of the column in all calculated conditions. The column surface is peeled off from the liquid column due to the strong shear force. In the highest AR case, the droplet is fastest to peel off, and the jet is difficult to maintain the continuous liquid column shape and break up quickly, resulting in a chaotic section shape. However, in the working condition with the lowest AR, the jet can still retain a highly continuous column shape and have a relatively symmetric surface fracture due to the lower windward area. The airflow velocity on the leeward side is low, and the aerodynamic is not obvious. The morphology of the windside jet does not change too much; the jet can still maintain the shape of the initial column with a certain length after the surface breakage occurs. Based on the deformation law of a cross-section in present works in Figure 7, the windward area of the liquid jet is generally small when AR < 1, the pressure is larger on the stagnation point on the windward side, R-T instability dominates, and the liquid on the windward side is rapidly pushed to both left and right sides of the column and forms a pairs of reverse vortex pairs; When AR = 1, the flow field under the two-dimensional top view is similar to the flow field around a cylinder, which can be simply equivalent to the two-dimensional flow around a cylinder for analysis. The Kelvin-Helmholtz instability and R-T instability exist simultaneously. The liquid column will still undergo pushing deformation. Compared with the cases (AR < 1), the deformation occurs later, and the reverse vortex pairs are closer to the downstream region. When AR > 1, the windward area is generally larger. The aerodynamic force is larger at the left and right ends in the windward side of the jet. The surface breakup occurs earliest, and the influence of the K-H instability is greater than the R-T instability at this time. However, when the surface breakup occurs, the windward area decreases rapidly, and the R-T instability gradually becomes dominant and forms pairs of reverse vortex pairs.
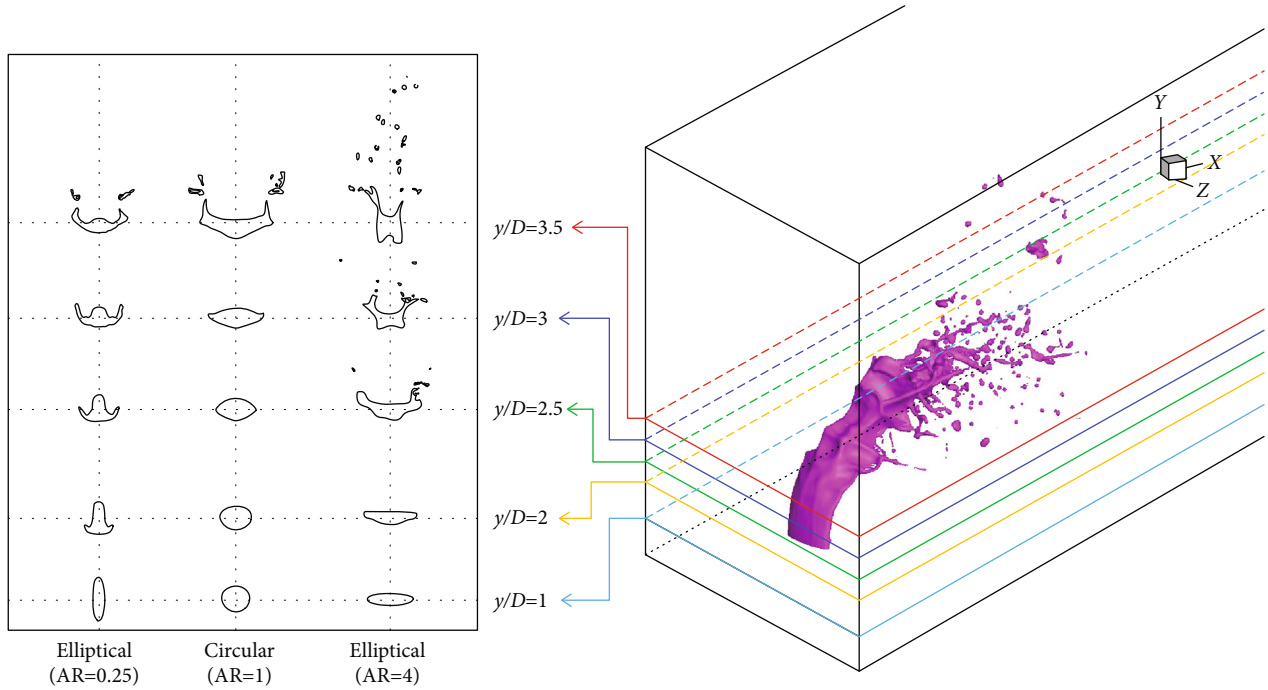
FIGURE 6: Cross-sectional shapes at $y/D = 2$, 2.5, and 3 for Case 1, Case 3, and Case 5, respectively, $t = 56.4\,\mu s$.

3.2. Spatial Distribution of Elliptical Jets. To obtain the penetration depth of the elliptical liquid jet clearly and accurately, we extracted 22 transient spray images at $z = 0$ section and superimposed them in Figure 8. In the primary breakup stage, the larger AR is, the lower the penetration depth is. The reason is that the length vertical to the gas flow direction becomes longer with the increase of the aspect ratio. The windward area of the jet becomes larger, and the drag force of the crossflow to the jet becomes larger; thus, more droplets were stripped from both sides of the liquid column. The penetration depth of the jet becomes lower due to more liquid mass loss derived from more droplet stripping. The result is consistent with the conclusion in subsonic flow in [43]. The penetration depth of the elliptical liquid jet (AR = 0.25) is 20% higher than the round liquid jet in Figure 9.

The spreading angle is the next significant spray characteristics. The spreading angle is defined in the upper right corner in Figure 10. Under the two-dimensional top view, the liquid drops from the center of the spray hole to the outermost edges of the left and right sides are straight lines, and the clamped angle is the spreading angle [43]. Figure 10 shows the spread angles at five different aspect ratios. The round jet has the widest spread angle which is 50.2°. Through the analysis of Figure 6, we can better understand the reason for the large spray spreading angle of the round jet. Apparently, the surface breakup of the round jet occurs later, so it maintains a bigger windward area. The further the droplets splash, the wider the spreading angle is. Compared with the round jet, the droplets of elliptical jets move away through the axial direction fragment from the sides.

Another index of atomization quality is the breakup length which is divided into the breakup length in the x direction (CBL_x) and the breakup length in the y direction (CBL_y).
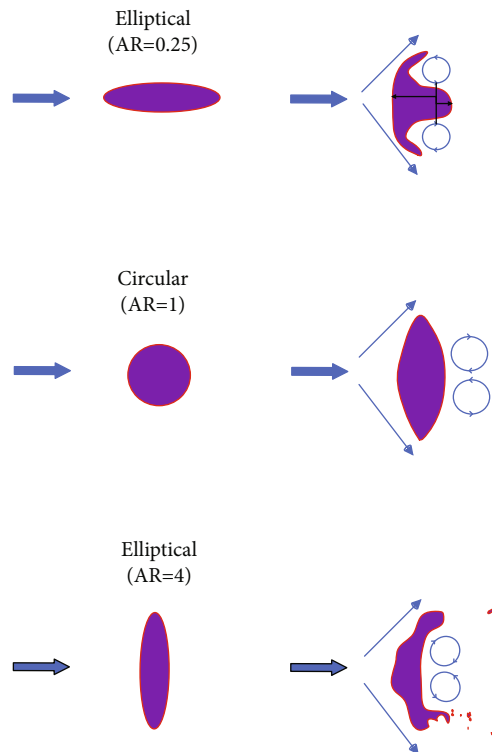

FIGURE 7: Breakup of elliptical liquid jets of three aspect ratios.

The breakup length represents the speed of the breakup of the liquid jet in the gas flow. Figure 11 shows that the isosurface ($\varphi = 0$) of the central section was extracted from the simulation results, and the liquid column breakup position was defined. The changing trend of the breakup
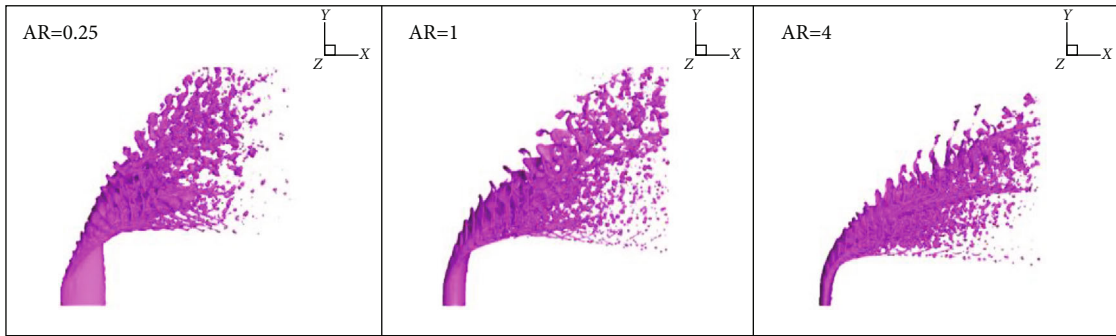
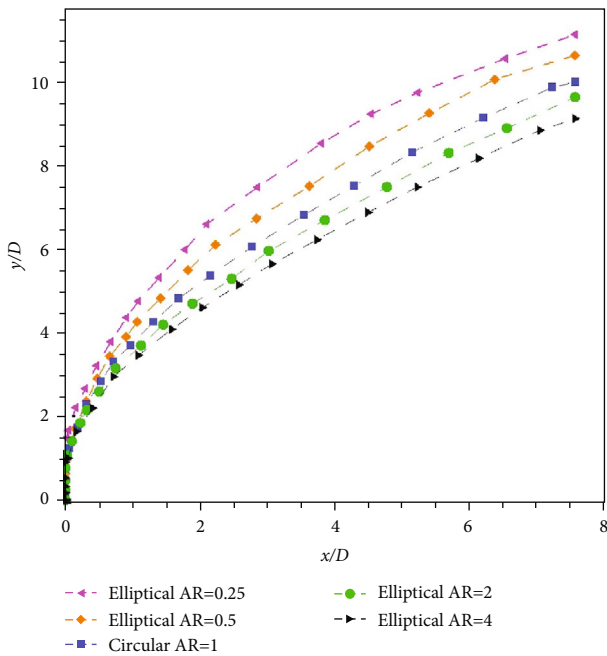FIGURE 8: Spray structure of the liquid jet in different AR.

FIGURE 9: Penetration depth of the liquid jet at different AR.

FIGURE 10: Spray spread angle of the round and elliptical orifice sprays.
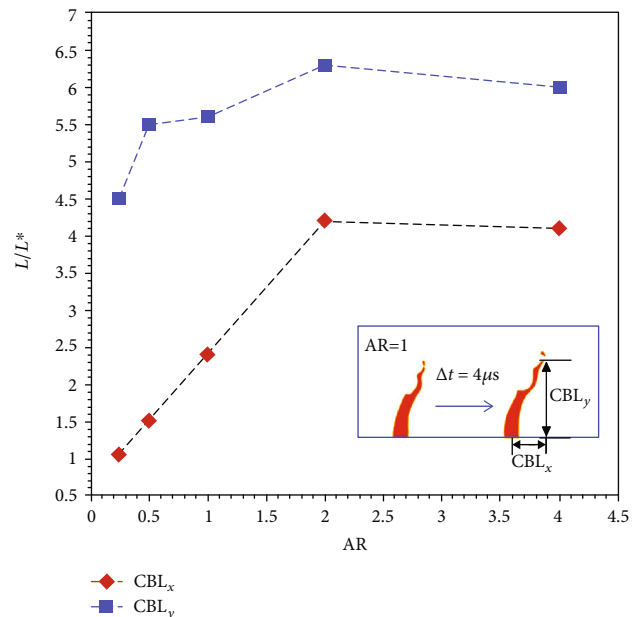
FIGURE 11: Liquid column breakup position and breakup length.

length between the x direction and y direction is basically similar. Apparently, in the cases $(AR < 1)$, the breakup length increases with the rise of AR, and the elliptical jet $(AR = 0.25)$ has the minimum breakup length in both directions, which is 59.2% lower than the round in the x direction, 18.8% lower than the round in the y direction, respectively. In the cases $(AR > 1)$, the breakup length increases first and then decreases slightly.

3.3. Flow Field Characteristics of Elliptical Jet and Round Jet.

Figure 12 presents a difference of the instantaneous vortex structures at three different AR. The column and surface breakup are observed at three AR at the same time. Compared with the round jet, there are more vortex structures in different scales near the location of surface breakup from the top left corner of Figure 12. The length of surface breakup in the y direction is lower, which leads to the vortex structure here being lower. As the aspect ratio increases, the blocking effect of the liquid jet on the crossflow is enhanced gradually. The induced horseshoe vortex structure is larger and becomes further away from the liquid column.
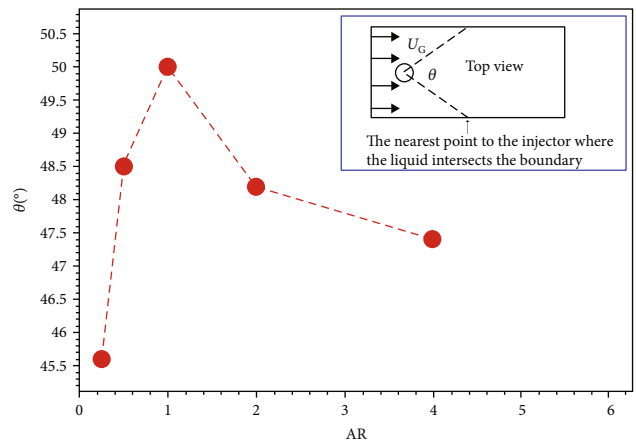
The dispersion of liquid droplets is determined by the large-scale vortices in the wake region which affects the mixing process of the spray deeply in the supersonic air flow in [35]. Figure 13 presents the vorticity distributions in slice
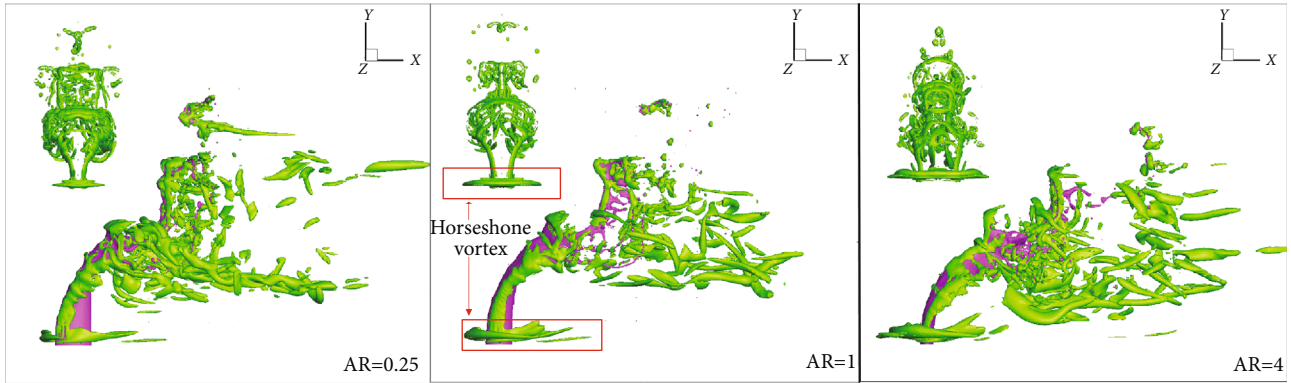
FIGURE 12: Instantaneous vortex structures in supersonic crossflow identified by isosurface of Q, $t = 56.4\,\mu s$.
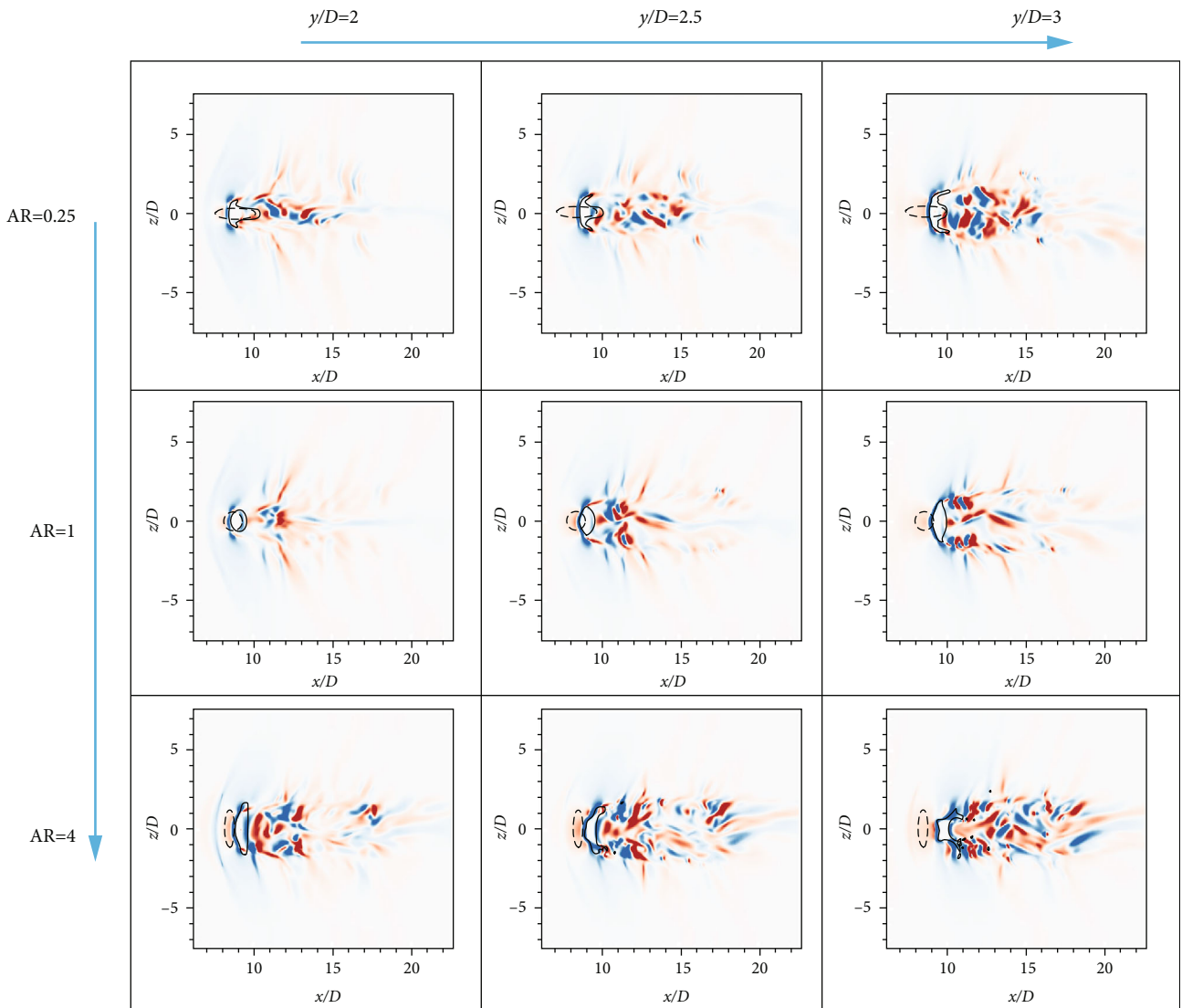
FIGURE 13: Vorticity distributions at $y/D = 2$, 2.5, and 3 for Case 1, Case 3, and Case 5.

$y/D = 2$, 2.5, and 3 for Case 1, Case 3, and Case 5, respectively. Anticlockwise vortexes and clockwise vortexes are shown in blue and red, respectively. The wake region of the elliptical liquid jet (AR = 4) is 18.4% larger than the round liquid jet.

The width of the wake region directly is reflected by the width of the windward side of the liquid column, which will change continuously due to the continuous breaking of the liquid column. The reason is that the occurrence of the surface

(a) Case 1

(b) Case 3

(c) Case 5

FIGURE 14: Streamlines with U^* contours in slice $x/D = 2$, 4, and 6 for three AR, $t = 56.4\,\mu$s.
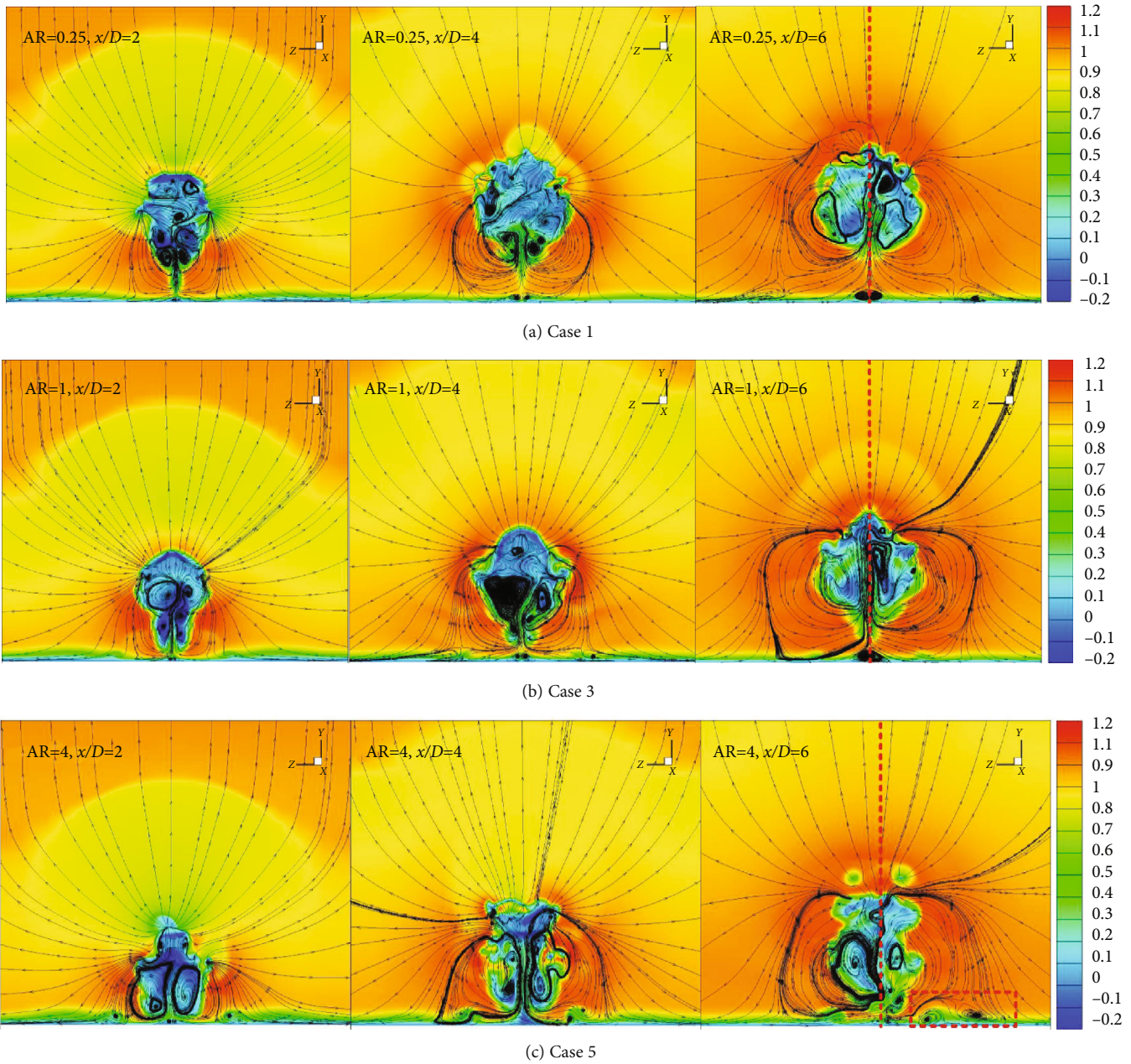
break is difficult to be synchronized, so there is a time difference when the gas goes through the column.

Figure 14 shows the two-dimensional streamlines at different slices, i.e., $x/D = 2$, 4, and 6 with the contours of the nondimensionalized x direction velocity (U^*) for three AR of 0.25, 1, and 4. Two pairs of reversal vortex pairs with obvious characteristics can be found under all working conditions. The first vortex pair located at the leeward side is relatively higher in height. The location of the vortex pairs becomes higher with the decrease of the aspect ratio due to the higher penetration depth. Furthermore, the vortex pairs will expand gradually with the increase of the flow distance. The direction of this vortex is straight up in the center line. The second vortex pairs located near the bottom wall have

a nice symmetry. But, there is a certain offset from the center line in the case ($AR = 4$). The liquid column has the largest windward area in this condition and breaks up fastest. The time of the surface breakup on both sides of the column is out of sync.

A three-dimensional liquid jet structure in space is presented in Figure 15. After the supersonic flow is obstructed by the liquid column, a separation zone is forming located ahead of the column represented by the green circle. The gas flows into the separation zone and forms a pair of horseshoe vortex represented by the purple circle. The red transparent region represents the bow shock. Furthermore, the green squares indicate the column breakup position and surface breakup position, respectively. It can be seen that two
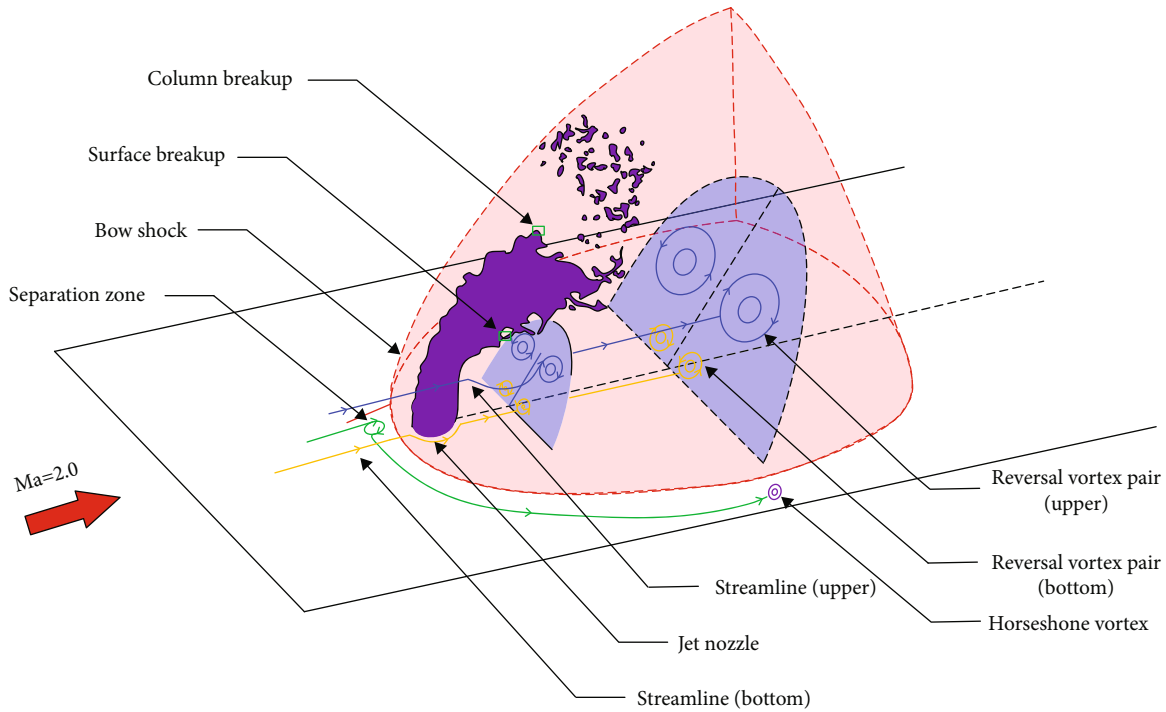
FIGURE 15: The flow field structure of the elliptical liquid jet in supersonic crossflow.

sections are taken in turn along the direction of the gas flow which is represented by dark blue, and two pairs of reverse vortex pairs are indicated by blue and orange circles. The vortex pairs become larger and larger gradually with the increases of the distance of gas flow.

4. Conclusions

In the current study, the primary breakup of a liquid jet of different orifices has been evaluated numerically. The aspect ratios are set to be 0.25, 0.5, 1, 2, and 4. The spatial distribution including the changes of the jet's cross-section, liquid penetration depth, spreading angle, and breakup length has been compared at different aspect ratios. The flow field characteristics of the elliptical jet and round jet have been analyzed through the simulations. We have come to the following conclusions:

(1) Under the condition of supersonic crossflow, the surface breakup dominated by the R-T instability occurs earlier than that of the round liquid jet. The main reason is that the initial segment of the liquid column has different lengths in both the flow direction and spanwise direction. This result breaks the sequence and dominant degree of the K-H instability with the R-T instability in the round orifice indirectly and promotes the occurrence of the surface breakup, so the surface breakup of the elliptical orifice jet occurs earlier than the round liquid jet. As a result, elliptical orifices can shorten the time of the surface breakup effectively

(2) In the liquid jet spatial distribution, the jet has a higher penetration depth at a larger aspect ratio normally. The penetration depth of the elliptical orifice with AR = 0.25 is 20% higher than the round orifice. When the jet orifice is round, the maximum spreading angle is 50.2. The windward area of the jet becomes larger, and the resistance of the crossflow to the jet becomes larger. The jet becomes more curved, so the penetration depth is smaller. At the same time, the surface breakup of the elliptical orifice jet occurs earlier than the round orifice; the round orifice can maintain a larger windward area in the downstream area of primary breakup, so it has the largest spreading angle. Therefore, the round orifice can enable the spray to reach a moderate penetration depth and a maximum spreading angle

(3) The changing trends of the breakup length of the jet in both directions are basically similar. The CBL_x (AR = 0.25) is 59.2% lower than the round orifice, and the breakup length in the y direction is 18.8% lower than the round orifice, resulting in the smaller the aspect ratio is, the smaller the windward area is. The greater the aerodynamic force on the unit area of the windward surface of the jet is, the more prone the jet column is to liquid column breakup, so the breakup length is smaller

(4) After analyzing the flow field characteristics of the liquid jet, it is found that the horseshoe vortex structure in front of the jet increases with the increase of the aspect ratio and becomes further away from the

liquid column. The width of the wake area of the elliptical orifice ($AR = 4$) is 18.4% larger than that of the round orifice. Secondly, the surface breakup on both sides of the elliptical orifice liquid jet is generally difficult to synchronize. Two pairs of reversal vortex pairs with obvious characteristics can be found under all working conditions. The first vortex pair located at the leeward side is relatively higher in height. The location of the vortex pair becomes higher with the decrease of the aspect ratio due to the higher penetration depth. Furthermore, the vortex pairs will expand gradually with the increase of the flow distance. The direction of this vortex is straight up in the center line. The second vortex located near the bottom wall has a nice symmetry. The time of the surface breakup on both sides of the column is out of sync. After the airflow passes through the surface breakup position, there is a time difference when it flows into the rear of the liquid column, which eventually leads to the asymmetric center offset vortex pairs behind the liquid column different from the round liquid jet

Nomenclature

AR:	Orifice cross-section aspect ratio (b/a)
CBL_x:	Breakup length in the x direction
CBL_y:	Breakup length in the y direction
CLSVOF:	Coupled level set and volume of fluid
D:	Equivalent liquid jet diameter
F:	Liquid volume fraction
LS:	Level set
Ma:	Mach number
P_G:	Gas static pressure
P_L:	Water pressure
P^*:	Nondimensionalized pressure $P/(\rho_G U_G^2)$
Q:	Second invariance of velocity gradient tensor
T_G:	Temperature
U_L:	Liquid density
U_G:	Gas velocity
U^*:	Nondimensionalized x direction velocity U/U_G
VOF:	Volume of fluid
a:	Orifice diameter parallel to the gas flow
b:	Orifice diameter normal to the gas flow
q:	Liquid/gas momentum flux ratio
λ:	Surface wavelength
μ_G:	Gas viscosity
μ_L:	Liquid viscosity
ρ_G:	Gas density
ρ_L:	Liquid density
σ:	Surface tension
φ:	Level set function
We_G:	Relative gas-liquid Weber number $\rho_G U_G^2 D_{eq}/\sigma$.

Data Availability

The datasets generated during and/or analyzed during the current study are available from the corresponding author on reasonable request.

Conflicts of Interest

The authors declare that they have no conflicts of interest.

Acknowledgments

References

[1] E. A. Kush and J. A. Schetz, "Liquid jet injection into a supersonic flow," *AIAA Journal*, vol. 11, no. 9, pp. 1223-1224, 1973.

[2] J. A. Schetz, E. A. Kush, and P. B. Joshi, "Wave phenomena in liquid jet breakup in a supersonic crossflow," *AIAA Journal*, vol. 18, no. 7, pp. 774–778, 1980.

[3] K.-C. Lin, P. Kennedy, and T. Jackson, "Structures of water jets in a Mach 1.94 supersonic crossflow," in *Proceedings of the 42nd AIAA Aerospace Sciences Meeting and Exhibit*, Reno, Nevada, January 2004.

[4] C. Li, C. Li, F. Xiao, Q. Li, and Y. Zhu, "Experimental study of spray characteristics of liquid jets in supersonic crossflow," *Aerospace Science and Technology*, vol. 95, p. 105426, 2019.

[5] L. Y. Wu, Z. G. Wang, Q. Li, and C. Li, "Study on transient structure characteristics of round liquid jet in supersonic crossflows," *Journal of Visualization*, vol. 19, no. 3, pp. 337–341, 2016.

[6] Z. G. Wang, L. Wu, Q. Li, and C. Li, "Experimental investigation on structures and velocity of liquid jets in a supersonic crossflow," *Applied Physics Letters*, vol. 105, no. 13, article 134102, 2014.

[7] J. B. Perurena, C. O. Asma, R. Theunissen, and O. Chazot, "Experimental investigation of liquid jet injection into Mach 6 hypersonic crossflow," *Experiments in Fluids*, vol. 46, no. 3, pp. 403–417, 2009.

[8] P. K. Wu, K. A. Kirkendall, R. P. Fuller, and A. S. Nejad, "Breakup processes of liquid jets in subsonic crossflows," *Journal of Propulsion and Power*, vol. 13, no. 1, pp. 64–73, 1997.

[9] F. Jabbari, M. Jadidi, R. Wuthrich, and A. Dolatabadi, "A numerical study of suspension injection in plasma-spraying process," *Journal of Thermal Spray Technology*, vol. 23, no. 1-2, pp. 3–13, 2014.

[10] M. Jadidi, S. Moghtadernejad, and A. Dolatabadi, "A comprehensive review on fluid dynamics and transport of suspension liquid droplets and particles in high-velocity oxygen-fuel (HVOF) thermal spray," *Coatings*, vol. 5, no. 4, pp. 576–645, 2015.

[11] S.-Y. No, "A review on empirical correlations for jet/spray trajectory of liquid jet in uniform cross flow," *International Journal of Spray and Combustion Dynamics*, vol. 7, no. 4, pp. 283–313, 2015.

[12] M. Jadidi, S. Moghtadernejad, and A. Dolatabadi, "Penetration and breakup of liquid jet in transverse free air jet with application in suspension-solution thermal sprays," *Materials & Design*, vol. 110, pp. 425–435, 2016.

[13] M. Jadidi, S. Moghtadernejad, and A. Dolatabadi, "Numerical simulation of primary breakup of round nonturbulent liquid jets in shear-laden gaseous crossflow," *Atomization and Sprays*, vol. 27, no. 3, pp. 227–250, 2017.

[14] K. Lee, C. Aalburg, F. J. Diez, G. M. Faeth, and K. A. Sallam, "Primary breakup of turbulent round liquid jets in uniform crossflows," *AIAA Journal*, vol. 45, no. 8, pp. 1907–1916, 2007.

[15] K. A. Sallam, C. Aalburg, and G. M. Faeth, "Breakup of round nonturbulent liquid jets in gaseous crossflow," *AIAA Journal*, vol. 42, no. 12, pp. 2529–2540, 2004.

[16] J. Song, K. Ahn, M.-K. Kim, and Y. Yoon, "Effects of orifice internal flow on liquid jets in subsonic crossflows," *Journal of Propulsion and Power*, vol. 27, no. 3, pp. 608–619, 2011.

[17] M. Herrmann, "Detailed numerical simulations of the primary atomization of a turbulent liquid jet in crossflow," *Journal of Engineering for Gas Turbines and Power*, vol. 132, no. 6, 201061506-61510.

[18] S. E. Bechtel, J. A. Cooper, M. G. Forest et al., "A new model to determine dynamic surface tension and elongational viscosity using oscillating jet measurements," *Journal of Fluid Mechanics*, vol. 293, pp. 379–403, 1995.

[19] T. V. Kasyap, D. Sivakumar, and B. N. Raghunandan, "Flow and breakup characteristics of elliptical liquid jets," *International Journal of Multiphase Flow*, vol. 35, no. 1, pp. 8–19, 2009.

[20] G. Amini and A. Dolatabadi, "Axis-switching and breakup of low-speed elliptic liquid jets," *International Journal of Multiphase Flow*, vol. 42, pp. 96–103, 2012.

[21] P. Sharma and T. Fang, "Breakup of liquid jets from non-circular orifices," *Experiments in Fluids*, vol. 55, no. 2, p. 1666, 2014.

[22] F. Wang and T. Fang, "Liquid jet breakup for non-circular orifices under low pressures," *International Journal of Multiphase Flow*, vol. 72, pp. 248–262, 2015.

[23] M. Marzbali, *Penetration of circular and elliptical liquid jets into gaseous crossflow*, Doctoral dissertation, Concordia University, 2011.

[24] M. R. Morad and H. Khosrobeygi, "Penetration of elliptical liquid jets in low-speed crossflow," *Journal of Fluids Engineering*, vol. 141, no. 1, 2019011-301.

[25] D. H. Fontes, V. Vilela, L. Souza Meira, and F. José de Souza, "Improved hybrid model applied to liquid jet in crossflow," *International Journal of Multiphase Flow*, vol. 114, pp. 98–114, 2019.

[26] N. Liu, Z. G. Wang, M. B. Sun, R. Deiterding, and H. Wang, "Simulation of liquid jet primary breakup in a supersonic crossflow under adaptive mesh Refinement framework," *Aerospace Science and Technology*, vol. 91, pp. 456–473, 2019.

[27] C. H. Chang, X. Deng, and T. G. Theofanous, "Direct numerical simulation of interfacial instabilities: a consistent, conservative, all-speed, sharp-interface method," *Journal of Computational Physics*, vol. 242, pp. 946–990, 2013.

[28] J. C. Meng and T. Colonius, "Numerical simulation of the aerobreakup of a water droplet," *Journal of Fluid Mechanics*, vol. 835, pp. 1108–1135, 2018.

[29] F. Xiao, Z. G. Wang, M. B. Sun, N. Liu, and X. Yang, "Simulation of drop deformation and breakup in supersonic flow," *Proceedings of the Combustion Institute*, vol. 36, no. 2, pp. 2417–2424, 2017.

[30] D. P. Garrick, W. A. Hagen, and J. D. Regele, "An interface capturing scheme for modeling atomization in compressible flows," *Journal of Computational Physics*, vol. 344, pp. 260–280, 2017.

[31] D. P. Garrick, M. Owkes, and J. D. Regele, "A finite-volume hllc-based scheme for compressible interfacial flows with sur-face tension," *Journal of Computational Physics*, vol. 339, pp. 46–67, 2017.

[32] V. B. Betelin, N. N. Smirnov, V. F. Nikitin, V. R. Dushin, A. G. Kushnirenko, and V. A. Nerchenko, "Evaporation and ignition of droplets in combustion chambers modeling and simulation," *Acta Astronautica*, vol. 70, pp. 23–35, 2012.

[33] P. B. Li, Z. G. Wang, X. S. Bai et al., "Three-dimensional flow structures and droplet-gas mixing process of a liquid jet in supersonic crossflow," *Aerospace Science and Technology*, vol. 90, pp. 140–156, 2019.

[34] P. B. Li, Z. G. Wang, M. B. Sun, and H. Wang, "Numerical simulation of the gas-liquid interaction of a liquid jet in supersonic crossflow," *Acta Astronautica*, vol. 134, pp. 333–344, 2017.

[35] Y. H. Zhu, F. Xiao, Q. L. Li, R. Mo, C. Li, and S. Lin, "Les of primary breakup of pulsed liquid jet in supersonic crossflow," *Acta Astronautica*, vol. 154, pp. 119–132, 2019.

[36] M. Sussman and E. G. Puckett, "A coupled level set and volume-of-fluid method for computing 3D and axisymmetric incompressible two-phase flows," *Journal of Computational Physics*, vol. 162, no. 2, pp. 301–337, 2000.

[37] F. Xiao, *Large eddy simulation of liquid jet primary breakup*, PhD, Loughborough University, 2012.

[38] F. Xiao, Z. G. Wang, M. B. Sun, J. H. Liang, and N. Liu, "Large eddy simulation of liquid jet primary breakup in supersonic air crossflow," *International Journal of Multiphase Flow*, vol. 87, no. 12, pp. 229–240, 2016.

[39] F. Xiao, M. Dianat, and J. J. McGuirk, "A robust interface method for drop formation and breakup simulation at high density ratio using an extrapolated liquid velocity," *Computers & Fluids*, vol. 136, pp. 402–420, 2016.

[40] R. P. Fedkiw, T. Aslam, B. Merriman, and S. Osher, "A non-oscillatory eulerian approach to interfaces in multimaterial flows (the ghost fluid method)," *Journal of Computational Physics*, vol. 152, no. 2, pp. 457–492, 1999.

[41] X. D. Liu, R. P. Fedkiw, and M. Kang, "A boundary condition capturing method for poisson's equation on irregular domains," *Journal of Computational Physics*, vol. 160, no. 1, pp. 151–178, 2000.

[42] G. S. Jiang and C. W. Shu, "Efficient implementation of weighted eno schemes," *Journal of Computational Physics*, vol. 126, no. 1, pp. 202–228, 1996.

[43] E. Farvardin and A. Dolatabadi, "Breakup simulation of elliptical liquid jet in gaseous crossflow," in *42nd AIAA Fluid Dynamics Conference and Exhibit*, New Orleans, Louisiana, June 2012.